MECHANISMS UNDERLYING PROTEIN SORPTION AND TRANSPORT WITHIN POLYSACCHARIDE-BASED STATIONARY PHASES FOR ION-EXCHANGE CHROMATOGRAPHY

by

James Michael Angelo

A dissertation submitted to the Faculty of the University of Delaware in partial fulfillment of the requirements for the degree of Doctor of Philosophy in Chemical Engineering

Spring 2016

MECHANISMS UNDERLYING PROTEIN SORPTION AND TRANSPORT WITHIN POLYSACCHARIDE-BASED STATIONARY PHASES FOR ION-EXCHANGE CHROMATOGRAPHY

by

James Michael Angelo

Approved: _____

Abraham M. Lenhoff, Ph.D.
Chair of the Department of Chemical and Biomolecular Engineering

Approved: _____

Babatunde A. Ogunnaike, Ph.D.
Dean of the College of Engineering

Approved: _____

Ann L. Ardis, Ph.D.
Senior Vice Provost for Graduate and Professional Education

I certify that I have read this dissertation and that in my opinion it meets the academic and professional standard required by the University as a dissertation for the degree of Doctor of Philosophy.

Signed: _____

Abraham M. Lenhoff, Ph.D.
Professor in charge of dissertation

I certify that I have read this dissertation and that in my opinion it meets the academic and professional standard required by the University as a dissertation for the degree of Doctor of Philosophy.

Signed: _____

Norman J. Wagner, Ph.D.
Member of dissertation committee

I certify that I have read this dissertation and that in my opinion it meets the academic and professional standard required by the University as a dissertation for the degree of Doctor of Philosophy.

Signed: _____

Christopher J. Roberts, Ph.D.
Member of dissertation committee

I certify that I have read this dissertation and that in my opinion it meets the academic and professional standard required by the University as a dissertation for the degree of Doctor of Philosophy.

Signed: _____

Mark R. Schure, Ph.D.
Member of dissertation committee

I certify that I have read this dissertation and that in my opinion it meets the academic and professional standard required by the University as a dissertation for the degree of Doctor of Philosophy.

Signed: _____

Chandran Sabanayagam, Ph.D.
Member of dissertation committee

ACKNOWLEDGMENTS

I would like to thank all of the people that have had an influence on me in the pursuit of my academic goals. First and foremost, Bramie Lenhoff has been the quintessential advisor to me. His guidance and wealth of knowledge has furthered my understanding in the field of chromatography immeasurably, and for that I am forever grateful. Even when the hurdles of research seemed too challenging to overcome, I knew I could always count on Bramie to point me in the right direction and give me the motivation to soldier on. His encouragement to find my own path (even when my path was sometimes a bit rough on the suspension) has shaped me in a way that I believe will be invaluable for whatever the future may bring. Thank you, Bramie.

I'd also like to thank all the past and current members of the Lenhoff research group. Brian Bowes, Harun Koku and Steve Traylor gave me a great basis of experimental and theoretical knowledge during my time starting out in the lab. I'll always appreciate the hours Steve and Harun spent with me at DBI to train me to do EM and confocal imaging. Steve's expertise in Matlab was also genuinely helpful in the modeling of adsorptive data during that formative time for me. Nick Levy was a great officemate and friend for four years and made coming to work all that more enjoyable. Rahul Bhambure was a superb collaborator and colleague during his time with the group, as the sharing of knowledge between our respective projects was mutually beneficial and fulfilling. Steve Timmick was a splendid undergraduate researcher to work with and I'm happy to have convinced him to choose to go to RPI for graduate school (sorry other Steve). Anvar Samadzoda, Dan Greene, Stijn Koshari,

Amit Vaish, Kristin Valente, Leigh Quang, Kelley Kearns, Tao Liu, David Rosenman, and Ohnmar Khanal were all wonderful groupmates to have and I wish all of them success in the future.

I'd also like to thank the technicians at the DBI Bioimaging Center that helped train and assist me on much of the imaging results presented in this dissertation. Chandran Sabanayagam, Shannon Modla, Debbie Powell, and Mike Moore all were critical in instructing me in the operation of advanced electron and confocal microscopes and discussions with them helped further my understanding of these techniques that I had the pleasure and opportunity to learn.

Thank you to all of the professors and teachers that have fostered my quest for knowledge. Back in high school, I looked up most to my calculus teachers, Mr. and Mrs. Davis, and my physics teacher, Mr. Gilroy, whom I attribute my foundation of math and science to. My time at Rensselaer Polytechnic Institute before attending UDel was a great experience primarily due to Professor Steve Cramer's exuberant and highly-energetic classes in unit operations and bioseparations. His mentorship during my tenure in his research group also reaffirmed the choice I made to pursue further study in the field of chromatography. I'd also like to thank all of my professors that guided me and my classmates during the first few years of graduate school, especially Chris Roberts and Ed Lyman, who instructed me in the very intellectually stimulating areas of statistical mechanics and protein biophysics.

Of course, without the people that I've had the pleasure of building friendships with over the years, I don't really know where I'd be, as spending time with all of them has truly made Delaware my home for five and a half years. Friends like Marc, Zack, Doug, Jarrid, Angie, Olga, Chris, and Abhinav don't come around all too often

and I'd like to thank them for all the good times we had together. I'd like to thank Kyle, Heejae, Jey, Nate, and Shy (especially Shy) for tolerating all my bad habits at home. Living, cooking, brewing, and having fun with all of these wonderful people has provided me with so many great memories that I will never forget. I can't even begin to express the ways Shy'Ann has changed my life for the better, and I will always love her for it.

Finally, I must express my deepest gratitude for the most important people in my life: Mom, Dad, and Matt. My family has given me the drive, the focus, the support, and the love to propel me to where I'm at today. My mother has always been there for me, helping me through tough times with tenderness and care. I'm always grateful for everything she does for me and our family. My father has been an inspiration to me for as long as I can remember. I've always had it in the back of my mind that one day I could achieve everything he has achieved throughout his life, both as a personal goal of mine and as a point of pride for us both. I hope that this work, and the culmination of my academic career, can make my family proud, as it has been a wonderfully fulfilling experience for me. Thank you all.

TABLE OF CONTENTS

LIST OF TABLES

LIST OF FIGURES

ABSTRACT

Ion-exchange chromatography is a powerful tool that is widely utilized in the downstream purification of biomolecules. As the biotechnology industry continues to grow and develop new molecules and therapeutics, resins that exhibit enhanced chromatographic performance are widely desired to streamline purification processes and meet production requirements. Polysaccharide-based ion-exchange adsorbents meet many performance standards by possessing high binding capacities and enhanced uptake rates of protein, while being highly compatible with biologics and remaining relatively cost-efficient. The characterization of these materials is crucial for informed decisions during stationary-phase selection and process design.

The structural characteristics of agarose-based, dextran-modified agarose-based and cellulosic ion-exchange materials were assessed using methods to gauge the pore dimensions and the effect of ionic strength on intraparticle architecture. Inverse size exclusion chromatography (ISEC) analysis yielded an average pore radius on the order of 5 nm within cellulosic and polymer-modified adsorbents, which also presented particularly narrow pore-size distributions. Electron microscopy techniques were used to visualize particle structure and relate it to macroscopic experimental data. Microscopy of cellulosic anion-exchangers with varying salt-tolerances presented qualitative differences in pore structure that can be attributed to their derivatization using conventional quaternary ammonium and salt-tolerant ligands. The effect of ionic strength was studied through the use of salt breakthrough experiments to determine to what extent Donnan exclusion plays a role in restricting the accessible pore volume for

small ions. It was determined that Donnan effects were prevalent at total ionic strengths (TIS) less than 150 mM, suggesting the presence of a ligand-containing partitioning volume within the pore space.

Adsorption behavior in these materials was characterized using methods to assess, quantitatively and qualitatively, the dynamics of protein uptake as a function of ionic strength and protein concentration using several model proteins. The cellulosic exchangers studied all presented relatively high adsorptive capacities under low ionic strength conditions, comparable to resins containing polymer functionalization aimed at increasing that particular characteristic. The strong cation- and anion-exchange moieties showed higher sensitivity to increasing salt ranges, but protein affinity on the salt-tolerant exchanger remained strong at ionic strength ranges normally used in downstream processing to elute material fully during ion-exchange chromatography. Fast uptake rates were observed in both batch kinetics experiments and time-series confocal laser scanning microscopy (CLSM) for the cellulosic media, suggesting low intraparticle transport resistances relative to external film resistance, even at higher bulk protein concentrations where the opposite is typically observed.

The rate processes involved in elution during preparative chromatography can affect both peak resolution and hence selectivity, as well as practical factors such as facility fit. These processes depend on the physical structure of the adsorbent particles, the amount of bound solute, the solution conditions for operation or some combination of these factors. While polysaccharide-based materials possess easily accessible microstructures that offer substantial binding capacities and fast uptake rates, elution has sometimes been observed to be undesirably slow. In order to determine which physicochemical phenomena control elution behavior, the materials

were characterized by their uptake and elution profiles at various conditions, including different degrees of loading. Elution data were analyzed under the assumption of purely diffusion-limited control, including the role of pore structure properties such as porosity and tortuosity. In general, effective elution rates decreased with the reduction of accessible pore volume, but differences among different proteins indicated the roles of additional factors. Additional measurements and analysis, including the use of CLSM to observe elution within single chromatographic particles, indicated the importance of protein association within the particle during elution. The use of protein stabilizing agents was explored in systems presenting atypical elution behavior, and L-arginine and disaccharide excipients were shown to alleviate the effects for one protein, lysozyme, in the presence of sodium chloride. Incorporation of these excipients into eluent buffer gave rise to faster elution and significantly lower pool volumes in elution from polymer-modified agarose adsorbents.

Finally, thermodynamic modeling based on molecular theory was used in conjunction with single-molecule super-resolution microscopy to further develop the understanding of fundamental mechanisms of protein adsorption within polymer-modified surface layers. Molecular theory and binary adsorption experiments gave insights into preferential adsorption on charged surfaces with and without dextran modification, analogous to the agarose-based media studied throughout this work. Dextranized surfaces presented adsorption systems more tolerant of acidic environments compared to their non-polymer modified counterparts due to changes in the local pH and charge of protein close to the surface. The trajectories of tracked single molecules on dextran-derivatized surfaces acquired via total internal reflection fluorescence microscopy (TIRFM) were analyzed to obtain mean-squared

displacements. The effect of solution salt concentration on the adsorption and lateral diffusion of fluorescently-labeled lysozyme revealed characteristics that were in agreement with protein transport in stationary phase analogues to these surfaces. The ability to visualize protein movement directly and relating it to the environment within porous adsorbents could have implications for future stationary phase design and operation of these materials.

Chapter 1

INTRODUCTION

1.1 The Role of Protein Purification in Biologics Manufacturing

Over the past few decades, the biotechnology industry has matured and expanded rapidly, especially in the reliable manufacturing of biopharmaceutical drugs. In 2014, the cumulative market value of all biotech companies surpassed $1 trillion (Morrison and Lähteenmäki, 2015), a large portion of which is comprised of biopharmaceutical manufacturing. With the advent of engineered therapeutic proteins such as monoclonal antibodies (mAb), used to target specific epitopes for the treatment of a multitude of cancer and autoimmune diseases, a platform process approach has become the paradigm for downstream purification. Nevertheless, providing optimized and efficient separation of target molecules has been a necessity to satisfy the regulatory requirements for all types of biological drugs.

Typically, biologics such as mAbs are cultured in mammalian or bacterial host cells, after which feedstocks containing the species of interest are clarified and concentrated before the application of more downstream purification steps. With components such as extraneous cell lysate, infectious agents (e.g., viruses) and protein aggregates still being present in the feed to the purification chain, the stringent purification process requires a significant investment of time and money to remove these types of impurities and meet regulatory standards. In a 2010 report on the biopharmaceutical industry, it is stated that purification costs may comprise up to 80% of the total cost of production (Walsh, 2010).

While Protein A affinity chromatography is currently the standard for mAb capture, providing high purity of the target protein directly following upstream clarification, ion-exchange chromatography (IEX) is widely used in the remainder of the purification process, being utilized in steps from capture (Gräslund et al., 2002; Necina et al., 1998), to viral clearance (Curtis et al., 2003; Strauss et al., 2009), to polishing. In purification platforms that are not dependent on Protein A for capture, IEX chromatography can comprise up to 75% of the purification steps employed (Boschetti, 1994). A distinct advantage that IEX has over affinity resins is the much lower cost (Follman and Fahrner, 2004) as well as reusability, as Protein A resins have a shorter cyclical lifetime due to ligand leaching (Swinnen et al., 2007).

The adsorptive mechanism in IEX chromatography is also conceptually simple, taking advantage of differences in the charge of the protein solutes. Cation exchangers (CEX) bind positively-charged proteins by being derivatized with negatively-charged functional groups, such as sulfonate (CH_2-SO_3^-), while anion exchangers (AEX) bind negatively-charged proteins by being derivatized with positively-charged functional groups, such as quaternary ammonium (CH_2-N^+-$(CH_3)_3$). CEX materials are typical for steps requiring adsorption and retentivity of mAbs due to the relatively high isoelectric point (pI) of those types of proteins (pI ~ 7.5-8.5), while AEX materials are well suited for viral clearance operated in the flow-through mode (Curtis et al., 2003; Strauss et al., 2009).

There is a societal need to have more effective solutions in all types of industry. New technologies and methods are essential in realizing the changes necessary to implement more cost-effective pharmaceutical manufacturing (Gottschalk et al., 2012). Employing more recently developed types of purification strategies, such

as continuous chromatography and simulated moving bed technologies (Juza et al., 2000; Migliorini C., 1998; Müller-Späth et al., 2010; Seidel-Morgenstern et al., 2008), may provide an overall increase in productivity. However, the development of optimized adsorbent materials is also critical in improving performance in such respects as selectivity, adsorptive rates and binding capacities, which are all tied to the overall throughput of the purification processes.

To address this concern, many novel materials for bioseparations have been designed over the years to help improve chromatographic performance. For example, materials that provide three-dimensional binding volumes for proteins, such as "gel-in-a-shell" resins like HyperD, have been shown to have enhanced uptake rates as well as increased binding capacities (Boschetti and Coffman, 2008; Lewus et al., 1998; Weaver and Carta, 1996). However, the full extension of the binding layer to occupy the entirety of the pore space does have the disadvantage of excluding larger proteins or solutes that may be incompatible with finer mesh sizes. Polymer-modified materials, or resins that possess covalently attached polymer extenders within the pore volume, provide a compromise between the "gel-in-a-shell" type of adsorbent and conventional macroporous resins.

In this work, characteristics of both polymer-modified and non-polymer-modified resins were explored on matrices fully composed of natural carbohydrate polymers, i.e., polysaccharides. The carbohydrates that typically comprise these adsorbents are based on cross-linked agarose, dextran, cellulose, or a combination of several polymers. The distinct advantage of polysaccharide-based adsorbents is their compatibility with biological molecules, like mAbs, due to their low non-specific binding (de Oliveira and Glasser, 1996; Peterson, 1970) and their highly

interconnected pore networks (Yao et al., 2006). These features provide ample surface area for adsorption in the case of non-polymer-modified resins and ample pore volumes for polymer extenders to occupy in the case of polymer-modified resins. The softer and more flexible nature of these resins causes them to be somewhat more compressible than beads composed of silica, ceramic or methacrylate. However, the cross-linked nature still allows for mechanical as well as chemical stability, even in conditions typical for harsh cleaning protocols.

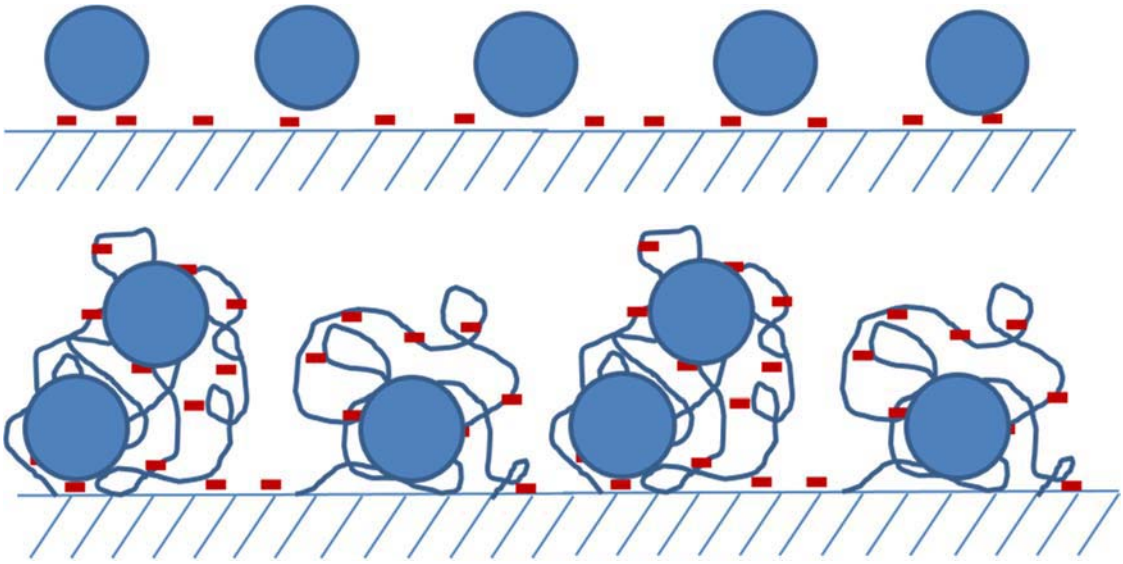

Figure 1.1 Schematic representation of monolayer protein adsorption on a conventional stationary phase pore surface (top) and protein adsorption within a polymer-modified stationary phase (bottom).

The extension of the adsorptive surface area into a volumetric partitioning layer provides a drastic increase in dynamic and static capacities as effectively multilayer adsorption is facilitated (Bowes et al., 2009; Kawai et al., 2003; Lenhoff, 2011; Yu et al., 2011), as shown in Figure 1.1. Uptake of protein is faster in these

adsorbents as well, as homogeneous diffusion (also called solid diffusion) is often the dominant transport mechanism. Here, sorbed protein is able to move within the polymeric layer at a rate that, although limited by lower mobilities in the polymer, is increased by the high local protein concentration (Bowes and Lenhoff, 2011a; Stone and Carta, 2007; Yu et al., 2011). Figure 1.2 shows the uptake of protein with time in several different IEX resins, all possessing the same functional moiety. The primary difference here is in adsorbent composition, and hence pore microstructure, a facet that will remain an overarching theme throughout this dissertation.

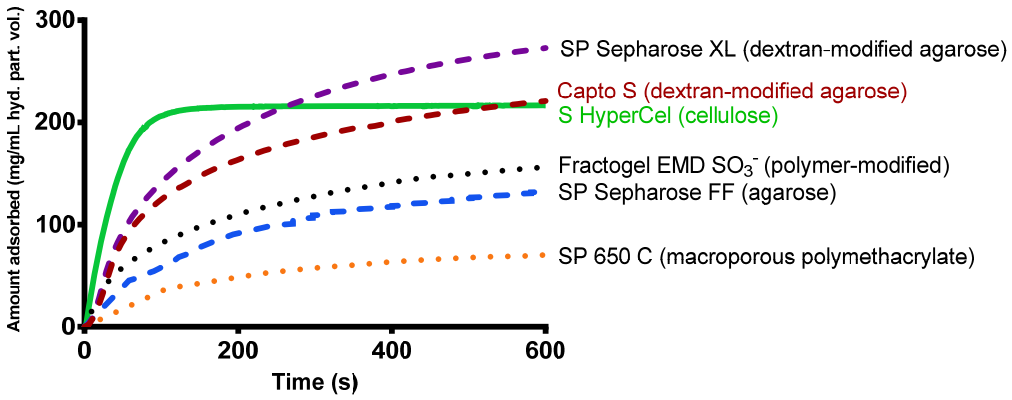

Figure 1.2 Adsorptive uptake of lysozyme on commercially available cation-exchange adsorbents in terms of mass per unit hydrated particle volume of resin (10 mM sodium phosphate, pH 7). The type of material and general base matrix composition is listed to the right of each plot. SP 650 data from (Dziennik, 2002); Fractogel data collected by Rahul Bhambure.

A special case that is explored extensively in this dissertation is the rapid saturation observed in S HyperCel, a fully cellulosic base matrix, which is a distinctive

result that initially motivated much of this work. The polysaccharide-based resins examined here outperform their synthetic polymer counterparts as well, with SP Sepharose FF typically displaying higher uptake rates and capacities than SP 650 C (both of which are non-polymer-modified) and SP Sepharose XL displaying higher rates and capacities than Fractogel EMD SO_3^- (both of which are polymer-modified).

During bind-and-elute mode separations using these chromatographic supports, both uptake as well as elution of protein should be considered. Often overshadowed by loading optimization and adsorption metrics in purification process development, optimizing the elution step can present challenges based on the operating conditions or the characteristics of the solutes meant to be desorbed. Elution is a critical step in process performance in that it determines separation selectivity and the pool volume containing the product. Attention to elution is therefore necessary to maintain high recoverability of products and enable reuse of packed beds.

The increased use of stationary phases allowing higher binding capacities, such as polysaccharide-based media, potentially presents something of an optimization bottleneck. Increases in the total adsorptive capacity could translate into increases in the total elution volume due to more prevalent protein-protein association occurring within the pore volume of the adsorbent material. Increases in pool volumes would result in more dilute product pools and increases in processing time. Where minimal post-processing, such as buffer exchange and concentration of products, is favored in the downstream environment, the elution process merits some careful consideration.

Another potentially challenging problem, especially within IEX systems, is the increase of product self-association during elution, as elution from an IEX material typically requires an increase in the solution salt concentration. An increase in the salt

concentration of a protein solution, even with monovalent salts such as sodium chloride, can have a strong effect on the interactions leading to aggregation (Coen et al., 1995; Curtis et al., 1998; Dumetz et al., 2008; Lewus et al., 2014, 2011). The high loading capacities afforded by polysaccharide-based absorbents can compound this effect, as increases in protein-protein association are expected with increasing salt as well as mobile-phase protein concentration.

In order to obtain a more complete understanding of the physical and functional properties of resins of this type, macroscopic studies (similar to those for which results are shown in Figure 1.2) may be complemented with advanced imaging techniques performed on the microscopic scale. At this level, it is possible to determine aspects of protein sorption and transport that are not readily obtainable on the larger, macroscopic scale.

Scanning and transmission electron microscopy are useful for directly visualizing surface topography and intraparticle void space, respectively, and in the case of phases containing protein, characteristics such as protein localization may be observed (Bowes et al., 2009; Koku, 2011). However, electron microscopy does not enable any dynamic comparison with macroscopic studies such as protein uptake kinetics. Confocal laser scanning microscopy (CLSM) may be used to observe protein transport on the particle level by visualizing uptake, or elution, of fluorescently labeled proteins in single chromatographic particles in real-time (Dziennik et al., 2005, 2003; Hubbuch and Kula, 2008; Ljunglöf and Hjorth, 1996; Ljunglöf and Thömmes, 1998). These observations show where protein is located within the particle at any given moment during uptake, but also provide insight into the transport mechanism via

the type of profile observed (Bowes and Lenhoff, 2011a; Dziennik et al., 2003; Hubbuch et al., 2003; Yang et al., 2008; Zhou et al., 2006).

Single-molecule imaging on functionalized surfaces has been used to measure lateral diffusion and kinetic parameters of adsorbing species at the liquid-solid interface (Daniels et al., 2012; Honciuc et al., 2008; Isailovic et al., 2007; Kisley et al., 2014; Mabry et al., 2014; Ries et al., 2008; Skaug et al., 2013). The most common technique utilizes total internal reflection fluorescence (TIRF) in order to observe adsorption events within a small focal volumes directly above the solid-liquid interface. Particle tracking and autocorrelation analyses have been used in previous work (Cooper and Harris, 2014; Daniels et al., 2012; Kihm et al., 2004; Skaug et al., 2013; Thompson, 1981; Thompson and Axelrod, 1983) to back out kinetic and diffusive parameters at the adsorptive interface. Through the use of molecular methods such as these, direct observations can be made in how proteins behave along surfaces that are analogous to chromatographic stationary phases, e.g., dextran surface layers similar to those found in materials like Sepharose XL and Capto (both agarose-based media with covalently attached dextran extenders). Relating protein sorption on the macroscopic level, single-particle level and single-molecule level within polysaccharide-based materials provides a more complete understanding of how adsorbent structure dictates the functional characteristics of these types of exchangers.

1.2 Overview of this Work

This dissertation aims to increase our understanding in the field of chromatographic bioseparations through the characterization and assessment of polysaccharide-based stationary phases for IEX chromatography. Macroscopic studies to assess both structural and functional characteristics are coupled with microscopic

observations performed via advanced imaging techniques. In this way, a thorough investigation into how these materials adsorb, transport and elute proteins can be conducted on the batch and column level, to the particle level, and finally, down to the molecular level. The information gathered at each length scale helps to interpret observations and results obtained on each other level, and therefore, increases our fundamental understanding of the materials themselves and their mechanisms of protein sorption and transport.

The basis of the research stems from the characteristic differences in the particle and pore structure of the polysaccharide-based materials. Chapter 2 focuses on structural characterization of adsorbents comprised of agarose, cellulose and agarose modified with dextran extenders, the properties of which can be seen in Tables 1.1 and 1.2 for CEX and AEX moieties, respectively. Microscopic investigations were coupled with inverse size exclusion techniques in order to interrogate the pore space and obtain parameters for the pore-size distributions in these materials. A fundamental understanding of the adsorbent structure is essential in a functional characterization and assessment, because, as with many biological systems, structure often dictates function.

Chapter 3 covers an in-depth functional analysis of protein adsorption in the IEX materials using a set of model proteins. Both static and dynamic experiments were performed in order to obtain values such as the binding capacities and retention parameters at different values of the total ionic strength (TIS). Batch uptake kinetics experiments were coupled with CLSM imaging to obtain real-time uptake profiles on the macroscopic (batch) and single-particle level, respectively. Transport models were used to obtain quantitative parameters based on qualitative single-particle uptake

profiles. The use of both polymer-modified and non-polymer-modified adsorbents allows a direct comparison of how the adsorptive characteristics may be enhanced in materials with increased adsorptive capacities. The cellulosic exchangers were emphasized as the uptake behavior in these materials deviates from that in conventional stationary phases for IEX. While much of this work was done in single-component systems, some binary adsorption experiments were performed on the single-particle scale to observe displacement effects and anomalous uptake behavior, but binary adsorption experiments performed in batch systems (to obtain static capacities) are covered to some extent in Chapter 5.

Chapter 4 presents an analysis of the elution behavior from these materials. As stated previously, elution in adsorbents containing polymer extenders could potentially be troublesome due to the high binding capacities afforded by these resins. The elution rates from step elution experiments were modeled across the set of CEX materials with three different model proteins. Observation of single-particle elution via CSLM helped to elucidate anomalous behavior and the use of several excipients was also explored in determining how to ameliorate some of these drawbacks. The techniques presented here would be readily applicable to other stationary phases in order to compare their elution characteristics and to make informed decisions about stationary-phase selection when looking to optimize bind-and-elute separations.

Chapter 5 focuses on two studies in which adsorption in dextran-modified surfaces and materials is explored at the molecular level in both thermodynamic simulation and single-molecule imaging. In a collaboration with Igal Szleifer and Claudio Narambuena at Northwestern University, the molecular theory developed by Fang and Szleifer (2001) was extended to represent protein adsorption on surfaces

with and without dextran extenders in order to compare how proteins of differing affinity would adsorb at such interfaces at varied TIS and pH conditions. This molecular simulation is meant to represent adsorption in stationary phases such as Sepharose FF, which does not contain polymer extenders, and Sepharose XL, its counterpart that is modified with 40 kDa dextran extenders. The theoretical models are corroborated in binary adsorption isotherm experiments performed at comparable solution conditions with lysozyme and cytochrome c. The single-molecule imaging of dextran-modified surfaces was also conducted to observe differences in the lateral diffusion and residence time of fluorescently-labeled lysozyme though the utilization of a TIRF super-resolution microscope. While the ionic capacity of the dextranized surfaces was not adjusted, solution conditions were altered at varied TIS and pH conditions. Analysis of the mean-squared displacement of tracked particles provides a quantitative measure of protein movement on the molecular level that can be tangentially related to more macroscopic transport parameters at the same operating conditions.

Finally, Chapter 6 provides conclusions and recommendations for future work. Insight is provided into how the techniques and analyses presented here are applicable for industrial downstream processing and how this work may be built upon in the future for the development and characterization of novel materials and methods for large-scale chromatographic bioseparations.

Resin	Base matrix	Functional group	Particle size (μm)	Ionic capacity (μmol/mL)
SP Sepharose FF	Cross-linked agarose (6%)	SO_3^- on 6-carbon spacer	45-165	180-250
SP Sepharose XL	Cross-linked agarose (6%) with dextran extenders	SO_3^- on 6-carbon spacer	45-165	180-250
Capto S	Highly cross-linked agarose (>6%) with dextran extenders	SO_3^- on 2-carbon spacer	90 (mean)	110-140
S HyperCel	Cross-linked cellulose	SO_3^-	60-90	59-84

Table 1.1 Physical properties of CEX stationary phases as reported by manufacturers.

Resin	Base matrix	Functional group	Particle size (μm)	Ionic capacity (μmol/mL)
Q Sepharose FF	Cross-linked agarose (6%)	Quaternary ammonium	45-165	180-240
Q Sepharose XL	Cross-linked agarose (6%) with dextran extenders	Quaternary ammonium	45-165	180-260
Capto Q	Highly cross-linked agarose (>6%) with dextran extenders	Quaternary ammonium	90 (mean)	160-220
Q HyperCel	Cross-linked cellulose	Quaternary ammonium	60-90	99-138
STAR AX HyperCel	Cross-linked cellulose	Proprietary primary amine	80 (mean)	n/a

Table 1.2 Physical properties of AEX stationary phases as reported by manufacturers.

Chapter 2

STRUCTURAL CHARACTERIZATION OF CELLULOSE- AND AGAROSE-BASED ION-EXCHANGE ADSORBENTS

2.1 Introduction

Cellulosic ion-exchange materials display qualities very well suited for liquid chromatographic processes. The fine, fibrous structure provides a large surface area for protein adsorption (Graham and Fook, 1982; Peterson and Sober, 1956) and the natural carbohydrates that comprise these materials give them a hydrophilic quality that minimizes non-specific binding due to hydrophobic and other effects (Peterson, 1970). These features have led to a variety of beaded cellulosic supports (Bai and Li, 2006; Boeden et al., 1991; Du et al., 2010; Wang et al., 2007). Ion-exchange chromatography (IEC) resins based on cellulose presumably have an open microstructure for easily accessible transport of proteins (Peterson, 1970), and characterization of these materials from a more quantitative standpoint has shown that varying the cellulose concentration or the degree of cross-linking can be used to tailor pore dimensions and interconnectivity (Bai and Li, 2006; de Oliveira and Glasser, 1996; Du et al., 2010; Wang et al., 2007). However, differences in the pore structures of cellulosic supports can be expected to result from differences in synthesis procedures, and additional variations may be caused by functionalization. Of particular interest is whether significant functional differences are due solely to differences in the ligand chemistry or also to effects on the physical structure.

Due to the complex nature of the fibrous networks in these polysaccharidic materials, it is difficult to quantify an average pore radius and pore-size distribution in a way that can be related to the adsorption capacity. Inverse size-exclusion chromatography (ISEC) may be used to estimate the pore size distribution (PSD) of a stationary phase from experimental size-exclusion chromatography results for non-interacting solutes of known size, such as uncharged dextran or PEG standards (Hagel et al., 1996; Halasz and Vogtel, 1980; Knox and Ritchie, 1987). The PSD can then be used to estimate the accessible binding area per unit pore volume (the phase ratio) and the mean pore radius. ISEC analysis has been carried out for carbohydrate-based resins in previous studies (DePhillips and Lenhoff, 2000; Yao and Lenhoff, 2006), with the mathematical PSD function used to fit the calibration curves optimized for a simplified pore model assuming a sphere-in-cylinder geometry. Comparison of data obtained under different conditions allowed the dynamics of the internal structure, specifically the robustness of the pore-size distribution to changes in solution conditions, to be estimated.

Although ISEC provides a functional measure of the pore-size distribution, it does not directly reflect the details of the pore architecture and geometry (Knox and Ritchie, 1987). To complement the macroscopic structural characterization of these resins, electron microscopy techniques may be used to gain a qualitative understanding of the particle morphology and pore architecture. Scanning electron microscopy (SEM) is used to image the topography of the particle surface, but it also provides ample resolution to investigate the porous structure. Transmission electron microscopy (TEM) is used to complement the images obtained via SEM and provide a more detailed picture of the intraparticle space.

Salt accessibility studies allow the extent of salt exclusion within the pore space at low total ionic strengths to be determined. This is the regime in which the Donnan equilibrium effect (Donnan and Barker, 1911) is most pronounced. This effect was considered in much earlier studies of ion-exchange chromatography (Helfferich, 1962) but has not been examined extensively as an effect in ion-exchange of biopolymers. The effect, where present, can result in a significant difference between the salt concentration in the ambient electrolyte solution and the actual concentration of co- and counter-ions in the medium of interest. This medium is one in which immobilized ionic groups are sufficiently closely spaced that the electrostatic interaction between them is at most only partially screened by the ions in the intervening solution. In ion exchangers this occurs when charged ligands are immobilized on a polymer matrix, giving rise to a 3-D distribution of fixed charge. It occurs, for instance, in polymer-derivatized ion exchangers (Bowes et al., 2012), and it is possible that the cellulosic materials, such as HyperCel adsorbents, exhibit similar structural characteristics to the broader class of polymer-derivatized resins if cellulose chains span the extended pore space, acting much like grafted polymer extenders. Cellulosic exchangers exhibiting functionalized polymer grafts have been synthesized previously (Wang and Sun, 2007), which greatly increased adsorptive capacity but hindered flow through pores. The inclusion of a polymer layer such as this would greatly increase exclusion due to Donnan equilibrium at low ionic strengths, including solutes such as proteins, but in this study only salt exclusion was assessed as protein effects would be much more complex to analyze.

In this chapter, several cellulosic exchangers comprised of the same base matrix with functionalities providing varying levels of salt-tolerance are compared,

specifically materials belonging to the HyperCel family of adsorbents. This is supplemented by additional work on agarose exchangers, specifically Sepharose materials, which have been studied previously in a similar manner (Bowes and Lenhoff, 2011a, 2011b; Bowes et al., 2012, 2009; DePhillips and Lenhoff, 2000; Hubbuch et al., 2003; Langford et al., 2006; Staby et al., 2000; Stone and Carta, 2007; Yao and Lenhoff, 2006). The characterization performed here provides structural information that aids in the interpretation of functional characteristics of these stationary phases, which are discussed in Chapter 3.

2.2 Materials and Methods

2.2.1 Stationary Phases

S, Q and STAR AX HyperCel (lots AU31072012-3, -4 and -5 for Q, S and STAR AX, respectively) were provided by Pall Corporation (Northborough, MA). All resins were synthesized from the same cellulosic base matrix with different functionalities: sulfonate on S HyperCel, quaternary amine on Q HyperCel, and a proprietary primary amine group on STAR AX HyperCel. The average particle size is on the order of 75-80 μm for all three resins.

The structural characteristics of agarose-based resins were also explored, namely strong cation- and anion-exchange varieties of Sepharose Fast Flow (FF) and Sepharose XL, which were obtained from GE Healthcare (Piscataway, NJ). The FF material consists of a 6% cross-linked agarose base matrix with either a quaternary ammonium (Q) or sulfopropyl (SP) functionality while the XL material consists of the same base matrix but carries 40 kDa dextran extenders that are grafted to the agarose prior to functionalization (Berg, 2003). Structural details of these resins have

previously been determined by electron microscopy (Bowes et al., 2009; Koku, 2011; Staby and Jensen, 2001; Yao et al., 2006) and inverse size exclusion techniques (DePhillips and Lenhoff, 2000; Yao and Lenhoff, 2006). Manufacturer-reported properties of these resins and HyperCel materials can be found in Tables 1.1 and 1.2.

2.2.2 Buffers

Monobasic sodium phosphate (NaH_2PO_4) and bis-tris were purchased from Fisher Scientific (Fair Lawn, NJ) and Sigma-Aldrich (St. Louis, MO), respectively, and used to prepare buffer solutions at pH 7. The packing buffers used were 20 mM bis-tris with 1 M NaCl for use with the anion-exchange (AEX) resins and 10 mM monosodium phosphate with 1 M NaCl for the cation-exchange (CEX) resins. The running buffers for the ISEC experiments contained 20 mM bis-tris or 10 mM monosodium phosphate with 0 mM, 100 mM or 1 M NaCl added. The running buffers for the salt exclusion experiments consisted of 50 mM bis-tris with the total ionic strengths (TIS) adjusted with NaCl to 50, 100 and 200 mM. Buffers containing 10-200 mM sodium phosphate were also used to determine phosphate exclusion in separate experiments.

2.2.3 Inverse Size Exclusion Chromatography

2.2.3.1 Standards

A set of dextran standards ranging from 180 to 3,000,000 Da was purchased from Polymer Standards Service (Silver Spring, MD). PEG standards (Sigma Aldrich) ranging from 100 to 35,000 Da were also used in complementary ISEC experiments. Characteristics of the dextran and PEG standards used are shown in Tables 2.1 and 2.2, respectively.

Dextran	M_w (kDa)	M_p (kDa)	M_n (kDa)	PDI	R_η (nm)
dxtp1	0.18	0.18	0.18	1.00	0.36
dxtp2	0.342	0.342	0.342	1.00	0.50
dxt1n	1.35	1.08	1.16	1.16	0.88
dxt5	5.2	4.4	3.3	1.58	1.77
dxt12	11.6	9.9	8.1	1.43	2.65
dxt25	23.8	21.4	18.3	1.30	3.89
dxt50	48.6	43.5	35.6	1.37	5.53
dxt150	148	124	100	1.48	9.32
dxt270	273	196	164	1.66	11.71
dxt410	410	277	236	1.74	13.91
dxt3000k	3000	2800	1230	2.44	44.02

Table 2.1 Dextran characteristics, including weight-average molecular weight (M_w), number-average molecular weight (M_n), molar mass at peak maximum (M_p), polydispersity index (as reported by Polymer Standards Service) and viscosity radius (R_η, derived from Equation 2.2 (Kremer et al., 1994)).

PEG	M_w (kDa)	R_η (nm)
100	0.1	0.29
400	0.4	0.60
2000	2.05	1.40
3000	3.35	1.80
4000	4	1.97
8000	8	2.82
20000	20	4.54
35000	35	6.06

Table 2.2 PEG characteristics; viscosity radii derived from Equation 2.3 (Kremer et al., 1994).

Standard solutions were prepared by dissolving dextran or PEG standards in running buffer to a concentration of 1 mg/mL and storing them at 4 °C for at least 24 hours prior to their use in ISEC experiments. All samples were filtered through 0.22 μm syringe filters prior to injection to remove any higher molecular weight aggregates.

2.2.3.2 ISEC Procedures

Resin was slurried in a 75/25 resin-to-buffer ratio and poured into a graduated cylinder to a volume of 180-200 mL. Packing buffer was added and the resin was suspended and then allowed to settle to a target volume of 135-140 mL. Packing buffer was added and decanted a total of three times. Packing buffer was then added to produce a suspension of 50% v/v resin. The suspension was poured along the inside wall of a vertical GE Healthcare XK 16/70 (i.d. 1.6 cm) column with attached reservoir column. The column was topped off with packing buffer and the top flow adapter attached. The flow of packing buffer was initiated and gradually increased to 4 mL/min (120 cm/hr). The top flow adapter was repeatedly lowered to the top of the bed every hour while packing continued until no noticeable further drop in bed height was observed. The final packed bed height was 50 ± 3 cm in all cases (total column volume 100.5 ± 6.0 mL). Properties of the individual columns are shown in Table 2.3. Intraparticle void fractions, ε_p, were determined based on the retention of glucose injections, and interstitial void fractions, ε, were determined based on the retention of dxtb3000k (3,000,000 Da dextran) injections. Chromatography was performed using a Waters 2695 separation module equipped with a Waters 2414 RI detector. Solute injections of 100 μL were used at a flow rate of 1.5 mL/min (45 cm/hr).

	ε	ε_p	ε_t	L (cm)
S HyperCel	0.35	0.74	0.83	49.5
STAR AX HyperCel	0.35	0.66	0.78	47.6
SP Sepharose XL (no added NaCl)	0.34	0.65	0.77	51.4
SP Sepharose XL (1500 mM NaCl)	0.36	0.70	0.81	51.4

Table 2.3 Column characteristics, including interstitial, intraparticle and total porosities and the bed height of each packed column.

2.2.3.3 ISEC Analysis

Following methods described in DePhillips and Lenhoff (2000) and Yao and Lenhoff (2004), analysis of the ISEC measurements was carried out in order to determine quantitative characteristics of the stationary phases. ISEC data are presented in the form of a calibration curve of distribution coefficients, or K_d values, determined by

$$K_d = \frac{V_r - V_0}{V_t - V_0} \tag{2.1}$$

where V_r is the elution volume of the solute, V_0 is the interstitial void volume determined from an excluded solute (such as dxtb3000k), and V_t is the total mobile-phase volume determined from a glucose injection.

The K_d calibration curve, expressed as a function of the size of each standard probe, is used to estimate the pore-size distribution of the resin, from which the mean pore size and the accessible pore area can also be estimated. The probe size is most often expressed as the viscosity radius, R_η, based on empirical correlations (Kremer et al., 1994). For dextran standards the form used is

$$R_\eta = 0.0271 M_p^{0.498} \tag{2.2}$$

where M_p is the peak molecular weight of the dextran standard, in Daltons, and the radius is in nm. For PEG standards the correlation used was

$$R_\eta = 0.0271 M_p^{0.517} \tag{2.3}$$

The ISEC procedure fits the experimental K_d values to a PSD function. Since this regression is based on a finite number of data points, it is best carried out using a suitable functional form characterized by a small number of parameter values. We generally use the log normal distribution

$$f(r) = \frac{1}{r} \exp\left[-\frac{1}{2} \left(\frac{\log\left(\frac{r}{r_p}\right)}{s_p} \right)^2 \right] \tag{2.4}$$

where the two parameters directly characterize the shape of the distribution: r_p is a measure of the mode of the distribution and s_p a measure of the width. The PSD is related to the distribution coefficients by

$$K_d = \frac{\int_{r_m}^{\infty} f(r)[1-(r_m/r)]^2 dr}{\int_0^{\infty} f(r) dr} \tag{2.5}$$

where r_m is the solute viscosity radius for one particular standard. This relationship simply represents K_d as a ratio of accessible pore volume to total pore volume, with partitioning represented as that of a sphere in a cylindrical pore. This partitioning model is highly idealized, and although it provides a reasonable estimate of the characteristic size distribution of the pore space, the limitations of the model should be borne in mind.

Although the sensitivity to pore size is much greater than that to pore shape, we also explored PSD fits for the Ogston model (Ogston, 1958), which is more plausible as a physical representation of the fibrous nature of the natural carbohydrate

polymer networks. An adaptation of the Ogston model was derived from the work of Laurent and Killander (1964) and Slater et al. (1988) that describes the available volume by assuming that the cellulosic matrices are comprised of a network of straight, rigid fibers that are infinitely long and distributed at random, and assuming that the solute radius is much greater than the radius of the cellulosic fibers:

$$f(\mathrm{r}) = \frac{\pi \mathrm{r}}{2\mathrm{r}_{\mathrm{mean}}} \exp\left[-\frac{\pi}{4}\left(\frac{\mathrm{r}}{\mathrm{r}_{\mathrm{mean}}}\right)^2\right] \tag{2.6}$$

Here r_{mean} is simply the mean pore radius provided by the distribution. Dividing the K_d values obtained from this PSD by the total column porosity (ε_t) provides a more accurate model prediction by accounting for empirical interstitial and intraparticle porosities of the materials.

Fitting of the experimental data was performed in Matlab using the 'quadgk' function to evaluate the integrals and 'nlinfit' to fit the PSD parameters using nonlinear least-squares regression. Once the PSD was determined, values for the mean pore radius were found from the first moment

$$\mathrm{r}_{\mathrm{mean}} = \frac{\int_0^\infty \mathrm{r} f(\mathrm{r}) \mathrm{dr}}{\int_0^\infty f(\mathrm{r}) \mathrm{dr}} \tag{2.7}$$

Area based phase ratios, i.e., surface area available for adsorption per unit pore volume, were calculated for the materials but determined to not hold much weight as these calculations do not take into account the volume of polymer layers (since the uncharged dextrans do not partition into this volume) and become convoluted with materials that exhibit pore sizes that exclude dextran standards of intermediate size.

2.2.4 Electron Microscopy

2.2.4.1 Scanning Electron Microscopy

Samples were prepared by dehydrating resin in ethanol and placing the particles in 30 μm microporous capsules. Samples were critical-point dried using a Tousimis Autosamdri-815B critical-point drier and mounted on aluminum stubs using double-sided carbon tabs. Samples were then sputter-coated with gold-palladium in a Denton Bench Top Turbo III coater for 4 minutes at a current of 30 mA and an argon pressure of 65 mtorr. Several samples were left uncoated in order to observe the effects of electron charging on the materials while imaging was performed.

Additional samples were temporarily fixed with 1% glutaraldehyde and 1% paraformaldehyde before being chemically fixed with 1% osmium tetroxide (OsO_4) in DI water. Samples were washed with DI water and dehydrated in ethanol before the same processing method was followed as for the samples that were not chemically fixed, to allow for a qualitative comparison between particles with and without chemical fixation. All SEM imaging was performed using a Hitachi S4700 FESEM operated in secondary electron mode with a voltage of 3.0 kV and a working distance of 2-3 mm.

2.2.4.2 Transmission Electron Microscopy

Resin particles were temporarily fixed with 1% glutaraldehyde and 1% paraformaldehyde before being chemically fixed with 1% osmium tetroxide in DI water. Samples were dehydrated into 100% acetone and infiltrated with Embed-812 resin in increasing fractions of resin in acetone. Samples were cured at 65 °C for 72 hours before being sectioned via microtome into slices 50-70 nm in thickness.

Sections were post-stained with uranyl and lead acetate and placed on 200-mesh formvar-carbon supported copper grids.

Q and STAR AX HyperCel were also stained using 1% glutaraldehyde and 1% tannic acid followed by the remainder of the standard sample processing. This fixation method, referred to as the TAGO method (tannic acid-glutaraldehyde-osmium tetroxide) (Hayat, 2000), provides increased contrast in samples with fewer binding sites for osmium, e.g., amine functional groups, as the tannic acid acts as a mordant between the heavy metal and the sample. All TEM imaging for particle sections was performed on a Zeiss LIBRA 120 transmission electron microscope operated at 120 kV.

2.2.5 Salt Exclusion

Apart from steric exclusion effects of the kind measured by ISEC, there may also be electrostatic exclusion effects for proteins (Harinarayan et al., 2006; Zydney et al., 2009). However, small ions may also be excluded due to the Donnan equilibrium effect (Donnan and Barker, 1911) within a 3-D volume bearing fixed charges; the effect is apparent at ambient salt concentrations lower than the local volumetric density of fixed charge (Figure 2.1). When the material is regenerated using high salt concentrations and then equilibrated with a running buffer with a relatively low salt concentration, a higher counterion concentration will be present within the polymer layer than in the bulk fluid. Conversely, because of the presence of the fixed charges, the free co-ion concentration in the polymer is lower than that in the bulk fluid. The resulting concentration gradients tend to drive counterions into the bulk fluid and co-ions into the polymer layer. However, these opposing fluxes would disrupt the required electroneutrality within the polymer, so the exchange would give rise to an

electrical potential difference between the polymer interior and the bulk fluid. The energetic cost of the potential difference gives rise to an equilibrium that prevents the exchange from occurring. As a result, at low bulk salt concentrations the effective salt concentration inside the polymer is appreciably below that in the bulk fluid, and it is only when the bulk salt concentration approaches the local volumetric density of fixed charge inside the polymer that the intrapolymer salt concentration approaches the bulk value (Helfferich, 1962).

Donnan exclusion measurements were performed as described by Bowes et al. (2012). Resin was packed into 5 mm i.d. Waters AP Minicolumns with a bed height of 10 ± 1.0 cm. Salt breakthrough experiments were carried out on a GE Healthcare ÄKTA Purifier system equipped with a conductivity meter to measure salt concentration. Low-salt buffer was fed through pump A and high-salt buffer (either 50, 100 or 200 mM TIS buffer) was fed through pump B. Starting at 10% B, the concentration of high-salt buffer was increased stepwise by 5% every 20 minutes until 70% B was achieved. Mixtures below 10% B and above 70% B were omitted as those ranges produced the least accurate mixing by the ÄKTA. All steps were conducted at a linear velocity of 120 cm/hr. Steps were performed with and without the column in place in order to find the mixture-dependent dead volume for each step and subtract it from the integrated area for salt breakthrough on the column at the same concentration steps. Column properties were determined in a similar manner to that used in the ISEC experiments.

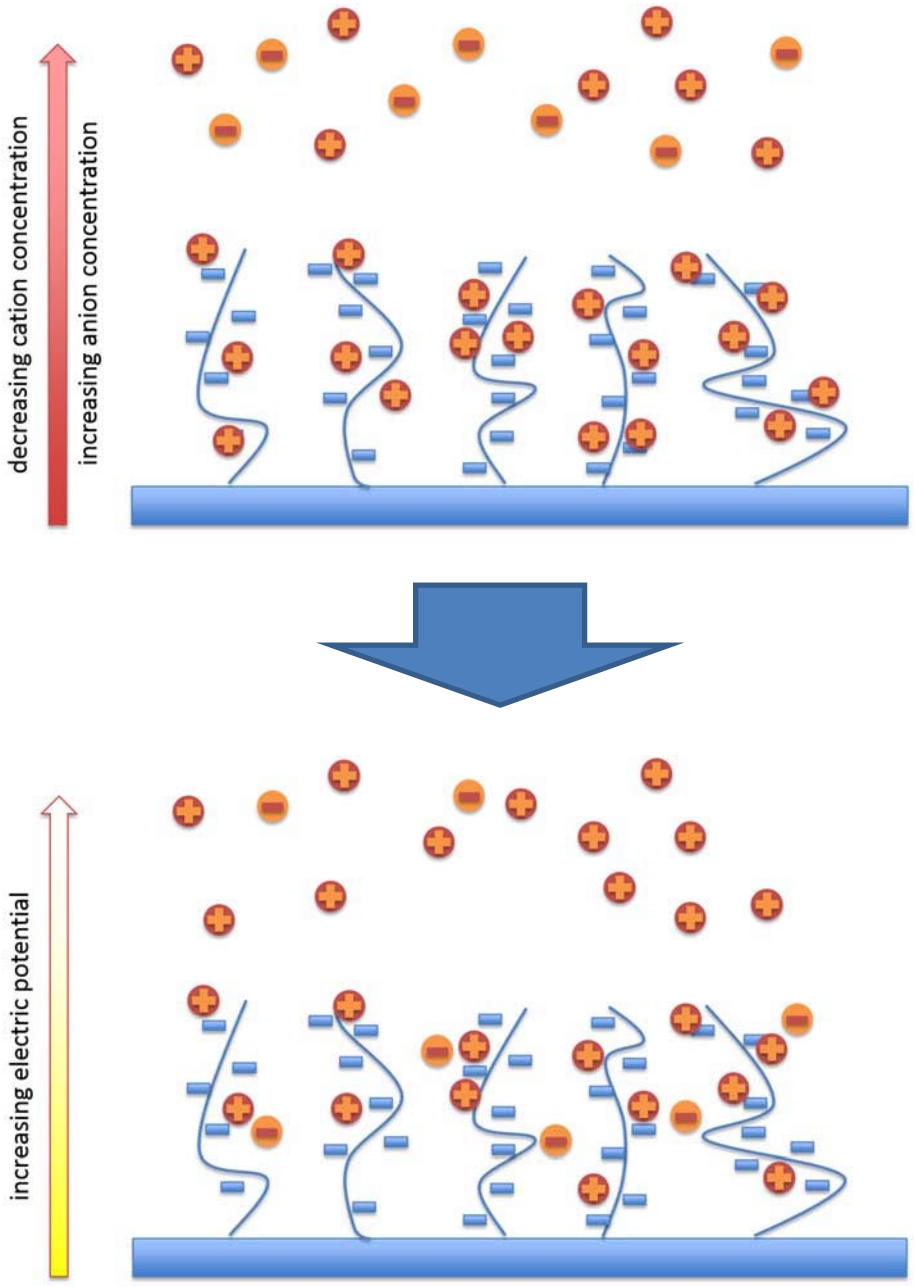

Figure 2.1 Schematic representation of Donnan equilibrium in a cation exchanger. Salt counter- and co-ions exchange between the bulk fluid and functionalized polymeric layer, developing a concentration difference (top) after initial equilibration. The electric potential gradient that is created by co-ions partitioning into the functionalized layer (bottom) is what gives rise to Donnan equilibrium and the exclusion of salt at low ionic strengths.

The analysis of the data is in terms of apparent partitioning behavior. The interstitial porosity is given by $\varepsilon = V_0/V_c$, where V_0 is the intraparticle void volume determined from dxtb3000k injections and V_c is the total column volume. The intraparticle porosity is $\varepsilon_p = (V_T/V_c - \varepsilon)/(1 - \varepsilon)$, where V_T is the total mobile phase volume determined from glucose injections. The apparent pore volume fraction accessed by salt at each step is $(V_{BT}-V_{d,BT}-\varepsilon V_c)/[\varepsilon_p(1-\varepsilon)V_c]$, where V_{BT} is the column breakthrough volume for a single concentration step, determined by the integrated area under the conductivity breakthrough curve, and $V_{d,BT}$ is the dead volume for the same step determined by the integrated area without a column in place.

2.3 Results and Discussion

2.3.1 Inverse Size Exclusion Chromatography

Figure 2.2 shows chromatograms for the dextran standards in STAR AX HyperCel, in units of column volumes. These raw SEC data readily elucidate which standards are on the order of the mean pore size of the material. Total exclusion and inclusion are clearly apparent at the extremes of probe size, while dextran standards of intermediate size show the transition between the two extremes. The peaks with intermediate retention appear non-ideal in both shape and width, but their first moments were still calculated in order to estimate the retention volumes. The non-ideal peak shapes appear to be due to the chemical character of the interaction between dextran and cellulose, as PEG standards of intermediate size show much more symmetric peak shapes (Figure 2.3).

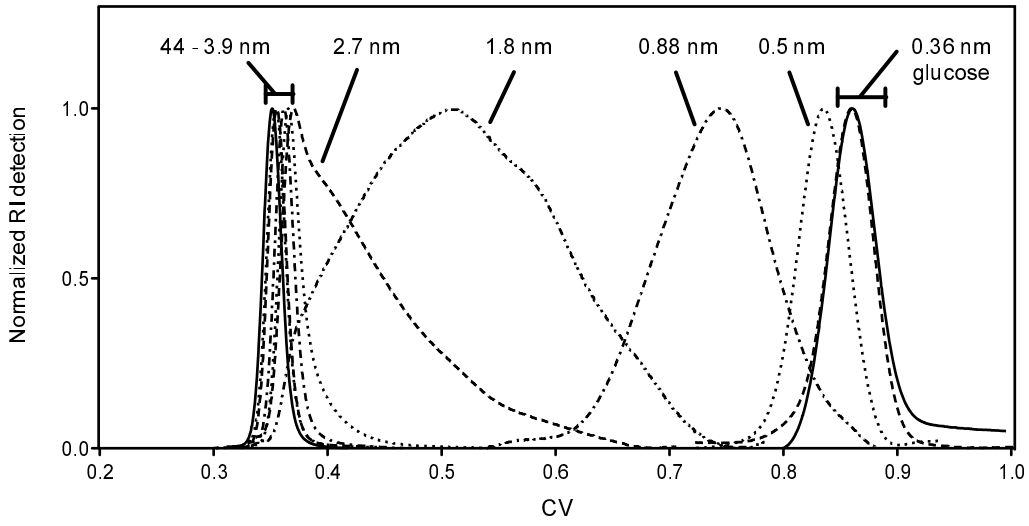

Figure 2.2 Dextran retention volume chromatograms in STAR AX HyperCel (20 mM bis-tris, 100 mM NaCl, pH 7).

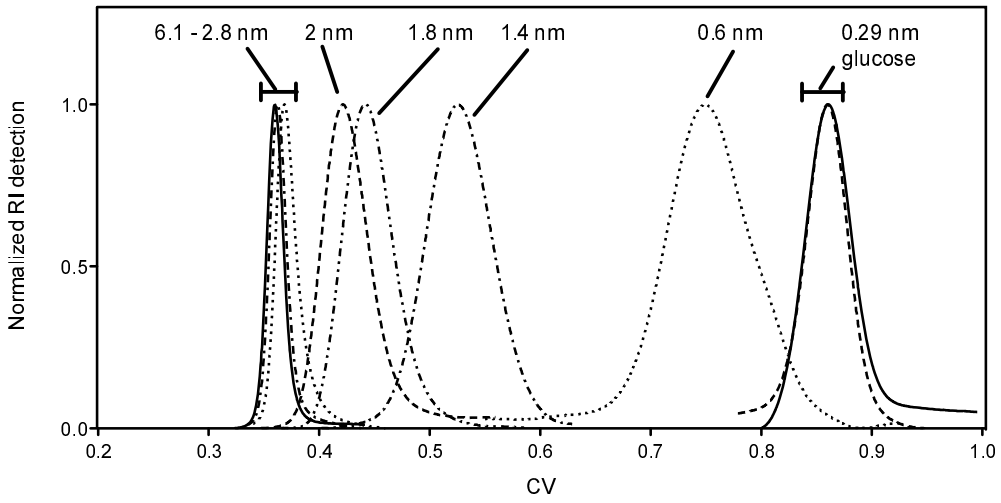

Figure 2.3 PEG retention volume chromatograms in STAR AX HyperCel (20 mM bis-tris, 100 mM NaCl, pH 7).

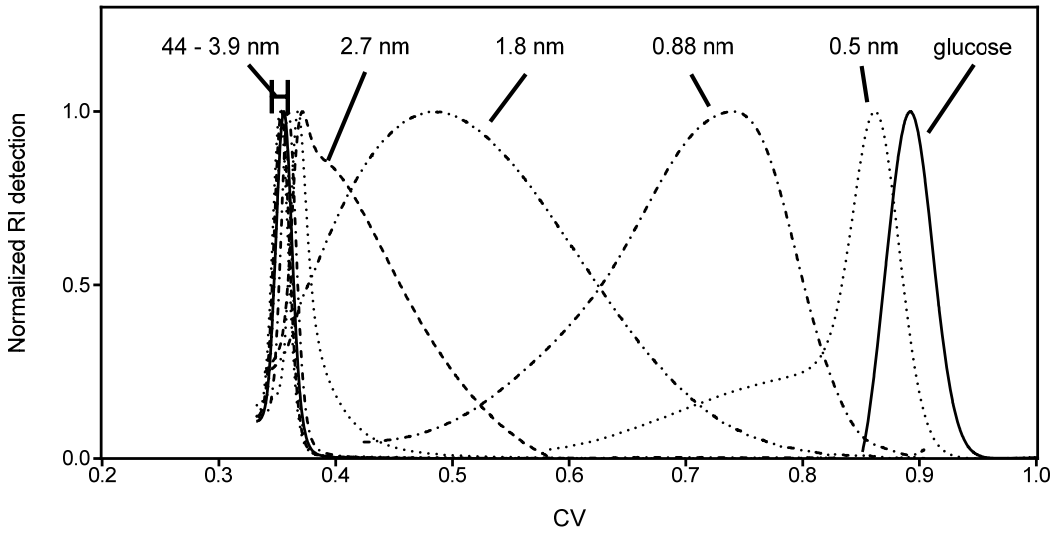

Figure 2.4 Dextran retention volume chromatograms in S HyperCel (10 mM sodium phosphate, 100 mM NaCl, pH 7).

Figure 2.4 shows the chromatograms for the dextran solutes in S HyperCel. Again, non-ideal peak shapes are seen for some of the dextran solutes of intermediate sizes, presenting some fronting and tailing behavior for solutes that have more accessibility and less accessibility, respectively. As with the STAR AX material, the first moment analysis was necessary to discern the retention volumes for each solute.

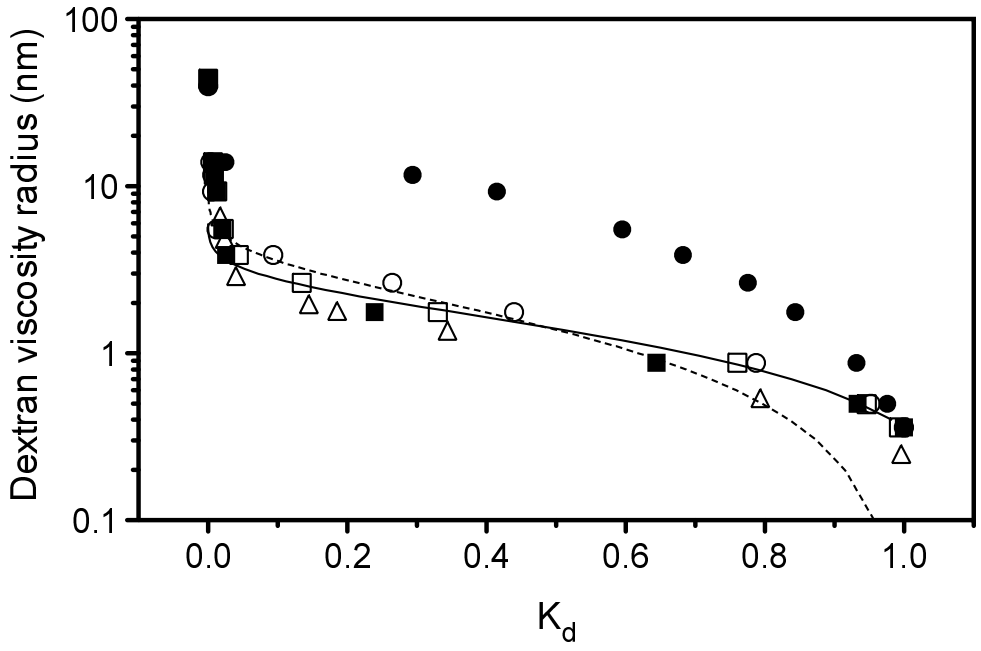

Figure 2.5 Dextran calibration curves for S HyperCel (■), STAR AX HyperCel (□), Q Sepharose FF (●), and Q Sepharose XL (○); PEG calibration curve for STAR AX HyperCel (△) also shown. Log-normal (---) and Ogston (—) models are applied to the dextran calibration curve for STAR AX HyperCel (100 mM NaCl, pH 7).

The ISEC calibration curves, developed using raw data such as those shown in Figures 2.2-2.4, are shown in Figure 2.5 for four IEC materials: S HyperCel, STAR AX HyperCel, Q Sepharose FF and Q Sepharose XL (Yao and Lenhoff, 2004). Manufacturer information suggests that the only difference between Q and SP type Sepharose materials is the functional group, so it is understood that these curves are similar in shape to those of the SP variants. Consistent with the qualitative interpretation of the data in Figures 2.2-2.4, the set of dextran standards shows K_d values ranging from almost 1 (completely included) to near zero (completely excluded). It is clear that the two HyperCel materials and the dextran-modified Sepharose XL have very similar pore space dimensions. Q Sepharose FF presents a pore space with a much larger characteristic size, implying that the pore structure of HyperCel shares characteristics with regard to pore size with the polymer-modified variant, Sepharose XL, but not Sepharose FF, which lacks polymer derivatization. Pore dimension parameters for the Q Sepharose materials have previously been evaluated by ISEC (Yao and Lenhoff, 2006) and are shown in Table 2.4.

The sensitivity of the K_d data to several experimental parameters was investigated. First, the large differences apparent in the peak shapes of dextran and PEG probes of intermediate size (Figures 2.2 and 2.3) are not reflected in appreciable differences in the K_d values for STAR AX HyperCel (Figure 2.5). Indeed, the small offset may be due to uncertainties in the empirical correlations used for determining the viscosity radii of PEGs and dextrans, as well as to contributions of the polydispersity of both sets of probes.

The effect of ionic strength had on pore size was studied by using running buffers with different concentrations of sodium chloride. Figure 2.6 shows the dextran

calibration curves of STAR AX and S HyperCel at 0 M NaCl, 100 mM NaCl and 1 M NaCl. For the salt-tolerant AEX resin, the small shift in K_d with salt concentration indicates a more open structure with increasing salt, which may be interpreted as a collapse of the polymer. However, the effect is small, leading to the conclusion that different ionic strengths do not significantly alter the pore structure, and hence the pore volume. This appears not to be implicated in the mechanism for the salt tolerance. Calibration curves for S HyperCel at various salt concentrations also show similar curvature, so it can be inferred that changes in solution ionic strength do not severely affect the pore structure of the standard derivatizations along with the salt-tolerant material. The apparent insensitivity to ionic strength that the HyperCel materials display is most likely due to the high degree of cross-linking within the particle structure.

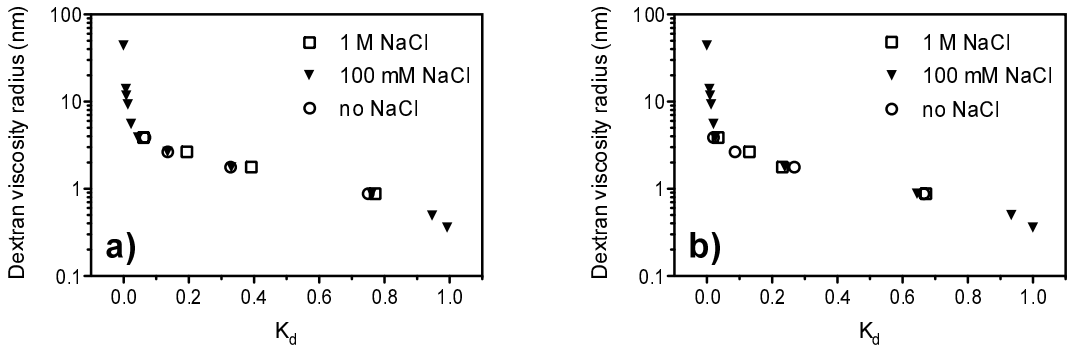

Figure 2.6 Dextran calibration curves for (a) STAR AX HyperCel and (b) S HyperCel at different NaCl concentrations (20 mM bis-tris, pH 7).

This is contrary to the behavior of some other ion-exchange materials, including polymer-modified resins, that show an expansion in pore size at elevated salt, presumably due to contraction or collapse of the polymer layer (DePhillips and Lenhoff, 2000; Müller, 2005). Figures 2.7 and 2.8 show just how pronounced this contraction is in SP Sepharose XL at conditions with no added NaCl and with 1500 mM NaCl added.

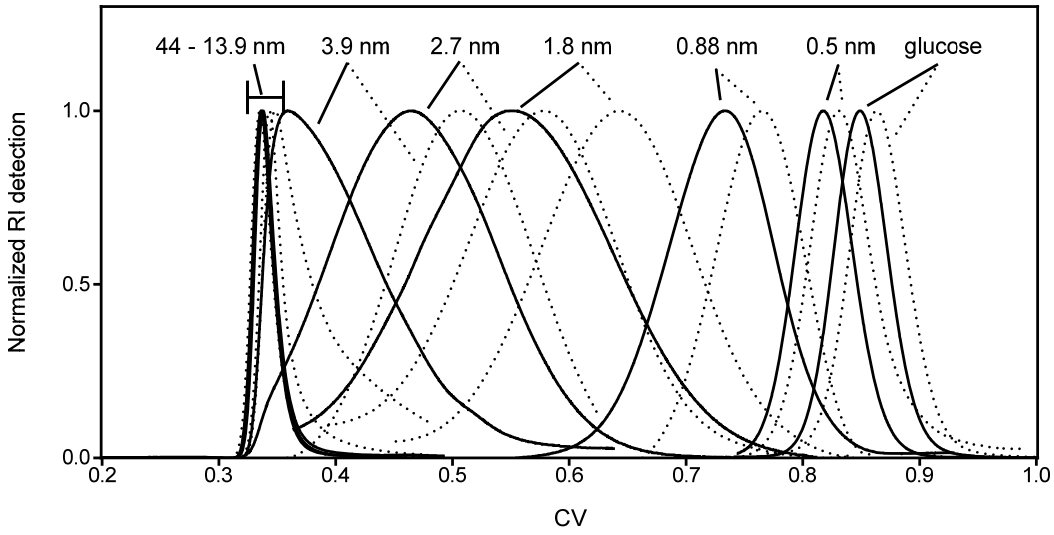

Figure 2.7 Dextran retention volume chromatograms in SP Sepharose XL with no added NaCl (solid) and 1500 mM NaCl added (dotted) (10 mM sodium phosphate, pH 7).

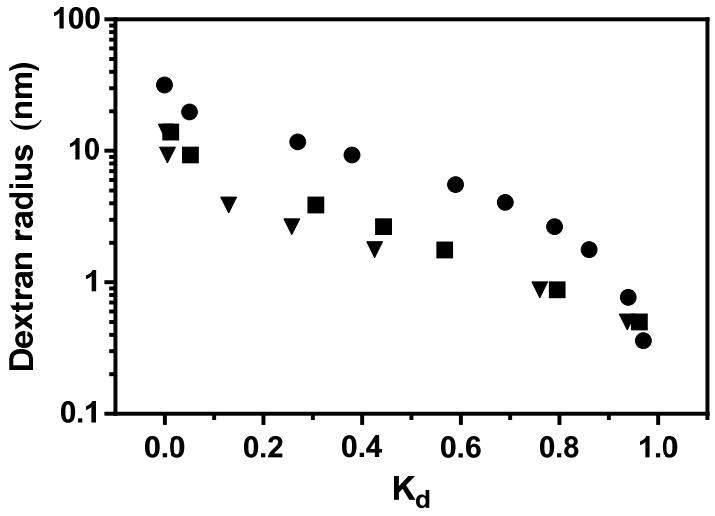

Figure 2.8 Dextran calibration curves for SP Sepharose FF (●) (DePhillips and Lenhoff, 2000), SP Sepharose XL (▼) and SP Sepharose XL at 1500 mM NaCl (■) (10 mM sodium phosphate, pH 7).

It is evident in both the raw chromatograms and the calibration curves that the dextran solutes of intermediate size, i.e., solutes that are on the order of the mean pore size, have greater retention volumes and hence much more accessibility at the higher ionic strength. Figure 2.9 shows a schematic representation of the differences in pore size for SP Sepharose materials based on a cylindrical-pore model. The results of DePhillips and Lenhoff (2000) revealed the mean pore radius of SP Sepharose FF to be 24.7 nm. With SP FF comprising the base matrix of SP XL (omitting the dextran extenders), we may estimate the thickness of the dextran layer to be approximately 19 nm and 15 nm under low salt conditions and high salt conditions, respectively. Of course, because of the nature of the ISEC experiment, only the pore lumen may be probed in polymer-modified resins as the larger uncharged dextran solutes presumably do not partition into the narrow mesh of the polymer layer. This would inevitably

skew some results of polymer-modified adsorbents, but it is still undeniable in this case that there is a significant alteration of the pore microstructure that is not apparent in the cellulose-based resins.

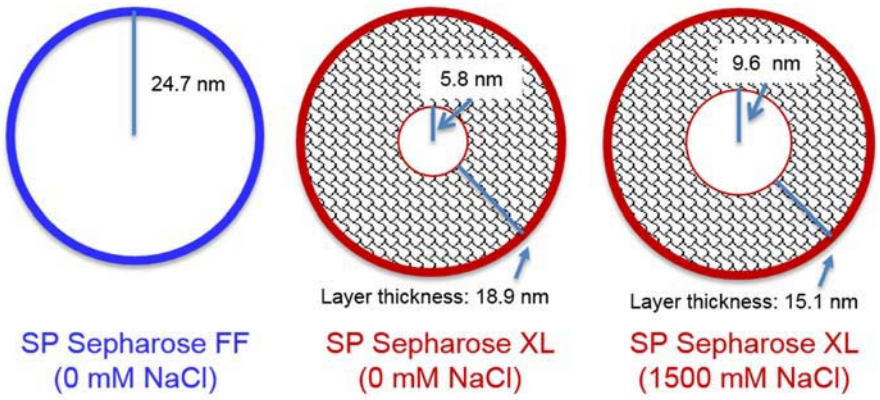

Figure 2.9 Schematic representation of mean pore sizes for SP Sepharose FF and SP Sepharose XL based on inverse size exclusion chromatography analysis. The rightmost image displays the contraction of the polymer layer within Sepharose XL at high ionic strengths of solution.

Figure 2.5 also shows fits of the log-normal and Ogston PSD models to the STAR AX HyperCel dextran calibration curve. The poor fit at high K_d (small probes) for the log-normal model appears to be a result of the narrowness of both the pores and the PSD, engendering inaccuracies in the sphere-in-cylinder model for the log-normal distribution. Applying the Ogston model to the calibration curve gives a good quality fit. It was developed to estimate the pore size distribution in a network of randomly placed fibers, such as a gel (Laurent and Killander, 1964; Slater et al., 1988), but this does not affect the intrinsic conclusions regarding the effective pore size.

	Cylindrical pore model			Ogston model
	r_p	s_p	r_{mean} (nm)	r_{mean} (nm)
S HyperCel	4.4	1.1	4.4	3.6
STAR AX HyperCel	5.0	1.2	5.1	4.7
SP Sepharose FF	24.2	0.82	24.7	NA
SP Sepharose XL (no added NaCl)	5.7	0.88	5.8	NA
SP Sepharose XL (1500 mM NaCl)	8.6	0.64	9.5	NA
Q Sepharose FF	25.8	0.47	28.8	NA
Q Sepharose XL	5.9	0.006	5.9	8.6

Table 2.4 Pore size distribution parameters and mean pore radii for HyperCel and Sepharose materials determined by ISEC analysis; Q Sepharose parameters were taken from Yao and Lenhoff (2006) and SP Sepharose FF parameters were taken from DePhillips and Lenhoff (2000).

Fitting parameters and derived characteristics of the S and STAR AX HyperCel materials and SP Sepharose XL at different ionic strengths are shown in Table 2.4, including r_p, s_p, and the mean pore radii determined by the ISEC analyses, r_{mean}, by application of the log-normal cylindrical pore and Ogston models. Small-angle neutron scattering (SANS) (Koshari et al., 2015) on HyperCel resin revealed a radius of gyration in the intermediate-q region of 3.5 nm, providing very good agreement in measures of the mean pore size between ISEC and SANS. The relatively narrow pore structure of the HyperCel material is comparable to those of dextran-modified Sepharose XL or other polymer-grafted resins (Jerabek et al., 1993; Yao and Lenhoff, 2006). However, on such resins, the access (or lack thereof) of uncharged probe molecules can provide a misleading indication of accessibility. The exclusion of large biomolecules such as monoclonal antibodies would not likely be an issue due to

the presence of an electrostatic driving force (Bowes et al., 2009; Perez-Almodóvar et al., 2011), which has no effect on the retention or partitioning of the uncharged dextrans used for ISEC.

2.3.2 Scanning Electron Microscopy

Whole-particle SEM was performed on particles with and without chemical fixation by OsO_4, and with no adsorbed protein and with adsorbed protein (in which the samples were required to be chemically fixed beforehand). Results for only protein-free materials are presented here for the purpose of structural characterization, but TEM images of phases containing protein are presented in Chapter 3. Corresponding results are presented in Figures 2.10 and 2.11, which differ only in the magnification.

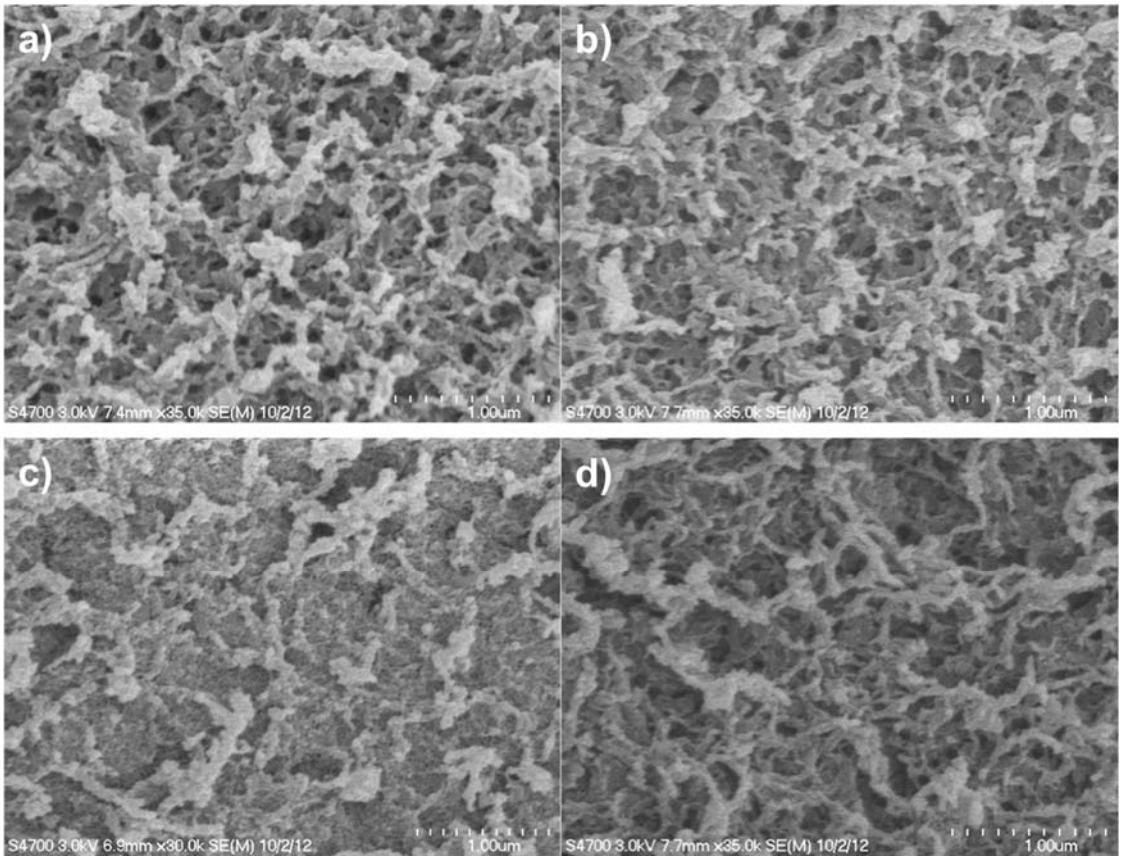

Figure 2.10 SEM images of Q (a and b) and STAR AX (c and d) HyperCel at 35000x. a and c show the resin chemically fixed with OsO_4; b and d show resin without chemical fixation.

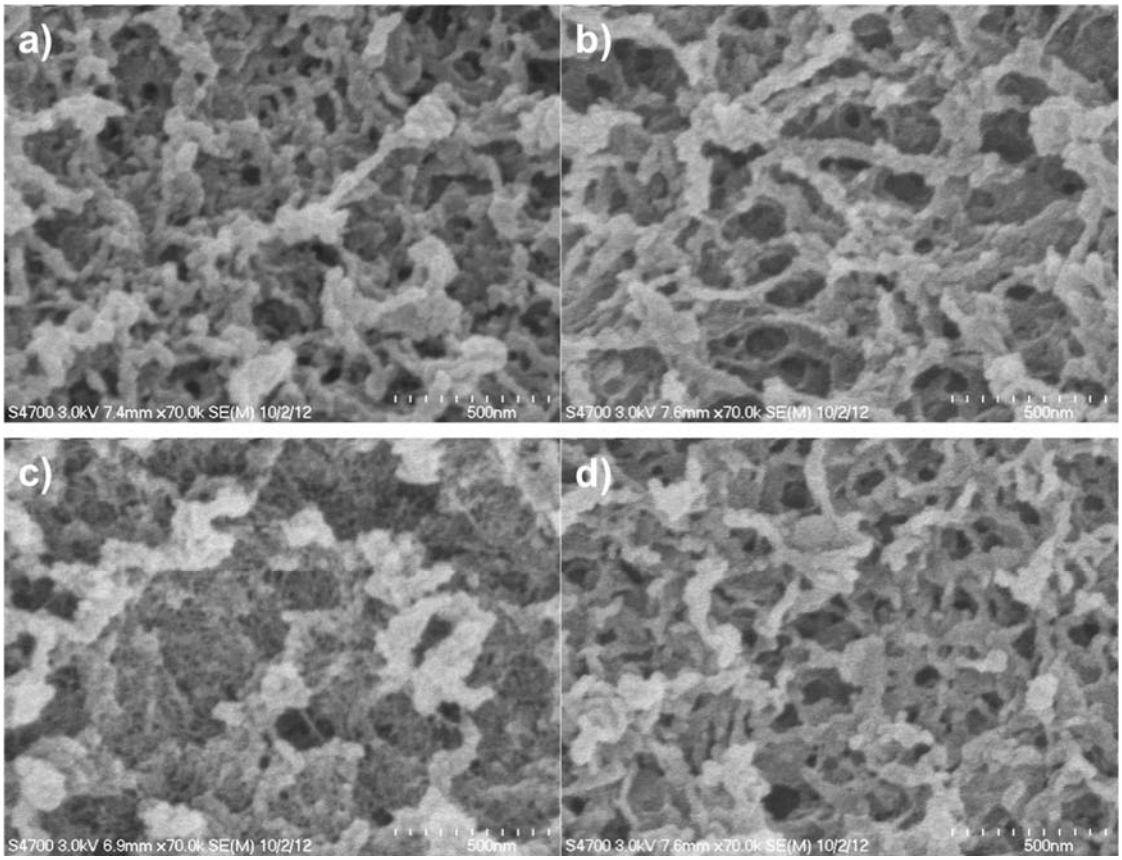

Figure 2.11 SEM images of Q (a and b) and STAR AX (c and d) HyperCel at 70000x. a and c show the resin chemically fixed with OsO_4; b and d show resin without chemical fixation.

As shown in Figures 2.10-2.11a and b, there is little difference between Q HyperCel samples that are and are not chemically fixed. The fibrous network shown is characteristic of natural carbohydrate polymer adsorbents (Bowes et al., 2009; Koku, 2011), and appears to contain "pores" on the order of 10-50 nm in characteristic dimension. Small-angle neutron scattering on HyperCel shows an intermediate fractal region that corresponds to dense fractal structures of approximately 16-42 nm (Koshari et al., 2015), closely in line to what is observed microscopically.

STAR AX HyperCel appears to include a finer network of fibers within the larger pore volume when chemical fixation is performed (Figures 2.10-2.11c), but appears qualitatively similar to Q HyperCel without any prior fixation (Figures 2.10-2.11d). This suggests that fixation of the material either alters the inner pore structure or locks the native structure in place, revealing the true nature of the pore volume and suggesting that this structural characteristic is lost without performing chemical fixation.

That the observed pore space has features noticeably larger than suggested by the results from ISEC could stem from several factors. First, cellulose, being very hydrophilic, may have its native structure significantly altered when undergoing sample processing, specifically critical-point drying. While this would suggest that the microscopy results are unreliable, the micrographs still provide a qualitative comparison between the materials and display these materials' significant pore connectivity due to the fibrous nature of the carbohydrate base matrix. Second, the resolution of the microscopy images may not have been high enough to visualize structural details that were postulated, such as the possibility of freely bound cellulosic chains that extend into the pore space, similarly to how grafted functionalized polymers comprise the porous space in "tentacle"-type exchangers. The conditions required for sample processing may have caused a collapse of this layer. Figure 2.12 shows images (Koku, 2011) of Q Sepharose FF and XL. While the XL exhibits slightly smaller pore radii than the FF material due to the addition of dextran extenders, the pore shapes of the two stationary phases remain qualitatively similar, even though it was previously reported that the dextran occupies a significant portion of the pore space (Bowes et al., 2009), suggesting a collapse of the polymer layer in

the case of the XL material. Finally, the EM methods may simply not resolve pore dimensions of order 5 nm as suggested by ISEC, leaving the larger features as the more visible ones.

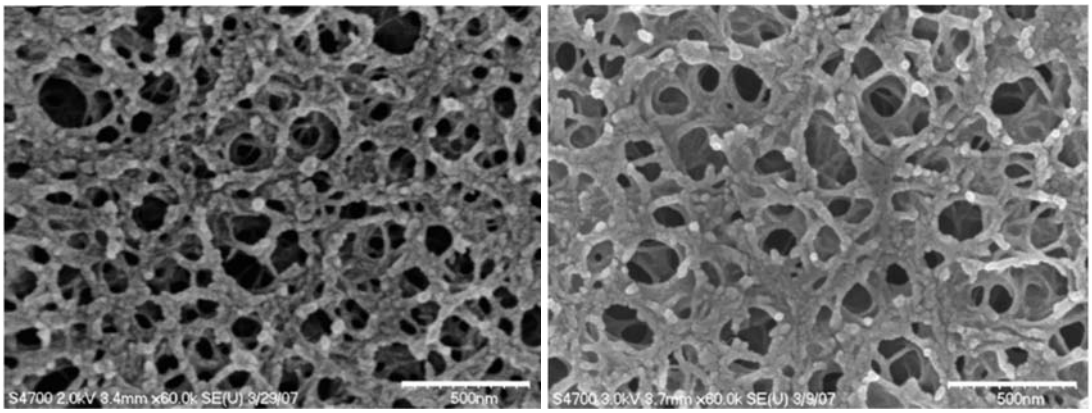

Figure 2.12 SEM images of Q Sepharose FF (left) and Q Sepharose XL (right) at 60000x (Koku, 2011).

Based on the theoretical assessment of pore size via ISEC, the pore dimensions for S and STAR AX HyperCel are quantitatively similar. Also, Q and S HyperCel are assumed to have almost identical architecture, as the only fundamental difference is in the ion-exchange ligands. The ligand chemistry in the STAR AX material differs in character from that of both the S and Q adsorbents, and is the most likely reason for the difference in pore structure seen in the SEM images when the material was chemically fixed with OsO_4. However, without more detailed knowledge of the ligand chemistry it is not possible to draw further conclusions.

2.3.3 Transmission Electron Microscopy

2.3.3.1 Effect of Preparation Buffer

All TEM was performed on sections 50 nm thick. All sample preparation was done using 10 mM sodium phosphate buffer at pH 7 for the initial fixation, as the amine groups in bis-tris can cause undesired artifacts by reacting with glutaraldehyde (Hayat, 2000). Figure 2.13 shows a comparison of Q HyperCel initially prepared in 10 mM sodium phosphate, 50 mM bis-tris and 10 mM sodium cacodylate (a commonly used TEM buffer). The sample prepared in bis-tris lacks the generally fibrous appearance that is apparent in the sodium phosphate and cacodylate buffers. These artifacts are likely present due to residual bis-tris buffer not being completely washed from the sample prior to osmication, leaving excess positively charged functional groups within the pore space of the sample and acting as a mordant for the heavy-metal stain. Therefore, for all TEM imaging experiments, sodium phosphate buffer was used in lieu of bis-tris buffer for the anion-exchange adsorbents.

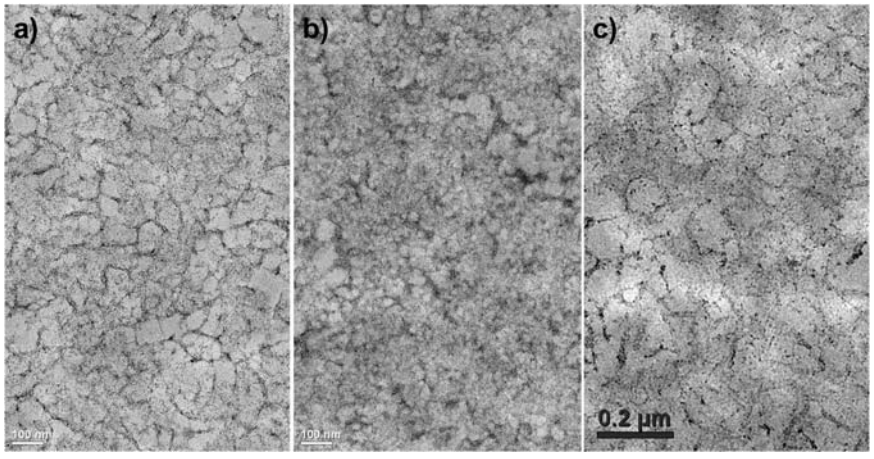

Figure 2.13 TEM images of Q HyperCel prepared in (a) 10 mM sodium phosphate, (b) 50 mM bis-tris and (c) 10 mM sodium cacodylate buffers during fixation.

2.3.3.2 Q HyperCel

Two different methods of chemical fixation were used: the standard method using 1% glutaraldehyde and 1% paraformaldehyde to temporarily fix the material, followed by OsO_4, and the TAGO method, which utilizes 1% tannic acid instead of 1% paraformaldehyde. Tannic acid acts as a mordant for the OsO_4, binding to the cellulosic backbone of the material as opposed to attaching only to the functionalized ligands of the ion exchangers. This increases the contrast provided by the OsO_4 as well as allowing the staining of material without a moiety with specific affinity for the heavy metal stain (e.g., sulfonated resins).

Figure 2.14 shows TEM images of Q HyperCel at 10000x and 31500x magnification using both methods of fixation. The TAGO method yields images showing a more disconnected pore network within the material. Pore diameters appear to be on the order of 50 nm, similar to those of other natural carbohydrate polymer matrices, e.g., Sepharose FF (DePhillips and Lenhoff, 2000; Yao and Lenhoff, 2004) and to some of the pore space seen in SEM. Possible reasons for the difference between these pore dimensions and those based on ISEC were discussed above. In the case of TEM, dehydration into solvent prior to resin infiltration may have been the culprit, as the cellulosic materials are highly hydrophilic, but the resolution of the microscope may also have been a factor. Since the heavy metal stain adheres to the positively-charged functional groups on the surface of the material, it may not give significant contrast to these extenders as they may have far less functionalization than the cellulosic backbone.

The dark spots present in the TAGO-fixed samples are probably deposits of OsO_4 that aggregated during osmication. It was verified that these were not artifacts

of the post-staining procedure by imaging sections that had undergone fixation but not post-staining.

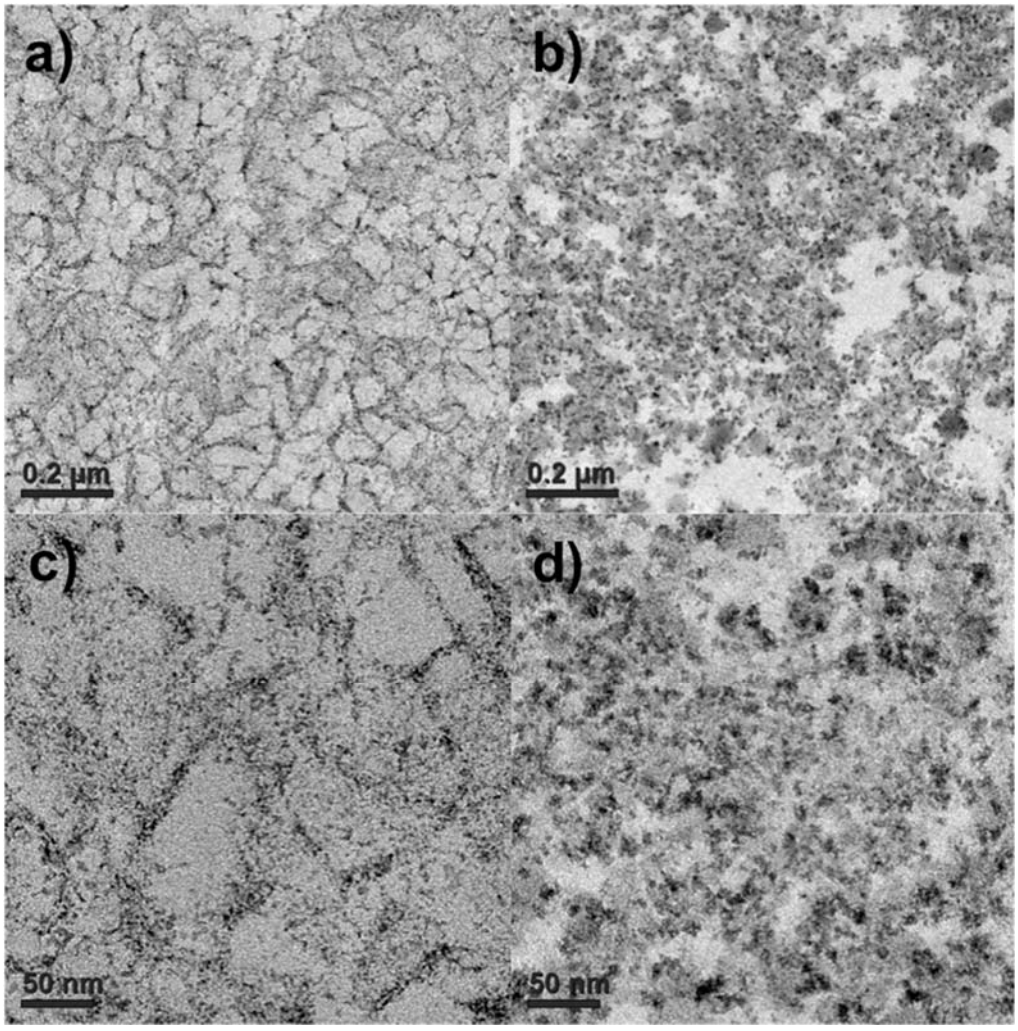

Figure 2.14 TEM images of Q HyperCel prepared using standard aldehyde fixation (a and c) and TAGO fixation (b and d); 10000x (a and b) and 31500x (c and d) magnification.

2.3.3.3 STAR AX HyperCel

Images of STAR AX HyperCel (Figure 2.15) differ from those of Q HyperCel in that the structure seems to be more homogeneous, with less definition between pore space and cellulose. The TAGO fixation method does not seem to change the result much from the standard aldehyde fixation, albeit there is more contrast in these samples since tannic acid acts as a mordant for the OsO_4. There is little to no heterogeneity in the structure, implying a much smaller and more complex pore network than the Q and S HyperCel moieties. Pore dimensions cannot be determined using either method of fixation and dark spots are most likely OsO_4 deposits (which are also seen for Q HyperCel) and do not signify any particular structural characteristic.

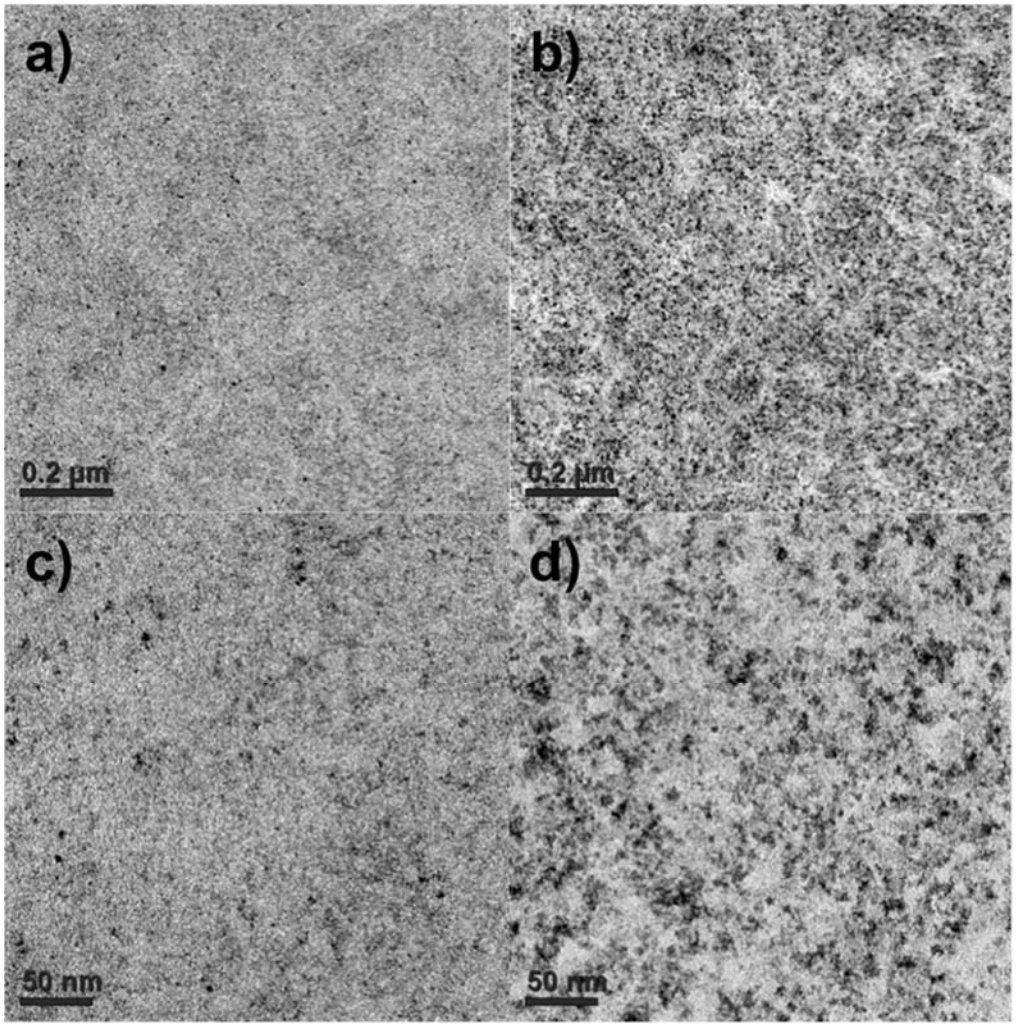

Figure 2.15 TEM images of STAR AX HyperCel prepared using standard aldehyde fixation (a and c) and TAGO fixation (b and d); 10000x (a and b) and 31500x (c and d) magnification.

2.3.3.4 Intraparticle Voids

A recurring feature that appeared in TEM and SEM images was intraparticle voids in sections of the HyperCel materials. These seemed to be areas of lower cellulosic content that may have been formed during the manufacturing process. These voids were also visible when protein uptake and elution were imaged by confocal microscopy (Section 3.3.4.4), so the possibility that they may have been formed by the sample processing methods or microtome sectioning can be ruled out. Although these voids were present in all HyperCel materials, they most likely do not contribute to any negative effects on protein sorption or transport; they do not contribute to the extraparticle volume as the large dextran probes used to determine the extraparticle porosity cannot access the pore space and they do not seem to hinder the adsorptive capacity or protein uptake rates (see Chapter 3). These voids were also imaged in two-dimensional slices, so the portion of intraparticle space they occupy is much less in a real three-dimensional volume.

Figure 2.16 shows some examples of the low-density voids within Q and STAR AX HyperCel, but similar formations were present in S HyperCel as well. It is easy to see from Figures 2.16a and b that the voids are lower in cellulosic content than the bulk of the material, but still appear functionalized. Figure 2.16c shows a low-magnification image of STAR AX HyperCel to display the distribution and relative sizes of these voids within the entire particle; Q and S HyperCel show a similar distribution of voids. Void sizes seem to range from approximately 100 nm to several hundred nanometers in diameter. Figure 2.16d shows protein-adsorbed STAR AX HyperCel, as voids were not apparent in the unadsorbed phase due to the increased level of homogeneity. If regions with higher contrast are assumed to be the cellulosic backbone, the voids in this case are actually higher in density than the surrounding

cellulose in the STAR AX material. If the regions of higher contrast are areas of more abundant protein localization, these voids could still be sparse in terms of cellulose content, but the ligand chemistry would still allow adsorption of protein.

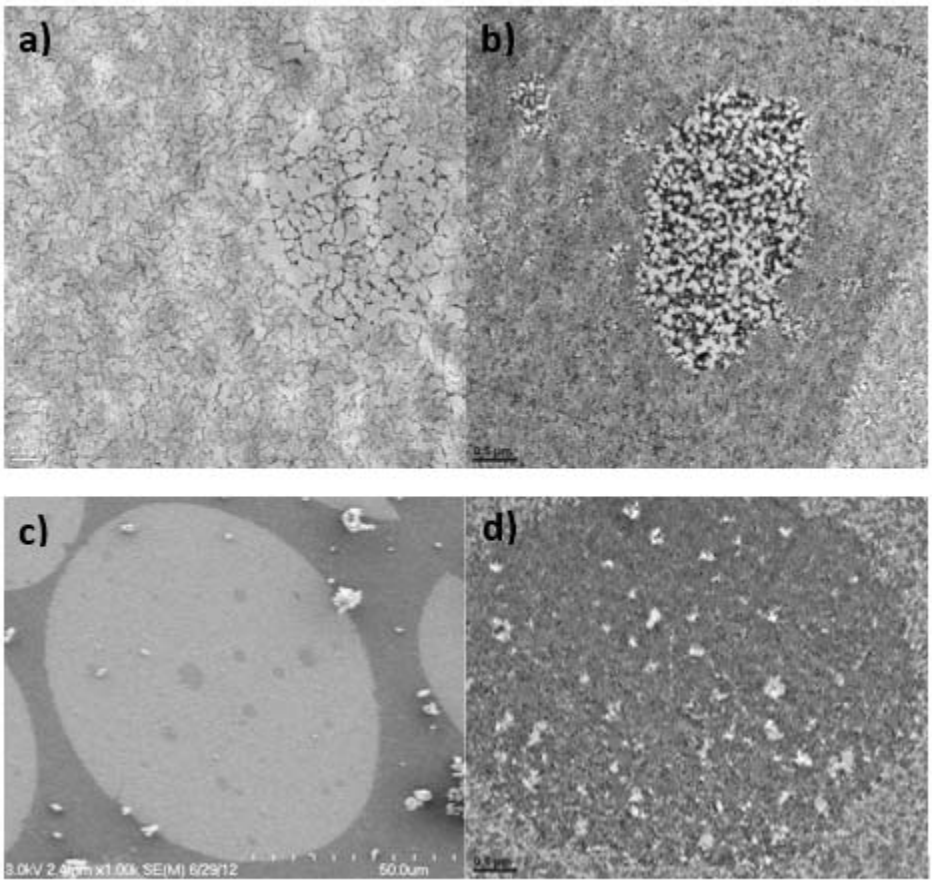

Figure 2.16 Micrographs of HyperCel materials showing void regions. a) TEM image of Q HyperCel without protein adsorbed (8000x); b) TEM image of Q HyperCel with 50% of maximum loading of β-lactoglobulin (4000x); c) SEM image of STAR AX HyperCel section (1000x); d) TEM image of STAR AX HyperCel with 50% of maximum loading of β-lactoglobulin (4000x).

2.3.4 Salt Exclusion

Data collected from salt step gradient experiments are shown in Figure 2.17 for Q and STAR AX HyperCel. The different symbols in Figures 2.17a and 2.17b correspond to the values of TIS for the high-salt buffers used in conjunction with the 50 mM bis-tris (13 mM TIS) low-salt buffer to generate feeds of different ionic strengths.

The STAR AX material displayed more scattered data for the same salt concentration steps than for Q, so these experiments were run in triplicate; the reason for the higher degree of scatter is not known. In both resins, salt exclusion is clearly apparent at low salt, but it becomes insignificant at TIS values greater than about 150 mM TIS. This similarity implies that the two resins have similar charge densities, despite their differing ligand chemistries.

In a standard polymer-modified material, SP Sepharose XL, the salt exclusion was found to become insignificant above about 300 mM TIS (Bowes et al., 2012), i.e., double the value found for AEX HyperCel materials. This presumably reflects differences in the local ligand charge density in the media concerned. The ligand density as reported by the manufacturers for SP Sepharose XL, 0.18-0.25 mmol/mL, is higher than that in the HyperCel media (0.099-0.138 mmol/mL for Q HyperCel and 0.059-0.084 mmol/mL for S HyperCel). However, a direct comparison is complicated by the dependence of the Donnan behavior on the local charge density within the polymer, not the value averaged over the whole particle, which is what is reported by the manufacturers.

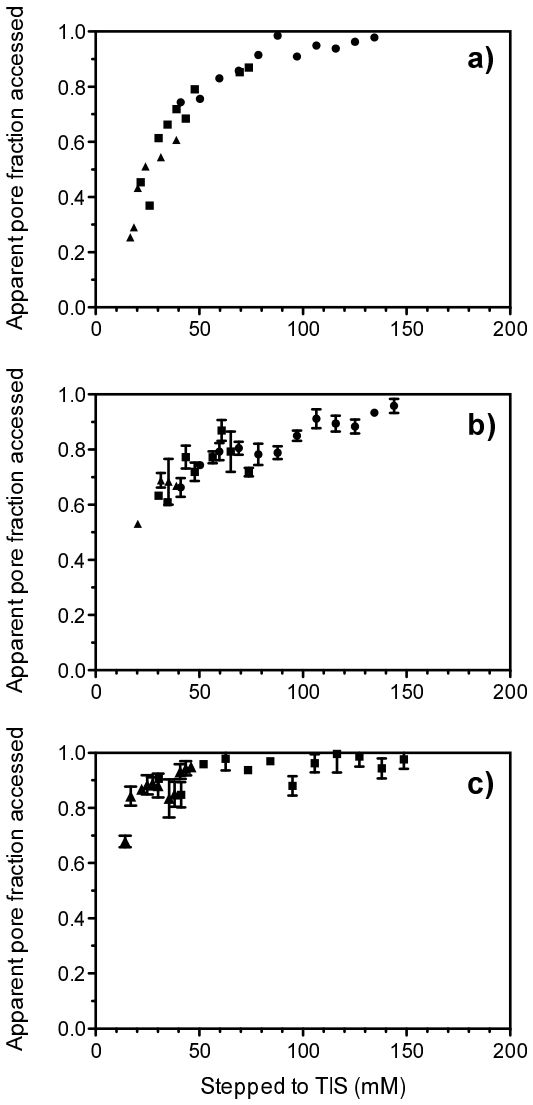

Figure 2.17 Salt exclusion in Q HyperCel (a) and STAR AX HyperCel (b, c). Solution conditions for (a) and (b) were 50 mM bis-tris, pH 7, with TIS adjusted with NaCl. Symbols denote maximum TIS of buffer used for each range of ionic strengths: 200 (●), 100 (■), and 50 (▲) mM TIS. Solution conditions for (c) were 10-100 mM sodium phosphate, pH 7. Symbols denote the maximum concentration of sodium phosphate used for each range of ionic strengths: 100 (■) and 30 (▲) mM sodium phosphate.

That the behavior seen is indeed a Donnan exclusion effect and not just the result of a reduction in double-layer thickness is indicated especially by the relatively steep approach to unity of the pore fraction accessed in each of the plots. Since the double-layer thickness varies inversely with the square root of ionic strength, a much slower approach would be expected if that were the basis for exclusion; such a slow approach is indeed seen for SP Sepharose FF (Bowes et al., 2012). It therefore appears appropriate to consider the ligand distribution within the HyperCel media to be a volumetric one, with the charges relatively closely spaced within the ligand-containing regions. In the case of the HyperCel media the possibility also exists of having ligands fairly uniformly distributed throughout the particle interior.

In addition to investigating the effect of salt exclusion in a bis-tris/NaCl buffering system, salt exclusion was assessed in a monobasic sodium phosphate buffering system for STAR AX HyperCel (Figure 2.17c). Using 30 and 100 mM sodium phosphate as the upper limits in the step gradients, salt exclusion was found to be insignificant above 50 mM TIS, 100 mM less than for the bis-tris/NaCl buffering system. This is consistent with the direction of change expected (Helfferich, 1962) for the multivalent phosphate ions, as opposed to the monovalency of Cl^-, although a direct quantitative comparison is not readily performed.

2.4 Conclusions

The structural characteristics of the polysaccharidic resins studied in this chapter are of interest because they directly dictate functional characteristics, such as protein sorption and transport within the porous network. The use of both macroscopic (column-level) and microscopic techniques was aimed at gleaning as much of a physical understanding of these materials as possible. The picture that emerges from

our results is of materials with a much greater degree of homogeneity of structure than is the case for another class of highly cross-linked carbohydrate-based adsorbents, namely those on agarose base matrices. Although electron microscopy shows apparent pores of dimension 10-50 nm and therefore approaching the typical mean pore size of agarose media such as Sepharose FF, the intrinsic pore space in the HyperCel cellulosic media is closer to 5 nm in dimension, as indicated by ISEC. EM imaging did reveal, however, significant apparent differences in pore structure between the salt-tolerant and non-salt-tolerant moieties, presumably due to the unique ligand chemistry of STAR AX HyperCel.

A specific aspect of interest here was whether the known differences in salt-tolerance between STAR AX and Q HyperCel are apparent in any of the structural characteristics probed. Although differences are seen in EM appearance, they may be due to the effects of ligand chemistry on EM sample preparation, and it is likely that differences in salt tolerance are simply due to the presence of the primary amine group on the STAR AX ligand.

Another structural characteristic that can have a direct impact on functional characteristics of the HyperCel media is the ligand distribution. Salt exclusion experiments suggest that, like the structure generally, the ligand distribution is relatively homogeneous, resulting in an effectively 3-D distribution of ligands. That the overall ligand density, based on the whole particle volume, is already somewhat low would result in a low local ligand density, which may have implications for protein transport in these media, as discussed in the following chapter.

Chapter 3

ADSORPTIVE AND TRANSPORT BEHAVIOR OF PROTEINS WITHIN CELLULOSE- AND AGAROSE-BASED ION-EXCHANGE ADSORBENTS

3.1 Introduction

Cellulosic IEX materials exhibit several advantages for the adsorption of proteins during chromatographic processes. The hydrophilic nature of cellulose minimizes non-specific binding (Peterson, 1970) and the intricate, yet open, microstructure provides a large surface area for protein adsorption (Angelo et al., 2013; Graham and Fook, 1982; Peterson and Sober, 1956). These characteristics give rise to transport rates higher than commonly observed in traditional, macroporous adsorbents under favorable binding conditions, which help facilitate rapid diffusion along with high adsorptive capacities. In this regard, cellulosic media have characteristics similar to those of polymer-modified adsorbents, namely high binding capacities and rates of uptake (Angelo et al., 2016; Bowes and Lenhoff, 2011a; Bowes et al., 2009; Fernandez and Carta, 1996; Lewus et al., 1998; Wang and Sun, 2007; Weaver and Carta, 1996), which typically exceed those of related conventional chromatographic media. That cellulosic media may be able to achieve comparable results without the use of end-grafted polymers (Wang and Sun, 2007) or covalently attached extenders (Bowes and Lenhoff, 2011b; Stone and Carta, 2007) makes them functionally attractive while being more homogeneously structured than conventional media.

In this chapter, a functional characterization of the family of HyperCel ion exchangers was performed in order to elucidate the principal features of their chromatographic performance. This work complements the previous chapter regarding the structural characterization of the same group of materials, allowing any clear structure–function relationships to be identified. As the adsorptive properties of dextran-grafted agarose materials have been extensively described previously (Bowes and Lenhoff, 2011a; Bowes et al., 2012, 2009; Hubbuch et al., 2003; Stone et al., 2009; Ubiera and Carta, 2006), more of a focus will be placed upon the cellulosic media as an in-depth analysis of these materials' functional characteristics remains to be performed. This chapter also includes additional structural characterization of protein-loaded media, as opposed to the bare stationary phases investigated in the preceding chapter.

The functional characteristics are studied via several experimental and analytical techniques. Adsorption isotherm measurements provide static binding capacities of each resin-protein system over a range of total ionic strength values. They are complemented by isocratic retention experiments to allow determination of protein binding affinity at different solution conditions. Apart from their value in interpreting adsorption behavior, the relative values of the retention factor for any pair of solutes provide a direct measure of selectivity.

In chromatographic practice, the dynamic binding capacity (DBC) is of greater interest than the static binding capacity, making measurement of protein transport rates essential (Müller, 2005; Shi et al., 2010). These measurements are confounded by the coupling between adsorption and transport, so mechanistic studies are of value. We pursue these here qualitatively, and to some extent quantitatively, using time-

series confocal laser scanning microscopy (CLSM) and quantitatively using batch uptake kinetic measurements in an agitated bath. The determination of intraparticle resistances encountered by solutes being taken up into these adsorbents is important in the predictive modeling of behavior, and the overall efficiency of processes in scaled-up applications.

As with many chromatographic systems with unconventional bead morphologies, structure often dictates functional characteristics, specifically with regard to transport and protein localization. Electron microscopy imaging of protein-adsorbed phases can help elucidate aspects of this behavior, as has been illustrated previously for agarose-based IEX materials (Bowes et al., 2009; Koku, 2011). Comparison of stationary phases with and without protein provides a qualitative understanding of how the particle structure, and therefore the space available for protein movement and binding within these materials, changes under different loading and operating conditions.

In this chapter, these techniques are put to use to characterize the adsorption of protein on three adsorbents. The roles of protein size, TIS of the solution, functional moieties, protein concentrations, and other operational factors are examined in order to assess characteristics of adsorptive behavior. The adsorbents are based on the HyperCel base matrix for standard strong cation- and anion-exchange, as well as a salt-tolerant anion exchanger, STAR AX HyperCel, developed to allow for high protein affinities and capacities under moderate to high conductivities (Angelo et al., 2016; Champagne et al., 2013). This allows for processing of feedstocks with high salt concentrations without the need for buffer exchange or dilution, resulting in more efficient downstream separations. Mechanisms of protein transport within these types

of materials and comparisons with strong IEX counterparts have yet to be studied extensively.

3.2 Materials and Methods

3.2.1 Buffers, Protein Solutions and Stationary Phases

Monobasic sodium phosphate (NaH_2PO_4) and bis-tris were obtained from Fisher Scientific (Fair Lawn, NJ) and Sigma-Aldrich (St. Louis, MO), respectively, and used to prepare 10 mM sodium phosphate (for CEX resins) and 50 mM bis-tris (for AEX resins) buffer solutions at pH 7. Acetic acid and sodium acetate were obtained from Fisher Scientific and used to prepare 10 mM sodium acetate buffer at pH 5 for monoclonal antibody adsorption. The TIS of solutions was adjusted using NaCl. Each resin was washed successively with DI water and 1 M NaCl and then equilibrated with the desired TIS-controlled buffer.

Hen egg white lysozyme (L6876, lot: 100M1897V), bovine serum albumin (BSA) (A0281, lot: 075K7545) and bovine β-lactoglobulin (L0130, lot: SLBF4545V) were purchased from Sigma-Aldrich and bovine lactoferrin was obtained from DMV-International. Solutions were prepared by dissolving lyophilized protein in the desired TIS-controlled buffer and concentrated using 10K Amicon centrifugal filters. Concentrated samples were rediluted with buffer and reconcentrated three times, and the final protein solutions were filtered using 0.22 μm syringe filters. Lactoferrin was first purified to remove impurities by using a sodium chloride gradient on a 56 mL SP Sepharose FF cation-exchange column and collecting the primary elution peak. A monoclonal antibody was obtained from Amgen, Inc. (Thousand Oaks, CA) in formulation buffer concentrated at approximately 35 mg/mL. Protein concentrations

were determined using UV spectrophotometry on a Shimadzu UV-1700 or a Thermo Scientific NanoDrop 2000. Target protein concentrations for stock solutions were 4-6 mg/mL. Protein properties, including isoelectric point, molecular weight, effective radius and extinction coefficient at 280 nm, are shown in Table 3.1.

Protein	pI	M_w (kDa)	r (nm)	ε (cm^2/mg)
Lysozyme	11.4 (Wetter and Deutsch, 1951)	14.3 (Canfield, 1963)	1.6 (Bowes et al., 2009)	2.64 (Sophianopoulos et al., 1962)
Lactoferrin	8.8 (Plate et al., 2006)	78 (Moore et al., 1997)	2.8 (Bowes et al., 2009)	1.51 (Groves, 1960)
mAb	~8	144 (Ahamed et al., 2007)	3.4 (Bowes et al., 2009)	1.47
β-lactoglobulin	5.4 (Nozaki et al., 1959)	18.3 (Sawyer and Kontopidis, 2000)	1.8 (Sawyer and Kontopidis, 2000)	0.962 (Sawyer and Kontopidis, 2000)
BSA	4.7 (Peula-Garcia et al., 1997)	66.5 (Dhubhghaill et al., 1992)	2.7 (Akiyoshi and Sunamoto, 1996)	0.659 (Peters, 1985)

Table 3.1 Physical characteristics of proteins used in adsorption experiments; r = radius of sphere of equivalent volume.

S, Q and STAR AX HyperCel, along with S and Q moieties of Sepharose FF and XL, were used for this work and previously described in Section 2.2.1. Capto Q (GE Healthcare, Piscataway, NJ) was also investigated, which consists of a highly cross-linked agarose based matrix (>6%) with 40 kDa dextran surface extenders, akin to the Sepharose XL material. However, Capto Q possesses a quaternary ammonium group on a shorter spacer arm than in Sepharose XL (Axen et al., 2008). Manufacturer-reported properties of these resins can be found in Tables 1.1 and 1.2.

3.2.2 Capillary Tube Calibration

Resin was drawn into Wiretrol II 100 and 200 µL capillary tubes (Drummond Scientific, Broomall, PA) to measure a given hydrated particle volume. For the AEX materials, capillary tubes were silanized using 4% 3-aminopropyltriethoxysilane (APTES) (Fisher Scientific) in acetone in order to reduce electrostatic interactions between the positively-charged resin and the inherently negatively-charged glass surfaces. Tubes were treated in an agitated vessel of aminosilane solution for 2.5 hours before being generously washed with pure acetone, followed by DI water three times. Tubes were then sonicated in DI water for 30 minutes to remove loosely physisorbed species and dried using high-pressure air.

Columns were packed by adding particles via capillary tubes after recording the gravity-settled height. The column was then allowed to gravity-settle and the top flow adapter was adjusted to sit at the top of the gravity-settled bed without any further compression. Bed heights of approximately 5 cm were targeted. Injections of 1 mg/mL blue dextran were used to measure the fully excluded volume. Volumes of 10 µL were injected on a Waters 2695 separations module equipped with a Waters 2996 photodiode array detector to measure the absorbance at 280 nm. A flow rate of 0.05 mL/min was used to limit further compression of the bed. The hydrated particle volume, V_{hyd}, was calculated from

$$V_{hyd} = V_c - (V_r - V_d) \tag{3.1}$$

where V_c is the gravity-settled column volume, V_r is the retention volume of the solute and V_d is the dead volume found by performing an injection without a column in place. Resin-specific calibration factors were determined by dividing the hydrated particle volume by the gravity-settled capillary tube height and are tabulated in Table

3.2 for the HyperCel materials. Calibration factors for Sepharose and Capto resins have been reported previously (Bowes, 2011).

	Calibration factor (mL hyd. part. vol./mm)
S HyperCel	0.00182
Q HyperCel	0.00197
STAR AX HyperCel	0.00182

Table 3.2 HyperCel calibration factors to convert resin height in Wiretrol II capillary tubes into hydrated particle volume.

3.2.3 Adsorption Isotherms

A series of protein dilutions were prepared in 1.6 mL Eppendorf tubes at concentrations ranging from 100% to 6.25% of that of the protein stock; the dilutions used the same TIS-controlled buffer in which the protein solutions were prepared. Small amounts of resin were dispensed into each tube via Wiretrol II capillary tubes after the gravity-settled height of the resin and the additional buffer volume added in each capillary tube were recorded. Samples were allowed to equilibrate by rotation for 5 days to 14 days (in the case of STAR AX HyperCel). In most cases, an equilibration time of 5 days was sufficient in order to observe no appreciable further decrease in the supernatant concentration (C). Final protein concentrations in the supernatant were determined by absorbance measurements at 280 nm. The amount adsorbed at the end of each experiment is determined by mass balance

$$q = \frac{V}{V_m}(C_0 - C) \tag{3.2}$$

where V is the total liquid volume, V_m is the hydrated particle volume, C_0 is the initial protein concentration, and the adsorbed concentration, q, is expressed in terms of mass

per unit volume of hydrated particle volume. Points were fit to the Langmuir isotherm model

$$q = \frac{q_{max} b C}{1 + bC} \tag{3.3}$$

in order to obtain maximum static binding capacities (q_{max}) and affinity coefficients (b) that characterize the softness of the isotherm. The Langmuir isotherm was used purely to obtain a curve to describe the data, with no assumptions made regarding the consistency of adsorption on HyperCel media with the assumptions underlying the derivation of the Langmuir isotherm.

3.2.4 Isocratic Retention

Isocratic retention measurements were made in 10 mM sodium phosphate buffer, pH 7, for S HyperCel and 50 mM bis-tris buffer, pH 7, for Q and STAR AX HyperCel, with NaCl added to adjust the TIS of the solution. A TIS of 1.5 M was used to obtain retention times of protein under unretained conditions. Various protein concentrations were used between roughly 0.25 mg/mL and 5 mg/mL for higher and lower TIS runs, respectively, in order for elution peaks of sufficient height to be developed. The measured retention time was not found to depend on the injection concentration for any of the cases examined. Samples of 20 μL were injected into 1 mL prepacked PRC HyperCel columns (Pall Life Sciences) at a flow rate of 0.2 mL/min (interstitial velocity ~ 60 cm/hr). Samples were run in triplicate, and the first moments of the resulting peaks were used to determine the retention times. The retention factor, k', was calculated by

$$k' = \frac{t_r - t_{hs}}{t_{hs} - t_d} \tag{3.4}$$

where t_r is the retention time of the sample of interest, t_{hs} is the retention of that sample under unretained conditions (1.5 M TIS), and t_d is the system dead time without a column in place. While t_{hs} as used here provides a functional measure of the retention time in the absence of binding to the resin, there is some uncertainty regarding the mechanistic interpretation because of the questions regarding partitioning of the protein into the resin in the absence of binding. However, our principal interest is in strongly retained conditions, where k' as calculated in Equation 3.4 provides an adequate measure.

3.2.5 Batch Uptake Kinetics

Batch uptake experiments were performed in a 100 mL baffled beaker agitated at 450 rpm by an impeller with a blade radius of 1 cm. A schematic representation of the apparatus is shown in Figure 3.1. The supernatant solution was continuously pumped at 20 mL/min, using an ÄKTA P960 sample pump (GE Healthcare), via an intake filter placed in the beaker directly above the impeller, through a UV detector on a GE Healthcare ÄKTA Explorer system, and back into the base of the beaker through a side port. The protein concentration was measured by UV absorbance at 280 nm and the dead volume of the loop was less than 2.5 mL.

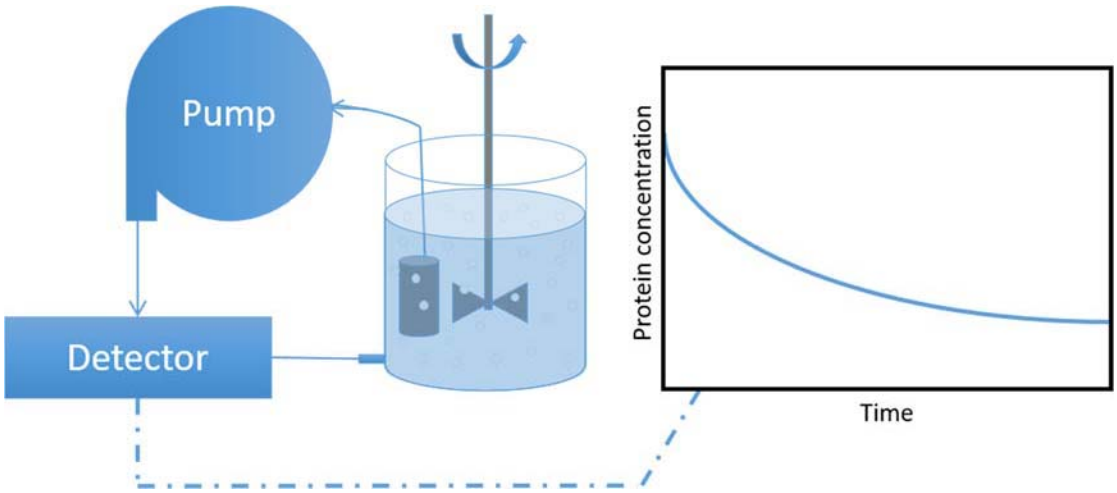

Figure 3.1 Schematic representation of apparatus for measuring batch uptake kinetics. UV detection is truncated to when the bath is dosed with resin particles and adjusted to account for system dead time.

Concentrated protein solutions were prepared in a similar fashion to those in the adsorption isotherm experiments. Aliquots of a concentrated protein solution and a buffer solution were then added to the beaker to bring the final volume to 60-70 mL at the desired initial protein concentration. Enough resin was measured using Wiretrol II capillary tubes to adsorb approximately 50% of the total protein in the beaker. The resin was quickly added and the protein concentration was recorded until there was little additional protein depletion. The remaining solution and resin were collected into Nalgene bottles and rotated for 24-48 hours in order to measure the final protein concentration after allowing a much longer time for adsorption to be complete.

To estimate the uptake rate parameters, the experimental data were fit to different analytical relations describing transport into a spherical particle using the nonlinear least-squares regression routine, 'nlinfit', in Matlab. The simplest transport model is for external mass transfer control, in which the intraparticle resistance is neglected and the uptake rate depends on an external mass transfer coefficient, k_f, via (Carta and Jungbauer, 2010; Weaver and Carta, 1996)

$$\frac{C-C_f}{C_0-C_f} = \exp\left(-\frac{3k_f V_m t}{R_p V}\right) \tag{3.5}$$

for the bulk solution protein concentration, or

$$\frac{\bar{q}}{q_{max}} = \frac{VC_0}{V_m q_{max}}\left[1-\exp\left(-\frac{3k_f V_m t}{R_p V}\right)\right] \tag{3.6}$$

for the adsorbed protein concentration, where C_f is the final concentration in the bath once uptake is complete, $\bar{q}$ is the average protein concentration adsorbed within the material, R_p is the particle radius and V and V_m are the volumes of the bulk solution and the resin respectively. If intraparticle transport is primarily by homogeneous diffusion with a near-rectangular isotherm, this limit would be expected to apply in the limit of low initial protein concentration. Conversely, in the case of high initial protein concentrations, the intraparticle resistance would be expected to be controlling (Fernandez and Carta, 1996; Helfferich, 1962; Weaver and Carta, 1996), and in the asymptotic limit of negligible external resistance, the homogeneous intraparticle diffusion model may be expressed as (Carta and Jungbauer, 2010; Weaver and Carta, 1996)

$$\frac{\bar{q}}{q_{max}} = 1-\frac{6}{\pi^2}\sum_{i=1}^{\infty}\frac{1}{i^2}\exp\left(-\frac{i^2\pi^2 D_h t}{R_p^2}\right) \tag{3.7}$$

where D_h is the homogeneous diffusivity.

Alternatively, for the case of dominant intraparticle resistance where transport is by pore diffusion, the analytical solution for the high-affinity limit (rectangular isotherm) is the shrinking-core model (Teo and Ruthven, 1986), for which the solution can be expressed as

$$\frac{D_e C_0}{R_p^2 q_{max}} t = \left(1 - \frac{1}{Bi}\right) I_2 - I_1 \tag{3.8.1}$$

$$I_1 = \frac{1}{6\lambda\Lambda} \ln\left[\frac{\lambda^3+\eta^3}{\lambda^3+1}\left(\frac{\lambda+1}{\lambda+\eta}\right)^3\right] + \frac{1}{\lambda\Lambda\sqrt{3}}\left[\tan^{-1}\left(\frac{2\eta-\lambda}{\lambda\sqrt{3}}\right) - \tan^{-1}\left(\frac{2-\lambda}{\lambda\sqrt{3}}\right)\right] \tag{3.8.2}$$

$$I_2 = \frac{1}{3\Lambda} \ln\frac{\lambda^3+\eta^3}{\lambda^3+1} \tag{3.8.3}$$

$$\eta = \left(1 - \frac{\bar{q}}{q_{max}}\right)^{\frac{1}{3}} \tag{3.8.4}$$

$$\Lambda = \frac{V_m q_{max}}{V C_0} \tag{3.8.5}$$

$$\lambda = \left(\frac{1}{\Lambda} - 1\right)^{\frac{1}{3}} \tag{3.8.6}$$

where D_e is the effective pore diffusivity. The Biot number, $Bi = k_f R_p / D_e$, can be estimated by finding the external mass transfer coefficient k_f either from a suitable correlation or by fitting uptake data under conditions for which the external resistance is dominant. In the limit of negligible external resistance 1/Bi approaches zero, simplifying the form of Equation 3.8.1. This modeling strategy applied only to systems that presented the characteristic shrinking-core behavior when observed via confocal microscopy (see Section 3.3.4).

Numerical solutions to the models were employed for external mass transfer control and homogeneous diffusion in order to compare fit diffusivity and transport parameters to those obtained assuming complete dominance of a single transport regime, which were determined via explicit analytical solutions. The numerical

solution for homogeneous diffusion incorporates the external mass transfer coefficient for the respective system, a distinct advantage to using this form over the simpler analytical form, which lacks this term. This was achieved by employing the partial differential equation solver routine within Matlab, 'pdepe', utilizing the conservation equations and boundary conditions for one-dimenstional homogenous diffusion within a spherical geometry

$$\frac{\partial q}{\partial t} = \frac{D_h}{r^2}\frac{\partial}{\partial r}\left(r^2\frac{\partial q}{\partial r}\right) \tag{3.9.1}$$

$$t = 0, \quad q = 0 \tag{3.9.2}$$

$$r = 0, \quad \frac{\partial q}{\partial r} = 0 \tag{3.9.3}$$

$$r = R_p, \quad D_h\frac{\partial q}{\partial r} = k_f(C - C_i) \tag{3.9.4}$$

where C_i is the solution concentration at the bulk solution-particle interface related by the adsorption isotherm. The Langmuir isotherm was used for simplicity and its accurate description of the equilibrium concentrations. Equation 3.9.4, the convective boundary condition, incorporates the external mass transfer coefficient into the model, allowing the fit homogeneous diffusivity value to be decoupled from the film resistance.

3.2.6 Protein Uptake Profiles via Confocal Microscopy Imaging

Particles were packed into a flow cell designed for use in a confocal microscope (Dziennik et al., 2003). Reservoirs of equilibration buffer, protein solution, and high-salt buffer (1 M NaCl) were connected to an LKB Bromma positive-displacement pump equipped with a multi-port valve to allow switching among buffer/protein solutions to be pumped through the flow cell. A schematic representation of the setup can be seen in Figure 3.2. Flow rates used ranged from 0.25

to 1 mL/min, corresponding to linear velocities of 525-2100 cm/hr. The proteins used were fluorescently labeled with either DyLight 650 (62266) or 488 (46403) NHS Ester (Thermo Scientific) in a 1-2% labeling ratio following protocols supplied by the manufacturer. Particles were imaged using a Zeiss 5 LIVE DUO high-speed confocal microscope equipped with a 40x C-Apochromat (NA 1.2) water-immersion lens (Carl Zeiss), with images collected approximately every 5 seconds. The microscope was also equipped with a piezoelectric motor for fast scanning in the *z* (vertical) direction. In order to allow comparison of intensities, the laser intensity and gain were kept constant for each experiment involving uptake of the same protein and were set to the highest setting possible without saturating the detector once nearly full saturation was achieved.

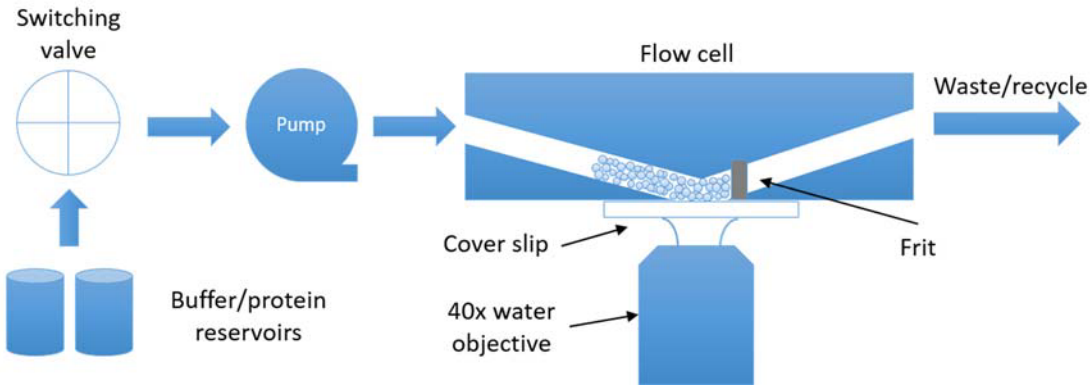

Figure 3.2 Schematic representation of confocal microscopy flow cell and setup. Resin particles were packed into the channel via capillary tubes and a high linear flow rate of 2100 cm/hr was used to hold particles in place against the 0.2 micron stainless steel frit.

Packed particles were washed with high-salt buffer and equilibrated at 1 mL/min before imaging began. A single particle was selected for continuous observation so as to capture the uptake and elution profiles in the *xz* plane using the *z*-stack functionality of the microscope. The time point at which feeding of the protein solution through the flow cell was started was marked in order to correct for the system dead volume (< 0.75 mL), and the protein solution was allowed to flow until apparent full particle saturation was achieved. The valve was then switched to feeding of high-salt buffer in order to observe elution behavior. Imaging was performed until no fluorescently-labeled protein remained visible inside the particle or no appreciable decrease in fluorescence was observed.

3.2.7 Electron Microscopy

3.2.7.1 Sample Preparation

Particle samples for SEM and TEM were prepared using similar methods to those described previously in Section 2.2.4. Samples of resin with adsorbed lysozyme (for S HyperCel) or β-lactoglobulin (for Q and STAR AX HyperCel) were prepared in the same manner as for the adsorption isotherms (Section 3.2.3). A target loading of 50% of the maximum static binding capacity for each resin was used.

3.2.7.2 Scanning Electron Microscopy

Samples were temporarily fixed with 1% glutaraldehyde and 1% paraformaldehyde before being chemically fixed with 1% osmium tetroxide (OsO_4) in DI water. Samples were then washed with DI water and dehydrated in ethanol before following the same processing method as for the samples without adsorbed protein (Section 2.2.4.1). Several samples without adsorbed protein were also chemically

fixed using this procedure to allow a qualitative comparison between phases. All particle samples were palladium-gold sputter-coated for 4 minutes at a current of 30 mA and an argon pressure of 65 mtorr. SEM imaging was performed using a Hitachi S4700 FESEM operated in secondary electron mode with a voltage of 2.0 kV and a working distance of 2-3 mm.

3.2.7.3 Transmission Electron Microscopy

All samples were prepared using 10 mM sodium phosphate buffer at pH 7 for the initial fixation, as amine groups in bis-tris cause undesired imaging artifacts (Section 2.3.3.1). Samples were temporarily fixed using 1% glutaraldehyde and 1% paraformaldehyde before being chemically fixed using 1% osmium tetroxide in DI water. Samples were then washed with DI water and dehydrated in acetone before the same processing method was followed as for the samples without adsorbed protein (Section 2.2.4.2). Q and STAR AX HyperCel materials were also stained using 1% glutaraldehyde and 1% tannic acid, followed by the remainder of the standard sample processing; this is the so-called TAGO fixation method (tannic acid-glutaraldehyde-osmium tetroxide) (Hayat, 2000). Tannic acid acts as a mordant for the OsO_4, binding to the cellulosic backbone of the material as opposed to only the functionalized ligands of the ion exchangers. This increases contrast provided by the OsO_4 as well as allowing the staining of material without a favorable affinity to the heavy metal stain (e.g., sulfonated resins). All particle samples were microtomed into sections approximately 50 nm in thickness and imaging was performed on a Zeiss LIBRA 120 transmission electron microscope operated at 120 kV.

3.3 Results and Discussion

3.3.1 Adsorption Isotherms

Adsorption isotherms of β-lactoglobulin and BSA on STAR AX and Q HyperCel are shown in Figure 3.3. Isotherms at 20, 50, and 100 mM TIS were measured for both resins, but only for STAR AX at 200 mM TIS since the 100 mM TIS data set on the Q resin revealed relatively low static capacity. The typical hyperbolic shape is seen for all the plots, and the fits to the Langmuir isotherm model are reasonable; values of the maximum static binding capacity and the affinity coefficient from the fits are given in Table 3.3. These results verify that the ligand chemistry of the STAR AX material allows a significantly increased maximum static binding capacity compared to that on Q HyperCel with increasing TIS, with STAR AX having more than double the capacity of Q at 100 mM TIS. Examination of these results also suggests that protein size is not a significant factor affecting adsorptive capacity for Q HyperCel, since β-lactoglobulin and BSA have molecular weights that differ by approximately 50 kDa. However, STAR AX HyperCel shows higher sensitivity to TIS of the static capacity for BSA compared to β-lactoglobulin. The increased scatter in the data at lower TIS values for STAR AX HyperCel may be due to variability in measuring resin volumes in the capillary tubes, where increased adhesion of STAR AX to the tube wall was noted.

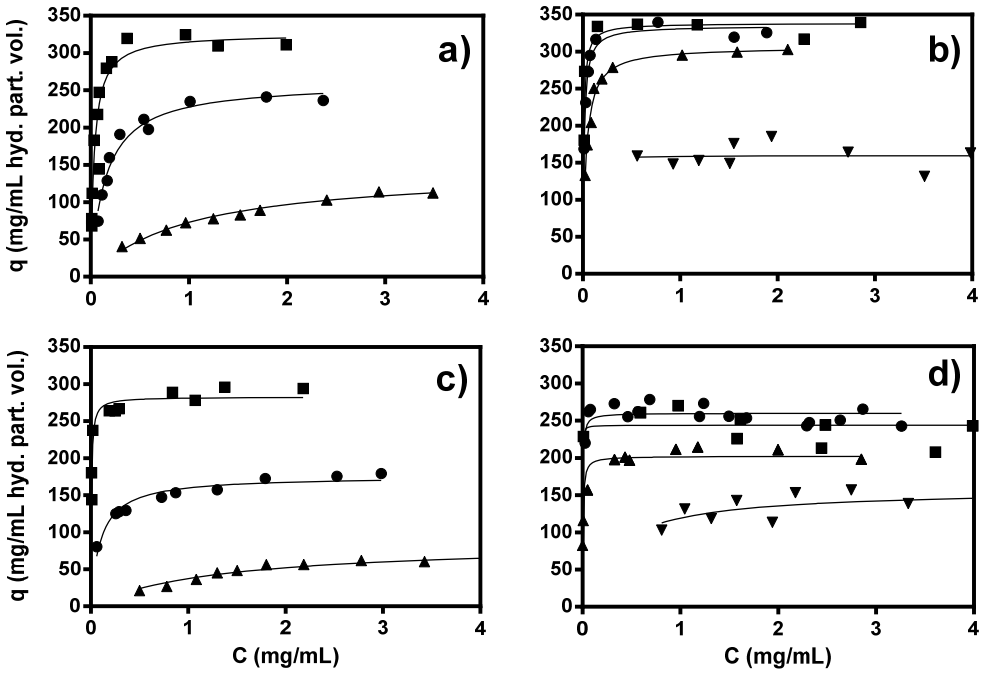

Figure 3.3 Adsorption isotherms for β-lactoglobulin (a, b) and BSA (c, d) on Q (a, c) and STAR AX (b, d) HyperCel. Performed in 50 mM bis-tris, pH 7 at 20 (■), 50 (●), 100 (▲), and 200 (▼) mM TIS. Data are shown with fits to the Langmuir isotherm for each condition.

Isotherms of lysozyme, lactoferrin and mAb on S HyperCel are shown in Figure 3.4 at 20, 50 and 100 mM TIS. Despite the difference in the protein sizes, capacities for lysozyme and lactoferrin at 20 mM TIS are very similar. The two-lobed structure of lactoferrin may contribute to this, as the highly positively charged lobe could orient the protein in the adsorbed state (Bowes et al., 2009). Alternatively, if adsorption on HyperCel materials is similar to that on polymer-functionalized media, the maximum capacity may be limited by the available volume for partitioning, which would result in similar capacities for different proteins. Another noteworthy feature is the sharper decline of the maximum capacity for lactoferrin with increasing salt concentration. This may reflect an exclusion effect similar to that seen on polymer-modified media for larger proteins (Bowes and Lenhoff, 2011a) or could be due, as above, to the surface charge distribution on lactoferrin, which may make it more susceptible to electrostatic screening (Kisley et al., 2014). The results for mAb adsorption show a similar trend in that raising the TIS from 20 to 50 mM is enough to halve the static capacity from approximately 200 to 100 mg/mL. The monoclonal antibody is roughly double the molecular weight of lactoferrin, so it is apparent that the increased size does not affect its binding capacity at these low to intermediate ionic strength conditions to any significant degree.

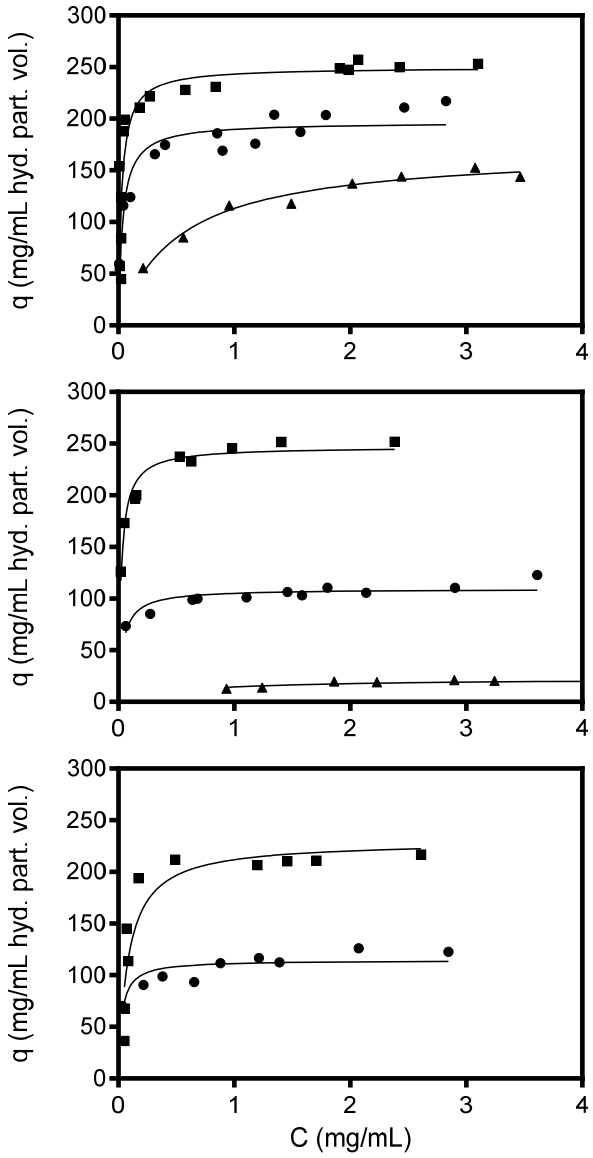

Figure 3.4 Adsorption isotherms for lysozyme (top), lactoferrin (middle) and mAb (bottom) on S HyperCel. Experimental conditions: 10 mM sodium phosphate, pH 7, for lysozyme and lactoferrin and 10 mM sodium acetate, pH 5, for mAb at 20 (■), 50 (●) and 100 (▲) mM TIS. Data are shown with fits to the Langmuir isotherm for each condition.

Resin	Protein	TIS (mM)	q_{max} (mg/mL)	b (mL/mg)
S HyperCel	lysozyme	20	250	37
		50	197	28
		100	170	2
	lactoferrin	20	247	41
		50	109	25
		100	23	2
	mAb	20	230	12
		50	115	35
Q HyperCel	β-lactoglobulin	20	326	28
		50	261	7
		100	144	1
	BSA	20	283	173
		50	176	10
		100	86	1
STAR AX HyperCel	β-lactoglobulin	20	338	121
		50	335	80
		100	307	30
		200	160	121
	BSA	20	244	1479
		50	260	333
		100	202	215
		200	157	3

Table 3.3 Langmuir isotherm parameters for model proteins on HyperCel adsorbents.

The relatively high binding capacities across all three materials are particularly noteworthy as capacities of these magnitudes have, for the most part, been achievable only on materials with polymer extenders used to expand the adsorptive surface area into a three-dimensional volume (Bowes and Lenhoff, 2011a, 2011b; Bowes et al., 2009; Stone and Carta, 2007; Wang and Sun, 2007; Weaver and Carta, 1996; Yu and Sun, 2013; Yu et al., 2013). Our investigation into the pore structure of HyperCel

resins (Angelo et al., 2013) discussed how these materials exhibit characteristics similar to those of polymer-modified stationary phases, although they are not polymer-modified themselves, as the base matrix does not undergo polymer grafting or covalent attachment during manufacturing. The gel-like quality of the cellulosic beads, narrow pore space and high pore interconnectivity permitted by the carbohydrate structure may provide a large enough surface area or volume for sorption to be comparable to that on this class of adsorbents.

3.3.2 Isocratic Retention

Results of the isocratic retention experiments for the three HyperCel materials are shown in Figure 3.5 for lysozyme and lactoferrin on S HyperCel and for β-lactoglobulin and BSA on Q and STAR AX HyperCel, as a function of TIS. Retention factors below 0.1 were truncated because of the uncertainties in these values under weakly-retained conditions, while retention factors greater than about 100 are difficult to determine because of the very long retention times and broad peaks.

Retention was found to be strongest on STAR AX HyperCel and weakest on Q HyperCel. This result was expected for the salt-tolerant primary amine ligand chemistry at higher TIS values and is consistent with the high static capacities that were determined from the adsorption isotherms. The high retention factors are also consistent with the highly-favorable near-rectangular isotherms that were obtained, as k' values are directly related to the slopes of the linear portions of the corresponding isotherms. Despite the differences between the k' values on the two anion exchangers, the slopes of the respective curves for the two proteins are very similar. This is consistent with previous results (Bowes et al., 2009; DePhillips and Lenhoff, 2001;

Traylor et al., 2014) that show the slope to be a strong function of the protein, independent of the adsorbent, at a given pH.

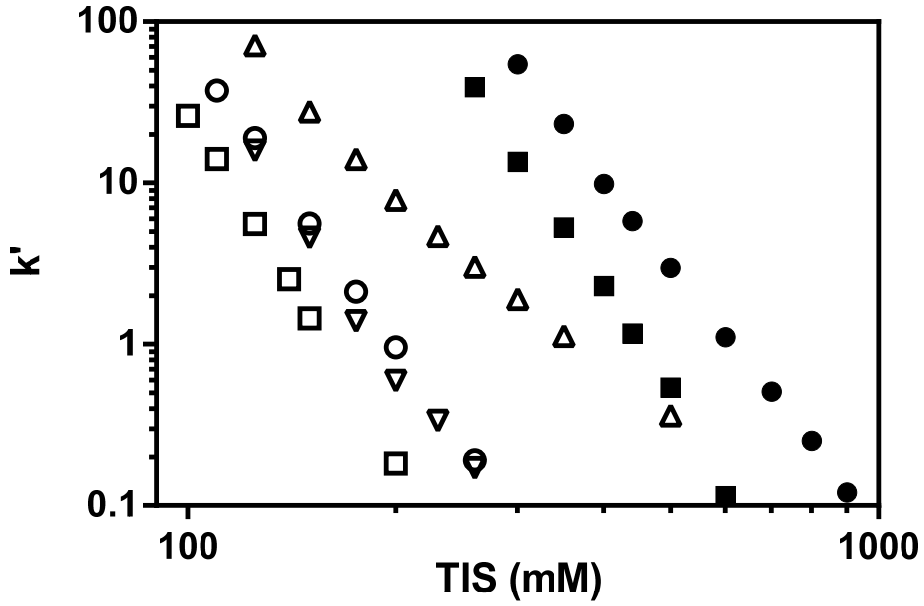

Figure 3.5 Isocratic retention data for HyperCel resins: BSA (□) and β-lactoglobulin (○) on Q HyperCel, BSA (■) and β-lactoglobulin (●) on STAR AX HyperCel, lactoferrin (▽) and lysozyme (△) on S HyperCel. Measurements were performed using 1 mL prepacked PRC columns operated at 60 cm/hr in 10 mM sodium phosphate, pH 7, for S HyperCel and 50 mM bis-tris, pH 7, for Q and STAR AX HyperCel; injection volume, 20 μL.

Retention data on S HyperCel show stronger retention of lysozyme than of lactoferrin. This is consistent with the results for the anion-exchange materials in which the larger model protein (BSA) exhibited lower strengths of adsorption than the smaller model protein (β-lactoglobulin). However, if the slopes of these curves were

extrapolated to lower TIS values (< 100 mM TIS), one would expect an intersection between the lysozyme and lactoferrin data, with lactoferrin then presenting higher k' values in this range. This may be related to its charge distribution, which exhibits a dense cluster of positively-charged residues on one of the lobes of the molecule (Bowes et al., 2009). At TIS values above 20 mM TIS, the electrostatics of this lobed region appear to be sufficiently screened to greatly reduce its strength of adsorption on the material, and possibly thereby the transport characteristics, differentiating it from the other model proteins investigated. The large decrease in the strength of adsoption for lactoferrin in the range of 20 to 100 mM TIS is illustrated in the adsorption isotherms discussed in Section 3.3.1.

3.3.3 Uptake Kinetics

Batch uptake kinetics were measured for lysozyme and lactoferrin on S HyperCel, β-lactoglobulin on Q and STAR AX HyperCel and BSA on Q HyperCel. Experiments were performed at 20 and 100 mM TIS for β-lactoglobulin and lysozyme and at 20 mM TIS for BSA and lactoferrin, all at pH 7. Two initial protein concentrations were also used in all cases, 2 ± 0.2 mg/mL and 0.2 ± 0.02 mg/mL, in order to exploit regimes where intraparticle and external mass transfer resistances respectively are expected to be dominant. Judgment of the applicability of particular mass transfer models was aided by CLSM observations of intraparticle intensity profiles, with diffuse profiles indicating a homogeneous diffusion mechanism and sharp uptake fronts a pore diffusion mechanism (Bowes and Lenhoff, 2011a; Dziennik et al., 2005, 2003; Hubbuch et al., 2003; Tao et al., 2011c; Yang et al., 2006). The former are generally seen at high TIS and the latter more often at low TIS, but the

distinction may sometimes be uncertain. Similarly, distinguishing whether the dominant resistance is intraparticle or extraparticle may also be uncertain.

Figure 3.6 shows the uptake of lysozyme and lactoferrin on S HyperCel. For a high initial concentration of lysozyme, the added particles reach full saturation in less than three minutes, which is very rapid when compared to other conventional materials (Dziennik et al., 2003; Weaver and Carta, 1996) and even to polymer-modified adsorbents (Bowes and Lenhoff, 2011a; Shi et al., 2010; Weaver and Carta, 1996). Fits to the rapid uptake are shown to both the homogeneous diffusion model and the external mass transfer model, as uptake this fast is indicative of very low intraparticle resistance.

There is much better agreement with the homogeneous diffusion model than the pure external control model, but both give reasonable descriptions of the data. The numerical solution of the homogeneous diffusion model that was utilized in these cases includes the external mass transfer resistance in the boundary conditions, which explains its closer fit than the analytical form of the external resistance model. The value of k_f was obtained from the experiments at the lower initial concentration, in which the external mass transfer model is appropriately applied.

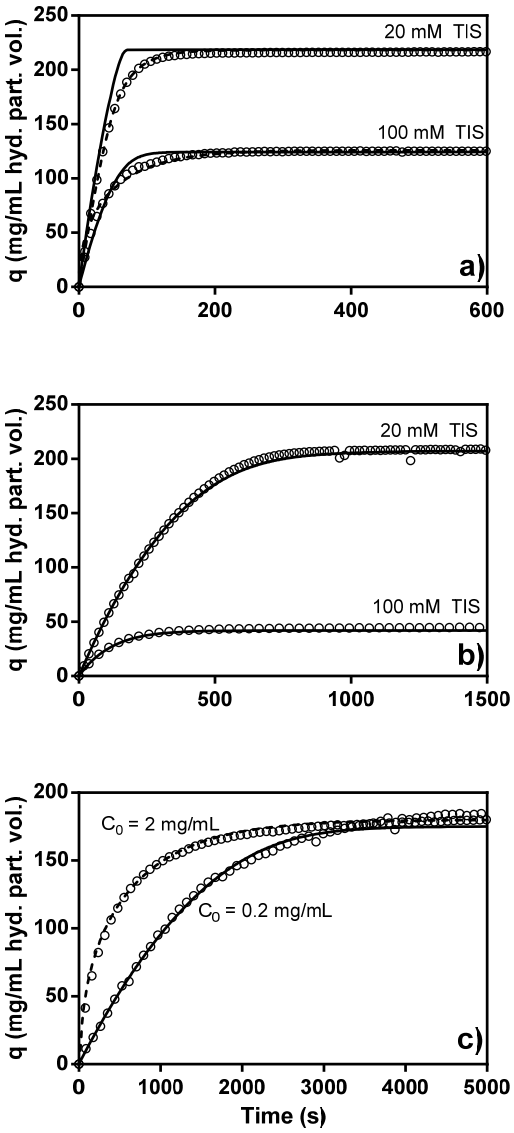

Figure 3.6 Batch uptake kinetics for lysozyme (a, b) and lactoferrin (c) on S HyperCel in 10 mM sodium phosphate, pH 7. a) C_0 = 2 mg/mL; TIS of solutions are shown on plot; data fit with external mass transfer (——) and homogeneous diffusion (---) models. b) C_0 = 0.2 mg/mL; TIS of solutions are shown on plot; data fit with external mass transfer model. c) C_0 values are shown on plot; data fit with external mass transfer (——) and homogeneous diffusion (---) models for low and high initial protein concentrations, respectively. Note of different time scale for each plot.

Lysozyme uptake at the lower initial protein concentration requires an increased time to achieve saturation under the stronger binding condition (20 mM TIS), and the external mass transfer model adequately describes the uptake behavior. The lower protein concentration in the bulk solution would decrease the extraparticle flux but not affect the intraparticle transport rate appreciably if this latter contribution is predominantly homogeneous. In this case, the bulk protein concentration becomes the driving force for the mass transfer as opposed to the adsorbed concentration in the case of homogeneous diffusion. Extremely good agreement between the external control model and the data was observed whenever it was applied to uptake curves obtained using a lower initial protein concentration.

Lactoferrin uptake was much slower than that of lysozyme (note the differences in time scale), indicating significant intraparticle resistance. The data were fit to the numerical solution of the homogeneous diffusion model and the external resistance model for the high and low initial protein concentrations, respectively. Both models provide good fits to their respective data sets. The increased time for apparent full saturation to occur for this system could be due to several factors, including steric hindrance for the larger lactoferrin molecule or the higher adsorption affinity and hence lower contribution from homogeneous diffusion inferred for lactoferrin under strong-binding conditions (Section 3.3.2). The propensity for homogeneous diffusion is thought to be related to the ability of adsorbed protein to diffuse and hence to the protein-surface affinity (Lenhoff, 2008; Wesselingh and Bosma, 2001). The analytical form of the pore diffusion model (i.e., the shrinking-core model) also provides a good fit to the high initial protein concentration data (not shown), indicating some

uncertainty in the transport mechanism for lactoferrin; this is addressed further in Section 3.3.4.

The external mass transfer coefficients and diffusivities gathered from these fits are shown in Tables 3.4 and 3.5, respectively, along with the results for the anion-exchange adsorbents discussed further below. Fitted k_f values are comparable to those predicted by standard correlations for mass transfer coefficients in stirred vessels (Armenante and Kirwan, 1989; Levins and Glastonbury, 1972). Homogeneous diffusivities (found numerically) are given for only the high initial protein concentration systems ($C_0 = 2 \pm 0.2$ mg/mL) as external mass transfer control is dominant for low initial protein systems and homogeneous diffusivity values would misrepresent the resistances present. However, the external mass transfer resistance was accounted for in all the systems studied in view of the rapid uptake and hence relatively low intraparticle resistance. The fact that there are only small differences in the fitted values of k_f between low and high initial protein concentrations for similar systems indicates that the external mass transfer resistance is a significant factor regardless of bulk solution concentration. The homogeneous diffusivities are, as expected, orders of magnitude lower than for the free-solution diffusivities (Chang and Lenhoff, 1998; Chen et al., 2002), and the generally increased values at higher salt concentrations are consistent with the relationship to strength of adsorption noted above (Lenhoff, 2008; Wesselingh and Bosma, 2001).

		C_0 = 2 ± 0.2 mg/mL		C_0 = 0.2 ± 0.02 mg/mL	
Resin	Protein	20 mM TIS	100 mM TIS	20 mM TIS	100 mM TIS
S HyperCel	lysozyme	3.02 ± 0.03	1.49 ± 0.05	3.40 ± 0.04	1.49 ± 0.03
	lactoferrin	n/a	n/a	0.71 ± 0.01	n/a
Q HyperCel	β-lactoglobulin	2.03 ± 0.04	1.02 ± 0.05	2.67 ± 0.03	1.03 ± 0.04
	BSA	1.73 ± 0.08	n/a	1.76 ± 0.07	n/a
STAR AX HyperCel	β-lactoglobulin	1.53 ± 0.04	1.45 ± 0.03	2.51 ± 0.07	2.07 ± 0.05

Table 3.4 External mass transfer coefficients for protein uptake in HyperCel materials (10^{-3} cm/s); 95% confidence intervals are shown for all values.

		C_0 = 2 ± 0.2 mg/mL	
Resin	Protein	20 mM TIS	100 mM TIS
S HyperCel	lysozyme	4.72 ± 0.01	7.92 ± 0.18
	lactoferrin	0.18 ± .0001	n/a
Q HyperCel	β-lactoglobulin	2.68 ± 0.002	5.77 ± 0.01
	BSA	1.44 ± 0.03	n/a
STAR AX HyperCel	β-lactoglobulin	2.87 ± 0.001	1.88 ± 0.001

Table 3.5 Homogeneous diffusivities for protein uptake in HyperCel materials (10^{-8} cm^2/s); 95% confidence intervals are shown for all values.

Discrepancies between the plateau concentrations in the uptake experiments and capacities found from the adsorption isotherms may be due to errors in measuring resin volumes in the capillary tubes, the inability to remove all fluid and resin material from the agitation vessel, leading to an improper final mass balance, or to a slow mode of uptake in the isotherm measurements. However, even the largest discrepancies in these values did not exceed 15% error, and capacities obtained for each individual uptake experiment were used for model fitting where appropriate.

Figure 3.7 shows protein uptake on Q HyperCel, and much as in the case of lysozyme on S HyperCel, all plots reflect very fast uptake and good fits to the external resistance model. That this is the case for both β-lactoglobulin and BSA indicates that protein size is not as significant in determining the mechanism of transport as protein affinity, with only lactoferrin uptake reflecting a dominant intraparticle resistance. Transport parameters for the β-lactoglobulin data are of the same order of magnitude as values for the lysozyme data, albeit somewhat slower transport is observed. The BSA data present even slower uptake, but only marginally. While this can again be inferred as a function of protein size relating to its mobility, it is also dependent on the protein-surface affinity for each protein-adsorbent system.

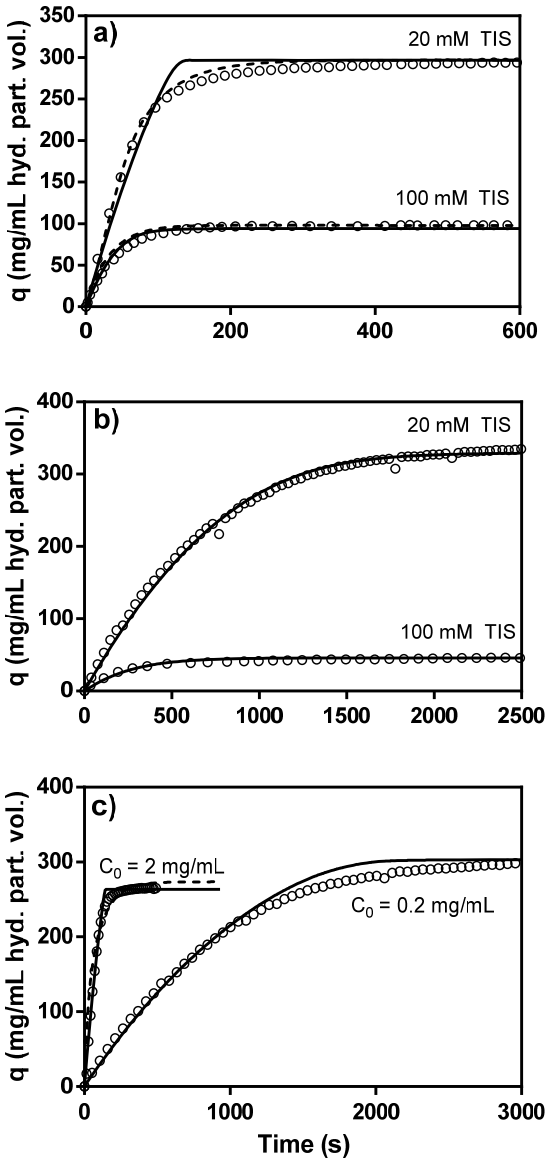

Figure 3.7 Batch uptake kinetics for β-lactoglobulin (a, b) and BSA (c) on Q HyperCel in 50 mM bis-tris, pH 7. a) C_0 = 2 mg/mL; TIS of solutions are shown on plot; data fit with external mass transfer (——) and homogeneous diffusion (---) models. b) C_0 = 0.2 mg/mL; TIS of solutions are shown on plot; data fit with external mass transfer control model. c) C_0 are shown on plot; data fit with external mass transfer (——) and homogeneous diffusion (---) models. Note different time scale for each plot.

Figure 3.8 shows the uptake of β-lactoglobulin on STAR AX HyperCel. Unlike uptake in the other two adsorbents, STAR AX exhibits a counterintuitive trend in the apparent capacity between 20 and 100 mM TIS. For both the high and low initial bulk concentrations, the uptake of β-lactoglobulin at 100 mM TIS overtakes the uptake at 20 mM TIS, although both have similar maximum static binding capacities based on isotherm measurements (Figure 3.3). However, the kinetic experiments were carried out for a period no longer than 45-75 minutes for either case, while the isotherm measurements had up to 14 days to equilibrate (which was the case for protein adsorption on STAR AX HyperCel at low TIS).

While uptake remains fairly rapid using a high initial bulk protein concentration, the apparent equilibrium reached was far below the maximum static capacity for each system, suggesting bimodal uptake that includes a period of slow uptake beyond the time range shown. This bimodal uptake behavior could be explained by a rapid superficial loading of protein that saturates particles to one- to two-thirds of the total capacity, followed by a slower contribution that may reflect protein rearrangement within the particle. This type of uptake has been modeled conceptually using a partial shrinking-core model (Bowes and Lenhoff, 2011a), characterized by rapid but incomplete shrinking-core uptake preceding a backfilling of additional free capacity over a longer time scale. During normal operation in a downstream purification setting, a nominal salt concentration (greater than 20 mM TIS, approximately a 2 mS/cm conductivity) may be present, in which case this unfavorable uptake behavior would become negligible.

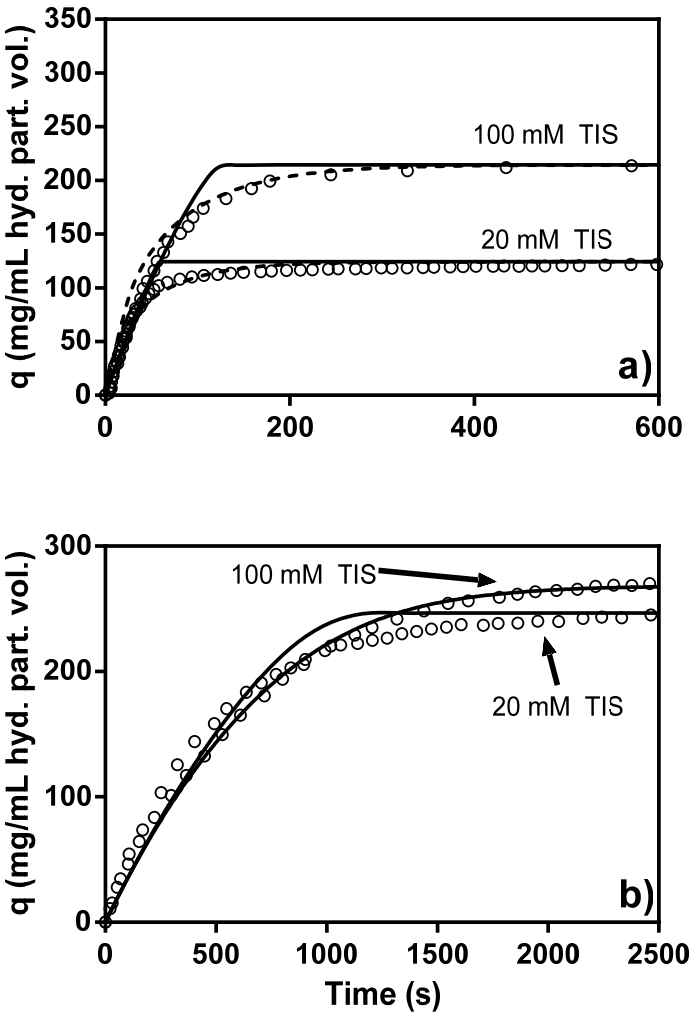

Figure 3.8 Batch uptake kinetics for β-lactoglobulin on STAR AX HyperCel in 50 mM bis-tris, pH 7. a) C_0 = 2 mg/mL; TIS of solutions are shown on plot; data fit with external mass transfer (——) and homogeneous diffusion (---) models. b) C_0 = 0.2 mg/mL; TIS of solution are shown on plot; data fit with external mass transfer model. Note different time scale for each plot.

It has been shown that the ligand chemistry of STAR AX has some effect on the nature of the pore architecture and may hinder fast transport of protein to some extent (Angelo et al., 2013, Chapter 2). The structural differences in conjunction with the much higher affinity for β-lactoglobulin on the salt-tolerant material could be what slows initial uptake to only a fraction of the total adsorptive capacity. Previous studies have shown that small relative pore sizes and strong retention contribute to hindering the diffusion of adsorbed species with slow kinetic off-rates, especially at higher loadings (Traylor et al., 2014). However, over longer time scales this behavior becomes less significant.

A mechanistic model that describes transport of this type is difficult to specify in detail, as the diffusion of protein is slowed by unfavorable binding kinetics and/or steric hindrance in the pore; an alternative interpretation is in terms of single-file diffusion in multicomponent systems (Perez-Almodóvar et al., 2012; Tao et al., 2012). However, the initial uptake (< 200 seconds) is still very rapid for high bulk protein concentrations, where it can be assumed that external mass transfer resistance is still dominant in the case of low bulk solution concentrations.

3.3.4 Protein Uptake Profiles via Confocal Microscopy Imaging

Confocal microscopy was used for real-time observation of intensity profiles of fluorescently-labeled protein in order to obtain information on the mechanism of protein transport within the stationary phase (Bowes and Lenhoff, 2011a; Bowes et al., 2012; Dziennik et al., 2005, 2003; Ljunglöf and Hjorth, 1996; Ljunglöf and Thömmes, 1998; Tao et al., 2011c). Batch uptake experiments allowed a quantitative analysis of uptake rates, as well as determination of the appropriate rate model to apply to the data. The qualitative form of the concentration profile that may be seen from confocal

microscopy can reveal two limiting cases, one consistent with homogeneous diffusion and the other consistent with pore diffusion, in the shrinking-core limit (see Section 3.2.5). A homogeneous uptake mechanism exhibits concentration profiles that are diffuse, and a shrinking-core mechanism gives rise to a sharp protein front that moves toward the center of the particle (Bowes and Lenhoff, 2011a; Dziennik et al., 2005, 2003; Hubbuch et al., 2003; Tao et al., 2011c; Yang et al., 2006).

All the confocal microscopy figures show uptake under a high linear flow rate of 2100 cm/hr (1 mL/min). This flow rate was required in order to reduce particle movement within the flow cell, as lower flow rates could allow particles to shift during elution, thereby providing inadequate axial profile data. Flow packing using both high-salt and equilibration buffer was used to ensure optimal packing. Intensity plots for uptake profiles at high and low superficial velocities were compared to determine that the intraparticle transport of protein was independent of the flow rates used for these systems.

3.3.4.1 HyperCel Materials

The very fast uptake seen in HyperCel under most conditions (Section 3.3.3) leads to the hypothesis that HyperCel displays a homogeneous diffusion mechanism; this is consistent with its similarities to hydrogels (Lewus and Carta, 1999; Weaver and Carta, 1996) and other natural polymers. Figure 3.9 shows the uptake of DyLight 650-labeled lysozyme in S HyperCel resin at 20 and 100 mM TIS. The value shown in the lower left of each image indicates the time elapsed after switching to the feed stream, corrected for the system dead time. Uptake is qualitatively homogeneous, with the images presenting no sharp uptake front that would indicate pore diffusion being the dominant mechanism of protein transport. Apparent full saturation of the

particle was achieved before three minutes had elapsed, in agreement with the batch uptake data for lysozyme on S HyperCel under similar conditions.

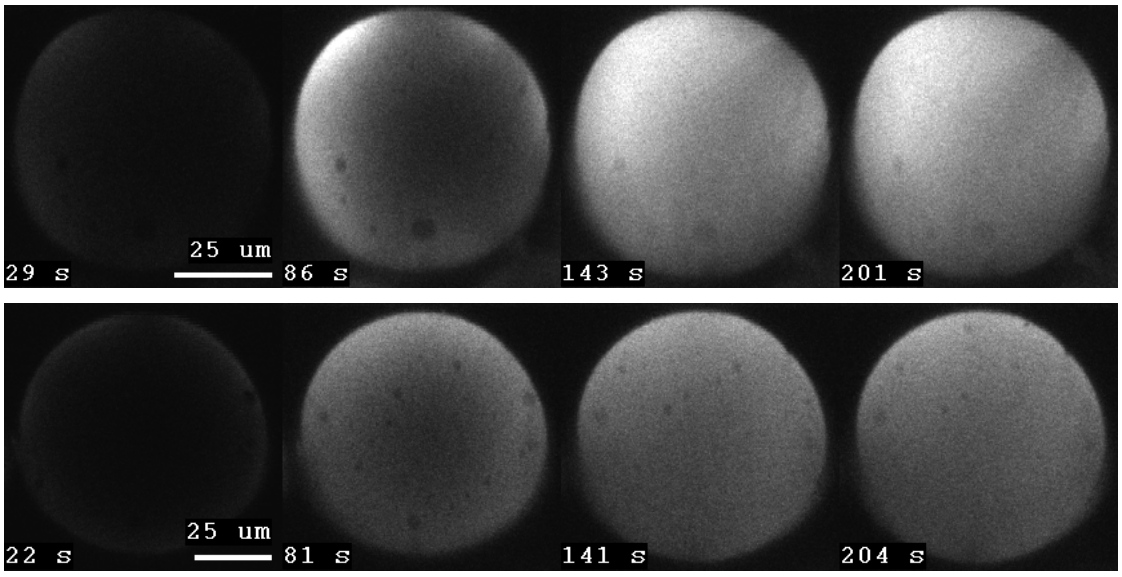

Figure 3.9 Uptake of DyLight 650-labeled lysozyme on S HyperCel at 20 (top) and 100 (bottom) mM TIS (10 mM sodium phosphate, pH 7). Feed solution contained 2 mg/mL protein flowing at 2100 cm/h.

The differences in fluorescence intensity between 20 and 100 mM TIS correspond to the lower overall binding capacities that are seen at higher TIS values, as with the batch uptake and adsorption isotherms. Relative adsorbed concentrations can be inferred from the differences in intensity, as laser power and gain settings were kept the same across runs at different operating conditions.

Much slower uptake is observed for lactoferrin uptake in S HyperCel (Figure 3.10), again consistent with the batch data. The fluorescence intensity profiles are sharp, consistent with a shrinking-core mechanism, indicating a strong pore-diffusion

contribution. As noted in Section 3.3.3, the batch uptake curves could be adequately described by either a pore- or a homogeneous-diffusion model, so the confocal images highlight the significance of obtaining real-time profiles to allow for more informed model discrimination. The homogeneous diffusion model was used in this case for consistency with the other uptake modeling that was performed.

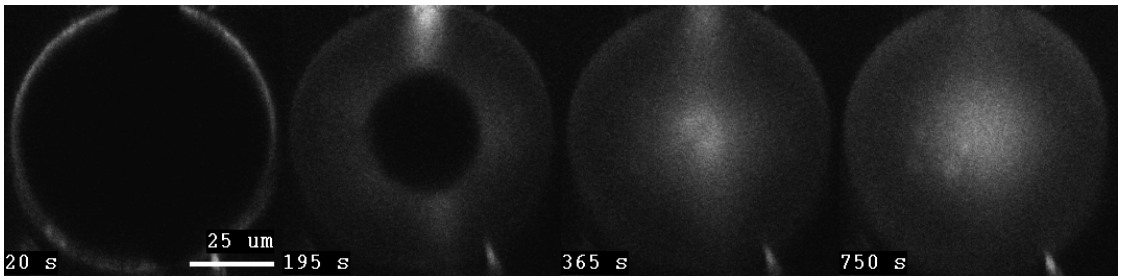

Figure 3.10 Uptake of DyLight 650-labeled lactoferrin on S HyperCel at 20 mM TIS (10 mM sodium phosphate, pH 7). Feed solution contained 2 mg/mL protein flowing at 2100 cm/hr.

Application of the shrinking-core model to batch uptake data gives an effective pore diffusivity value of 1.5×10^{-7} cm^2/s. Following an analysis described previously to determine shrinking-core diffusivities from the radial position of the sharp uptake front (Bowes and Lenhoff, 2011a; Dziennik et al., 2005), an apparent shrinking-core diffusivity of 4.9×10^{-7} cm^2/s was determined. Both the acquired diffusivities are of the same order of magnitude as for lactoferrin uptake on Capto S (Bowes and Lenhoff, 2011a), a polymer-modified material that presents higher uptake rates than its agarose-based counterparts (SP Sepharose XL and SP Sepharose FF) at similar conditions. The discrepancy between the two values for the effective shrinking-core diffusivity can be explained by the faster apparent saturation that is observed via confocal microscopy,

but the slower overall uptake that is described quantitatively by batch uptake. Due to this, it can be determined that uptake for this system can be described by the partial shrinking-core model, in which a significant portion of the particle saturation takes place after a rapid, but incomplete, shrinking-core type uptake (Bowes and Lenhoff, 2011a). A gradual increase in the fluorescent intensity throughout the particle after the sharp front reaches the center also validates the presence of a backfilling mechanism.

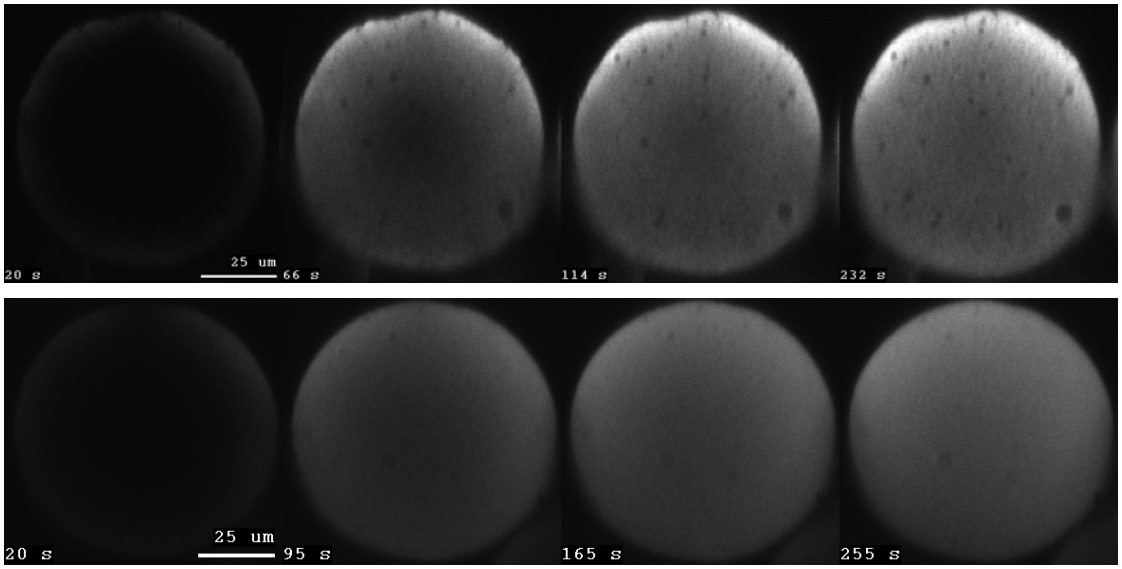

Figure 3.11 Uptake of DyLight 650-labeled β-lactoglobulin on Q HyperCel at 20 (top) and 100 (bottom) mM TIS (50 mM bis-tris, pH 7). Feed solution contained 2 mg/mL protein flowing at 2100 cm/h.

The uptake of Dylight 650-labeled β-lactoglobulin in Q HyperCel at 20 and 100 mM TIS (Figure 3.11) presented results very similar to those for lysozyme uptake in S HyperCel at the same operating conditions. The rapid apparent full particle

saturation again suggests low intraparticle resistance and a homogeneous-diffusion mechanism, as with lysozyme in S HyperCel.

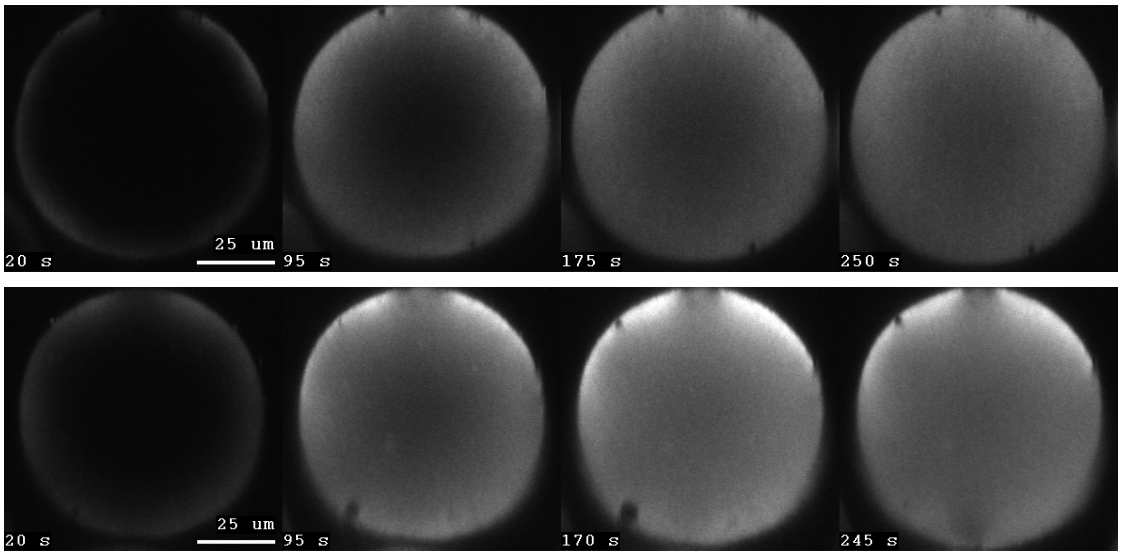

Figure 3.12 Uptake of DyLight 650-labeled β-lactoglobulin on STAR AX HyperCel at 20 (top) and 100 (bottom) mM TIS (50 mM bis-tris, pH 7). Feed solution contained 2 mg/mL protein flowing at 2100 cm/h.

Figure 3.12 shows uptake of DyLight 650-labeled β-lactoglobulin in STAR AX HyperCel at 20 and 100 mM TIS. The uptake front, while still diffuse, appears slightly sharper than for the other cases apart from lactoferrin, suggesting a reduced contribution from homogeneous diffusion. Rapid saturation, as with the S and Q moieties, is still observed, however. The lower fluorescence intensity at 20 mM TIS than at 100 mM TIS is consistent with the batch uptake results at the same operating conditions. For the time scale of these uptake experiments, STAR AX HyperCel has a higher capacity for protein at higher TIS and shorter time scales, presumably caused by attenuation of homogeneous diffusion caused by the strong affinity for protein at

low salt conditions. Despite the strong attraction for protein on this salt-tolerant resin, regeneration at 1 M NaCl was adequate to remove all protein from the system.

3.3.4.2 Displacement Effects in HyperCel Materials

The effect of displacement of protein was briefly investigated for the HyperCel resins in two different scenarios: displacement by a species of a higher affinity and displacement by the same species conjugated with a different fluorophore. Figure 3.13 shows the displacement of DyLight 650-labeled lysozyme by DyLight 488-labeled lactoferrin in S HyperCel at 20 mM TIS.

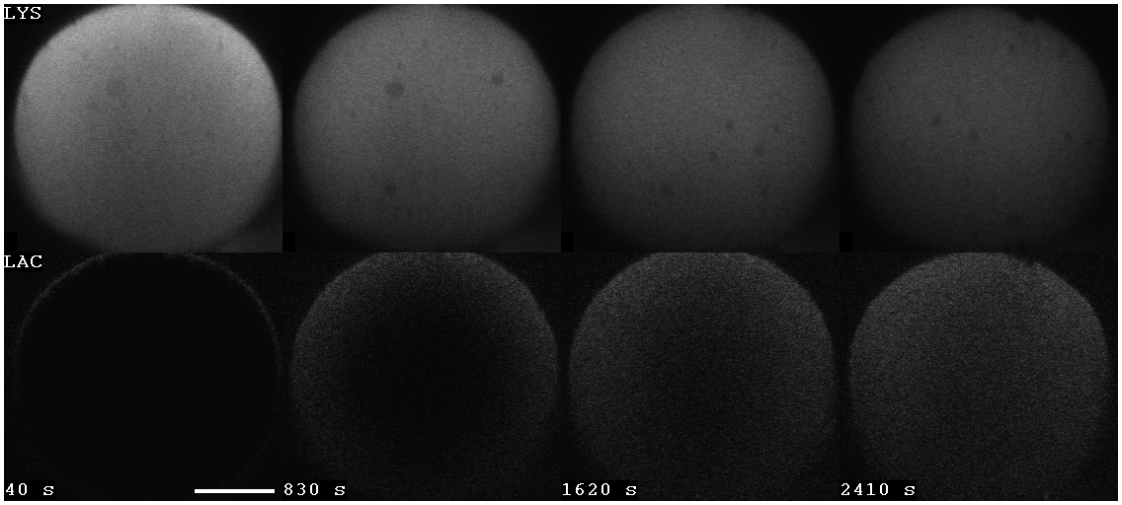

Figure 3.13 Displacement of DyLight 650-labeled lysozyme (top) by DyLight 488-labeled lactoferrin (bottom) on S HyperCel at 20 mM TIS, pH 7. Loading performed using 2 mg/mL lysozyme, and displacement performed using lysozyme/lactoferrin mixture in a 1:1 ratio flowing at 2100 cm/h. Displacement initiated at time t = 0 s (minus the dead time). Scale bar represents 25 microns.

Particles were preloaded with 2 mg/mL DyLight 650-labeled lysozyme until particles were well saturated (approximately 10 minutes), at which point the loading was switched to a mixture of DyLight 650-labeled lysozyme and DyLight 488-labeled lactoferrin in a 1:1 mass ratio (total protein concentration remained at 2 mg/mL). The choice was made to use a mixture with the preloaded species in order to limit the amount of kinetically-controlled exchange that would normally occur when the feed stream is switched. Performing the experiment in this manner allowed all displacement effects to be governed by the increased electrostatic affinity of lactoferrin to the S HyperCel material over lysozyme.

The displacement effect appears to be relatively slow when compared to single-component uptake of both lysozyme and lactoferrin on the same material, with the diffuse lactoferrin front taking on the order of 2500 seconds to reach the center of the particle, while lysozyme and lactoferrin took on the order of 200 and 800 seconds, respectively, to achieve apparent single-component saturation. This is consistent with previous work showing displacement to be characteristically slow compared to uptake onto protein-devoid stationary phases (Bowes et al., 2012; Perez-Almodóvar et al., 2012; Tao et al., 2012, 2011c). This may be partly due to the fact that the space occupied by protein in a previously saturated particle can introduce steric hindrance effects, slowing the subsequent uptake of protein (Tao et al., 2011c) and limiting homogeneous transport. However, the overall 650 nm fluorescence intensity decreased steadily across the particle over the course of the displacement, indicating that the expulsion of the preloaded DyLight 650-labeled lysozyme is not transport-limited and that exchange kinetics may be the dominant factor. Even though the lactoferrin could initially be seen localized around the periphery of the particle, the overall profile is

very diffuse, also consistent with exchange-limited kinetics as opposed to the shrinking-core effect that is observed in dextran-modified Capto S (Traylor, 2013), although a displacement feed stream containing only lactoferrin without any additional lysozyme was used in that case. After imaging ended, there remained a uniform increase in the overall 488 nm fluorescence as additional displacement occurred, but the experiment was ended due to insufficient protein mixture stock.

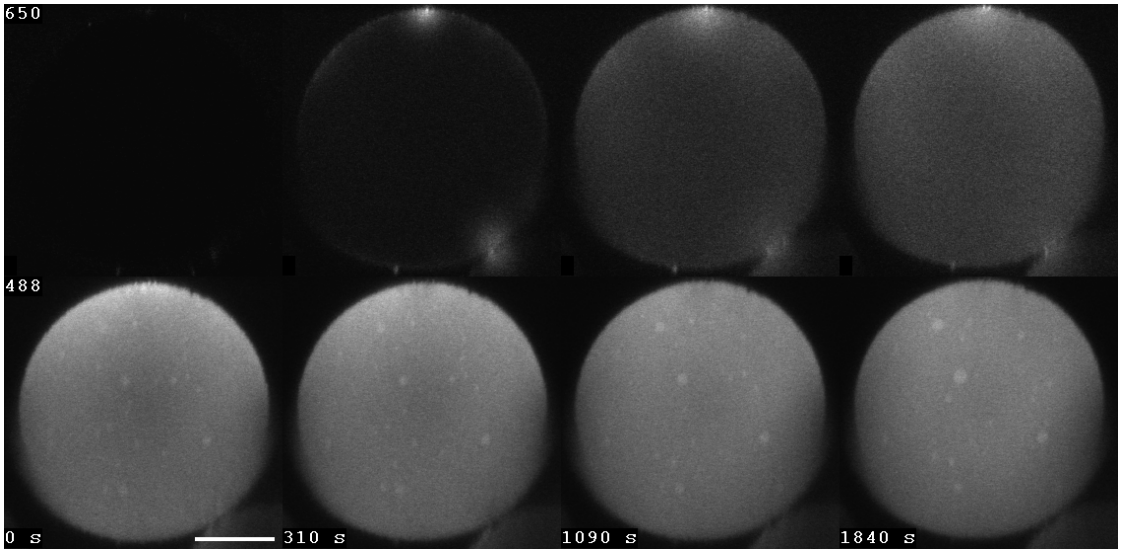

Figure 3.14 Uptake of DyLight 650-labeled β-lactoglobulin (top) following a 10 minute pre-load of DyLight 488-labeled β-lactoglobulin on STAR AX HyperCel at 20 mM TIS, pH 7; 488 nm channel is shown on the bottom. Pre-loading was performed using 2 mg/mL DyLight 488-labeled β-lactoglobulin, and subsequent loading was performed using 650/488 mixture in a 1:1 ratio flowing at 2100 cm/h. Mixture stream initiated at time t = 0 s (minus the dead time). Scale bar represents 25 microns.

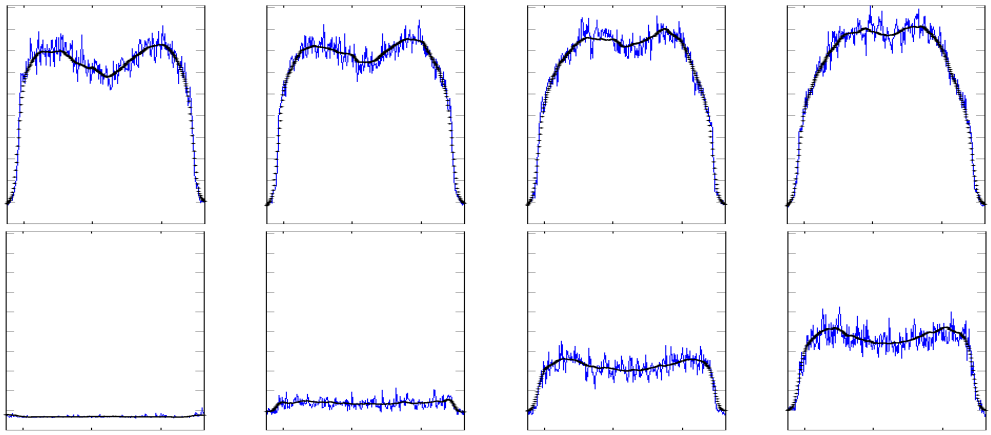

Figure 3.15 Normalized intensity profiles during uptake of DyLight-labeled β-lactoglobulin on STAR AX HyperCel, corresponding to the frames shown in Figure 3.14. The top row shows the gradual increase in 488 nm intensity along with the uniform increase of 650 nm intensity on the bottom row at times of 0, 310, 1090 and 1840 seconds after switching to the mixture feed stream, from left to right, respectively.

Attempted displacement by the same molecule with a different conjugated fluorophore was also investigated in order to elucidate the slow apparent uptake of protein at low ionic strength in STAR AX HyperCel. Figure 3.14 shows the uptake of a mixture of 2 mg/mL β-lactoglobulin labeled with DyLight 488 and DyLight 650 in a 1:1 mass ratio following the preloading of just DyLight 488-labeled β-lactoglobulin on STAR AX HyperCel at 20 mM TIS. Previous adsorption studies showed very slow uptake of protein at this condition on STAR AX HyperCel when compared to its strong ion-exchange counterpart, both in the equilibration time necessary for obtaining adsorption isotherms (Section 3.3.1) and in batch uptake kinetics measurements (Section 3.3.3). In both of these cases, an apparent bimodal uptake mechanism was observed, wherein a significant portion of the capacity was reached within a short period (similar to uptake on the S and Q HyperCel materials) followed by a slow

increase in the adsorbed capacity. Here, it is clear that the DyLight 650-labeled β-lactoglobulin does not displace the previously loaded DyLight 488-labeled β-lactoglobulin following the 10 minute preload as there is no appreciable decrease in the fluorescence intensity of the 488 nm channel during the time the imaging was performed; in fact, the 488 nm intensity continued to rise due to the feed stream containing a 1:1 ratio of the 488 and 650 labeled protein. This was confirmed by comparison of the fluorescence intensity plots between the channels as well (Figure 3.15). The uniform increase in the fluorescence intensity of the 650 nm channel indicates a gradual backfilling of labeled β-lactoglobulin, confirming that a bimodal adsorption process takes place on a long time scale. Since the overall combined fluorescence intensity increases throughout the adsorption process, and no decrease is seen in either channel, it can be determined that neither a displacement nor a kinetic exchange between the two species seems to be apparent due to the incomplete saturation of the particle following the 10 minute preloading period. This provides additional support for the proposed partial shrinking-core mechanism.

3.3.4.3 Sepharose and Capto Materials

Figures 3.16, 3.17 and 3.18 show the uptake of Dylight 650-labeled β-lactoglobulin in Q Sepharose FF, Q Sepharose XL and Capto Q, respectively, at 20 and 100 mM TIS. These results are qualitatively similar to those for previous work performed on SP Sepharose and Capto S with lysozyme (Bowes, 2011; Bowes et al., 2012), except that β-lactoglobulin uptake in Q Sepharose FF at 20 mM TIS does not show the shrinking-core type behavior seen for lysozyme uptake in SP Sepharose FF from 2-50 mM TIS (Dziennik et al., 2005, 2003). This is presumably due to the higher retention and affinity for lysozyme on cation-exchange materials than for β-

lactoglobulin on anion-exchange adsorbents. The general trend in the three figures is the more complete, as well as more rapid, saturation that is observed at 100 mM than at 20 mM TIS. Capto Q shows this effect to a great extent, displaying a much higher fluorescence intensity at 100 mM TIS in approximately half the time as at 20 mM TIS. Laser and gain settings were kept consistent for all these runs to allow for comparison of their adsorbed capacities, which are generally proportional to the fluorescence intensity.

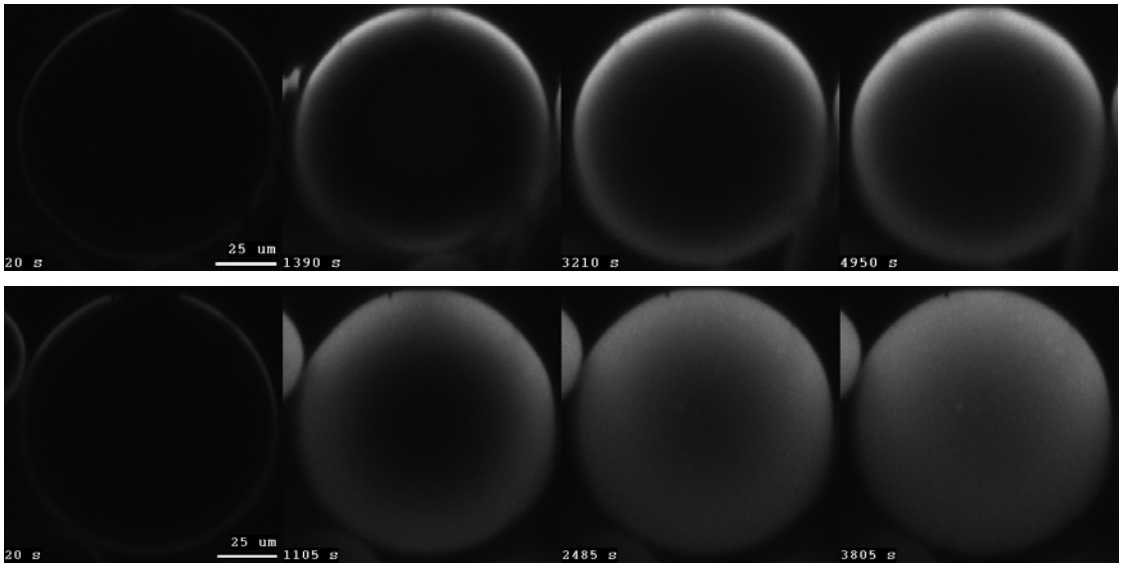

Figure 3.16 Uptake of DyLight 650-labeled β-lactoglobulin on Q Sepharose FF at 20 (top) and 100 (bottom) mM TIS (50 mM bis-tris, pH 7). Feed stream contained 2 mg/mL protein flowing at 2100 cm/h.

The generally diffuse profiles are consistent with a homogeneous diffusion mechanism, as previously reported for lysozyme adsorption in the CEX counterparts (Bowes, 2011; Bowes et al., 2012; Dziennik et al., 2005). This is expected for the higher TIS of 100 mM, but the results show that even under very strong binding

conditions, β-lactoglobulin still displays homogeneous transport, unlike lactoferrin and mAb in the sulfonated varieties (Bowes et al., 2012), which are indicative of pore diffusion. This is an effect of the lower overall retentivity of β-lactoglobulin (see Figure 3.5 as an example), the small size of the protein molecule, and could possibly be due to the effectiveness of the quaternary ammonium ligand in adsorbing protein that Q-type resins possess when compared to the sulfonate functionality in S-type resins, even though the two strong ion-exchange varieties have about the same ionic capacity (Tables 1.1 and 1.2).

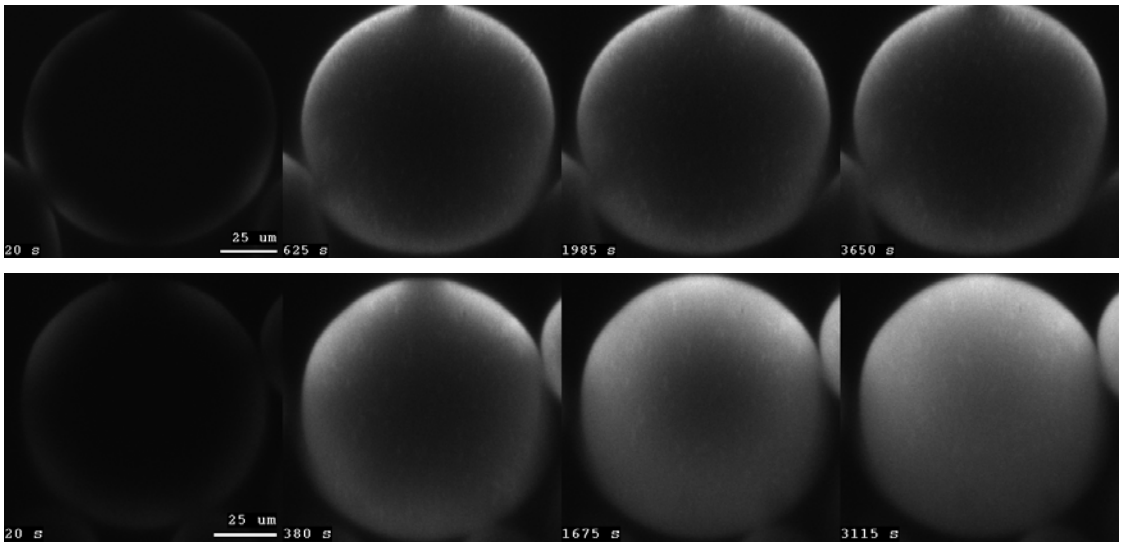

Figure 3.17 Uptake of DyLight 650-labeled β-lactoglobulin on Q Sepharose XL at 20 (top) and 100 (bottom) mM TIS (50 mM bis-tris, pH 7). Feed stream contained 2 mg/mL protein flowing at 2100 cm/h

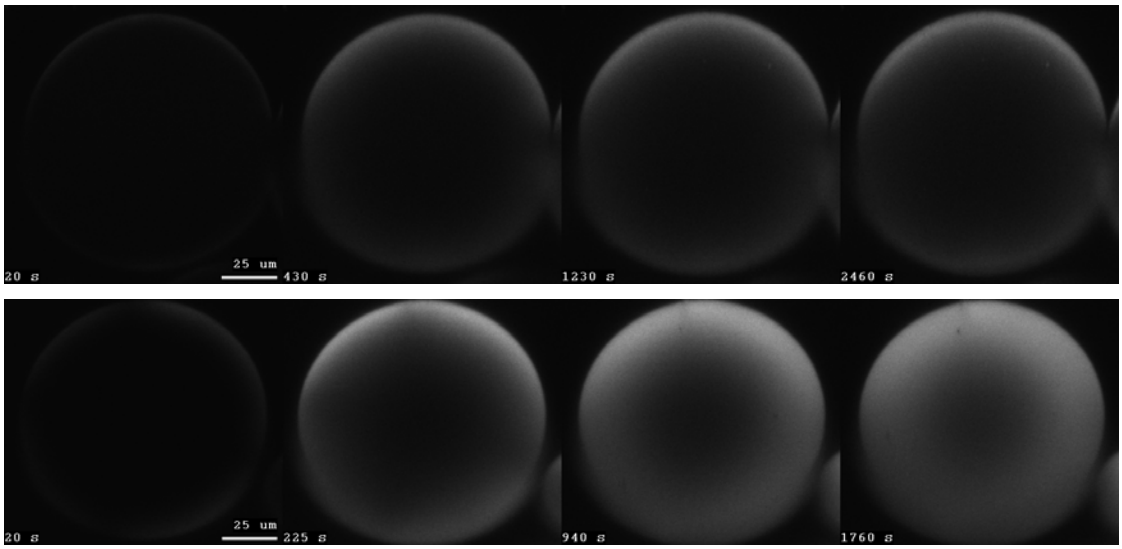

Figure 3.18 Uptake of DyLight 650-labeled β-lactoglobulin on Capto Q at 20 (top) and 100 (bottom) mM TIS (50 mM bis-tris, pH 7). Feed stream contained 2 mg/mL protein flowing at 2100 cm/h.

3.3.4.4 Intraparticle Voids

Intraparticle voids were visible in sections of all HyperCel materials when imaged using different microscopy techniques. The presence of the voids has been shown in the previous chapter, mostly in electron microscopy of these adsorbents. In this work, the voids could also be seen during the uptake of protein during real-time confocal imaging. During uptake, the voids are much lower in florescence intensity than the rest of the cross-section of the particle, most likely due to lower ligand density, as the cellulosic density is also assumed to be lower in these regions. Conversely, during protein elution, these spots have a higher fluorescence intensity than the rest of the particle, presumably because the lower backbone density facilitates pooling of fluorescently-labeled protein before it fully leaves the particle. The narrow pore size of these materials acts as a bottleneck, retarding full elution of protein to

some degree when compared to other, more open, stationary phases, but the overall effect is minimal.

3.3.5 Electron Microscopy

3.3.5.1 Scanning Electron Microscopy

Figure 3.19 shows whole-particle SEM images of Q and STAR AX HyperCel containing adsorbed protein. β-lactoglobulin was loaded to 57% of the maximum static binding capacity on Q HyperCel and to 45% of the maximum static binding capacity on STAR AX HyperCel. It is apparent that the protein gives rise to globular structures on the surfaces of the material, giving it a rough topography as opposed to the open fibrous network described previously for phases devoid of protein (Angelo et al., 2013, Chapter 2). The globular formations on Q HyperCel appear too large to be individual protein molecules or even small clusters, but the texture is much finer on the STAR AX resin, where the formations could be single protein molecules or clusters of molecules.

Comparison of these images to SEM micrographs of other stationary phases on carbohydrate base matrices (i.e., Sepharose materials) (Bowes et al., 2009; Koku, 2011) sheds light on what can be inferred about the protein localization. These images are qualitatively similar to those of dextran-modified Sepharose XL, which presents a volumetric layer engulfed with protein molecules under similar loading conditions. Sepharose FF, an agarose base structure lacking polymer extenders, does not exhibit any sort of volumetric swelling when loaded with protein, as can be seen in the comparison in Figure 3.20.

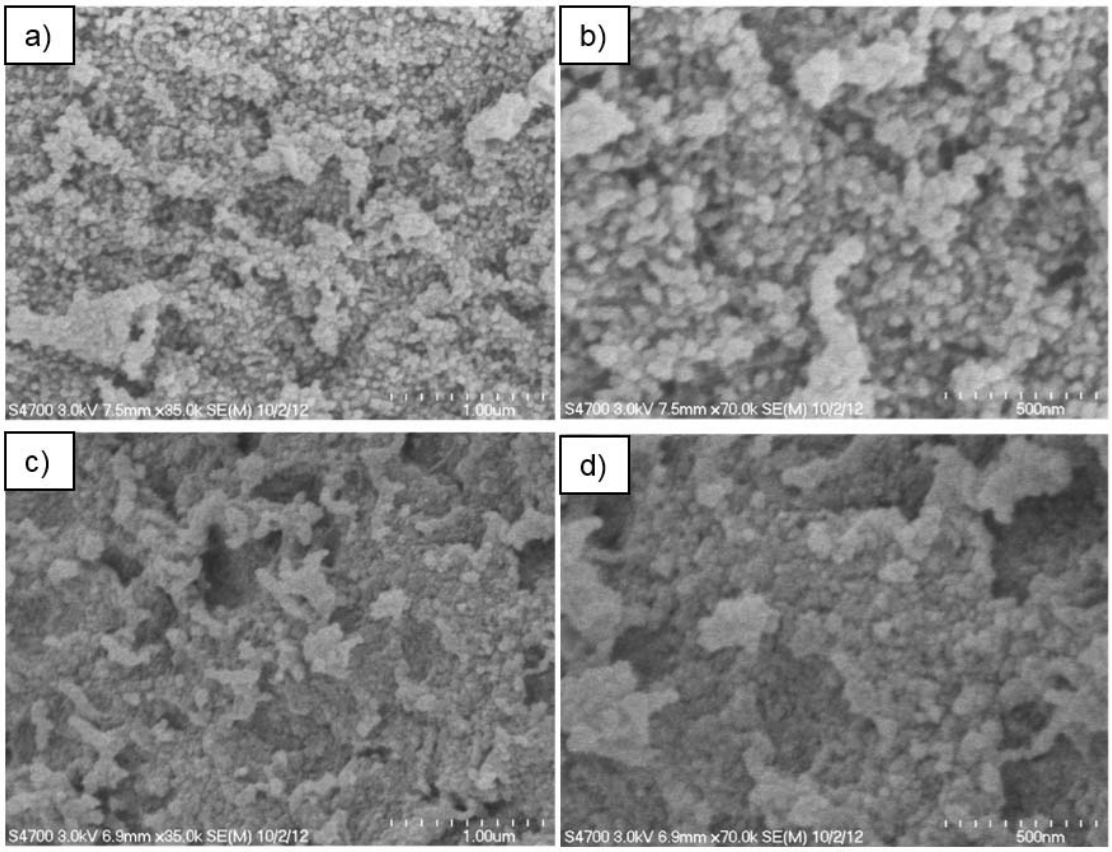

Figure 3.19 SEM images of Q (a, b) and STAR AX (c, d) HyperCel at 35000x (a, c) and 70000x (b, d) magnification. Both materials were adsorbed with approximately 50% of the maximum capacity of β-lactoglobulin and chemically fixed with OsO_4.

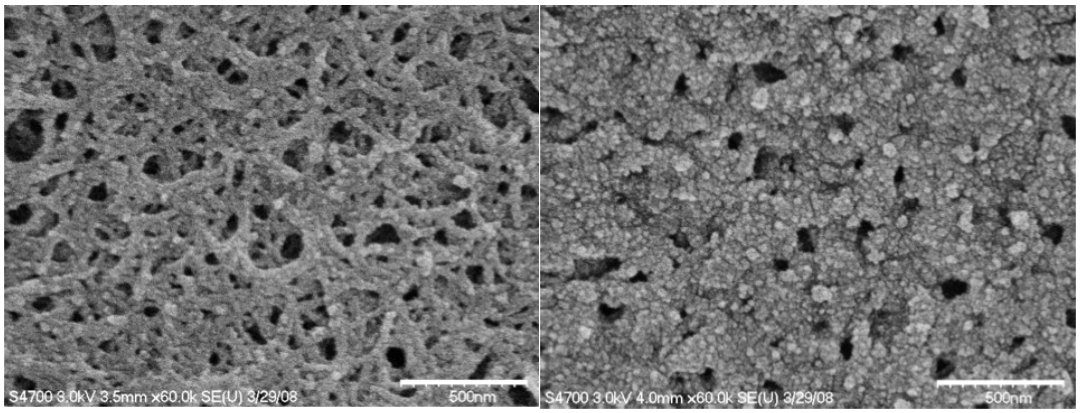

Figure 3.20 SEM images of Q Sepharose FF (left) and Q Sepharose XL (right) loaded to 50% of static capacity of α-lactalbumin at 60000x (Koku, 2011).

HyperCel may have cellulosic extenders akin to a polymer-grafted resin, suggesting that the HyperCel materials exhibit structural characteristics similar to those of polymer-modified stationary phases. Small-angle neutron scattering on these systems suggests that protein adsorbs fairly uniformly within the particle (Koshari et al., 2015), including the possibility of protein partitioning throughout most of the particle volume. The globular formations that can been seen in the electron micrographs makes the determination of other structural characteristics somewhat difficult. The use of a lower protein loading may be better for distinguishing the presence of extenders.

3.3.5.2 Transmission Electron Microscopy

TEM images of Q HyperCel with and without adsorbed protein chemically fixed to the material are shown in Figure 3.21. The protein loading on the protein-adsorbed samples was 52% of the maximum static binding capacity. Each figure shows the results of the two methods of fixation as well as the protein-free and

protein-adsorbed phases. With both methods of fixation, the protein-loaded phases seem to be less fibrous and open, suggesting that protein is filling the negative space and swelling the material. The TAGO fixation method presents a more disconnected pore network within the material without protein adsorbed, but does allow for sharper resolution and clearer delineation between the positive and negative spaces in the protein-adsorbed phase. The dark spots in the TAGO fixed samples are most likely deposits of OsO_4 that had aggregated during osmication. It was verified that these were not artifacts from the post-staining procedure by imaging sections that had undergone fixation but not post-staining.

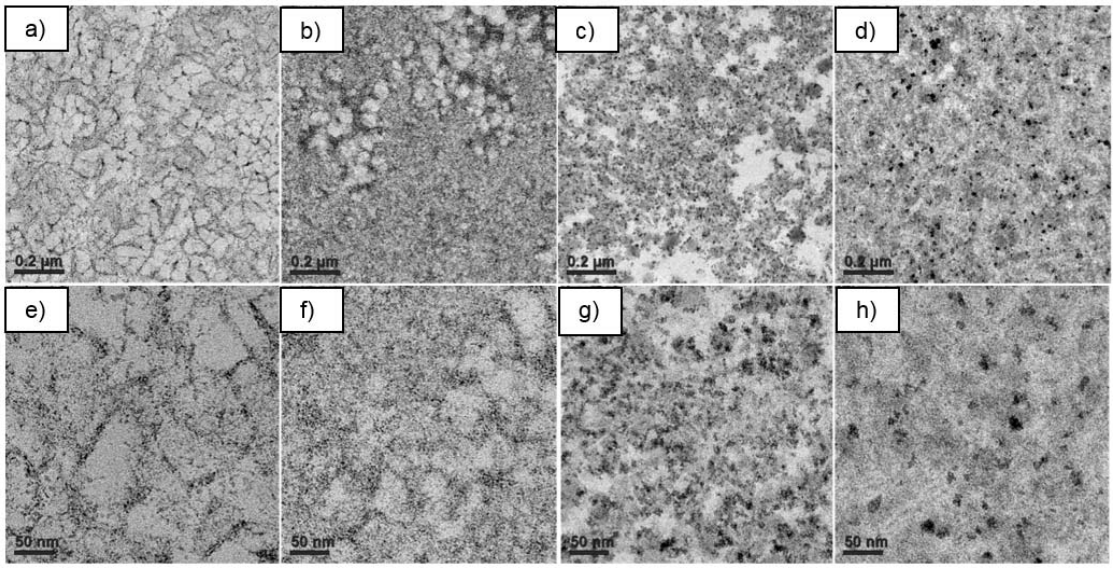

Figure 3.21 TEM images of Q HyperCel prepared using standard aldehyde fixation (a, b, e, f) and TAGO fixation (c, d, g, h); no protein adsorbed (a, c, e, g) and with approximately 50% of maximum loading of β-lactoglobulin (b, d, f, h). Magnification 10000x (a, b, c, d) and 31500x (e, f, g, h).

STAR AX HyperCel (Figure 3.22) differs from Q HyperCel in that the structure seems to be more homogeneous, with poorer discrimination between pore space and the cellulose backbone. The protein loading on the protein-adsorbed samples was 49% of the maximum static binding capacity. The TAGO fixation method does not seem to change the result much from the standard aldehyde fixation, albeit the contrast in these samples is better since tannic acid acts as a mordant for the OsO_4. In the case of the protein-free samples, there is little to no heterogeneity in the structure, implying a much smaller and complex pore network. When protein is adsorbed, the presence of pores becomes more apparent, especially in the TAGO-fixed case. Protein seems to localize in homogeneous pockets, and the fibrous nature of the cellulose becomes more apparent, as may be seen on the edges of these areas; it would seem that there are areas for protein localization interspersed with more vacant areas, which could be the pores. The dark spots are most likely OsO_4 deposits as seen in Q HyperCel and do not signify any particular structural characteristic or protein cluster.

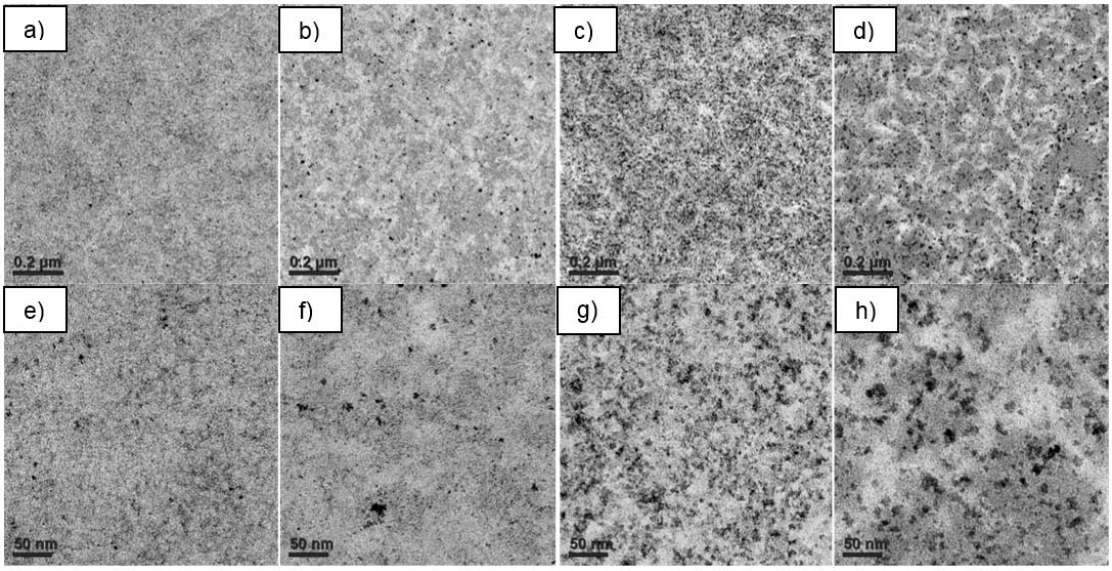

Figure 3.22 TEM images of STAR AX HyperCel prepared using standard aldehyde fixation (a, b, e, f) and TAGO fixation (c, d, g, h); no protein adsorbed (a, c, e, g) and with approximately 50% of maximum loading of β-lactoglobulin (b, d, f, h). Magnification 10000x (a, b, c, d) and 31500x (e, f, g, h).

S HyperCel (Figure 3.23) was stained using standard aldehyde fixation only. Because OsO_4 has an affinity for positive charges, such as amines, it did not stain the protein-devoid S HyperCel phase very well since not much definition in the image is apparent. The lysozyme itself in the protein-adsorbed phase acted as a mordant for the OsO_4, resulting in a much sharper image of the intraparticle morphology. Much like Q HyperCel, it shows a fibrous pore architecture with definite vacant pore spaces interspersed between regions of denser protein localization. This result suggests that the alternative ligand chemistry in STAR AX HyperCel in some way alters the pore structure and adsorption behavior within the material, even though the materials are based on the same cellulosic base matrix.

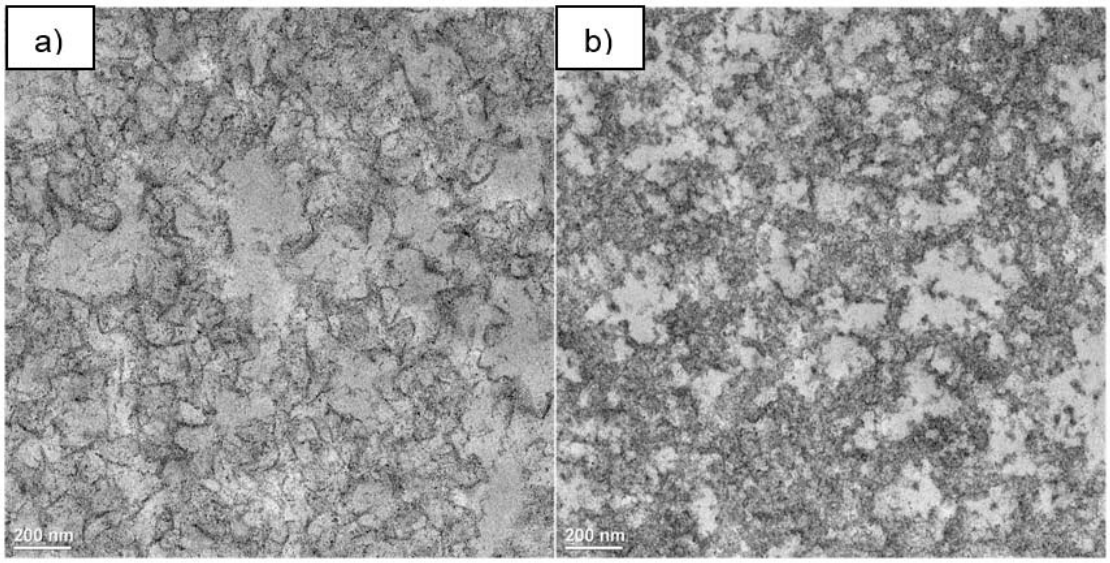

Figure 3.23 TEM images of S HyperCel with no protein adsorbed (a) and with approximately 50% of maximum loading of lysozyme (b). Magnification 12500x.

3.4 Conclusions

This work presents the adsorptive characteristics of protein onto both strong ion-exchange cellulosic adsorbents and a salt-tolerant moiety using changes in total ionic strength of solution as a variable condition in all cases. The cellulosic HyperCel materials allowed for a high static binding capacity of protein, especially in strong binding conditions (i.e., low salt concentrations), as well as very rapid uptake of protein, apparent via both batch kinetics and confocal microscopy. Analysis of the adsorptive protein uptake indicated that the intraparticle diffusion resistances, which are normally rate-controlling in most porous beaded materials, were near-negligible in comparison to external film transfer resistances. This exceptionally fast transport occurs by a homogeneous diffusion mechanism that is aided by protein-sorbent affinity that is not excessively high. The very fast uptake allows very efficient column loading and suggests that particles of the same composition but larger in total diameter would be feasible without a significant loss in uptake rate, allowing reduced pressure drop and the possibility of larger packed beds.

While the structure of these adsorbents has been studied previously (Angelo et al., 2013, Chapter 2), observing changes in the surface topography and TEM micrographs under protein-adsorbed conditions helps to elucidate the nature of the pore microstructure. Further evidence that HyperCel displays polymer-modified-like characteristics is apparent from small-angle neutron scattering (Koshari et al., 2015) and from SEM imaging of adsorbed phases, in which the pore architecture could be more clearly seen in STAR AX HyperCel when protein was adsorbed, a system where definite structural characteristics could not be resolved via TEM in a phase devoid of protein. The work presented provides a good complement to the investigation of the structural characteristics for the same materials, as adsorption of protein has a definite

impact on the native architecture of the beads, and by extension, the transport mechanisms that govern the movement of solutes through these stationary phases.

Chapter 4

DETERMINANTS OF PROTEIN ELUTION RATES FROM PREPARATIVE ION-EXCHANGE ADSORBENTS

4.1 Introduction

Elution is a critical step in process performance in that it determines separation selectivity and the pool volume containing the product. Attention to elution is therefore pivotal to maintain high recoverability of products and enable reuse of packed beds. However, few previous reports have focused directly on analyzing effective rates of elution. Concentration profiles in affinity-based separations have been modeled for desorption-controlled elution (Arnold et al., 1986, 1985), but the application of such methods to analyzing experimental data remains sparse, and diffusion-controlled elution appears not to have been investigated explicitly for bind-and-elute processes.

The elution process can depend on the composition of the eluent, the physical particle structure of the adsorbent, the nature and amounts of the adsorbates, or some combination of these factors. With the advent of polymer-modified materials, the protein capacities achievable can be considerably higher than for conventional adsorbents (Bowes et al., 2012; Lenhoff, 2011; Perez-Almodóvar et al., 2011). In both polymer-modified and cellulosic media, the matrix acts as a three-dimensional volume for sorption in a gel-like structure. A common feature these resins share is the reduction in size of the pore lumen, in which protein is able to diffuse freely. It has been shown that charged polymer extenders grafted on a surface tend to collapse

toward that surface in environments of increased total ionic strength due to screening of repulsion between like charges (DePhillips and Lenhoff, 2000; Yu and Sun, 2013). This would increase the size of the pore lumen in polymer-modified phases during elution carried out at increased TIS, making the dimensions of the lumen uncertain.

The addition of polymer extenders to macroporous adsorbents has been shown to increase protein transport rates during loading and hence dynamic capacities of proteins. This has been shown for comparisons between UNOsphere S and Nuvia S, a polymer-derivatized version of UNOsphere (Perez-Almodóvar et al., 2012, 2011), and between SP Sepharose FF and SP Sepharose XL (Bowes and Lenhoff, 2011a; Bowes et al., 2009). In these studies it was observed that both the adsorptive capacity and the rate of uptake were significantly higher in the polymer-modified material than in the non-polymer-modified counterpart. This rapid transport has been explained by diffusion of protein sorbed in the polymer phase, described as solid or homogeneous diffusion, even under relatively strong binding conditions where uptake would be dominated by pore diffusion in conventional non-polymer-modified adsorbents (Lenhoff, 2011; Stone and Carta, 2007). However, in the absence of an electrostatic driving force retaining the protein in the polymer layer, such transport is unlikely during elution from these stationary phases, with the protein likely to be released into in the pore lumen. Diffusion of macromolecular solutes has been measured through pores lined with polyelectrolytes even in the absence of a direct electrostatic attraction (Kim and Anderson, 1991, 1989), but such behavior in chromatographic materials has received less attention.

In this chapter, the elution behavior of three model proteins from cation-exchange media with and without polymer modification was investigated. Our

underlying hypothesis was that sorbed protein is desorbed rapidly in the presence of the eluent, with the rate-limiting step determining the overall elution rate being simple pore diffusion out of the particle. While the data appear to support the hypothesis in general, the biophysical properties of the protein are found to have an appreciable influence in some cases and warrant careful consideration in optimizing elution procedures.

4.2 Materials and Methods

4.2.1 Buffers and Protein Solutions

Monobasic sodium phosphate (NaH_2PO_4) and sodium bicarbonate ($NaHCO_3$) were purchased from Fisher Scientific (Fair Lawn, NJ) and used to prepare 10 mM sodium phosphate and 50 mM sodium bicarbonate buffer solutions at pH 7 and pH 9, respectively. The total ionic strengths of different solutions were adjusted using NaCl. L-arginine and trehalose were purchased from Fisher Scientific (Fair Lawn, NJ) and used to make buffer solutions containing 500 mM of either excipient in addition to 1 M NaCl and 50 mM sodium bicarbonate at pH 9.

Solutions of hen egg white lysozyme and bovine lactoferrin were prepared as previously described in Chapter 3. A monoclonal antibody was obtained from Genentech, Inc. (South San Francisco, CA) in formulation buffer concentrated to 30-40 mg/mL. Target protein concentrations for stock solutions were 2.5 ± 0.2 mg/mL for binding capacity and protein elution studies and 200-300 mg/mL for phase behavior experiments. Physical properties of the model proteins, namely the isoelectric point, molecular weight, effective hydrodynamic radius, and free-solution diffusion coefficient, are shown in Table 4.1.

Property	pI	M_w (kDa)	Stokes radius (nm)	D_0 (cm^2/s)
Lysozyme	11.4 (Wetter and Deutsch, 1951)	14.3 (Canfield, 1963)	2.0	$1.1x10^{-6}$ (Fuh et al., 1993)
Lactoferrin (monomer)	8.8 (Plate et al., 2006)	78 (Moore et al., 1997)	2.3	$9.6x10^{-7}$ (Chaufer et al., 2000)
Lactoferrin (tetramer)	-	312	4.4	$4.9x10^{-7}$
mAb	~8	144 (Ahamed et al., 2007)	5.7	$3.8x10^{-7}$ (Tao et al., 2011a)

Table 4.1 Physical characteristics of proteins used in elution experiments.

4.2.2 Stationary Phases

Prepacked 25 mm x 7 mm i.d. HiTrap columns containing SP Sepharose FF, SP Sepharose XL and Capto S, all strong cation exchangers, were purchased from GE Healthcare Life Sciences. A prepacked 50 mm x 5 mm i.d. S HyperCel column was obtained from Pall Life Sciences. The physical properties of the resins are presented in Table 1.1. All matrices carry a sulfonate functionalization, while Sepharose XL and Capto materials possess dextran extenders, substantially expanding the volume available for adsorption within this material as compared to their non-polymer-modified counterpart, Sepharose FF, but concomitantly reducing the pore space available for transport. The higher cross-linking density of the agarose base matrix that is present in Capto (Axen et al., 2008) results in a slightly smaller pore lumen (Tao et al., 2011b). S HyperCel is comprised of a fully cellulosic base matrix without any defined polymer modification (Chapter 2), but it exhibits properties comparable to those seen in polymer-modified stationary phases, including increased capacity and enhanced uptake rates (Chapter 3).

4.2.3 Dynamic Binding Capacity Measurements

Breakthrough experiments were performed on an ÄKTA Explorer 100 system (GE Healthcare) for each resin-protein system for which elution behavior was to be analyzed. All DBC measurements were performed at a linear velocity of 120 cm/hr, pH 7 and 20 mM TIS. To ensure consistency, DBC measurements were compared to values obtained previously for lysozyme and lactoferrin at these conditions on SP FF, SP XL and Capto S (Bowes and Lenhoff, 2011a).

Protein loading was continued until at least 25% of the feed concentration was measured in the eluate, monitored by absorbance at 280 nm. Protein was eluted using buffered solutions at 1 M TIS for lysozyme and mAb and at 1.5 M TIS for lactoferrin, due to an increased affinity of the latter protein on cation exchangers. Collection and spectroscopic measurement of eluted fractions showed close to 100% recovery of loaded protein in all cases.

DBC values were determined by integrating the area above the breakthrough curve up to 10% breakthrough and subtracting the system dead volume obtained by performing a breakthrough run without a column in line. Loadings for elution experiments followed the same procedures but were based on a fraction of the DBC values determined, depending on the system.

4.2.4 Column Elution and Determination of Apparent Elution Diffusivities

Columns were loaded with protein using the same operating conditions as in the determination of the DBCs. Multiple loading factors were employed, corresponding to 10, 60 and 100% of the DBC value at 10% breakthrough for each system. A 5-column volume wash step preceded a 100% step elution to an elevated TIS condition (1 M TIS, 1.5 M TIS, or 1 M NaCl + 500 mM excipient). Due to the

high protein concentrations in the eluate, the UV detector was saturated at times, causing a cutoff of the elution curve around 3000 mAU. Therefore, mass balances could not be performed by integration under the UV curve and instead were carried out by collecting and analyzing eluate fractions.

4.2.4.1 Theory

The hypothesized mechanism for elution at the single-particle level is a simple diffusional one. Upon desorption, which is assumed to occur instantaneously at t = 0, all the protein loaded into the particle is assumed to become desorbed and to be present in a protein solution of effective concentration c_0 in the particle; the concentration is expressed per unit particle volume and so the effective concentration is lower than the actual local concentration in the pore space. This protein then leaves the particle by simple pore diffusion to the particle surface (radial position $r = R_p$), from where it enters the mobile phase. The elution rate from the particle can depend on the rate of mass transfer from the particle surface to the bulk mobile phase, as described by the concentration difference between that at the particle surface and that in the bulk and by a mass transfer coefficient at the particle surface, k, which was obtained from the correlation of Carberry (1960) for flow in a packed bed

$$k = \frac{1.15 D_0^{2/3}}{(2R/u)^{1/2} \nu^{1/6}} \tag{4.1}$$

where D_0 is the free-solution diffusivity of the protein, u is the linear velocity of the interstitial fluid and ν is the kinematic viscosity, taken to be 10^{-6} m^2/s. Values of k of 2×10^{-4} to 6×10^{-4} cm/s were predicted for the systems studied.

For the situation in which the bulk protein concentration is negligible, the transient behavior of the effective intraparticle concentration, c_s, is described by the following conservation equation, boundary condition, and initial condition:

$$\frac{\partial c_s}{\partial t} = D_e \frac{1}{r^2}\frac{\partial}{\partial r} r^2 \frac{\partial c_s}{\partial r} \tag{4.2.1}$$

$$\frac{\partial c_s}{\partial r} = 0, \; r = 0 \tag{4.2.2}$$

$$-D_e \frac{\partial c_s}{\partial r} = k c_s, \; r = R_p \tag{4.2.3}$$

$$c_s = c_0, \; t = 0 \tag{4.2.4}$$

where D_e is the apparent effective pore diffusivity of elution to be estimated and, in this formulation, the intraparticle porosity is not explicitly accounted for. The solution is found as (Crank, 1975)

$$\frac{C_s}{C_0} = 2Bi \frac{R_p}{r} \sum_{i=1}^{\infty} \frac{1}{\beta_i^2 + Bi(Bi-1)} \frac{\sin\beta_i}{\sin\beta_i} \frac{r}{R_p} e^{-\beta_i^2 t D_e / R_p^2} \tag{4.3}$$

The Biot number, $Bi = kR_p/D_e$, reflects the relative importance of intraparticle and extraparticle transport resistances; high values ($Bi > 10$) indicate that the intraparticle resistance is dominant (Sherwood et al., 1975), as is usually the case in preparative chromatography of proteins. The β_i values are the eigenvalues determined as the roots of the characteristic equation for the unsteady-state diffusion problem

$$\beta \cot \beta + Bi - 1 = 0 \tag{4.4}$$

The eigenvalues tabulated in Crank (1975) were integrated into a cubic spline interpolation in Matlab to order to determine roots for different Biot number values.

Equation 4.3 can be used to calculate an instantaneous flux at the particle surface that will be for the form

$$J_s = \sum_{i=1}^{\infty} a_i \, e^{-\beta_i^2 t D_e / R_p^2} \tag{4.5}$$

which, for long-time behavior ($t >> R_p^2/D_e$), reduces to a monoexponential form that accurately describes the decreasing tail of the elution curve, expressed as

$$c_{eluate} = a_1 e^{-\beta_1 D_e t/R_p^2} \tag{4.6}$$

in which only the leading eigenvalue from Equation 4.4, β_1, plays a role. The effective elution pore diffusivity, D_e, was extracted by using the nonlinear least squares fitting routine, 'nlinfit', in Matlab to solve Equations 4.4 and 4.6 simultaneously. The data were placed on a logarithmic scale for ease in assessing the goodness-of-fit, which was also determined by the mean squared error.

In the presence of flow past the particle, the elution rate can be monitored by measuring the mobile-phase concentration. Since the diffusional problem is linear, the time-dependence of the mobile-phase concentration leaving the system will mirror that of the elution rate, as long as the mobile-phase concentration remains very small relative to that in the particle. Therefore if these conditions are satisfied at long times, the mobile-phase concentration should decay exponentially, which should allow estimation of D_e if R_p and k are known.

The more challenging situation is that of the behavior of a full column of particles, where the presence of multiple particles and the additional axial dimension are appreciable complicating factors. Three approaches of increasing complexity are presented in Appendix B; that they all yield similar results, albeit subject to different assumptions, provides reassurance that the method used to analyze the experimental data is reasonable

Resin	Mean pore radius (nm)	$\varepsilon_{p,acc}$				Mean pore radius in high salt (nm)	$\varepsilon_{p,acc,high\ salt}$			
		lysozyme	lactoferrin (monomer)	lactoferrin (tetramer)	mAb		lysozyme	lactoferrin (monomer)	lactoferrin (tetramer)	mAb
SP Sepharose FF	24.7	0.71	0.67	0.64	0.60	24.7	0.69	0.67	0.54	0.47
SP Sepharose XL	5.8	0.30	0.24	0.07	0.03	9.6	0.44	0.40	0.20	0.14
Capto S	4.8	0.19	0.14	0.02	0.01	7.1	0.34	0.30	0.10	0.06
S HyperCel	4.4	0.18	0.14	0.03	0.01	4.4	0.19	0.14	0.02	0.01

Table 4.2 Intraparticle porosities for different proteins, and mean pore radii, based on ISEC analysis. Data obtained at high salt concentrations, [NaCl] = 1-1.5 M.

4.2.5 Inverse Size Exclusion Chromatography and Size Exclusion Chromatography

ISEC experiments using dextran probes were carried out to determine apparent intraparticle porosities during elution for specific resin-protein systems. The procedures followed those used previously (Chapter 2) using the same experimental setup and similar methods to assess pore dimensions, by analysis of the calibration curves relative to the distribution coefficients for each dextran solute. ISEC data for SP FF (DePhillips and Lenhoff, 2000), Capto S (Tao et al., 2011b) and S HyperCel (Angelo et al., 2013, Chapter 2) have previously been investigated using this technique under different solution conditions. ISEC data for SP XL under low- (20 mM TIS) and high-salt (1.5 M TIS) conditions can be found in Section 2.3.1. Mean pore radii were determined from the first moment of the fitted pore size distributions and are reported in Table 4.2, along with accessible particle volumes for each resin-protein pairing (Section 4.3.1.2). Retention volumes of uncharged dextran standards were used to determine the accessible fraction of particle volume, $\varepsilon_{p,acc}$, from

$$\varepsilon_{p,acc} = \frac{V_r - V_0}{V_c - V_0} \tag{4.7}$$

where V_r is the retention volume of a given solute, V_c is the total column volume and V_0 is the column void volume determined using a 3000 kDa dextran standard, which is fully excluded from all the stationary phases used here.

Standard size exclusion chromatography was also performed on lactoferrin fractions on a 24 mL Superdex 75 column (GE Healthcare) to determine if protein oligomerization occurs at high salt, as lactoferrin has previously been shown to form tetramers above sodium chloride concentrations of about 200 mM TIS (Chaufer et al., 2000). Dextran standards of known radii were used as molecular size markers to

determine size differences for lactoferrin under low- (20 mM TIS) and high-salt (1 M TIS) running conditions.

4.2.6 Instantaneous Phase Behavior of Lysozyme in Sodium Chloride Solutions

Experiments were performed to determine the instantaneous phase boundary for lysozyme in the presence of sodium chloride in a manner similar to that reported previously (Dumetz et al., 2008; Lewus et al., 2014). Samples were prepared by mixing appropriate amounts of low- and high-salt buffered solutions (between 0 and 3 M NaCl in 10 mM sodium phosphate at pH 7 or in 50 mM sodium bicarbonate at pH 9) in 0.5 mL tubes to a volume of 170-190 μL. Ten to thirty μL of concentrated lysozyme solution (200-300 mg/mL) was pipetted into the tubes for a final volume of 200 μL and aspirated for at least 30 seconds afterward; in most cases, samples were then vortexed for an additional 30 seconds. At sufficiently high protein concentrations instantaneous precipitation was observed, but at intermediate concentrations the precipitate redissolved after vortex mixing. The boundary for instantaneous phase separation was taken as the highest protein concentration in which the precipitate that formed began to resolubilize into solution following vortex mixing.

4.2.7 Confocal Laser Scanning Microscopy Imaging of Single-Particle Elution

SP FF or XL particles were packed into a flow cell designed for use in a confocal microscope (Dziennik et al., 2003) and the formation of elution fronts of fluorescently-labeled protein was observed as described previously (Section 3.3.4). Lysozyme was fluorescently labeled with DyLight 650 in a 1-2% labeling ratio following protocols supplied by the manufacturer. Reservoirs of equilibration buffer (10 mM sodium phosphate, pH 7), of a solution of fluorescently-labeled protein (2 ±

0.2 mg/mL), high-salt buffer (1 M TIS), and high-salt buffer containing excipient (1 M NaCl, pH 9, 500 mM L-arginine) were used to load and elute protein successively, in order to allow imaging of elution behavior using a Zeiss 5 LIVE DUO high-speed confocal microscope equipped with a 40x C-Apochromat (NA 1.2) water-immersion lens (Carl Zeiss). The protein solution was recirculated through the flow cell for 40-45 minutes at 1 mL/min to ensure full saturation and the particles were then washed for one minute with equilibration buffer before the high-salt eluent was fed. Images were captured every 5 seconds from the time of switching to the eluent feed until no fluorescently-labeled protein remained visible inside the particle or no appreciable decrease in fluorescence was observed.

4.3 Results and Discussion

4.3.1 Apparent Elution Diffusivities

4.3.1.1 Estimation from Elution Data

Protein concentration profiles in the eluate following step elution were used to determine both the number of column volumes necessary for near-complete recovery and the apparent pore diffusivities during elution by application of Equations 4.4 and 4.6. Figures 4.1-6 display both the raw elution chromatograms and adjusted data for lysozyme, lactoferrin and mAb elution from SP Sepharose FF, SP Sepharose XL, Capto S, and S HyperCel. The number of column volumes necessary for near-complete elution (when the UV signal returned to 100 mAU above the baseline) is obtained directly from the raw data for each curve, and the values obtained are shown in Table 4.3. For most cases, three loading factors, namely 10, 60 and 100% of the DBC for each system (also given in Table 4.3), were used to determine if the extent of

column loading affected elution rates and volumes. Altering this factor had a significant impact on the elution pool volume as expected, due to the larger amounts of protein to be eluted. Only lysozyme was used at 100% loading factors for all systems due to constraints in protein availability. In general, for equivalent loadings, near-complete elution was achieved much sooner in the non-polymer-modified SP FF, while more column volumes were required for recovery in polymer-modified and cellulosic media. Solute size also appears to affect this metric, with mAb eluting from the Capto S adsorbent displaying the longest elution time at 60% loading factor, for instance.

The adjusted data in Figures 4.2, 4.4 and 4.6 were truncated to just after the end of detector saturation (the plateau region in the raw data at approximately 3000 mAU) and plotted on semilog axes, with linearity, at least at longer times, indicating a satisfactory fit to the model. The elution model was fit to only regions of < 85% of the maximum (saturated) UV signal to ensure linearity between detection measurements and true protein concentrations in the eluate. Despite the appreciable differences in elution volume with different column loadings, the fits to the post-saturation portion of the elution profile show only slight differences in the effective diffusivities. The diffusivities determined by analysis of the elution profiles are tabulated in Table 4.4. Similarly to the column volumes required for near-complete elution, the general trend remains in which the non-polymer-modified material shows the fastest elution, followed by, for the most part, an order of magnitude reduction in the rate for polymer-modified and cellulosic media.

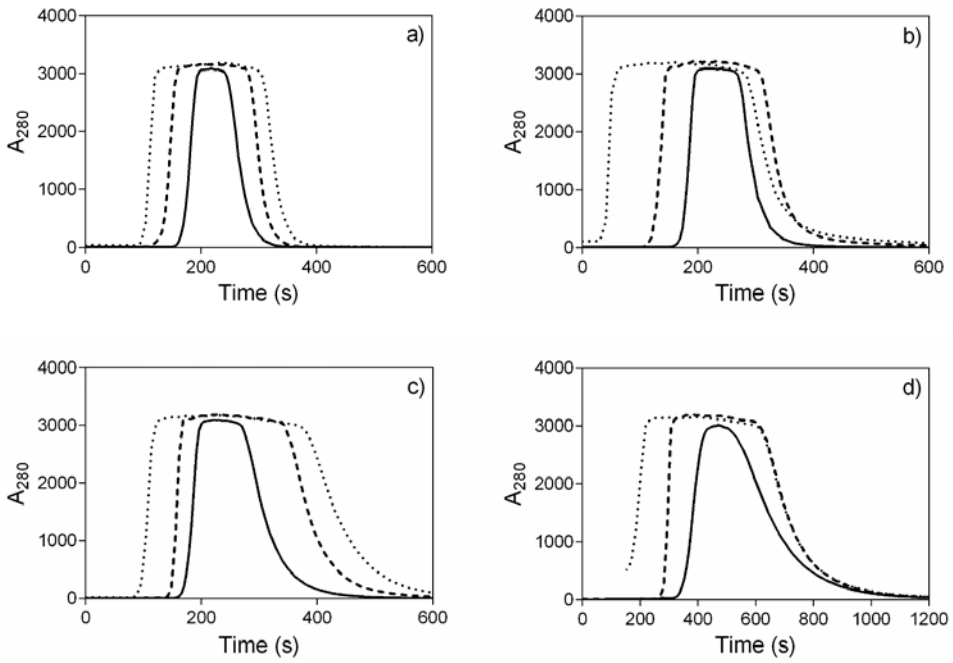

Figure 4.1 Lysozyme elution profiles on SP Sepharose FF (a), SP Sepharose XL (b), Capto S (c), and S HyperCel (d) using a 1 M TIS step elution for different loading factors: 10% (——), 60% (----) and 100% (·····) of the dynamic binding capacity at 120 cm/hr; take note of the difference in time scale for elution on the S HyperCel resin.

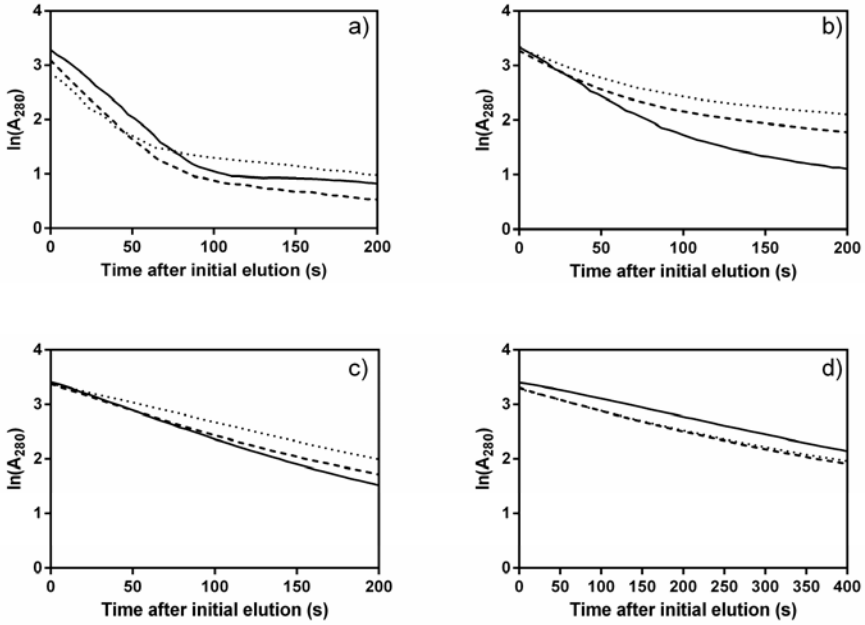

Figure 4.2 Lysozyme elution profiles truncated and time-shifted to just after the absorbance begins to decay from its maximum at the detection limit. Elution is shown on a logarithmic scale for SP Sepharose FF (a), SP Sepharose XL (b), Capto S (c), and S HyperCel (d) using a 1 M TIS step elution for different loading factors: 10% (——), 60% (----) and 100% (·····) of the dynamic binding capacity at 120 cm/hr; take note of the difference in time scale for elution on the S HyperCel resin.

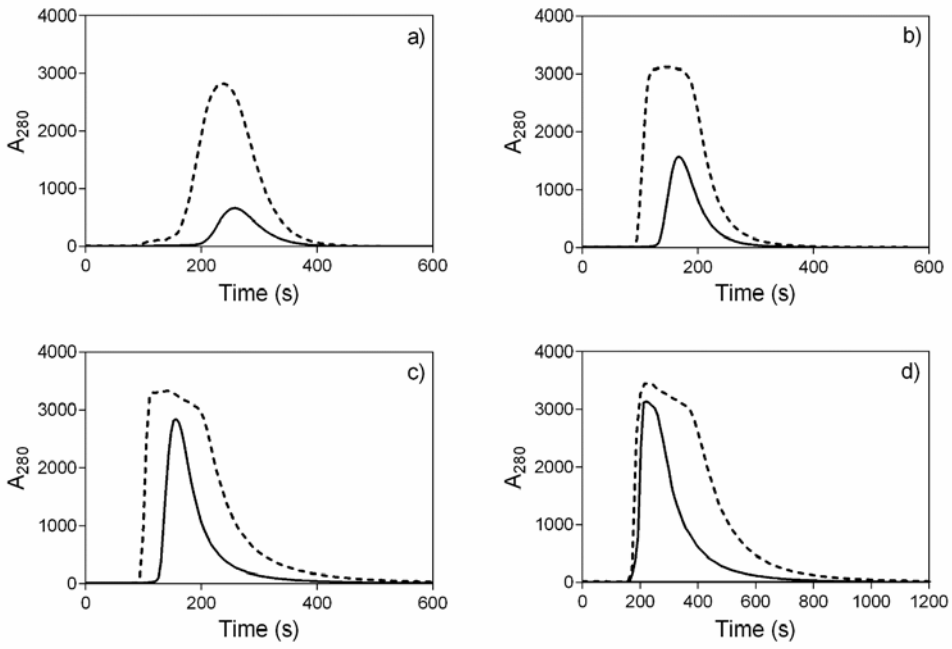

Figure 4.3 Lactoferrin elution profiles on SP Sepharose FF (a), SP Sepharose XL (b), Capto S (c), and S HyperCel (d) using a 1.5 M TIS step elution for different loading factors: 10% (——) and 60% (----) of the dynamic binding capacity at 120 cm/hr; take note of the difference in time scale for elution on the S HyperCel resin.

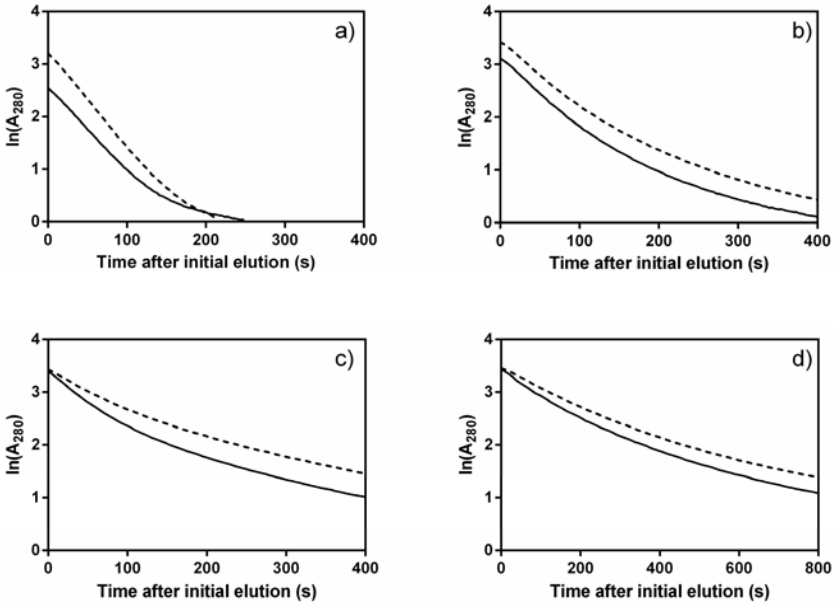

Figure 4.4 Lactoferrin elution profiles truncated and time-shifted to just after the absorbance begins to decay from its maximum at the detection limit. Elution is shown on a logarithmic scale for SP Sepharose FF (a), SP Sepharose XL (b), Capto S (c), and S HyperCel (d) using a 1.5 M TIS step elution for different loading factors: 10% (——) and 60% (----) of the dynamic binding capacity at 120 cm/hr; take note of the difference in time scale for elution on the S HyperCel resin.

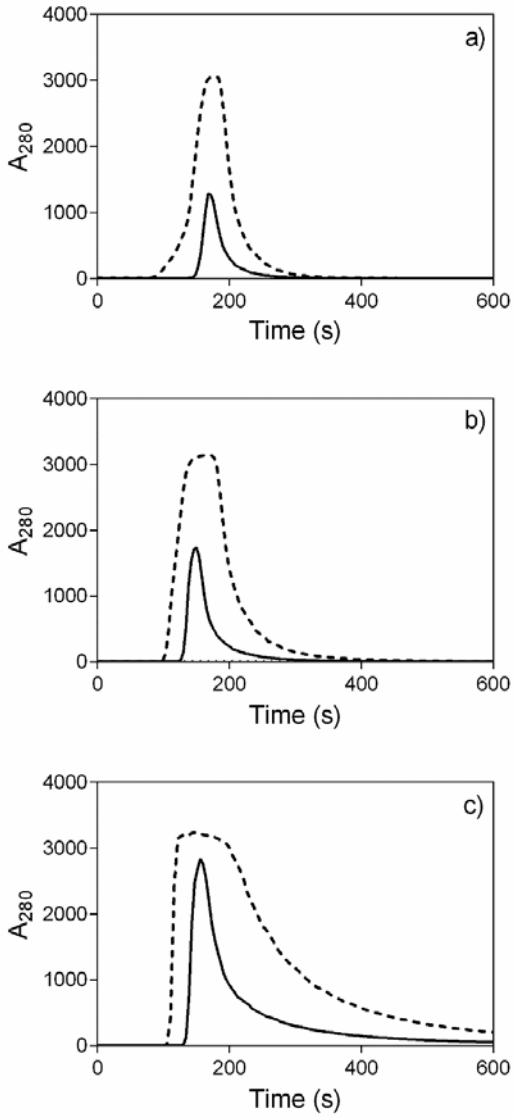

Figure 4.5 Monoclonal antibody elution profiles on SP Sepharose FF (a), SP Sepharose XL (b) and Capto S (c) using a 1 M TIS step elution for different loading factors: 10% (——) and 60% (----) of the dynamic binding capacity at 120 cm/hr.

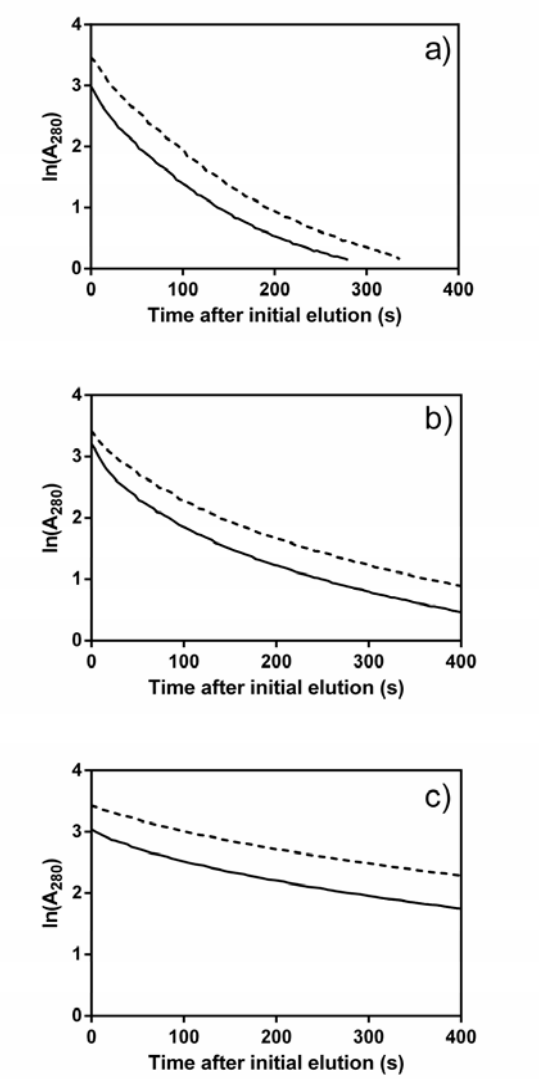

Figure 4.6 Monoclonal antibody elution profiles truncated and time-shifted to just after the absorbance begins to decay from its maximum at the detection limit. Elution is shown on a logarithmic scale on SP Sepharose FF (a), SP Sepharose XL (b) and Capto S (c) using a 1 M TIS step elution for different loading factors: 10% (——) and 60% (----) of the dynamic binding capacity at 120 cm/hr.

Resin	Dynamic binding capacity (mg/mL)			10% loading factor			60% loading factor			100% loading factor		
	lysozyme	lactoferrin	mAb	lysozyme	lactoferrin	mAb	lysozyme	lactoferrin	mAb	lysozyme	lactoferrin	mAb
SP Sepharose FF	108	25	17	2.2	2.0	1.2	3.1	4.0	2.8	3.9	n/a	n/a
SP Sepharose XL	211	45	28	2.8	1.9	1.5	4.9	3.1	3.1	7.0	n/a	n/a
Capto S	175	94	91	3.7	2.8	4.7	5.2	4.9	9.4	7.2	n/a	n/a
S HyperCel	133	158	n/a	4.6	3.1	n/a	5.2	4.6	n/a	6.2	n/a	n/a

Table 4.3 Dynamic binding capacities and eluent volume, in units of column volumes, required for elution (to 100 mAU) for each protein, resin and loading condition (loading performed at pH 7, 20 mM TIS).

Resin	Effective elution diffusion coefficient, D_e (10^{-8} cm^2/s)								
	10% loading factor			60% loading factor			100% loading factor		
	lysozyme	lactoferrin	mAb	lysozyme	lactoferrin	mAb	lysozyme	lactoferrin	mAb
SP Sepharose FF	13 ± 0.50	5.6 ± 0.047	9.6 ± 0.73	15 ± 0.42	5.9 ± 0.043	8.2 ± 0.41	13 ± 0.94	n/a	n/a
SP Sepharose XL	8.7 ± 0.20	6.4 ± 0.13	9.1 ± 0.96	6.5 ± 0.28	6.0 ± 0.13	6.1 ± 0.36	5.0 ± 0.30	n/a	n/a
Capto S	5.1 ± 0.13	5.3 ± 0.15	2.9 ± 0.25	4.5 ± 0.16	3.8 ± 0.087	2.0 ± 0.053	3.3 ± 0.11	n/a	n/a
S HyperCel	1.0 ± 0.079	1.5 ± 0.051	n/a	1.3 ± 0.029	1.2 ± 0.032	n/a	1.3 ± 0.029	n/a	n/a

Table 4.4 Fitted elution diffusivities for each protein, resin and loading condition (loading performed at pH 7, 20 mM TIS). Best fit results shown along with 95% confidence intervals.

Values of the Biot number, calculated using the fitted diffusivities, for the different resin-protein systems were of order 10 to 200, the high values indicating dominance of the intraparticle transport resistance. While the Biot numbers for all resins were of a similar order of magnitude, those for SP FF were generally the lowest, reflecting the generally higher pore diffusivities in the very open agarose structure.

The fitting of the effective diffusivities to Equation 4.6 is premised on their being pore diffusivities, as the high-salt conditions of elution would make adsorption on the pore walls or the polymer extenders negligible. What is less clear for the polymer-modified media is whether desorbed protein is totally excluded from the polymer, but this seems a reasonable assumption given ISEC results that show all but the smallest dextran probes being excluded from the polymer layer in the absence of an electrostatic driving force for adsorption. It may also be that the partitioning of uncharged solutes in a charged pore deviates from the purely steric limit as a result of the electrical double layer caused by the introduction of the uncharged solute (Deen, 1987; Stone and Carta, 2007). Indeed, the results for lysozyme and lactoferrin are similar in magnitude to shrinking-core (pore) diffusivities previously determined for SP FF during protein uptake (Traylor, 2013). However, the elution diffusivities are slightly higher than the uptake values, which were determined at low ionic strengths, where diffusion is coupled to adsorption that is strong enough to be considered irreversible.

4.3.1.2 Interpretation of Apparent Pore Diffusivity Values

The values obtained for the pore diffusivities can be interpreted within the theoretical framework in which the values are related to the corresponding free-solution diffusivities, D_0, by (Carta and Jungbauer, 2010)

$$\frac{D_e}{D_0} = \frac{\varepsilon_p \psi_p}{\tau_p} \tag{4.8}$$

where ε_p is the intraparticle porosity, ψ_p is the diffusional hindrance coefficient and τ_p is the tortuosity factor. The dependence on porosity, which more strictly reflects the accessible porosity $\varepsilon_{p,acc}$ and therefore depends on solute size, simply captures the space available for diffusion. The hindrance coefficient accounts for hydrodynamic drag as a solute diffuses in a narrow pore and is related to the relative sizes of the solute and the pore (Anderson and Quinn, 1974; Brenner and Gaydos, 1977; Deen, 1987), with a tighter fit giving rise to lower values. Most of the theoretical relationships that have been derived are for spherical particles in cylindrical pores, but especially for polymer-derivatized materials, in which the "pore wall" is in fact a polymer containing solvent, these values are highly questionable. Although transport through such pores has been modeled (Kim and Anderson, 1991), considerable uncertainty surrounds suitable values of ψ_p other than that they are of order unity. The tortuosity factor, while being a function of the pore geometry, is not necessarily explicitly dependent on solute or pore size, although the change in pore accessibility with solute size introduces such a dependence, again with considerable uncertainty.

Values of $\varepsilon_{p,acc}$ were measured directly by inverse SEC for both polymer-modified and non-polymer-modified adsorbents. Figure 4.7 shows results for SP FF at low ionic strength and SP XL at high and low ionic strengths. Figure 2.8 shares the same raw data but is plotted against the distribution coefficient as opposed to the accessible porosities of the solutes (Section 2.3.1). These data clearly show a higher pore accessibility of SP FF than of SP XL for any individual dextran probe, due directly to the effect of the polymer extenders in SP XL. The results also show the greater accessibility of SP XL at high than at low TIS due to screening of charge

repulsion between ligands and consequent collapse of the extenders (DePhillips and Lenhoff, 2000; Stone and Carta, 2007). This collapse of the polymer layer due to increased salt concentration fundamentally alters the intraparticle architecture which translates to larger pore volumes that the dextran solutes may access. The sensitivity to even moderate salt concentrations is a common trait among polymer-derivatized media (Bowes et al., 2009; Lenhoff, 2011; Yu and Sun, 2013).

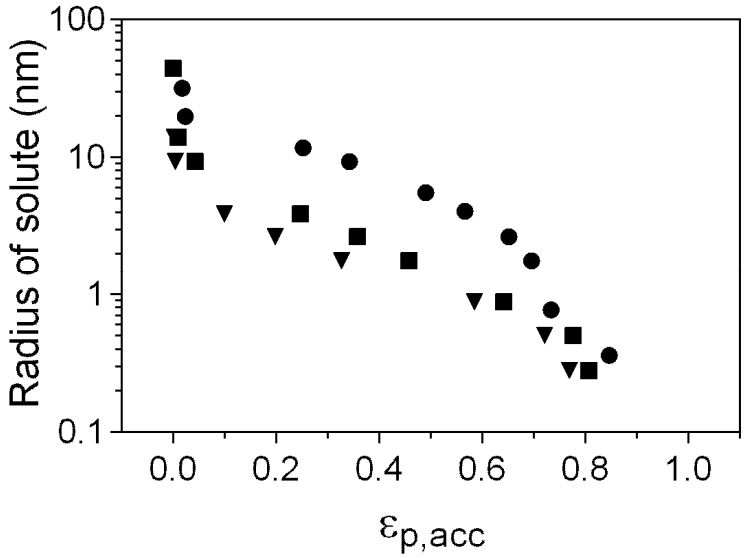

Figure 4.7 Dextran calibration curves for SP Sepharose FF (●) (DePhillips and Lenhoff, 2000), SP Sepharose XL (▼) and SP Sepharose XL at 1500 mM NaCl (■). Effective accessible intraparticle porosities for model proteins were interpolated based on exponential fits to these data sets.

Accessible particle volumes for the proteins studied are given in Table 4.2, determined by the calibration curves obtained from ISEC and the Stokes radius for each protein seen in Table 4.1. Accessible particle volumes were also found for Capto

S (Tao et al., 2011b) and S HyperCel (Chapter 2) based on previously generated ISEC data.

Figure 4.8 shows the dependence of the normalized apparent pore diffusivities during elution on the accessible particle volume at high salt. Different plot markers represent the different stationary phases and connected lines represent data for the same protein. The general trend is one of increasing normalized diffusivities with increasing accessible particle volumes, but the dependence is not uniformly linear as suggested by Equation 4.8. This may reflect experimental uncertainties but also more fine-grained architectural differences among the different media, including differences in pore-size distribution as distinct from just the porosity values, which may affect the hindrance and tortuosity factors.

Despite these uncertainties, one trend in Figure 4.8 that seems counterintuitive is that the normalized diffusivities increase with increasing protein size. Lysozyme has a molecular weight approximately 10 times smaller than that of a monoclonal antibody, and one would assume that a smaller molecule such as this would encounter less hindrance in pore diffusion during elution (Anderson and Quinn, 1974), but the opposite effect is suggested by the data.

Additionally, the lactoferrin tetramer displays faster relative diffusivities than the monomer relative to their respective free solution diffusivities. The slower free solution diffusivity that the tetramer complex displays (due to the increased size/molecular weight) increases the normalized diffusivity in turn, as the same effective elution diffusivity was used in both cases. The faster rates of the larger molecular species could also be attributed to an increase in intermolecular repulsions

these protein experience within the pore during elution as they occupy a greater fraction of the available pore space.

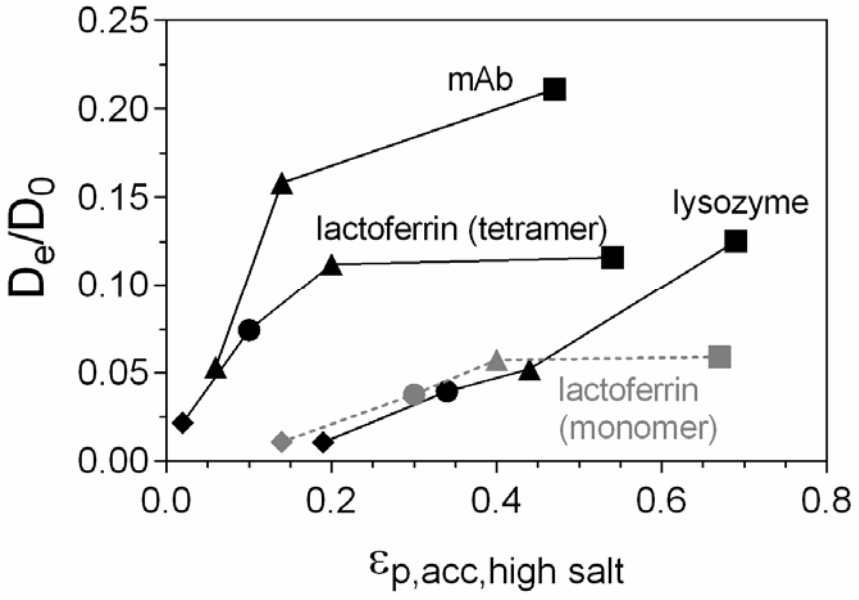

Figure 4.8 Normalized effective elution diffusivities based on the fit diffusivities and free-solution diffusivities at infinite dilution for lysozyme, lactoferrin and mAb as a function of the accessible porosity for the corresponding resin-protein system for SP Sepharose FF (■), SP Sepharose XL (▲), Capto S (●), and S HyperCel (◆). The lines corresponding to lactoferrin in tetramer and monomer forms reflect the difference in the free-solution diffusivities and accessible porosities.

The additional dependence on ψ_p and τ_p is more problematic and is investigated by a more absolute comparison of the values of the ratio τ_p/ψ_p (Figure 4.9), determined from Equation 4.8 using the normalized elution diffusivities and therefore reflecting the high salt concentrations used for elution. The hindrance coefficients are difficult to estimate, especially when the protein size and mean pore

radius are very close together, e.g., mAb in dextran-modified media. However, especially in cases involving polymer-derivatized media, the hindrance coefficients would be expected to be much closer to unity than expected from the theoretical results for solid pore walls (Anderson and Quinn, 1974; Brenner and Gaydos, 1977; Deen, 1987), so the ratio plotted in Figure 4.9 can be expected to reflect primarily the trends in the tortuosity factor, where values of 2 to 6 are reported to be reasonable (Satterfield, 1970). The values for mAb are at the low end of this range, but those for lactoferrin and lysozyme appear somewhat high for consistency with the diffusional model, especially in light of the much lower values for mAb in the same adsorbents.

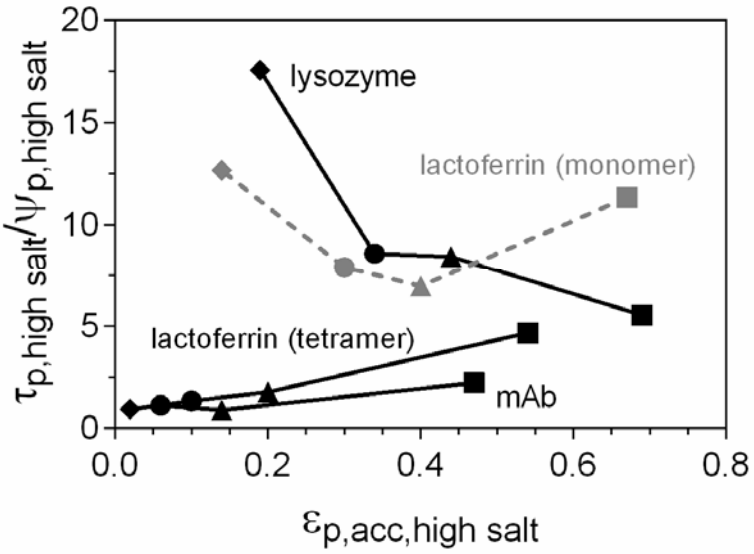

Figure 4.9 Ratio of tortuosity and hindrance factors for elution based on the fit diffusivities for lysozyme, lactoferrin and mAb, as a function of the accessible porosity for the corresponding resin-protein system for SP Sepharose FF (■), SP Sepharose XL (▲), Capto S (●), and S HyperCel (◆). The lines corresponding to lactoferrin in tetramer and monomer forms differ because of differences in the free-solution diffusivities and accessible porosities.

The result for lactoferrin can be explained by the formation of tetramers at and above sodium chloride concentrations of 200 mM (Chaufer et al., 2000), which increases the size of the eluting species and hence the free-solution diffusivity, D_0 (Table 4.1). Additional sets of normalized data for lactoferrin, accounting for the revised D_0 value and the adjusted accessible porosity $\varepsilon_{p,acc}$ at high salt, are shown in Figures 4.8 and 4.9. The trend lines based on the tetramer are much more consistent than the monomer case with those for mAb. SEC measurements performed on Superdex 75 on unpurified and purified lactoferrin at high and low concentrations of sodium chloride (Figure 4.10) suggest that the formation of tetramer is reversible and hence that the true trendlines for lactoferrin in Figures 4.8 and 4.9 may lie somewhere between the tetramer and monomer lines. However, at the high lactoferrin concentrations in the pore after desorption, mass-action considerations would be expected to favor tetramer formation.

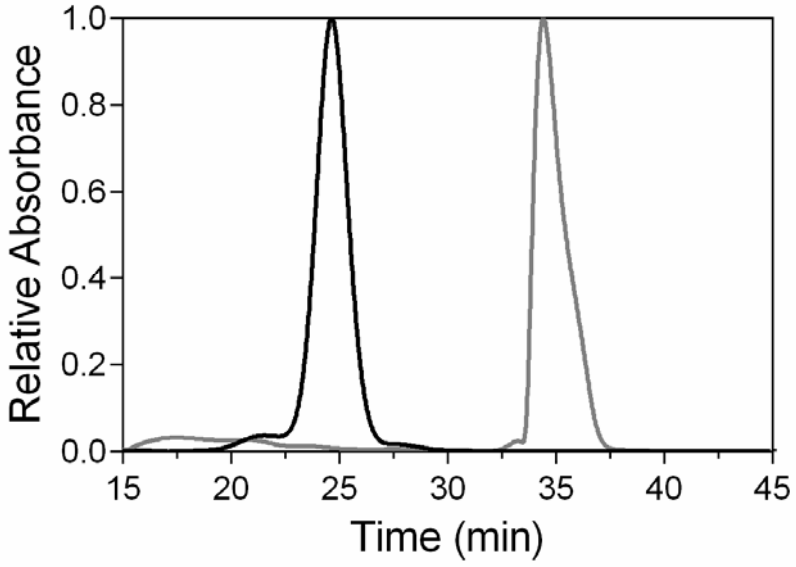

Figure 4.10 Size-exclusion chromatograms of eluted lactoferrin fractions on Superdex 75 for isocratic running conditions of 20 mM TIS (gray) and 1 M TIS (black); the lower retention time at the high-salt condition indicates formation of oligomer under elution conditions.

For both mAb and lactoferrin, Figure 4.9 shows a slight increasing trend of τ_p/ψ_p with $\varepsilon_{p,acc}$. This may reflect differences in the pore structures of the different adsorbents, but if anything one might expect a decreasing tortuosity with the more open structures encountered at high porosities, particularly for SP FF. A possible explanation emerges from the combination of the overall protein loading and porosity for each material, which together determine the estimated local pore concentration immediately following desorption, i.e., when the high-salt front penetrates a protein-loaded particle. Using lysozyme as an example, the resulting values for this concentration, plotted against the accessible intraparticle porosity for each material (Figure 4.11), suggest that in the cellulosic and polymer-modified media, where

average porosities are the smallest and the binding capacities are high, there is a transient period when the local pore concentration can be on the order of several hundred mg/mL. This concentration would decay as elution proceeds and protein leaves the stationary phase to enter the interstitial mobile phase, but the dependence of protein diffusivities on concentration (Anderson et al., 1978) may explain the higher diffusivities at lower porosities implied by the counterintuitive trends for mAb and lactoferrin in Figure 4.9.

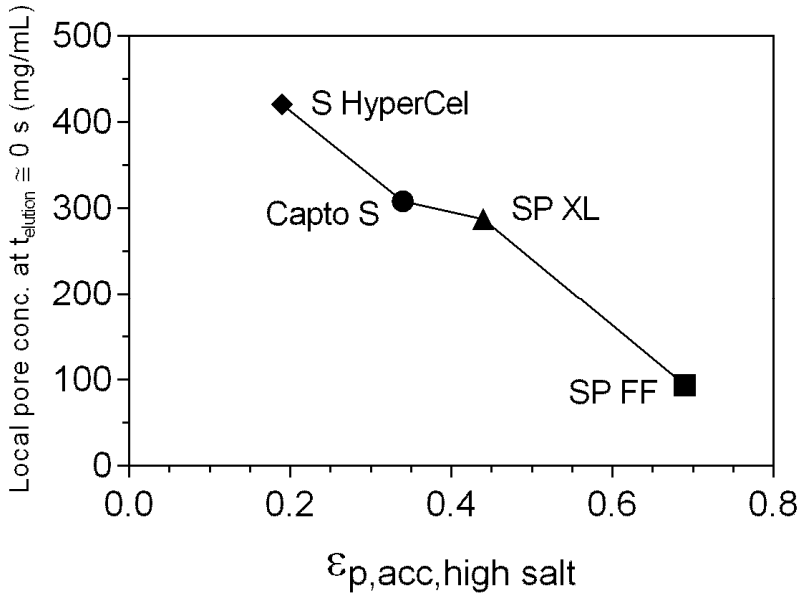

Figure 4.11 Estimated local pore concentrations of lysozyme at the moment of elution ($t_{elution} \approx 0$ s) as a function of accessible intraparticle porosities under high-salt conditions corresponding to the respective resins.

The results for lysozyme remain anomalous, based on the inconsistent trends for the elution diffusivity (Figure 4.8) and the high apparent tortuosity (Figure 4.9). One possible explanation is that lysozyme, the smallest of the model proteins used, can access micropores in these resins that are inaccessible to mAb or lactoferrin and that these pores have higher tortuosities. However, the very high absolute values seen for lysozyme in Figure 4.11 and the relatively high value in as open a structure as SP FF makes this seem unlikely. An alternative explanation is explored in the next section.

4.3.2 Phase Behavior of Lysozyme Under Elution Conditions

Maintaining protein solubility is crucial in preventing on-column aggregation and fouling, as well as ensuring product stability. Salting-out characteristics of proteins, such as lysozyme and monoclonal antibodies, have been studied outside of the column environment (Dumetz et al., 2008; Lewus et al., 2011; Muschol and Rosenberger, 1997), but not extensively in conditions that would mimic those of a typical elution from an ion-exchange material. The transient conditions that exist in the early stages of elution are somewhat similar in nature to these studies, even though phase separation cannot be readily observed directly on-column.

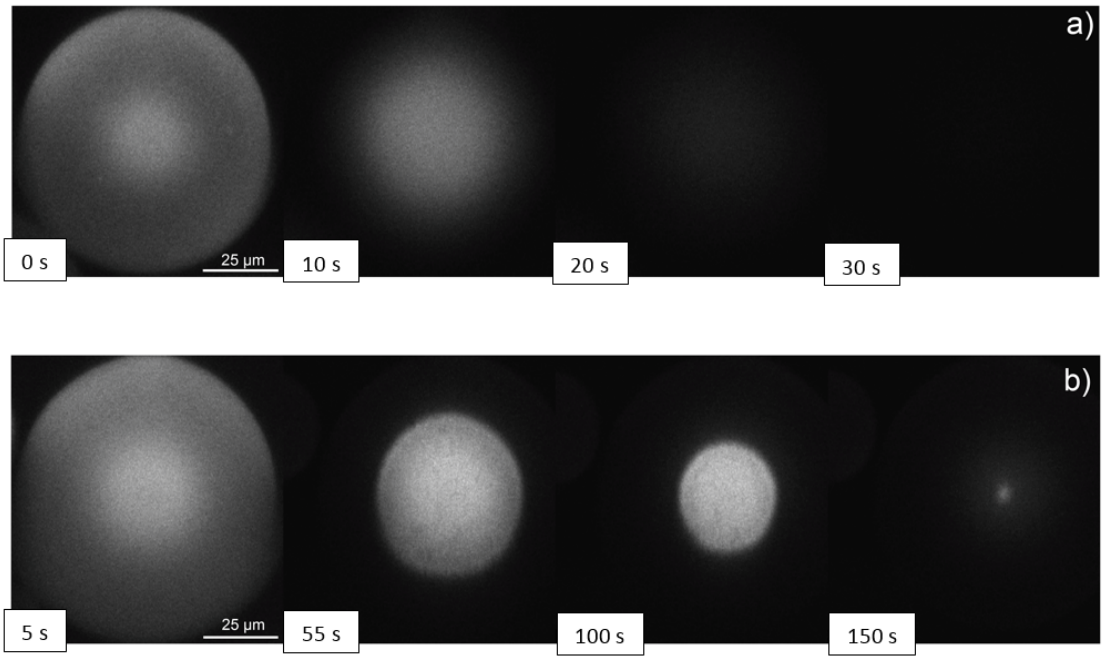

Figure 4.12 Elution of DyLight 650-labeled lysozyme from (a) SP Sepharose FF and (b) SP Sepharose XL at pH 7. Loading was performed using a recirculating stream of protein for 45 minutes and the particles were then washed with equilibration buffer for 5 minutes before a step change to the elution condition. Imaging was carried out until no additional decrease in fluorescence was observed.

Figure 4.12 shows the confocal microscopy profiles gathered during elution of DyLight 650-labeled lysozyme from SP FF and XL. The higher intensity at the center of the particle at t = 0 s can be explained as an overshoot attributed to differences in retention of labeled and unlabeled lysozyme (Teske et al., 2007); if loading were carried out for a longer period, the intensity would have become more uniform throughout the particle cross-sections (Dziennik et al., 2005). The sequences show the initial reservoir of protein in each particle gradually depleted from the outer edge, but there are clear differences between the results for the two materials. For SP FF, the outside edge of the intensity profile during exit of protein from the particle is diffuse,

as would be expected for diffusive transport of protein in solution. For SP XL, the profile is very different, with a sharp retreating front that can be described as a shrinking-core profile, with the very center of the particle retaining a relatively high fluorescence intensity until the last captured frames of elution. The time required for apparent full elution of protein from SP XL is also more than 5 times longer than what was required for SP FF. Similar elution behavior of lysozyme to that in SP XL was observed in S HyperCel, which is not polymer-derivatized but shares similar characteristics with SP XL, such as high binding capacity and low accessible porosity. As was seen in Figure 4.11, such conditions would result in extremely high protein concentrations in the pore space at the start of elution, and this is further compounded by the presence of a high salt concentration. This may lead to very rapid phase separation in which the protein in the pore, instead of being in free solution, is present as a dense phase, presumably a precipitate or gel. Elution from the particle would then first require redissolution of the dense phase, which would occur at its outer edge, giving rise to the kind of elution profiles seen for SP XL in Figure 4.12. The data in Figure 4.11 indicate that this kind of behavior is least likely in SP FF among the materials studied, consistent with the diffuse edges seen for this material in Figure 4.12.

Lysozyme tends to form chain-like aggregates, growing in a "head-to-tail" manner (Norton and Allerhand 1977, Banerjee et al. 1975). Small-angle neutron scattering work has shown that the aggregation of lysozyme occurs in both small (approximately 3 nm in radius) and large formations (approximately 20-60 nm in radius) (Niimura 1995). Obviously, the larger formations (deemed Type I aggregates) could pose an issue if the aggregate is formed within a pore of smaller radius than 20-

60 nm, effectively occupying a large fraction of the pore space. However, it is difficult to determine if lysozyme tends to aggregate in this manner within the pore environment when compared to free solution as molecular crowding could have an effect on the structure of the dense phase.

High salt and high protein concentrations (as well as pH approaching the isoelectric point of the protein) are of course prime conditions for phase separation, and lysozyme has previously been shown to phase-separate instantaneously under comparable conditions to those used here for elution (1-2 M sodium chloride, > 70 mg/mL protein) (Dumetz et al., 2008). Additional such measurements were made here, with instantaneous phase boundaries for lysozyme in sodium chloride solutions (at pH 9) shown in Figure 4.13. The leftmost curve is the aggregation boundary representative of normal elution conditions, which lies at around 60 mg/mL lysozyme for a sodium chloride concentration of 1 M, the condition used for elution experiments. Protein concentrations of higher than 60 mg/mL were difficult to achieve in the phase separation measurements due to the nature of the experiments and the limit to which the protein could be concentrated. Again, it is difficult to determine if these phase boundaries remain consistent when lysozyme is confined to the pore space within a stationary phase as opposed to free solution, such as in these experiments.

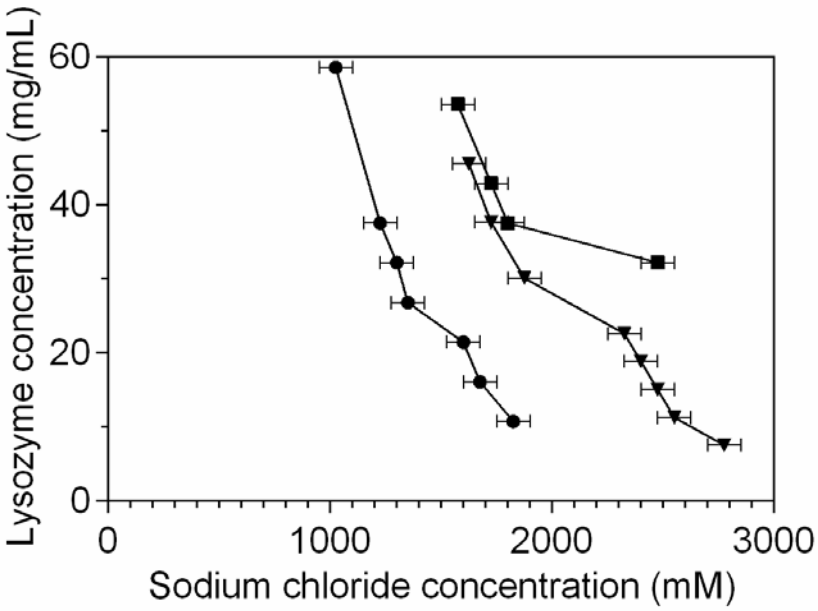

Figure 4.13 Instantaneous aggregation lines for lysozyme in sodium chloride without the use of an excipient (●), with 500 mM trehalose (▼), and with 500 mM L-arginine (■).

That behavior similar to that of lysozyme was not seen for the other two proteins presumably reflects the different physicochemical properties of different proteins. Even for lysozyme in SP XL, elution is complete after 2-3 minutes (Figure 4.12), so the effect would require instantaneous or near-instantaneous phase separation. Different proteins have different protein- and salt-concentration thresholds for such phase separation, and even where phase separation occurs it may do so only via a relatively slow nucleation step (Dumetz et al., 2008; Lewus et al., 2011).

4.3.3 Elution Using Excipients

The kind of behavior seen for lysozyme and the mechanism proposed above raise the question of whether any remedy is available to improve elution rates in such systems. Excipients, such as disaccharides and amino acids, are commonly used for formulation applications to stabilize proteins and prevent aggregation, e.g., trehalose and L-arginine have been shown to have stabilizing effects in protein systems (Baynes et al., 2005; Lins et al., 2004; Tsumoto et al., 2004; Xie and Timasheff, 1997). L-arginine has also been used to enhance elution behavior of antibodies in Protein A (Arakawa et al., 2004; Ejima et al., 2005), hydrophobic interaction and cation-exchange systems (Arakawa et al., 2007b), showing a reduction in eluted aggregates.

The mechanisms by which excipients such as disaccharides (e.g., trehalose and sucrose) and amino acids (e.g., arginine) stabilize proteins have still not been completely elucidated (Arakawa et al., 2007a). Most organic substances are known to lower the surface tension of water, but disaccharides and arginine appear to be an exception to this rule. The increase in surface tension has an unfavorable effect on the structure of water surrounding proteins in aqueous solution, as an increase in the exclusion volume of water is associated with an increase in surface tension. Therefore, the addition of these excipients to aqueous protein solutions results in an unfavorable, or positive, free-energy change for the system (Arakawa and Timasheff, 1982). This in turn causes proteins to become preferentially hydrated, which is understood to be the prevailing mechanism of action for protein stabilization in the presence of these excipients, even though there may be other molecular interactions at play.

Arginine is a special case, as the amino acid should be excluded from the protein surface, but it must have an affinity for the protein surface (presumably with amino acid side chains possessing negatively charged functional groups), which causes it to overcome the unfavorable surface tension effect (Breslow and Guo, 1990). However, since this is still a relatively weak interaction, arginine binding to the protein surface is expected to be fairly limited, which is significant in its ability to suppress aggregation but not totally destabilize the protein (Arakawa et al., 2007a). Regardless, the addition of an excipient such as arginine results in a positive change in the protein chemical potential, which should cause the system to favor the native state or conformation, as the free-energy of the system would be larger for a protein in a denatured state which is more thermodynamically unstable.

Additional data also included in Figure 4.13 show that the addition of 500 mM trehalose or L-arginine causes a significant shift in the aggregation boundary to higher sodium chloride concentrations. Due to the pK_a of the primary amino group and the buffering effect of the relatively high concentration of L-arginine, a pH of 9 was used for all the excipient experiments to ensure consistency. While this pH is atypical for IEX chromatography, adjustment of the pH to a value closer to the isoelectric point of the adsorbed species helps to promote desorption even in difficult-to-elute systems like the salt-tolerant STAR AX HyperCel (Appendix C).

Although the data in Figure 4.13 are limited to protein concentrations below about 60 mg/mL, extrapolation of these lines down to 1 M sodium chloride suggests that phase separation would still occur following desorption since the local protein concentrations would still be about 300-400 mg/mL for polymer-derivatized and cellulosic absorbents. However, the pronounced shift in the boundaries suggests that

the addition of excipients can still assist in reducing protein association within the pores following elution.

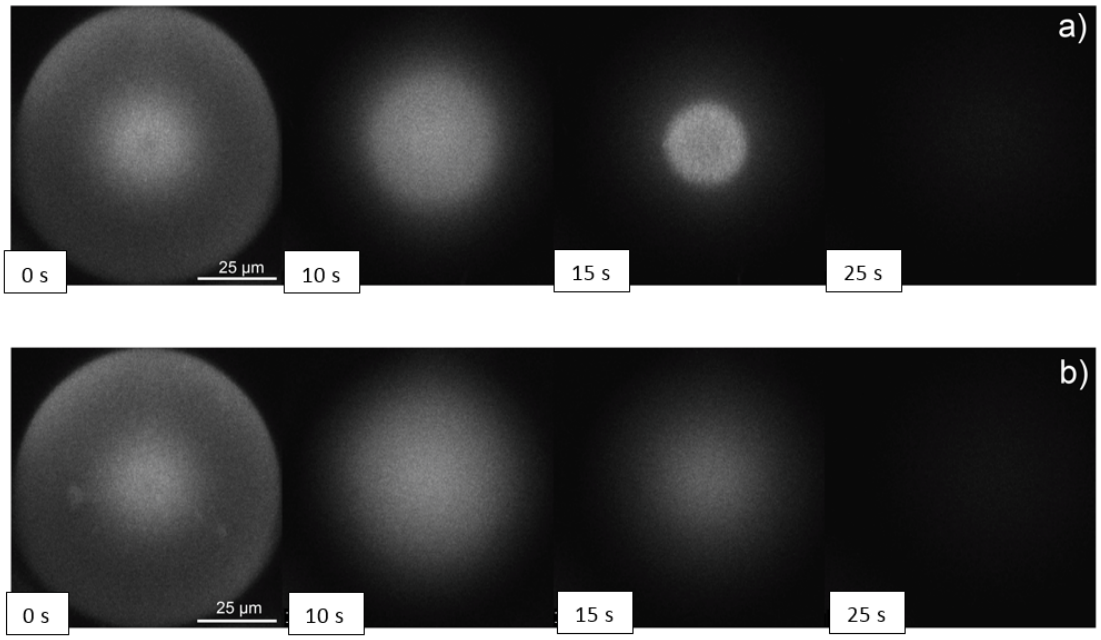

Figure 4.14 Elution of DyLight 650-labeled lysozyme from SP Sepharose FF (a) without the use of excipient at pH 9 and (b) with 500 mM L-arginine at pH 9. Loading was performed using a recirculating stream of protein for 45 minutes and the particles were then washed with equilibration buffer for 5 minutes before a step change to the elution condition. Imaging was carried out until no additional decrease in fluorescence was observed.

This conjecture was tested by confocal microscopy observations similar to those shown in Figure 4.12. Figure 4.14 shows time-series images for elution of DyLight-650-labeled lysozyme from SP FF with and without the inclusion of 500 mM L-arginine at pH 9. The L-arginine case shows diffuse edges similar to those without excipient at pH 7 (Figure 4.12), as would be expected for simple diffusive transport.

The shrinking-core profile seen at pH 9 without excipient is presumably due to phase separation allowed by the lower net charge of lysozyme at the higher pH. The addition of 500 mM L-arginine completely eliminates this effect, even though the pH remains at 9 in both cases.

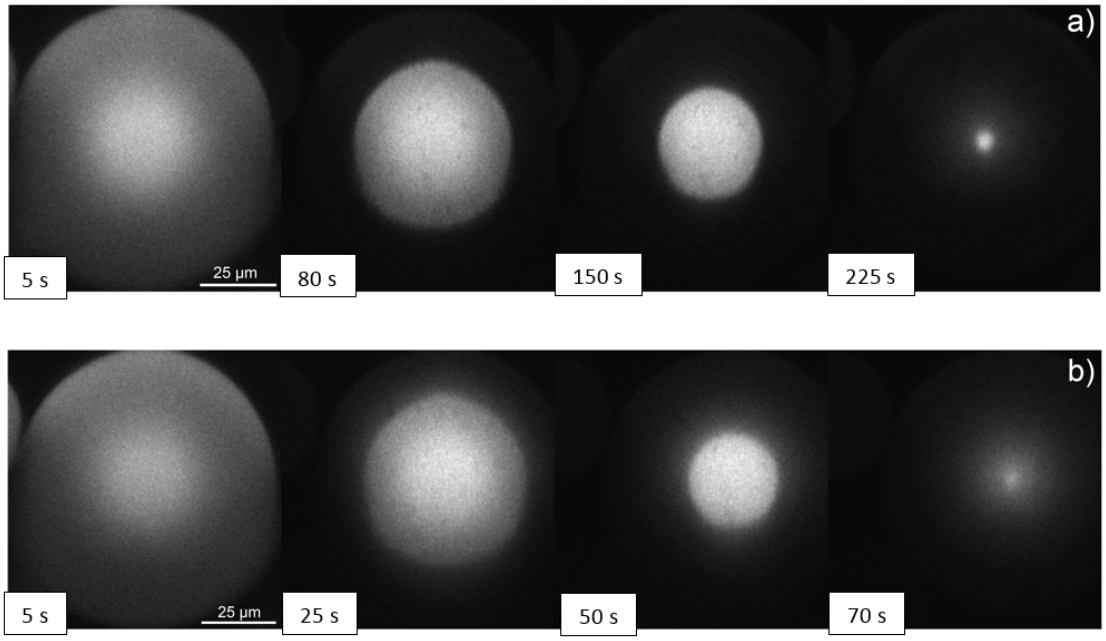

Figure 4.15 Elution of DyLight 650-labeled lysozyme from SP Sepharose XL (a) without the use of excipient at pH 9 and (b) with 500 mM L-arginine at pH 9. Loading was performed using a recirculating stream of protein for 45 minutes and the particles were then washed with equilibration buffer for 5 minutes before a step change to the elution condition. Imaging was carried out until no additional decrease in fluorescence was observed.

Figure 4.15 shows time-series images for elution of DyLight-650-labeled lysozyme from SP XL with and without the inclusion of 500 mM L-arginine at pH 9. Both cases display a shrinking-core profile during elution. While elution without the

use of L-arginine at both pH 7 (Figure 4.12) and pH 9 shows a very sharp front bounding a high-intensity core, a more diffuse front is observed around the periphery for elution with L-arginine.

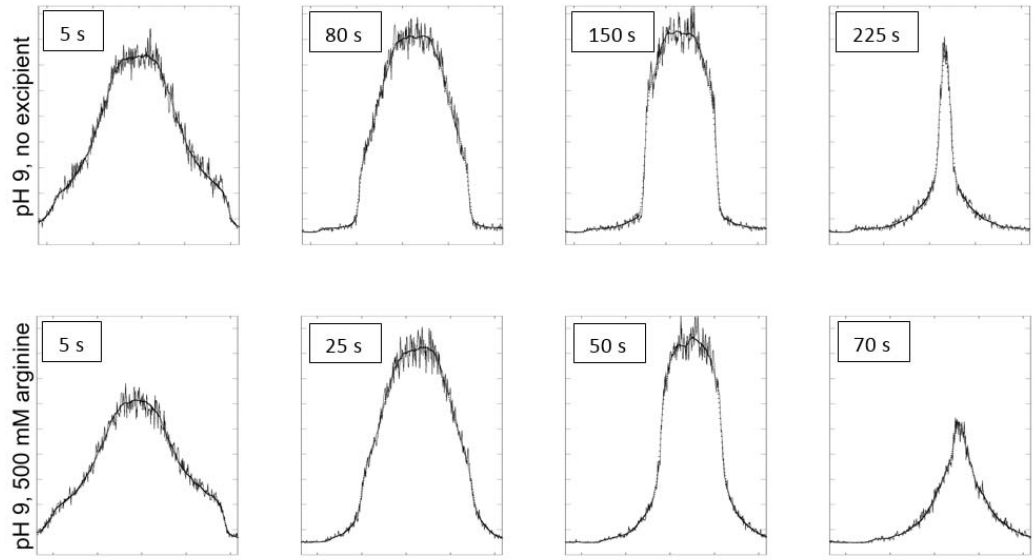

Figure 4.16 Normalized intensity profiles during elution of DyLight 650-labeled lysozyme from SP Sepharose XL without the use of excipient (top) and with 500 mM L-arginine (bottom) at pH 9.

Figure 4.16 shows radial intensity profiles during lysozyme elution from SP XL with no excipient and with 500 mM L-arginine at pH 9, all normalized to the same relative intensity scale. Comparison of the third panel for each case (105 seconds in the excipient-free case and 50 seconds in the L-arginine case) shows a broader intensity "peak" and a wider baseline in the L-arginine case, indicative of a more diffuse area around the sharp front. Qualitatively, this is the only indication that the use of the excipient is aiding in the elution of lysozyme by providing additional

protein stabilization and resistance to association. However, a very large difference is seen in the time scales of elution for each case. While elution at pH 9 and pH 7 takes approximately 250 seconds and approximately 160 seconds for completion respectively, elution with the use of L-arginine is complete after about 80 seconds, about half of what was observed for the base case of pH 7 and no excipient.

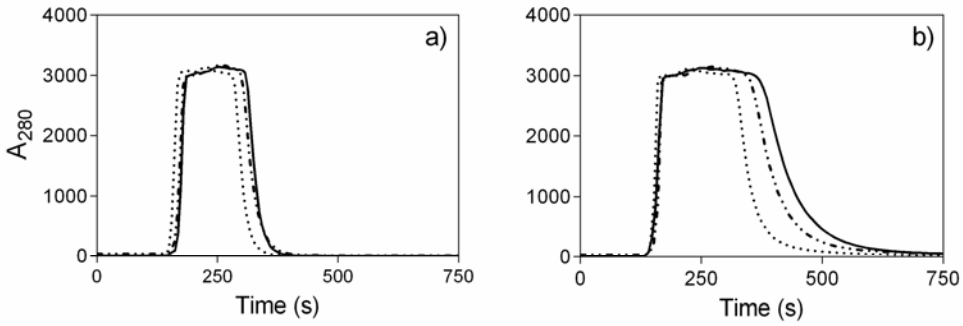

Figure 4.17 Lysozyme elution profiles on (a) SP Sepharose FF and (b) SP Sepharose XL using a 1 M NaCl step elution at pH 9 without the use of an excipient (——), with 500 mM trehalose (–··–··) and with 500 mM L-arginine (·····). Loadings in all cases were to 60% of the total DBC at 120 cm/hr.

A practical test of the potential benefit of using an excipient during elution for a system such as that of lysozyme is to perform column elution experiments directly. Figure 4.17 shows lysozyme step elution experiments conducted in the presence of 1 M NaCl and 500 mM trehalose or L-arginine at pH 9 on SP FF and XL. Conditions such as the loading and flow rate were kept the same in each case as those in the prior column elution experiments. Apparent elution diffusivities as well as the pool volumes needed for near-complete elution are shown in Table 4.5. While excipients had little to no effect on apparent elution diffusivities or volumes for SP FF, apparent

diffusivities were increased and elution volumes were significantly reduced for SP XL, consistent with the presence of a significant phase-separation effect in this system in the absence of excipient.

Condition	SP Sepharose FF		SP Sepharose XL	
	Elution diffusivity, D_e (10^{-7} cm^2/s)	Column volumes required for elution (to 100 mAU)	Elution diffusivity, D_e (10^{-8} cm^2/s)	Column volumes required for elution (to 100 mAU)
pH 7, no excipient	1.5 ± 0.042	3.1	6.5 ± 0.28	4.9
pH 9, no excipient	1.5 ± 0.35	3.1	3.3 ± 0.045	7.1
pH 9, 500 mM trehalose	1.1 ± 0.081	3.1	4.0 ± 0.086	6.3
pH 9, 500 mM L-arginine	1.6 ± 0.29	2.6	6.7 ± 0.39	4.8

Table 4.5 Elution characteristics for lysozyme on SP Sepharose materials (60% loading factor) with and without the use of excipients.

The confocal data in Figures 4.15 and 4.16 show that the addition of L-arginine is not sufficient to fully eliminate phase separation during elution in stationary phases with constricted pore volumes, as the sharp intensity front was not eliminated. However, it still provides a significant benefit in the reduction of pool volumes as observed in the column elution results, presumably because of a significant shift in the distribution of protein between dense and solution phases.

4.4 Conclusions

Protein elution is a critical step in preparative separations that merits similar attention to that of its counterpart, protein uptake. As with the design of protein loading, the ease and rate of elution depend on the structure of the adsorbent material and the operating conditions. In the absence of anomalous effects, elution appears to be controlled simply by pore diffusion out of individual particles. However, our results show that for some systems elution can also depend very strongly on the physicochemical properties of the proteins themselves. Slow elution rates and larger pool volumes are undesirable for bind-and-elute separations, but by tailoring elution schemes for certain systems, such as modifying elution operating conditions or utilizing protein stabilizing agents, the overall processing step can be improved greatly.

The results presented in this chapter show that polymer-derivatized and cellulosic cation-exchange adsorbents may present poorer elution performance than materials with higher accessible intraparticle porosities, such as SP FF. While these materials with higher binding capacities and uptake rates than traditional macroporous resins do have benefits with respect to efficiency and overall throughput, there is a tradeoff between optimization of uptake and elution. The results reported here may aid in elucidating poor elution performance and may offer pathways to ameliorating such issues. In addition to the use of excipients explored in this work, elution using pH steps with lower salt concentrations may help to reduce the possibility of phase separation such as that inferred here for lysozyme. Other approaches may include reducing column loadings and using shallower salt gradients. Such strategies can be assessed during stationary-phase selection to keep necessary downstream steps and processing time to a minimum.

Chapter 5

PROTEIN ADSORPTION ON DEXTRAN-DERIVATIZED SURFACES

5.1 Introduction

Taking a molecular approach to the investigation of protein adsorption and transport within systems resembling those encountered in downstream processing is the final echelon in building our understanding of these processes. Of course, both molecular theory and single-molecule experiments are widely used, yet they are rarely applied to chromatographic stationary phases, as high-throughput screening and industrial scaling normally take precedence. To understand the basic nature of these phenomena can clearly aid our understanding of more macroscopic operations. The aim of this chapter is to provide means for developing this understanding, and how it relates to the functional characterization described earlier in this dissertation. This chapter can be broken down into two distinct parts: a theoretical study of competitive adsorption on charged surfaces with and without dextran modification, and an exploration of visualizing single molecules adsorbing onto such surfaces at commonly utilized conditions for IEX by using advanced super-resolution microscopic techniques.

The molecular modeling presented was developed in a collaboration with Igal Szleifer and Claudio Narambuena at Northwestern University, and is still in progress (Narambuena et al., in preparation). The molecular theoretical approach used in previous work to study adsorption on charged surfaces (Fang and Szleifer, 2001) as well as lysozyme adsorption on thin films (Narambuena et al., 2015) was employed

here in an effort to understand the competitive adsorption between lysozyme and cytochrome c on charged surfaces with and without dextran modification. Similar studies of competitive adsorption on charged, planar surfaces (Fang and Szleifer, 2003; Gong and Szleifer, 2004) and single-component adsorption within polymer layers (Carignano and Szleifer, 2002; Szleifer, 1997) have been conducted, but we wish to extend that to understanding competitive adsorption within surface layers that mimic the inside of a pore within stationary phases such as Sepharose XL or Capto, which contain functionalized dextran extenders. Findings from these investigations can potentially aid in optimizing a separation process early in the planning stage.

As stated earlier in this dissertation, the use of advanced imaging techniques can provide important physical insights into how protein is adsorbed and transported. These empirical observations have been performed on relatively macroscopic scales when compared to the single-molecule resolution one can obtain with super-resolution microscopy. One such technique, total internal reflection fluorescence microcopy, or TIRFM, allows observation of a very thin layer above a surface (typically a glass coverslip) of approximately 100 nm. An incident laser is angled so that it is totally reflected back though the substrate due to the differences in the refractive index of the substrate and the medium beyond the surface boundary. This effect causes an evanescent wave to form just above the boundary that may excite fluorophores within the focal volume for fluorescent imaging on a confocal microscope. Previous studies using this technique have reported observation of intermolecular interactions (Isailovic et al., 2007), adsorption kinetics (Kwok et al., 2007) and real-time dynamics (Kang et al., 2001) and even what implications these have on capillary liquid chromatography (Kang and Yeung, 2002). TIRFM imaging has also been employed to observed protein

movement within small, reversed-phase chromatographic particles fixed to a substrate (Cooper et al., 2013). Fluorescence correlation spectroscopy (FCS) is often coupled with this type of imaging in order to further resolve the dynamic interactions (Cooper and Harris, 2014; Daniels et al., 2012; Ries et al., 2008), but requires the microscope to be outfitted with a correlator. We aim to extend these applications to an environment in which protein may bind and diffuse in a covalently-attached dextran surface layer in order to represent the interior pore walls in materials such as Sepharose XL and Capto. By obtaining both visuals of the adsorption events as well as quantitative data via particle-tracking algorithms, we can relate the observed states to interpretation of protein mobility on a more macroscopic scale.

5.2 Materials and Methods

5.2.1 Buffers, Proteins and Stationary Phases

Monobasic sodium phosphate (NaH_2PO_4), sodium acetate and citric acid were purchased from Fisher Scientific (Fair Lawn, NJ) and used to prepare 10 mM buffer solutions at pH 7, pH 4 and pH 3, respectively. Addition of NaCl was used to create buffers at 20, 100, 250 and 1000 mM TIS. No NaCl was added to the 10 mM citric acid buffer at pH 3, leaving the solution TIS to be 4 mM.

Solutions of hen egg white lysozyme and cytochrome c from bovine heart (C3131, lot: SLBB6437V) were prepared as described in Chapter 3 from lyophilized proteins purchased from Sigma-Aldrich (St. Louis, MO). Stock solutions were prepared to target protein concentrations of 4-6 mg/mL and were stored at 4 °C. The stationary phases for binary adsorption studies were SP Sepharose FF and SP

Sepharose XL, which have previously been characterized, structurally and functionally, in Chapters 2 and 3, respectively.

Lysozyme for TIRF imaging was conjugated with DyLight 550 (62263) NHS Ester dye in a 3-4% labeling ratio following protocols supplied by the manufacturer (Thermo Scientific). Initial fluorescently-labeled protein concentrations were determined using UV spectrophotometry on a Thermo Scientific NanoDrop 2000. Serial dilutions of the labeled stock were performed to achieve a calculated labeled protein concentration of 10 pM for each TIS of buffer (20, 100 and 250 mM TIS); the labeling ratio from initial conjugation to the dye was kept the same throughout. Solutions of BSA at the appropriate TIS were used in half of the stocks to achieve a final concentration of 1.5 μM BSA, in addition to the 10 pM of DyLight 550-labeled lysozyme, to act as a blocker of non-specific adsorption sites on the dextranized surfaces.

5.2.2 Binary Adsorption Isotherms

A series of protein dilutions were prepared in 1.6 mL Eppendorf tubes at concentrations ranging from 100% to 6.25% of that of the protein stock; each dilution used the same buffer in which the protein solution was prepared. Relatively high concentrations (4-5 mg/mL for each protein) were chosen to ensure that the plateau regions could be studied so that maximum static capacities could be determined. Measurements were made for both single-component systems and binary mixtures of lysozyme and cytochrome c in a 50:50 mass ratio. Small amounts of resin were dispensed into each tube after the gravity-settled height of the resin and the additional buffer volume added in each capillary tube were recorded. Samples were allowed to equilibrate by rotation for at least 72-96 hours. Concentrations were again measured in

the 24 hours following the initial reading to ensure that each sample had been adsorbed to completion. Final protein concentrations were determined by absorbance measurements at 280 and 405 nm. The extinction coefficients of lysozyme and cytochrome c at 280 nm (ε_{280}) are 2.64 cm^2/mg (see Table 3.1) and 1.96 cm^2/mg (Chang and Lenhoff, 1998), respectively. The UV absorbance at 405 nm is due solely to the heme group of cytochrome c, which has an extinction coefficient of 8.23 cm^2/mg (Xu and Lenhoff, 2009) at 405 nm (ε_{405}), so the cytochrome c concentration could be determined straightforwardly. Lysozyme concentrations in the supernatant could then be found by difference using the UV absorbance at 280 nm (and using a 1 cm corrected path length)

$$C_{lys} = \frac{(Abs^{280} - Abs^{405})\left(\varepsilon_{cyc}^{280} / \varepsilon_{cyc}^{405}\right)}{\varepsilon_{lys}^{280}} \tag{5.1}$$

The amount of protein adsorbed at the end of each experiment could then be determined by mass balance from

$$q_i = \frac{V_m}{V}(C_{0,i} - C_i) \tag{5.2}$$

where $C_{0,i}$ is the initial protein concentration of a given species, and C_i is the final protein concentration of that species in the supernatant.

5.2.3 Preparation of Dextran-Derivatized Surface

Glass coverslips (no. 1.5, 22 x 22 mm) were used as substrates for the dextran-derivatized surfaces prepared for TIRF microscopic imaging. Silicon wafers were also used to characterize the surfaces through methods that were difficult to achieve on non-reflective surfaces like glass, such as ellipsometry. The same dextranization

method was performed on both types of substrate to ensure consistency in the protocol.

5.2.3.1 APTES Surface Preparation

Surfaces were treated following methods described in Miksa et al. (2006) and Vandenberg et al. (1991). Substrates were first etched by immersion in piranha solution (3:1 v/v sulfuric acid:hydrogen peroxide) for 20 minutes at 80 °C. Hydrogen peroxide was stored at 4 °C and allowed to equilibrate to room temperature before preparation of the piranha solution. Etched substrates were then washed with DI water at least 3 times and allowed to sonicate in DI water for 30 minutes. A solution of 1% (v/v) 3-aminopropyltriethoxysilane (APTES) was prepared in pure acetone. Substrates were rinsed with pure acetone 3 times and allowed to react with the 1% APTES solution on an orbital shaker for 1.5 hours. Then, substrates were again washed with acetone, followed by a thorough rinsing of DI water, and sonication in DI water for an additional 30 minutes. At this point, substrates were cleaned and dried with a pure nitrogen stream and were ready for dextran attachment.

5.2.3.2 Dextran Immobilization

Solutions of oxidized dextran were prepared previously following methods detailed in Miksa et al. (2006). Dextran from *Leuconostoc* spp. with a mean molecular weight of 40 kDa (68084) was obtained from Sigma-Aldrich (St. Louis, MO). A 2 mg/mL solution was prepared by dissolving 50 mg in 25 mL of DI water. 148 mg of sodium periodate ($NaIO_4$) was dissolved in 25 mL of DI water as well. The two solutions were slowly mixed using a magnetic stir plate and left to react for 1.5 hours while protected from light with aluminum foil. The oxidized dextran solution was

then transferred to regenerated cellulose dialysis tubing with a molecular weight cutoff of 6-8 kDa and allowed to dialyze in DI water for at least 24 hours to remove excess sodium periodate.

The solution was then mixed with 65 mg of sodium cyanoborohydride ($NaBH_3CN$) and filtered with a 0.22 μm sterile syringe filter. The presence of sodium cyanoborohydride with oxidized dextran and the APTES treated substrates initiates a reductive amination reaction that covalently attaches the dextran to the substrate. Cleaned substrates (with DI water and pure nitrogen) were placed on an orbital shaker with the reaction mixture overnight (at least 18 hours), while being protected from light with aluminum foil. Substrates were again washed with DI water, sonicated for 30 minutes to remove loosely physisorbed reactants and dried with pure nitrogen. Dextranized surfaces were stored under vacuum at room temperature.

5.2.3.3 Dextran Functionalization via Vinyl Sulfonic Acid

Some dextranized surfaces underwent an additional step to apply sulfonate moieties to the dextran layer using methods similar to those used to functionalize some polymer-modified resins. Previous methods using sodium metabisulfite have been used to functionalize stationary phases for CEX (Berg et al., 2002; Stone and Carta, 2007), but the use of vinyl sulfonic acid (VSA) has been shown to provide a more robust and higher capacity adsorbent, while also having a much simpler protocol (Axen et al., 2008). Dextran-derivatized surfaces were washed with 25 wt. % vinyl sulfonic acid solution (278416, Sigma-Aldrich) and immersed in a staining dish containing 135 mL of VSA solution and 105 mL of 50 wt. % NaOH solution at 45 ºC. The staining dish was partially submerged in a water bath to maintain temperature. A coverslip rack was used to allow up to 24 surfaces to be treated at once by vertically

orienting them within the staining dish. The surfaces were treated with the VSA/NaOH solution for 6 hours with intermittent agitation to the bath. Surfaces were then removed, rinsed with DI water, sonicated in DI water and dried with pure nitrogen before being stored under vacuum at room temperature.

5.2.4 Total Internal Reflection Fluorescence Microscopy

Total internal reflection fluorescence microscopy (TIRFM) was used in order to observe the thin region above a polymer derivatized substrate immersed in solution where surface interactions occur at the liquid-solid interface. A schematic representation of the TIRFM setup can be seen in Figure 5.1. TIRFM imaging was performed on a custom-built TIRF system assembled upon a Zeiss Axio Observer A1 body. The system uses four diode lasers used to excite fluorescence: 50mW Coherent Cube at 404 nm, 30 mW Coherent Sapphire at 488 nm, 50mW Coherent Sapphire at 561 nm, and a 50 mW Coherent Cube at 642 nm. For a majority of this work, only the 50 mW Coherent Sapphire at 561 nm was utilized. The laser intensity was modulated by an acousto-optic modulator (MDS4C, AA Opto-Electronic, Orsay, France) to 17.6 dBm. The laser lines were expanded 5x and diverted to the objective back aperture with a quad dichroic filter (Semrock Inc., Di01-R405/488/561/635. A movable achromatic doublet lens was used to focus the expanded beam onto the back focal plane of a 100x NA 1.46 Zeiss Plan Apo objective.

The total internal reflection condition was achieved by translating the lens to the periphery of the back aperture such that the emerging beam exceeds the critical angle at which total internal reflection occurs. As the light travels from the optically denser medium (glass coverslip) to a less optically dense medium (buffer), the laser

beam cannot pass the boundary and is totally reflected back through the substrate medium. The critical angle of the interface may be determined by Snell's law

$$n_1 \sin\theta_1 = n_2 \sin\theta_2 \quad (5.3)$$

where θ_2 equals 90° and n_1 and n_2 are the refractive indices of glass and water (or buffer), respectively (n_1 = 1.51 and n_2 = 1.33). Equation 5.3 can then be expressed as

$$\theta_{crit} = \sin^{-1} \frac{n_2}{n_1} \quad (5.4)$$

The critical angle of incidence for the system in which total internal reflection occurs is therefore 61.7°.

An evanescent wave is formed beyond the boundary surface that results from the total internal reflection phenomenon, and is responsible for excitation of the fluorophores within the focal volume of the TIRF imaging, which is approximately 100 nm above the surface. Excitation light is removed by a quad notch filter (Semrock Inc., FF01-446/523/600/677-25). The field of view is magnified 2x after the tube lens and projected onto an electron multiplying CCD camera (ProEM512, Princeton Instruments). Focus in the z-direction was then adjusted on the scope in order to obtain a highly resolved images which were acquired with software provided by the camera manufacturer.

The sample position was translated using a Physik Instrument C867 stage controller. An acrylic flow cell was used to situate the surface on the stage above the microscope and allowed different buffer and protein conditions to be flowed over the surface by drawing these solutions using a syringe. The flow cell accommodates a 22 x 22 mm coverslip that is placed with the functionalized surface facing upwards towards the inner chamber of the cell, and is separated from the top acrylic piece of the apparatus by a 0.03125 inch thick silicone spacer.

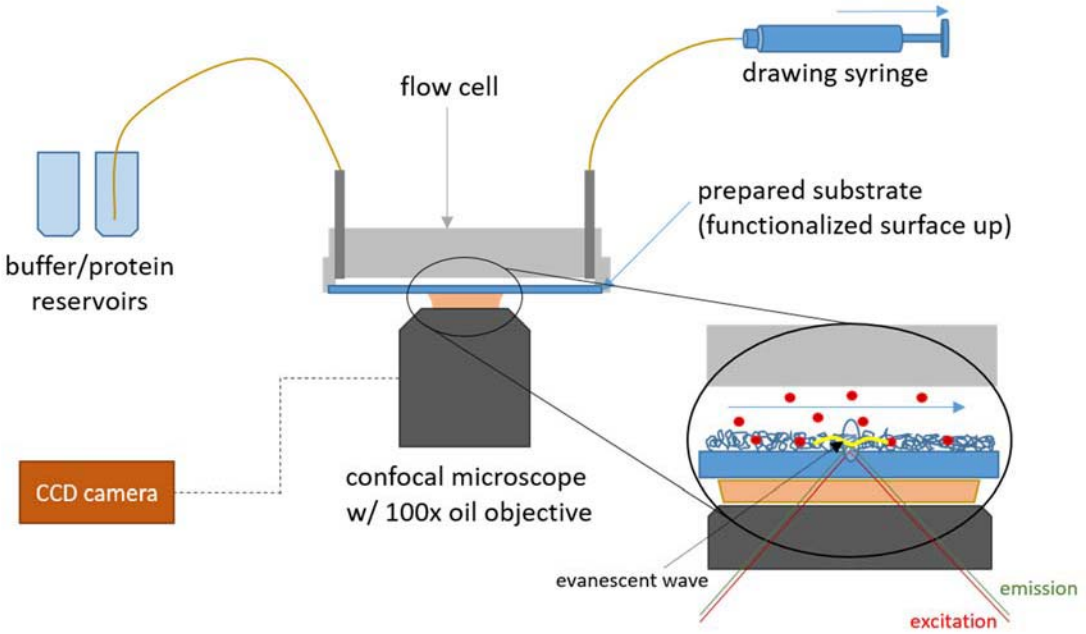

Figure 5.1 Schematic representation of total internal reflection fluorescence microscopy setup. Dextranized 22x22 mm no. 1.5 glass coverslips were placed functionalized surface up inside the flow cell apparatus. Buffer and protein mixtures were flowed over the surface using a drawing syringe. The incident laser used to excite fluorophores at the liquid-surface interface was adjusted to the critical angle to allow total internal reflection, producing an evanescent wave that excites a focal volume approximately 100 nm above the surface. Focus of the 100x objective (with an additional 2x magnification) was adjusted to observe adsorption events at the dextranized surface.

5.3 Results and Discussion

5.3.1 Preferential Adsorption of Lysozyme and Cytochrome C on Non-Modified versus Modified Surfaces

The results presented in the section are compiled from collaborative work with Igal Szleifer and Claudio Narambuena at Northwestern University. The experimental data were acquired as part of the work towards this dissertation to complement the molecular and thermodynamic modeling performed by Dr. Narambuena.

5.3.1.1 Theoretical Molecular Modeling

In IEX chromatography, the surface-protein electrostatic interaction is the driving force for adsorption, but the protein excluded volume also has significance. Since lysozyme and cytochrome c have comparable sizes, it is expected that the protein with the higher net charge would adsorb preferentially. The net charge depends on the ionization state of the titratable residues, which in turn depends on the acid-base equilibrium of their functional groups. It also depends on the electrostatic environment (salt concentration, charged ligands) and local concentration of protons (H^+). The net charge as a function of pH for lysozyme and cytochrome c shown in Figure 5.2 was calculated based on the charges of the titratable residues. The net charges are mostly positive, with lysozyme predicted to have a higher net charge at higher pH values. However, below pH 3 cytochrome c is predicted to have a higher positive charge than lysozyme. Cytochrome c also shows a steeper charge loss with increasing pH. The isoelectric points resulting from these predicted curves are in good agreement with empirical values.

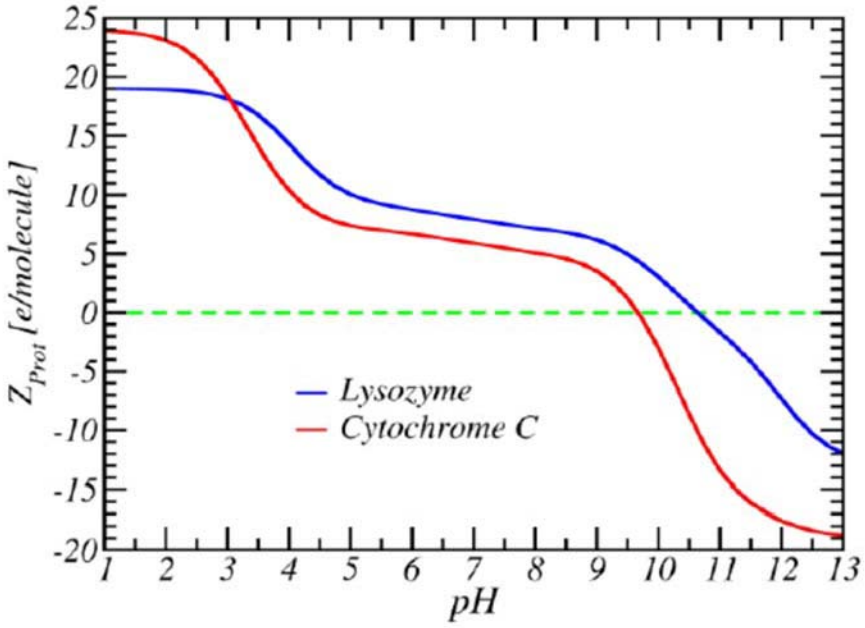

Figure 5.2 Net charge (Z) of lysozyme and cytochrome c as a function of solution pH determined by charge of their titratable residues.

A generalized molecular theoretical approach was employed that has been used previously to study competitive adsorption on charged surfaces (Fang and Szleifer, 2001) and lysozyme adsorption in pH-responsive thin-films (Narambuena et al., 2015). The minimization of the total free energy of the charged surface in contact with a solution of proteins provides the local molar concentration of the molecular species. The surface coverage of protein on a charged surface as a function of distance from the surface (z) is defined as

$$\Gamma_i = M_{w,i} \int_0^\infty (C_i(z) - C_i^{bulk})\, dz \qquad (5.5)$$

where $M_{w,i}$ is the molar mass of the adsorbing species. This gives the total mass per unit area of proteins located on the charged surface and in the interfacial region.

Figures 5.3 and 5.4 show the theoretical modeling results of the competitive adsorption on a charged surface without and with dextran extenders, respectively, as a function of pH. The two scenarios are meant to represent competitive adsorption on a non-modified stationary phase, such as SP Sepharose FF, and one with dextran modification, such as SP Sepharose XL. Results for the non-modified surface show how changes in surface charge density (σ_{surf}) (Figure 5.3a) and salt concentration (Figure 5.3b) affect the surface coverage of lysozyme and cytochrome c. The lysozyme is preferentially adsorbed on the surface in a broad range of pH values (from approximately pH 4 to pH 10), but close to pH 4, cytochrome c adsorption begins to increase as pH decreases. The cytochrome c adsorption is accompanied by a decrease in lysozyme adsorption, suggesting that the lysozyme is displaced by cytochrome c. The pH value at which both proteins have equivalent surface coverages is called the critical pH of preferential adsorption, or pH_c, and indicates where this transition between lysozyme and cytochrome c adsorption takes place. As surface charge density decreases or solution salt concentrations increases, this pH_c value shifts to more acidic values.

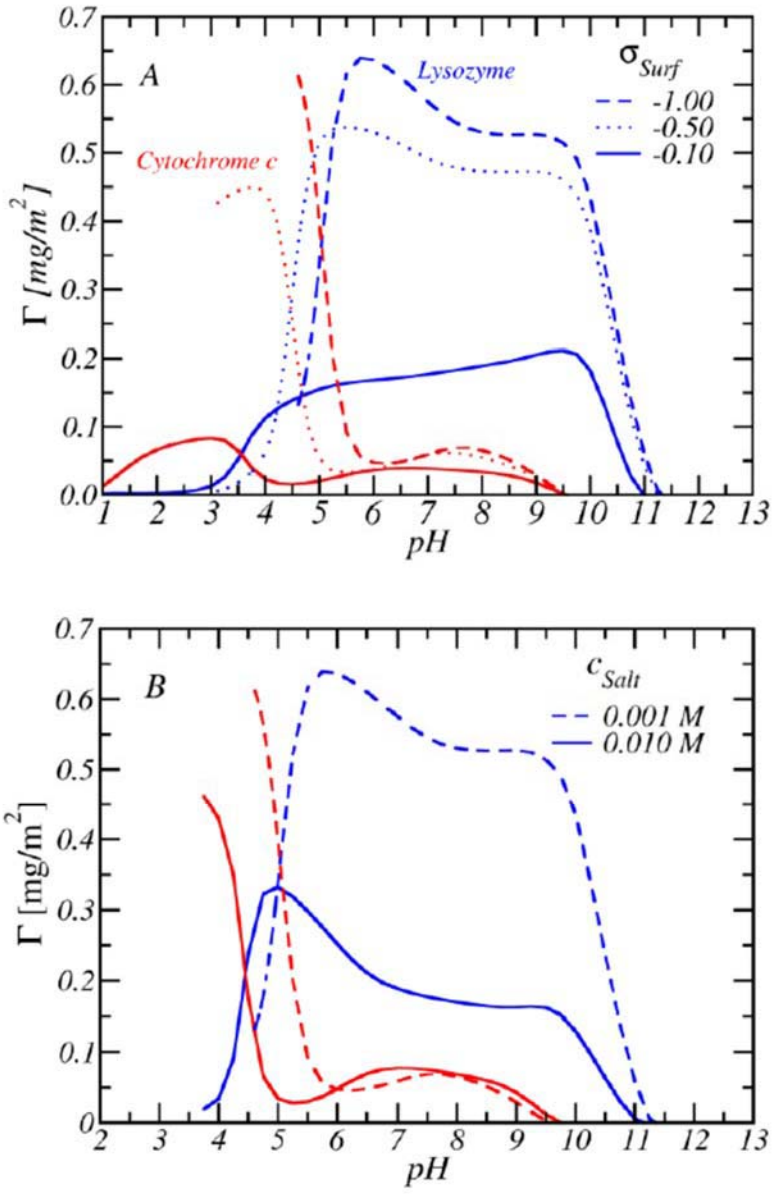

Figure 5.3 Surface coverages (Γ) of lysozyme and cytochrome c for an equimolar mixture ($c_{lys} = c_{cyc} = 50$ μM) on charged surfaces for (a) different charge densities of the surface at a solution salt concentration of 1 mM and (b) different solution salt concentrations for a surface charge density of -1 e/nm^2.

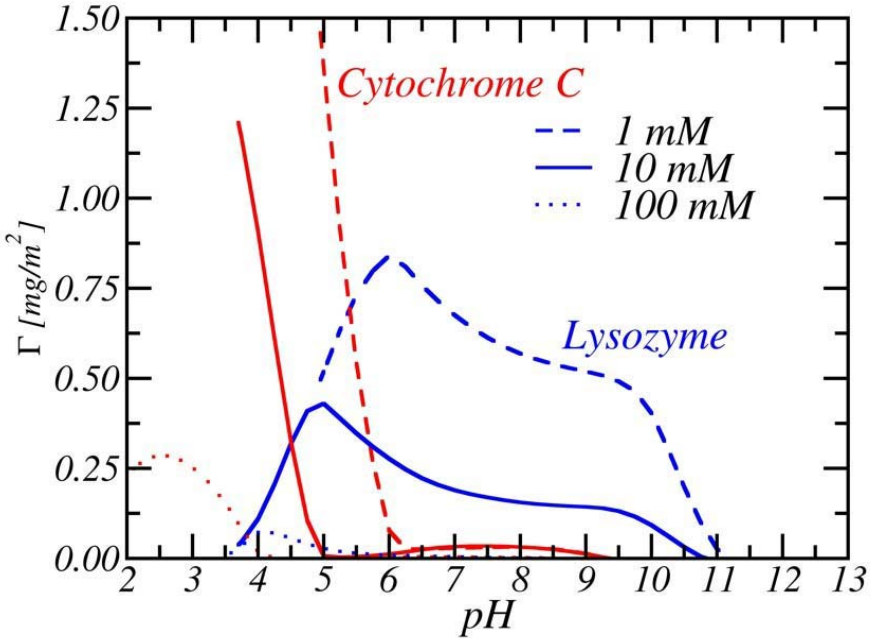

Figure 5.4 Surface coverages (Γ) of lysozyme and cytochrome c for an equimolar mixture ($c_{lys} = c_{cyc} = 50$ μM) on charged surfaces under different solution salt concentrations for a surface charge density of -2.7 *e*/nm^2 and a dextran density of 1 molecule (5 kDa) per nm^2.

Figure 5.4 shows the theoretical modeling results for a dextran-derivatized surface with a surface charge density of -2.7 e/nm^2 at different salt concentrations from 1 to 100 mM TIS. The dextran density was set to 1 molecule per nm^2 and a 5 kDa extender was used as a model. The surface charge density was selected to be -2.7 e/nm^2 by converting the manufacturer-reported ionic capacity using the phase ratio of SP Sepharose FF (DePhillips and Lenhoff, 2001), which gives a charge density value of approximately -2.2 to 3 e/nm^2. The preferential adsorption of cytochrome c is much more pronounced in this system, especially at the 1 mM TIS condition, for which the critical pH has a value of approximately 5.5 to 6. The decrease in overall adsorption is

also much more apparent at higher ionic strength values than on the non-modified surface, which is in agreement with single-component adsorption studies presented in Chapter 3. This is an effect of the salt screening of attractive electrostatic interactions between the surface and the proteins as well as the salt concentration modifying the preferential adsorption of proteins on the surface. The increase in salt concentration encourages preferential lysozyme adsorption in both the non-modified and dextran-modified cases.

5.3.1.2 Binary Adsorption Isotherms

A direct quantitative comparison of the molecular theory predictions with experimental results is a demanding task due to the complexity of controlling certain variables in this system. However, a qualitative comparison for the preferential adsorption under different conditions may be carried out where a focus is placed on the relative adsorbed amounts, rather than the absolute values. The pH and salt concentration conditions were varied in order to observe regimes where lysozyme is preferentially adsorbed, where the coadsorption of both proteins occurs, and, finally, where cytochrome c replaces the lysozyme on the charged surface.

5.3.1.2.1 SP Sepharose FF

The simultaneous adsorption of lysozyme and cytochrome c on SP Sepharose FF for pH values of 7, 4 and 3 are shown in Figure 5.5. The preferential adsorption of lysozyme on SP Sepharose FF at neutral pH can be clearly seen in Figure 5.5a. These data are supplemented by previous measurements on this system (Xu and Lenhoff, 2009). Adsorbed concentrations here are described in terms of mass of protein per unit of hydrated particle volume, as opposed to mass per unit surface area, as this is

somewhat difficult to determine without certain generalizations and assumptions of the pore structure and protein accessibility. The dominance of lysozyme adsorption presents a static binding capacity of approximately 187 mg/mL. Cytochrome c, however, only reaches an adsorbed capacity of only about 30% of the corresponding lysozyme adsorbed concentration.

Figure 5.5b (pH 4) displays a significant shift in the behavior where cytochrome c adsorption becomes dominant over lysozyme in the system. At this condition, lysozyme displays a binding capacity of 68 mg/mL compared to a binding capacity of 109 mg/mL for cytochrome c. Under these solution conditions, the critical pH value has been crossed, resulting in a shift to cytochrome c adsorption dominance. The increased coadsorption of protein appears to decrease the total amount of protein adsorbed by mass, as lysozyme was adsorbed at much higher quantities at higher pH. This could also be due to an overall decrease in affinity for protein at pH values lower than the critical pH, as seen in Figure 5.3. This trend is further amplified when the pH value is brought down to 3 (Figure 5.5c). Here, little lysozyme is left adsorbed and cytochrome c presents an even higher capacity than at pH 4 and 7, with a binding capacity of about 137 mg/mL. At this point, there is nearly total displacement of lysozyme by cytochrome c within the adsorbent, as the bound lysozyme concentrations measured do not exceed 25 mg/mL. The complete shift in the preferential adsorption results in an overall lower protein capacity when the pH is reduced from 7 to 4, but this could be due to partial protein unfolding or protonation of the ligand functional groups as the acidic environment is increased.

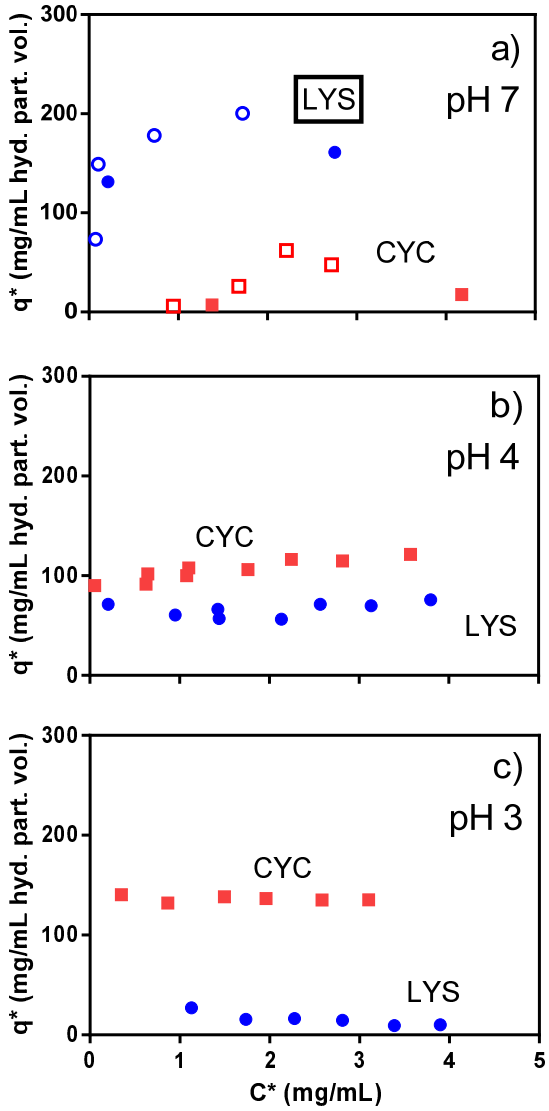

Figure 5.5 Binary adsorption isotherms of lysozyme and cytochrome c on SP Sepharose FF at (a) 20 mM TIS and pH 7, (b) 20 mM TIS and pH 4 and (c) 4 mM TIS and pH 3. Buffers at pH 7, 4 and 3 were prepared using 10 mM monobasic sodium phosphate, sodium acetate and citric acid, respectively. Initial total protein concentrations for each point were 50/50 lys/cyc by mass. Adsorbed and supernatant concentrations correspond to individual protein concentrations, not total concentration. Open symbols on top plot are from previous results on this system (Xu and Lenhoff, 2009).

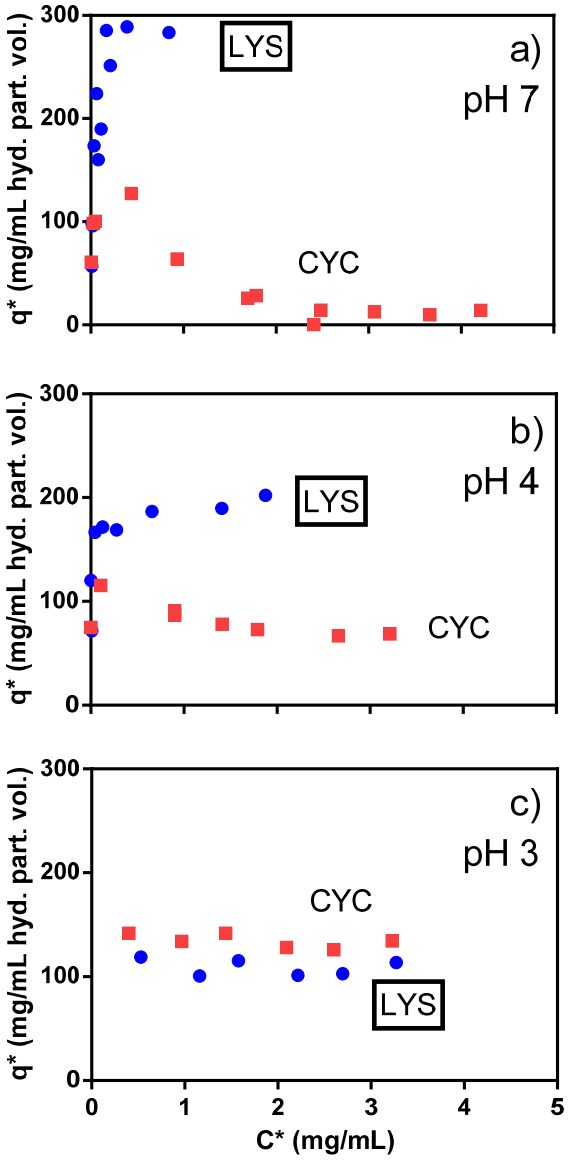

Figure 5.6 Binary adsorption isotherms of lysozyme and cytochrome c on SP Sepharose XL at (a) 20 mM TIS and pH 7, (b) 20 mM TIS and pH 4 and (c) 4 mM TIS and pH 3. Buffers at pH 7, 4 and 3 were prepared using 10 mM monobasic sodium phosphate, sodium acetate and citric acid, respectively. Initial total protein concentrations for each point were 50/50 lys/cyc by mass. Adsorbed and supernatant concentrations correspond to individual protein concentrations, not total concentration.

5.3.1.2.2 SP Sepharose XL – Effect of Dextran Layer

The simultaneous adsorption of lysozyme and cytochrome c on SP Sepharose XL for pH values of 7, 4 and 3 are shown in Figures 5.6. Much like binary adsorption on SP Sepharose FF at neutral pH, lysozyme displays preferential adsorption over cytochrome c, having a binding capacity of approximately 285 mg/mL. One major difference between the two systems is observed: at low overall supernatant concentrations (< 1 mg/mL), within the region where a linear isotherm is present, cytochrome c has a higher binding capacity, exceeding 127 mg/mL, than at the higher supernatant concentrations (> 1 mg/mL) where the adsorbed capacity of cytochrome c becomes negligible. The generally higher amounts of adsorption are probably due to the increased volumetric capacity within a polymer-modified stationary phase over one such as Sepharose FF, as the former allows three-dimensional partitioning. Within the linear region of the isotherm, there exists plenty of space for protein to occupy within the particle, and it is only when the adsorbent approaches full saturation that we see a decrease in the cytochrome c adsorbed concentration as it starts to become displaced by the high concentration of lysozyme in the supernatant.

A much lower capacity for lysozyme is observed when the pH is lowered to 4. The capacity drops from almost 300 mg/mL at neutral pH to 201 mg/mL, while cytochrome c reaches an equilibrium at higher supernatant concentrations at approximately 70 mg/mL. While this is an increase from the value at pH 7, there still exists a peak within the linear isotherm regime where cytochrome c has a higher adsorbed concentration than at higher supernatant concentrations. The reduction to pH 3 finally displays the crossover of preferential adsorption, with cytochrome c binding to a higher capacity than lysozyme. Lysozyme displays a capacity of approximately 110 mg/mL while cytochrome c lies just above with a capacity of approximately 129

mg/mL. The existence of a peak at low supernatant concentration for the less adsorbed species is not prevalent at this condition, but that may be due to the fact that both proteins present similar binding capacities and both proteins have highly rectangular isotherms, possibly due to the lower TIS of the citrate buffer system (4 mM TIS). It is also worth noting that lysozyme still remained adsorbed at this acidic condition, but it had little to no capacity at this same condition in the SP Sepharose FF material.

It is clear that the addition of a dextran layer causes the critical pH for preferential adsorption to shift to more acidic values when compared to the results on SP Sepharose FF, which exhibited more cytochrome c adsorption at pH 4 while SP Sepharose XL did not. This may be because the local environment within the dextran layer is less susceptible to changes in the bulk solution conditions. The local net charge of protein as well as the local pH changes as proteins approach a functionalized surface with no polymer layer (Narambuena et al., in preparation), as shown in Figure 5.7. This effect is caused when the concentration of protein increases close to the surface. The electrostatic environment is modified due to the presence of the adsorbed protein, therefore the electrostatic potential and the local pH profiles are modified self-consistently.

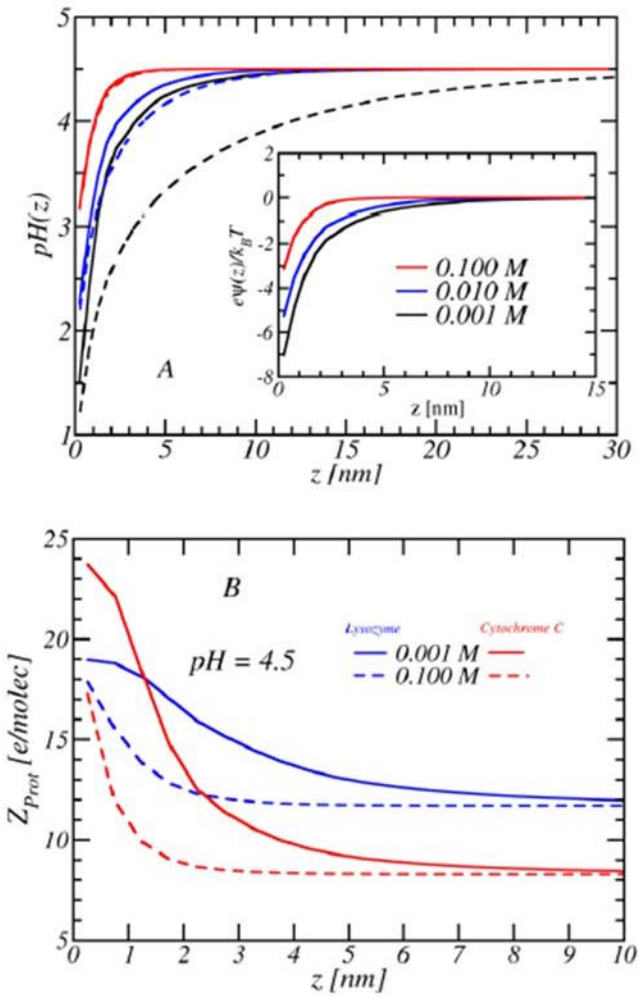

Figure 5.7 (a) Local pH and (b) net charge of protein as a function of distance from a charged surface (with no polymer modification) for a bulk solution pH of 4.5. Different salt concentrations are listed for each plot. Local pH values are shown with (solid) and without (dashed) the presence of protein. Corresponding local electrostatic potentials (inset) at different salt concentrations are shown in (a). The general trend is that local pH decreases and net charge of protein increases as the distance to the surface is reduced.

However, since the dextran layer in Sepharose XL extends out from this surface by approximately 10 to 20 nm (see Chapter 2), protein could become trapped deeper within the grafted polymer layer due to other interactions besides purely electrostatic, such as hydrophobic or repulsive intermolecular interactions (Fang et al., 2005; Sukhishvili and Granick, 1999). Exchange in a polymer-modified adsorbent does not happen as readily as in a conventional material, which exhibits, for the most part, monolayer adsorption. This would account for the lysozyme adsorbed within the Sepharose XL material to be more resistant to a change in the preferential adsorption, and hence, less sensitive to more acidic pH conditions that would cause its displacement by cytochrome c. This shift in the critical pH for the dextran-modified adsorbent could have benefits if an adsorbent material is sought that may retain a particular protein of interest under relatively acidic conditions. Molecular modeling in dextran-derivatized systems is currently ongoing, but the results presented here offer a brief description of the molecular interactions that proteins experience in ion-exchange systems.

5.3.2 Total Internal Reflection Fluorescence Microscopy Imaging of Dextran-Derivatized Surfaces

TIRFM imaging was used to visualize protein adsorption and movement on the molecular level to complement the macroscopic batch and column analyses presented earlier in this dissertation. Even on the single-particle level (CSLM), no individual protein molecules could be discerned, let alone tracked, with only highly concentrated fronts of protein visualized. While parameters determined using a method such as TIRFM may not have macroscopic applicability, a comparison of how proteins behave at different conditions and differently functionalized surfaces provides insight into

how protein would move within a porous environment, something that can only be theoretically assessed otherwise.

5.3.2.1 Characterization of Dextran-Derivatized Surfaces

A challenging aspect of this work has been in exploiting a surface chemistry that would result in glass coverslips containing a dextran layer similar to the 40 kDa dextran extenders that are present in Sepharose XL and Capto materials. Working from patents for these chromatographic matrices (Axen et al., 2008; Berg, 2003; Berg et al., 2002), in conjunction with previously-conducted surface chemistry on similar surfaces (Elender et al., 1996; Miksa et al., 2011, 2006), it was possible to construct a surface with a 40 kDa dextran layer covalently attached to the substrate through a reductive amination reaction. Ellipsometry conducted on silicon wafers following the procedure detailed in the Methods section revealed a 3.6 ± 0.8 nm layer on the substrate. This thickness is smaller than that inferred from the ISEC analysis of Sepharose FF and XL in Chapter 2, but the ellipsometry was conducted in an atmospheric environment and not an aqueous one. Carbohydrate polymers are readily hydrated and swell when in solution (Kuhner and Sackmann, 1996; Miksa et al., 2006).

Atomic force microscopy (AFM) was performed on both silicon wafers and glass coverslips following the dextranization procedure. Figures 5.8 and 5.9 show surface roughness AFM imaging in an aqueous environment on silicon wafers and glass coverslips, respectively, using a Bruker Bioscope Catalyst atomic force microscope operated in quantitative nanoscale mechanical (QNM) tapping mode. Both sets of images display surface roughness and positive force of adhesion (not shown) when the substrates are dextran-derivatized compared to the bare surfaces when

imaged in an aqueous medium, indicating the deposition of a surface layer. Dextran formations that appear to be on the order of 40-50 nm may have been more highly polymerized, as it was challenging to control the degree of surface homogeneity and dextran polymerization on the glass substrates.

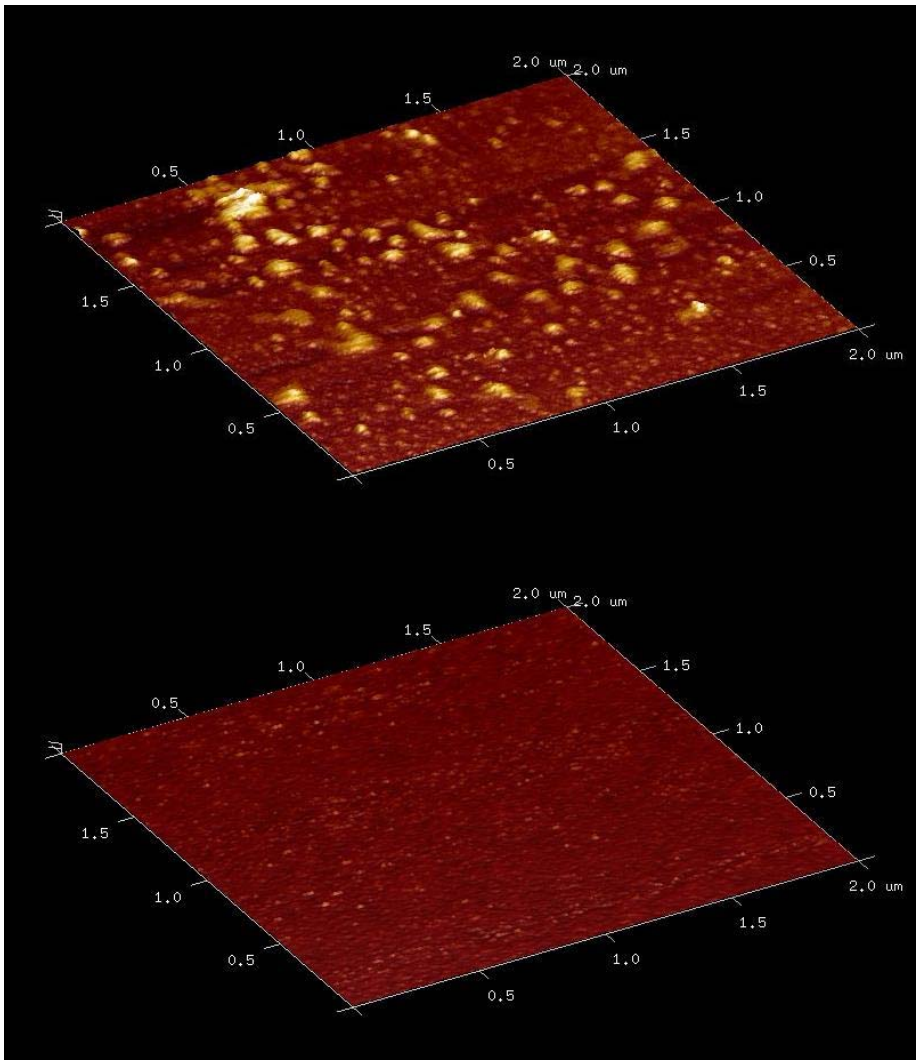

Figure 5.8 AFM imaging of silicon wafer derivatized with dextran (top) and a bare silicon wafer with no dextran (bottom). Color scale ranges from 0 to 50 nm.

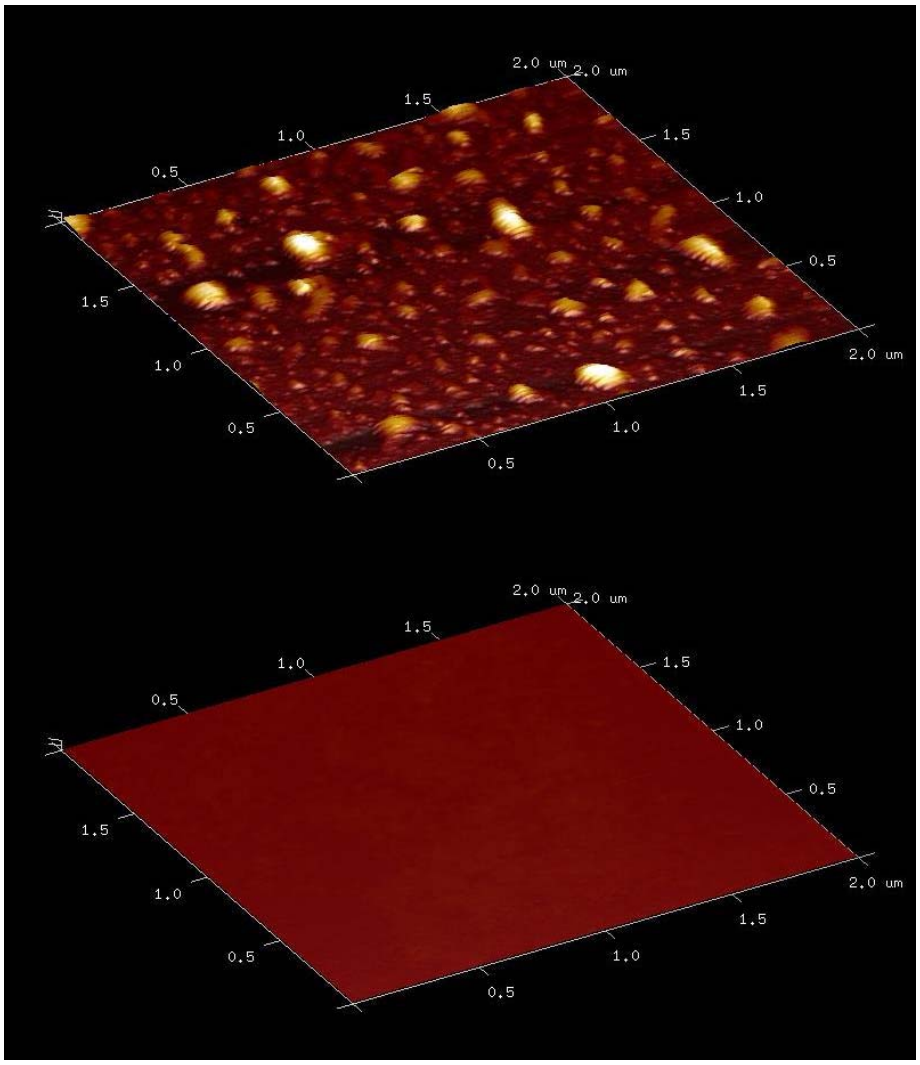

Figure 5.9 AFM imaging of no 1.5 glass coverslip derivatized with dextran (top) and a bare no. 1.5 glass coverslip with no dextran (bottom). Color scale ranges from 0 to 50 nm.

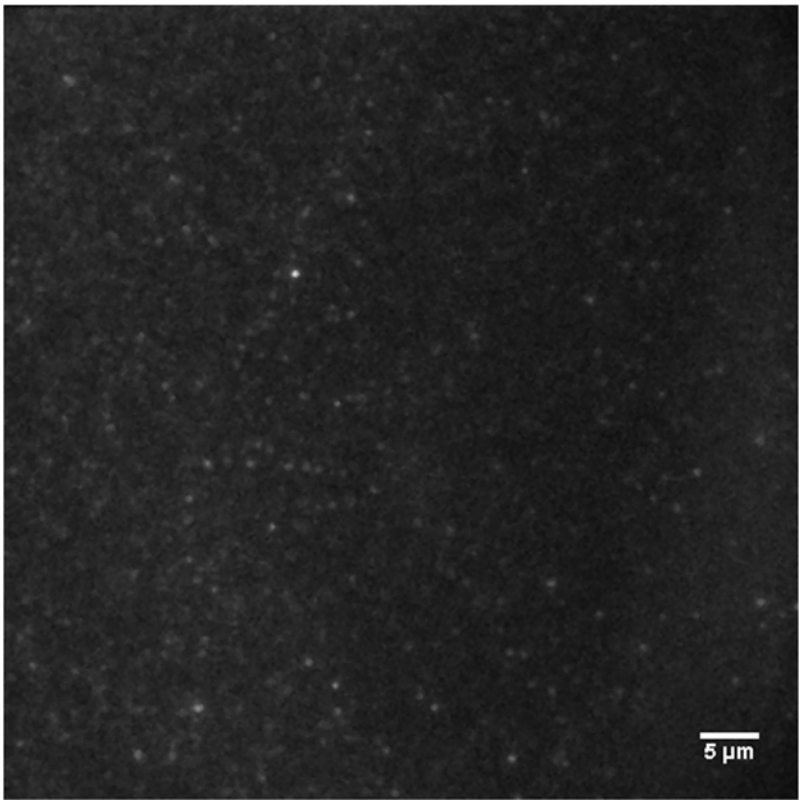

Figure 5.10 TIRF image of FITC-dextran derivatized surface (no. 1.5 glass coverslip) using an excitation wavelength of 488 nm. Fluorescence emission events confirm homogeneous surface coverage of labeled dextran.

Figure 5.10 shows a TIRF image of a glass coverslip substrate that was dextranized using an FITC-conjugated 40 kDa dextran standard, allowing the surface itself to emit a fluorescence signal in response to an excitation wavelengths of 488 nm. Solution conditions were 10 mM sodium phosphate at pH 7. No fluorescently labeled protein was included in this sample, so all fluorescence events are due to the FITC-dextran attached to the surface. Changing solution conditions did not affect the fluorescence signal, so it was determined that the surfaces were mechanically stable during buffer exchanges. These analytical methods supported the view that the

dextranization protocol employed was successful in allowing a homogeneous layer of dextran to be deposited on the substrates for further work.

5.3.2.2 Protein Adsorption on Dextranized Surfaces

TIRF results for dextranized surfaces with and without sulfonate functionalization are shown for three TIS values in Figure 5.11. Each image is only a single frame within a TIFF image stack of 5000 images with a 30 ms frame rate (33.3 frames per second). The pixel dimensions are 256 x 256 pixels even though the CCD camera used is capable of 512 x 512 pixel image capture, due to a 2 x 2 binning that was employed during the imaging experiment in an effort to increase the frame rate. Smaller regions of interest (ROI) were also used to increase the frame rate of the image capture to approximately 4 ms. However, this resulted in a significant reduction in the signal-to-noise ratio (SNR), making further processing of the data difficult and very computationally intensive. A higher frame rate is beneficial in the quantitative analysis of these data set, since the characteristic diffusion time, especially in the high TIS case, is seemingly lower than the acquisition time allowed from a 30 ms frame rate.

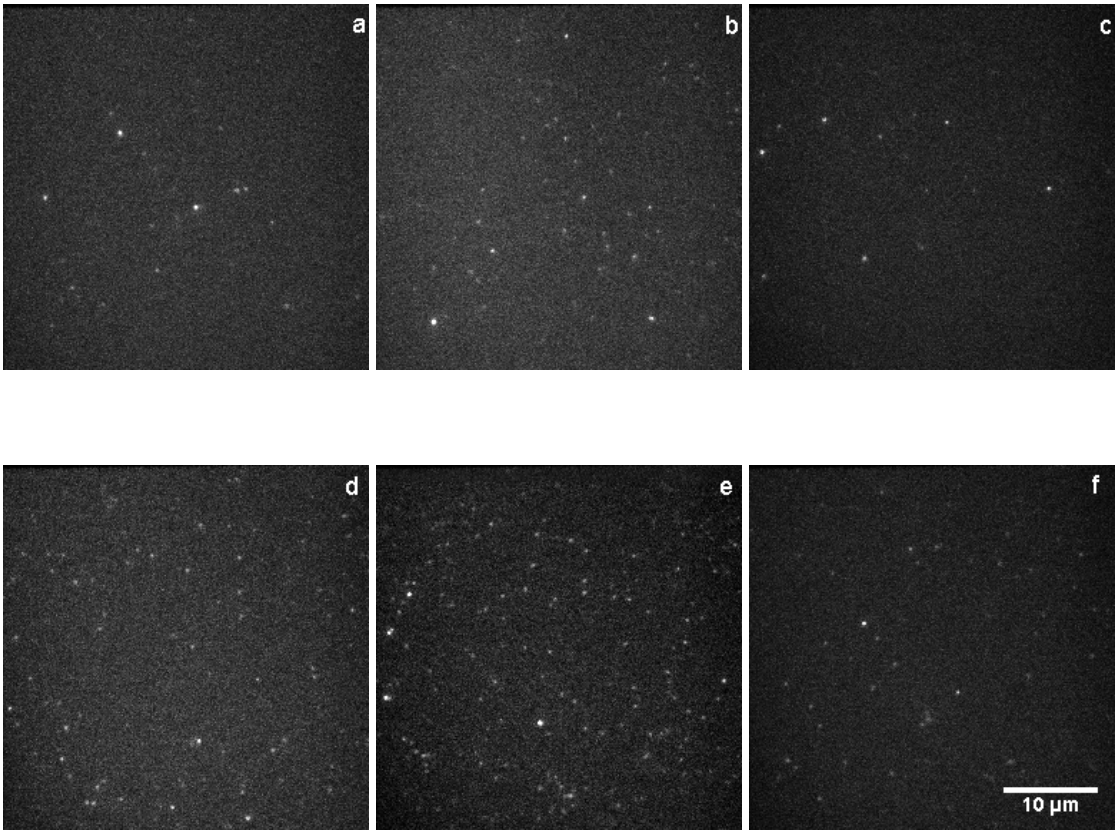

Figure 5.11 TIRF images of 10 pM DyLight 550-labeled lysozyme on non-sulfonated (a, b, c) and sulfonated (d, e, f) surfaces derivatized with 40 kDa dextran. Total ionic strengths of solutions are 20 mM (a, d), 100 mM (b, e) and 250 mM (c, f). 30 ms frame rate, 256 x 256 pixels (2 x 2 binning).

As the total ionic strength was increased for each of these samples, a significant increase in particle movement was observed. For the most part, under 20 mM conditions, adsorption events would occur and last for approximately 50 to 150 frames at fixed points with little lateral movement. Increasing the TIS to 100 mM, still with the same labeled protein concentration, an increase in the number of adsorption events was observed, albeit the duration of the events was shorter. The

increase in the number of adsorption events is likely due to the faster adsorption kinetics protein would experience at elevated TIS, meaning more particles would pass through the sample volume. Photobleaching could explain the lower apparent surface coverage at the low TIS condition as well, as particles remained on the surface for much longer than at increased TIS, causing them to be exposed to the excitation source for longer.

It was also clear that labeled molecules at 100 mM TIS remained within the focal volume while diffusing laterally along the surface, an effect that was much less prevalent at the lower ionic strength. However, raising the TIS to the 250 mM condition resulted in a decrease in apparent surface coverage of the molecules as well. This is most likely due to the faster desorption kinetics at higher salt concentration causing more transient interactions. Due to the relatively low frame rate in these cases, the fast diffusion was difficult to capture with the 256 x 256 ROI. Smaller ROI's displayed an apparent increase in the surface coverage, but with much lower residence time of the molecules (not shown), confirming that the insufficient frame rate was the cause of the apparently lower surface density.

The discussion up to this point has not distinguished the sulfonated and non-sulfonated dextran-derivatized surfaces, but a comparison between the two types of prepared surfaces is relevant. Due to the nature of the experiment, it was difficult to discern if molecules were moving within the deposited dextran layer, as they would in a homogeneous diffusion mechanism within a polymer-modified stationary phase, or whether they were desorbing and readsorbing on the top of the dextran layer without penetration into the polymeric volume. The only evident driving force for adsorption in this type of experiment is assumed to be electrostatic in nature, but non-specific

adsorption is also clearly evident with no blocker molecule (such as BSA) present. The fact that there are adsorption events in both the sulfonated and non-sulfonated samples confirms this, but the number of adsorption events is much higher in the case where the surfaces underwent VSA treatment to functionalize the dextran layer, something that is further explored in the next section.

Limiting non-specific adsorption is a challenge, especially in this type of single-molecule imaging, where differences between a functionalized surface and a non-functionalized one are to be discerned. Unlabeled BSA was added to the protein stocks to act as a blocker for these non-specific adsorption sites. A concentration of 1.5 μM is sufficient to perform this task while not hindering to any great extent the ability of the fluorescently-labeled lysozyme to adsorb to the surface. Since BSA has a net negative charge at neutral pH, it should not compete for sulfonated binding sites with the positively-charged lysozyme. Of course, BSA still has 60 positively-charged surface residues (lysine) that could bind with negatively-charged moieties (Brewer et al., 2005), so employing this method may cause some undesired effects.

Figure 5.12 compares TIRF images of the two types of dextranized surfaces, non-sulfonated and sulfonated, at the same three TIS conditions presented in the previous figure, except with 1.5 μM of BSA present. Across all ionic strengths, a drastic reduction in the overall number of molecular binding events is observed when compared to Figure 5.11. This could be due to there being a large number of non-specific adsorption sites in each type of surface, on which the BSA can adsorb and therefore reduce access of labeled lysozyme to the surface. However, the BSA could also be competing with lysozyme for binding to the negatively-charged functional groups, reducing the overall fluorescently-labeled protein coverage.

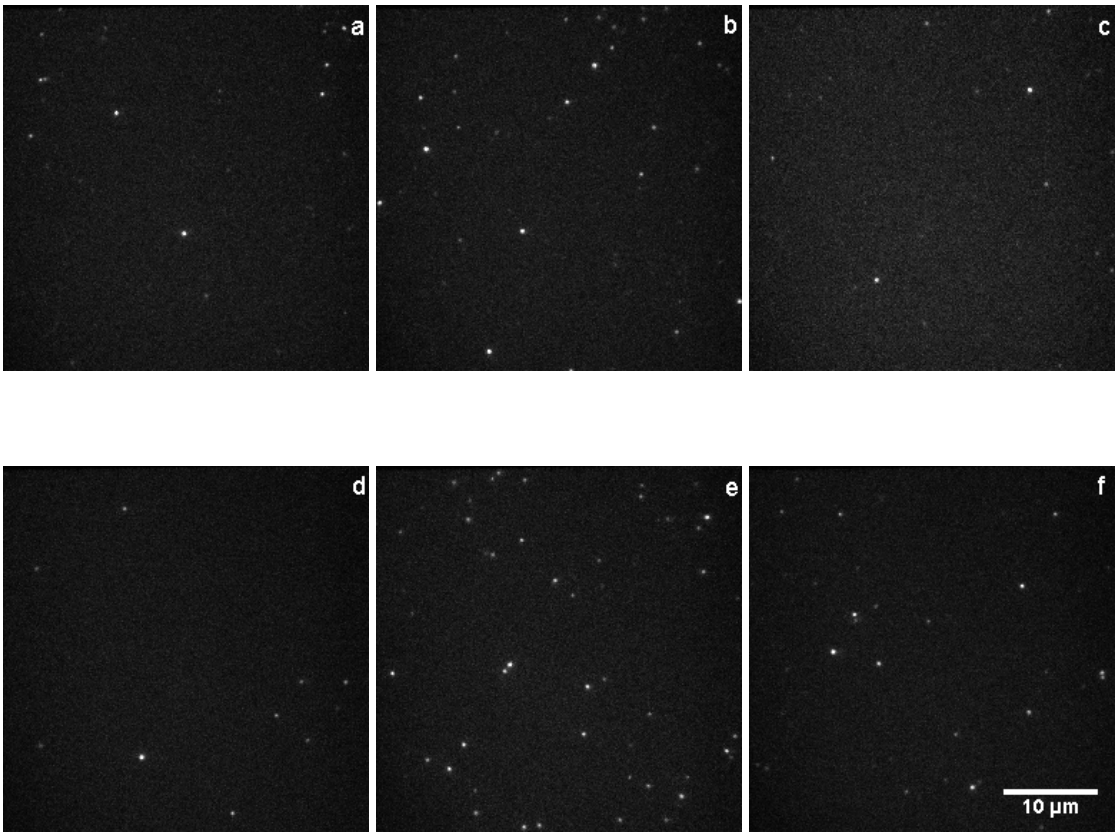

Figure 5.12 TIRF images of 10 pM DyLight 550-labeled lysozyme with 1.5 µM unlabeled BSA on non-sulfonated (a, b, c) and sulfonated (d, e, f) surfaces derivatized with 40 kDa dextran. Total ionic strengths of solution are 20 mM (a, d), 100 mM (b, e) and 250 mM (c, f). 30 ms frame rate, 256 x 256 pixels (2 x 2 binning).

A similar trend is observed in that there appears to be a greater surface coverage at 100 mM TIS. Since the protein stocks in Figures 5.11 and 5.12 were prepared independently, errors in the protein concentration during serial dilution were likely not the cause. The effect of BSA is presumably due to a combination of photobleaching effects at lower TIS, where protein remained exposed for longer times, and increased diffusivity at higher TIS, causing rapid protein movement in and out of the focal volume that could not be captured with just a 30 ms frame rate. Although the

total number of binding events was lower with the inclusion of BSA, a beneficial side effect is the increase in the SNR when compared to imaging without BSA in solution, making further processing a great deal easier.

To reiterate, the images presented in Figures 5.11 and 5.12 are just single frames from a large set of image files. A quantitative analysis of these qualitative imaging experiments is necessary to discern further information about the functional characteristics of these surfaces.

5.3.2.3 Particle Tracking and Mean-Squared Displacement

Tracking of the fluorescently-labeled molecules allows the mean-squared displacement to be determined over time, from which relative diffusivities can be determined between the two types of surfaces and among the three TIS conditions. A Matlab code authored by Daniel Blair and Eric Dufresne and utilized in previous work by members of the Furst research group (Chae and Furst, 2005; Huh and Furst, 2006; Huh et al., 2007; Larsen and Furst, 2008) was used to track particles in each frame of the TIFF image stacks and to derive two-dimensional trajectories for adsorbed molecules. The code consists of a band pass filter to first remove noise in each image, followed by the location and identification of particles in a single frame based on location of the brightest pixel clusters, and then a particle location refinement based on calculating the centroid of the intensity distribution around the brightest pixel. A feature size of 5 pixels was used to describe the diameter of the fluorescent molecules. Although the protein molecules are much smaller than this feature size, the diffraction limit of the system is approximately 250 nm, which makes biological molecules smaller than this limit appear larger than they are due to the wavelength of the incident laser beam and the numerical aperture of the lens (Lipson et al., 2010).

Once particles were tracked in each single frame, trajectories could be built as a function of time by identifying the same particle in neighboring frames. A maximum distance threshold of 15 pixels was set so that if a tracked particle were to move past this threshold a new trajectory would be assembled. Of course, particles could diffuse into and out of the focal volume as well, in which case new trajectories would be assembled and treated as entirely new particles in the sample space. The final step is to calculate the mean-squared displacement (MSD) for non-overlapping lag times based on the tracked trajectories. Using the raw input from the previous subroutines, the MSD in pixels^2 versus the lag time can be found. The pixel size for the 256 x 256 ROI (with 2 x 2 binning) is 0.152 μm/pixel. The frame rate of the camera can be used to convert the lag time (expressed in frames) to real time. Based on the slope of the MSD at short lag times, a short-time diffusion coefficient, D_0, can be determined for each system.

Figure 5.13 shows the MSD plotted versus time for experiments corresponding to those shown in Figure 5.11 on linear and logarithmic scales. The number of trajectories used for the non-sulfonated surfaces are 1716, 3659 and 2256 for 20, 100 and 250 mM TIS, respectively, while the number of trajectories used for the sulfonated surfaces are 3821, 4073 and 2768 for 20, 100 and 250 mM TIS, respectively.

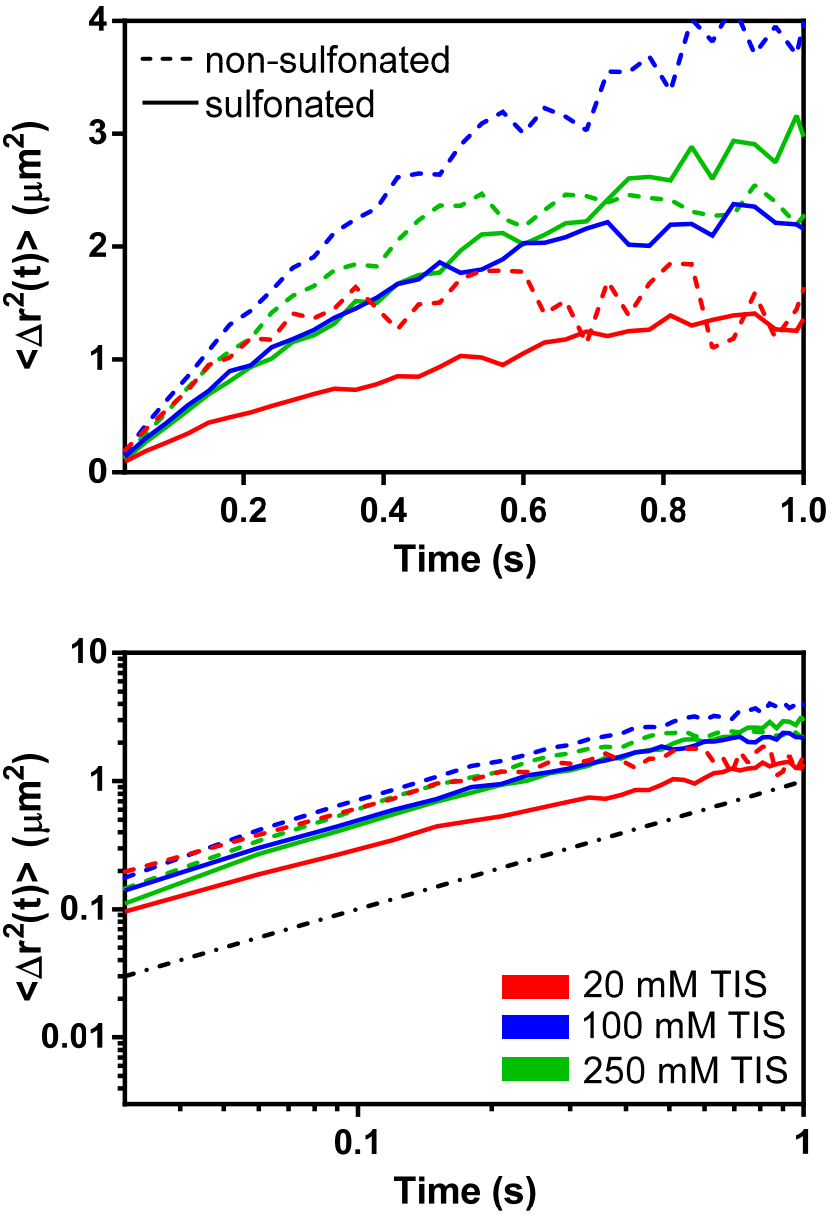

Figure 5.13 Linear (top) and log scale (bottom) plots of mean-squared displacements of 10 pM DyLight 550-labeled lysozyme on sulfonated (solid) and non-sulfonated (dashed) dextran surfaces. Red, blue and green curves correspond to 20, 100 and 250 mM TIS conditions, respectively. Dot-dashed black line on log scale plot (bottom) has a slope of 1 for comparison.

More trajectories were analyzed for the sulfonated surface, suggesting that a larger number of adsorption events occur. This would be expected as the functionalized surface would be expected to draw in protein molecules from the bulk fluid due to electrostatic attraction. Even though more trajectories are drawn for the sulfonated case, it can be seen in these plots that the MSD is actually lower than for the non-sulfonated case for each of the corresponding conditions. This can be indicative of hindered lateral movement in the case of the sulfonated surface. Even though more molecules are being adsorbed (since more trajectories are analyzed), adsorbed proteins tend to be less mobile on the surface. It is likely that molecules are held in place due to the electrostatic attraction between the protein and surface, something that is much less significant in the case of the non-sulfonated surfaces. Since there are no discrete negatively-charged moieties on the latter surfaces that facilitate specific adsorption, non-specifically adsorbed protein may be able to roll and diffuse more freely without the diffusive hindrance of electrostatic interactions.

The congruency of the MSD curves at 100 and 250 mM TIS on the sulfonated surfaces, and the lower MSD at 250 mM than at 100 mM TIS on the non-sulfonated surfaces, could be due to the insufficient frame rate of the image capture. Protein at this higher ionic strength has a shorter characteristic diffusion time, and therefore may not be captured by the camera. The exposure time of this camera is approximately $1/10^{th}$ of the time between frames, leaving only about a 3 ms window for fluorescence events to be captured at this frame rate. Therefore, the resolution allowed with TIRF may not be compatible with certain conditions, but still provides good quantitative data for the 20 and 100 mM TIS conditions, where protein has a much higher capacity on IEX resins than at 250 mM, a condition normally suitable to screen all electrostatic

interaction within the system anyway. The 250 mM TIS condition was selected only to give a full spectrum of states on the functionalized surface: bound and stationary, bound and not stationary, and largely unbound, which were achieved with the 20, 100 and 250 mM TIS conditions, respectively.

The curvature of the plots on the linear scale also indicates the insufficient exposure time to capture longer lag times. Generally, the mean-squared displacement should be increasing and linear. The asymptotic behavior that is displayed, especially in the 250 mM TIS case, suggests that there are a limited number of trajectories for longer lag times (approximately > 0.4 s) to be sufficiently correlated, which is why there is a plateau in the overall displacement of particles in the system.

Figure 5.14 shows the MSD plotted versus time for experiments corresponding to the ones shown in Figure 5.12, which contain 1.5 μM BSA in the fluorescently-labeled protein stocks, on linear and logarithmic scales. Much lower MSD values are observed than in the previous figure in which BSA was not included. This coincides with the observation that there were many fewer binding events occurring under this condition as revealed by the TIRF images themselves (Figure 5.12). The number of trajectories analyzed for the non-sulfonated surfaces are 835, 3024 and 741 for 20, 100 and 250 mM TIS, respectively, while the number of trajectories analyzed for the sulfonated surfaces are 714, 4197 and 1544 for 20, 100 and 250 mM TIS, respectively.

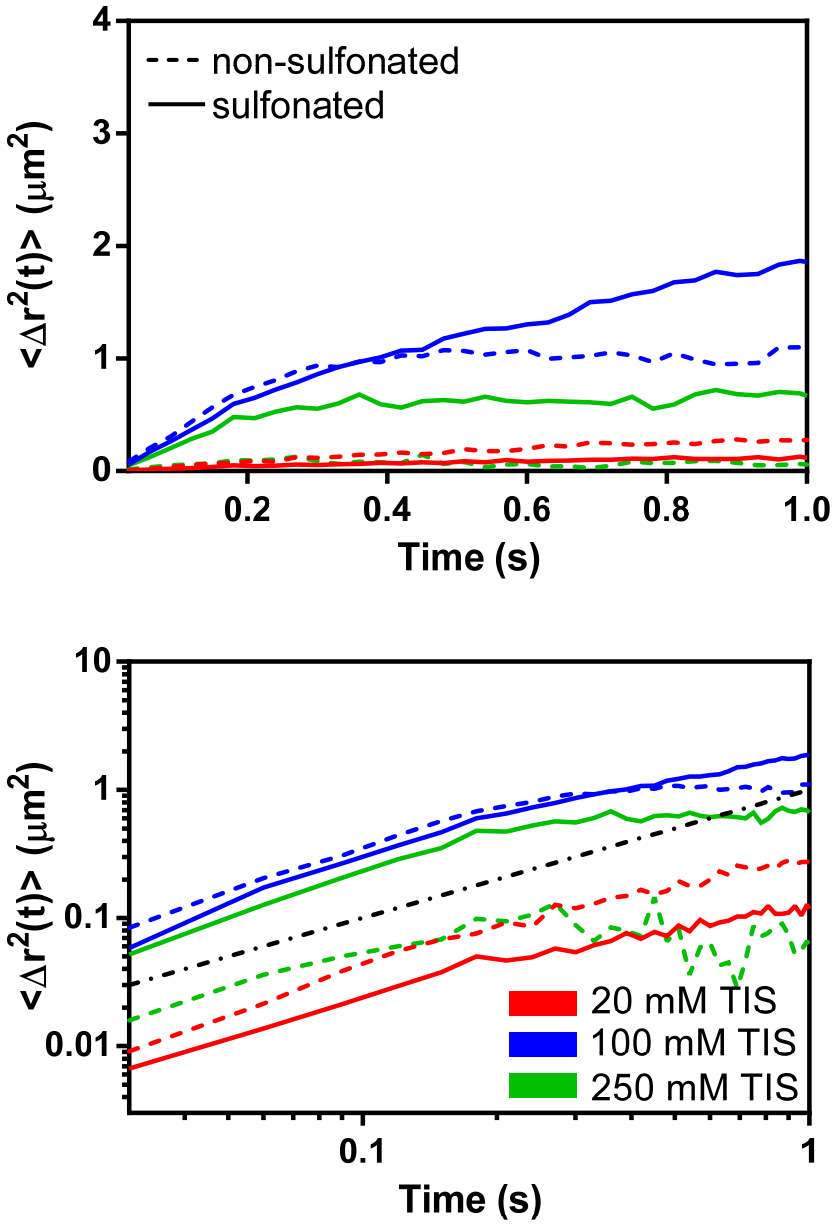

Figure 5.14 Linear (top) and log scale (bottom) plots of mean-squared displacements of 10 pM DyLight 550-labeled lysozyme with 1.5 μM unlabeled BSA on sulfonated (solid) and non-sulfonated (dashed) dextran surfaces. Red, blue and green curves correspond to 20, 100 and 250 mM TIS conditions, respectively. Dot-dashed black line on log scale plot (bottom) has a slope of 1 for comparison.

All experiments with BSA included displayed a smaller number of trajectories than their counterparts where BSA was omitted, except for 100 mM TIS on the sulfonated surfaces. This case had a much greater mean-squared displacement than both the 20 and 250 mM TIS condition, both of which showed very little displacement over the course of the experiment, as can be seen on the plots by comparison to the calibration line of unit slope. Again, the low displacement at 250 mM TIS can be explained by the characteristic diffusion time and the insufficient frame rate and exposure time provided by the camera at this condition. However, the 250 mM TIS case on the sulfonated surface has a higher displacement than on the non-sulfonated surface, presumably due to the longer residence time of particles on the negatively-charged surface, leading to an increase in the number of trajectories tracked, hence a larger total displacement overall.

The short-time diffusion coefficients can be estimated from the MSD plots for short lag times, or the initial times where the MSD plots appear linear. As the MSD gets to longer lag times, it begins to drop off since fewer neighboring frames are correlated. The short-time diffusion coefficients are shown in Figure 5.15 for all cases as a function of TIS with error bars that represent the standard error of the linear regression analysis. Experiments that do not include BSA as a blocker have relatively similar diffusion coefficients. The diffusivities on non-sulfonated surfaces are slightly higher than on the sulfonated surfaces, as expected due to electrostatic attraction hindering particle movement, but they are all still within the same order of magnitude. There exists a much greater difference in the experiments that include BSA as a blocker, as the diffusion coefficients at 20 mM TIS are roughly an order of magnitude lower than they are at 100 mM TIS, for both non-sulfonated and sulfonated surfaces.

Again, the sulfonated surfaces present diffusion coefficients that are slightly lower than for the non-sulfonated surfaces, but not by very much. The diffusion coefficients at 250 mM TIS may be skewed from their true values as the diffusion was faster than the image capture. As the TIS is increased, protein-protein interactions become dominant over protein-surface or protein-polymer interactions due to the increase in protein diffusivity and the screening of electrostatic interactions.

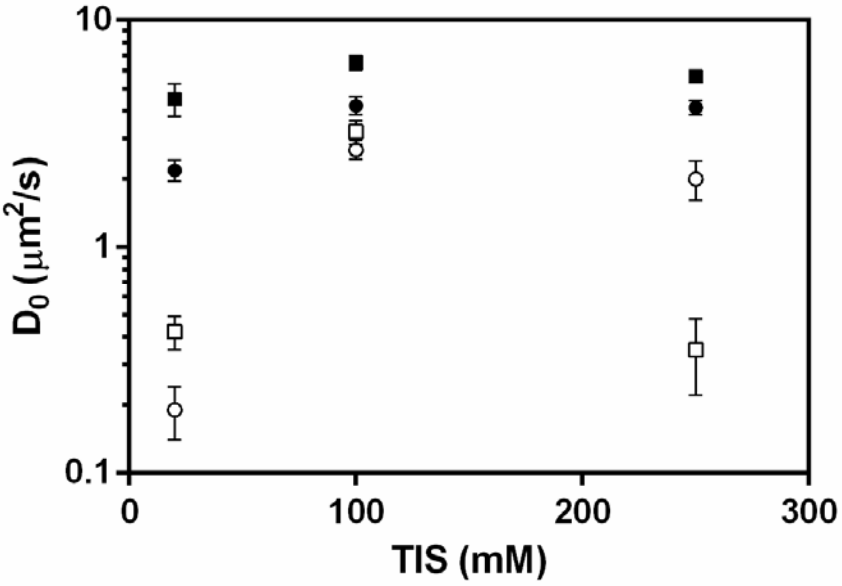

Figure 5.15 Short-time diffusion coefficients of 10 pM DyLight 550-labeled lysozyme estimated from mean-squared displacements as a function of TIS in solution. Squares represent experiments on non-sulfonated surfaces, circles represent sulfonated surfaces. Filled symbols are experiments with no BSA included in the solution, open symbols include 1.5 μM BSA. Error bars represent the standard error of the regression fitting.

The inclusion of BSA as a blocking molecule undoubtedly had a significant impact as shown in the MSD plots and the short-time diffusion coefficients. This is a good indicator that non-specific adsorption was occurring within the TIRFM system and needed to be addressed in order to observe the adsorption of protein with purely an electrostatic driving force at work. Of course, this could be remedied only partially, as there was still significant adsorption even on non-sulfonated surfaces. The inclusion of BSA could also have affected the measured diffusivity, as the increased concentrations of protein (both lysozyme and BSA) may have contributed to diffusivity values dominated by protein-protein interactions among the labeled and unlabeled species. In this case, pure protein-surface interactions may have not been observed and it becomes hard to differentiate the mechanism of the fluorescent binding events.

It is possible that with faster image capture or longer exposure time, the dynamics at conditions like 250 mM TIS could have been better resolved. Keeping large ROI's is beneficial for the particle tracking algorithm that was employed, as it analyses an ensemble average of particle movement, but the drawback here is the reduction in the frames per second. Fluorescence correlation spectroscopy could have corroborated some of our results regarding the hindered diffusion of protein at different TIS, although the TIRF microscope used did not have a correlator card included. Normal FCS operation would not have allowed us to 1) visualize the binding events or 2) obtain fluorescence fluctuations in the very small focal volume at the solid-liquid interface without the assistance of TIR. Performing single point, or single binding site, FCS would have not worked too well with our system either, as the sulfonate functionalization is presumably spread out homogeneously across the

surface, so binding sites are not easily discernible. Clusters of charged functional groups have been shown to be more successful in this type of analysis (Daniels et al., 2012).

5.4 Conclusions

The study of protein adsorption on surfaces meant to represent pore surfaces within a chromatographic particle is still a relatively new endeavor within the realm of protein separation applications. Adsorption on the molecular scale is typically not of direct interest in downstream processing when scale-up is the ultimate goal. However, to understand the governing mechanisms fundamentally, information on the molecular length scale provides a sense of how proteins move and adsorb.

We have shown in this chapter how this can be done using both molecular theory and experimental measurement via single-molecule microscopic techniques. The study of preferential adsorption on non-modified and dextran-modified surfaces provided molecular insight into the significance of local charge and pH conditions via calculations that were validated by experimental binary adsorption studies. It was found that the critical pH, pH_c, has a non-trivial dependence on salt concentration and that it increases significantly with decreasing salt concentration.

The use of TIRFM imaging allowed visualization of single-molecule adsorption on dextran surface layers, similar to those within Sepharose XL and Capto materials. The dependence on salt concentration was again illustrated, with interactions ranging from totally immobile proteins at a strong binding condition, to relatively mobile but still adsorbed, to totally desorbed behavior. The displacements garnered from tracked particles elucidated these adsorptive states. With further refinement, this advanced microscopy technique could have broader use when

attempting to discern mechanisms of protein transport that would otherwise be undiscernible on a macroscopic scale.

Chapter 6

CONCLUSIONS AND RECOMMENDATIONS

This dissertation explores the structural and functional characteristics of polysaccharide-based ion-exchange adsorbents and how these traits dictate the adsorption, transport and elution behavior of proteins. An understanding of the fundamental mechanisms that govern this behavior is built upon through both macroscopic and microscopic studies. The findings presented here have salient implications in stationary-phase selection and the design of downstream chromatographic processes. This chapter summarizes the insights gained from this work, provide recommendations for future studies, and discusses the implications for downstream process design.

6.1 Considerations for Chromatographic Particle Structure and Function

The work described in Chapters 2 and 3 contributes to the understanding of the structure and function of chromatographic stationary phases comprised of carbohydrate polymers, specifically with regard to dextran-modified and cellulosic adsorbents. The use of these types of IEX materials is shown to be greatly beneficial for process designs requiring either high adsorbent capacity or rapid protein uptake. HyperCel, in particular, possesses the capability to achieve full saturation at rates higher than seen for other polymer-modified materials that support enhanced rates of protein transfer. These cellulosic materials also afford substantial binding capacities

that are on a par with polymer-modified materials developed specifically for this purpose (e.g., Sepharose XL and Capto), without being polymer-modified themselves.

It is clear in the comparative analysis presented that particle structure has a significant bearing in the types of transport that assert dominance. The small pore sizes revealed by ISEC in both dextran-modified and cellulosic adsorbents support the observation that homogeneous diffusion is a dominant transport mechanism in these materials, and this appears to be corroborated in the microscopic study of single-particle uptake. Even despite the small pore sizes in the HyperCel materials, the intraparticle diffusion resistances, which are normally rate-controlling in most porous materials, were near-negligible in comparison to external film transfer resistances. For this situation, particles of similar composition could be manufactured with larger particle sizes without the adverse effect of a significant increase in intraparticle resistance, allowing rapid uptake as well as lower pressure drops across packed beds of the adsorbent.

Modeling of the uptake behavior on these adsorbents has also generated transport parameters that are of considerable value when developing purification strategies, as predictive modeling is an important tool in process optimization. The homogeneous diffusivities and external mass transfer coefficients presented in this work should have applicability in the future development and use of these chromatographic supports that display such rapid uptake behavior.

It was also shown that the adsorption of protein has a clear effect on the particle microstructure, in that there exists a significant swelling of the adsorbed phase that translates to a significant portion of the pore volume being occupied at higher loadings. This had been found to be the case in polymer-modified materials

previously, but has now been shown to be evident within cellulosic stationary phases as well, again highlighting the functional similarities between these types of adsorbents.

The salt-tolerant anion-exchange adsorbent, STAR AX HyperCel, displayed particularly intriguing results even when visualizing the particles with just chemical fixation in protein-devoid phases. The ligand chemistry in this adsorbent not only modified its adsorptive properties, but appeared also to affect its fundamental pore architecture. While its salt-tolerant characteristic is indeed uniquely advantageous, there are implications regarding characteristically slower bimodal uptake of protein, even though it is based on the same support as the S and Q HyperCel materials, which exhibit vary rapid uptake kinetics. Regardless, extremely low TIS of solution would not be generally recommended for operation anyway, since the cellulosic media exhibits an exclusion of salt at these conditions due to the Donnan effect, which may negatively affect its binding capacity for protein.

These cellulosic materials offer the distinct advantage of rapid particle saturation that is crucial in the fast loading of protein during bind-and-elute separations. Even though only batch uptake and static capacity studies were explored in great detail in this work, further studies can be undertaken in investigating the ability of these resins to achieve high dynamic capacities and short load times within larger column operations. A study of how to modulate the loading conditions for optimal loading efficiency in these cellulosic exchangers also has yet to be performed.

6.2 Considerations for Elution Design in IEX Adsorbents

The elution of protein was thoroughly examined in Chapter 4 within agarose-based adsorbents, dextran-modified agarose-based adsorbents and cellulosic

adsorbents for CEX. It is clear that slower elution rates are present within cellulosic stationary phases and those with dextran extenders, a result that may be linked to the particle structure as well as being influenced directly by the increased adsorptive capacity.

The narrow pore sizes of adsorbents that exhibit increased adsorptive capacities are directly related to the accessible porosities for proteins of different hydrodynamic radii as well as the effective elution rates garnered from elution experiments performed on the column level. Even though this could be viewed as a potential disadvantage, there exists a tradeoff between having rapid elution versus increased adsorptive capacities. On the one hand, the small pore sizes (combined with polymer extenders in some cases) increase the overall surface area or volume for adsorption, but reduce the pore lumen radius, which restricts protein movement during elution.

The other factor to consider is the overall amount of protein that is to desorb during the process. A front of high salt typically used for elution in IEX is able to penetrate the chromatographic systems much more rapidly than protein, and thus elution takes place on a much shorter timescale than uptake. The screening of nearly all the attractive electrostatic interactions within these particles can happen in a matter of seconds. This means a significant increase in the protein concentration within the local pore. In a stationary phase like S HyperCel or Capto S, for example, this could be greater than several hundred mg/mL. Therefore it is evident how protein phase behavior is a legitimate concern for these types of systems when employing bind-and-elute processes.

Of course, the physicochemical properties of the proteins themselves are an important factor as well, but many biomolecules present some degree of salting-out behavior. Monoclonal antibodies, for example, are notorious from a regulatory standpoint for aggregating in small yet significant fractions, and while not all aggregation may stem from high salt concentrations, elution conditions for IEX can still be relatively harsh. In this work, lysozyme emerged as a suitable model to represent a "worst-case scenario" in which the protein eluted very clearly displayed salting-out behavior in the presence of a high sodium chloride concentration.

This behavior was corroborated with the use of single-particle visualization via confocal microscopy, in which the anomalous elution profiles could be observed in a manner that is not feasible on the macroscopic scale. The abnormal shrinking-core behavior displayed was apparent in both the cellulosic and dextran-modified media, but not in the material with a much larger pore size as well as lower binding capacity, SP Sepharose FF. The balance of maintaining open microstructures while still affording ample surface area for proteins to adsorb is something to be considered during the design of this class of adsorbent material. Reducing this bottleneck during elution from high capacity materials is definitely something that can be addressed during the preliminary design stage of chromatographic media.

A final consideration that was presented in this chapter was the use of excipients to aid in more rapid elution. While typically high concentrations of excipients are needed to effectively stabilize protein aggregation, it was shown here to be possible during the course of IEX column elution with a relatively high initial loading of protein. L-arginine and disaccharides were among the excipients tested, with L-arginine providing the most overt benefit in accelerating the elution of

lysozyme, but there are numerous other excipients that may prove to be useful in a similar manner. This would of course depend on the molecular components in the system as well as the costs of introducing such excipients to the elution stream, as L-arginine is not a particularly cost-efficient reagent.

The analysis presented in this work has significant implications for downstream chromatographic separations. It could easily be applied to different systems and types of stationary phases to assess whether protein elution could be modified to perform more efficient purification processes. A logical next step would be to screen a library of industrially relevant biomolecules, such as monoclonal antibodies, to find a suitable model protein for further elution studies, as most of this work focused on single-component lysozyme elution within polymer-modified and cellulosic systems. A more rigorous analysis to the elution pool or tailing region could be employed as well to quantify the amount of high molecular weight species or aggregates by using SEC-HPLC.

Additionally, screening of mobile-phase modifiers and excipients that assist in protein solubility within the column would certainly be beneficial. Arginine and disaccharides were investigated in this work, but surfactants such as polysorbate or other stabilizers typically used for formulation applications could prove to be more effective depending on the type of column and operating condition used. For example, if a possible mechanism of aggregation during IEX is related to hydrophobic interactions within the system, an amphipathic excipient such as Tween (polysorbate) could disrupt those non-specific interactions within the IEX material. A mechanistic approach to alleviate such aggregation issues is important in efficiently designing these elution steps.

6.3 Considerations for Single-Molecule Investigations of Protein Sorption and Transport

Chapter 5 describes adsorption onto surfaces meant to represent pore walls within the chromatographic stationary phases studied earlier in this dissertation in two different manners, one mostly theoretical and one mostly experimental. Using molecular theory to complement and build on our understanding of how protein molecules bind to the surfaces within porous adsorbents is both challenging and informative. Having a mechanistic basis built from molecular theory greatly aids in the development of generalized adsorption models on the more macroscopic, i.e., ensemble-averaged, scale.

Our work with Igal Szleifer and Claudio Narambuena at Northwestern University is an ongoing effort. Currently more effort is being devoted to gaining a better understanding of adsorption on dextranized surfaces that better represent the dextran-modified surfaces in materials such as Sepharose XL and Capto. Yet, it is a challenging task to infer attributes such as the dextran surface density and polyelectrolyte fraction per dextran molecule as that type of characterization is difficult to perform. A better approach would be to obtain these characteristics directly from the manufacturers, where possible, to be used with thermodynamic modeling.

The importance of preferential adsorption in downstream applications is especially high since selectivity is a critical metric for chromatographic performance. In this work we found that a dextran-modified material does have a decreased sensitivity to changes in the solution pH when compared to its non-modified counterpart. The modification of pH is not a widely-used method for altering specific interactions in IEX, where it is instead seen to be more reliable to modify salt

concentration to perform a similar function. However, the adjustment of pH can be especially useful for co-eluting species that cannot be resolved with simple changes in the salt gradient. For example, lysozyme and cytochrome c have both a similar molecular size as well as isoelectric point, but they possess different numbers and types of titratable surface residues. Modification of the pH to very acidic conditions causes a shift in the binding affinity without the need to alter the salt concentration, which would result in a reduction of the capacity as it is increased due to the screening of attractive protein-sorbent interactions.

Preferential adsorption was investigated on a fundamental level in this work, ranging from molecular simulation to batch adsorption isotherm experiments. However, a study of how these preferential interactions translate into the adsorptive properties within a packed bed of IEX resin would be a logical next step in this investigation. The selectivity and retentivity of these species on a column in which they are co-adsorbed or simultaneously loaded may reveal that the results of the molecular modeling are indeed scalable to macroscopic systems, which are more representative of the typical usage of these materials.

In our experimental approach to interrogating molecular interactions with polymer-derivatized surfaces, we succeeded in bringing our empirical knowledge base of adsorption down to the molecular length scale. Up to this point, inferences were made on how protein molecules move within a stationary phase, or within a polymer layer, usually based on theoretical approximations or particle-level observations. Now with the visualization tool of TIRFM, we can observe and record these events directly. While our investigation of dextran-derivatized surfaces resulted only in reaffirming

some of the assumptions made about how protein behaves at different TIS conditions, it has the potential for much more refined analyses of similar surfaces in the future.

One possibility is to synthesize surfaces that mimic the pore networks of other polymer-modified adsorbents, such as Fractogel, which exhibits a linear chain end-grafted polymer extender as opposed to the isotropic structure of dextran. Surfaces could also be further developed to better represent the stationary phases; for example, spin coating an ultra-thin layer of agarose onto the substrate before dextran modification may have been more representative of the pore space in Sepharose XL or Capto materials.

Better control of the charge density on the surfaces could lead to more in-depth understanding of the protein-surface interactions. Titration of strong acids or bases to quantify the ionic capacities of adsorbent particles is the standard method of determining the charge density on the material following functionalization. However, our substrates are flat functionalized surfaces as opposed to three-dimensional resin beads, which have the capability of carrying much more charge, making titration to determine the ionic capacity much less sensitive and much more difficult. It may have been possible that our VSA treatment was insufficient to apply negatively-charged moieties to the dextranized surfaces, but without a suitable method for quantifying the ionic capacity this remains unclear.

A developmental custom-built TIRF setup was used for this work, but prebuilt TIRF microscopes could provide better resolution and higher-speed image capture. The ability to increase the frame rate while still maintaining a large ROI would have been extremely beneficial in further analysis of the imaging data, as that would have allowed for both an increase in the number of particles to track (i.e., a larger sampling

size) and better correlation between neighboring frames. Due to the diffraction limitation of the confocal system, single molecules smaller than 250 nm were difficult to resolve because of the wavelengths that were used and the numerical aperture of the lens. Shorter wavelengths, such as UV or X-rays, could be used to increase resolution but are more destructive to biological samples. The flow cell was also compatible only for static flow conditions, as applying flow during imaging altered the focal distance of the objective lens due to suction. TIRFM imaging under flow conditions could help reduce photobleaching effects of fluorophores by allowing more exchange with new stock solution.

The particle tracking analysis employed was helpful in generating quantitative data from the very qualitative set of images captured. The result that more trajectories were assembled for the sulfonated surfaces gave confidence that our sulfonation protocol was successful, but a more in-depth study could have been performed to assess the ionic capacity of each substrate. An autocorrelator component within the experimental TIRF apparatus would also have been useful in allowing for FCS-TIRF and a more straightforward acquisition of particle diffusivities. Performing imaging FCS after the fact yielded convoluted results. Regardless, there are still distinct advantages of this form of microscopy in giving direct comparison and correlation to theoretical approaches for investigating protein adsorption, such as the molecular theory-based approach discussed previously. Future work in this field and its relative impact on our understanding of chromatography at the fundamental level appears to be very promising.

REFERENCES

Ahamed, T., Esteban, B.N.A., Ottens, M., van Dedem, G.W.K., van der Wielen, L.A.M., Bisschops, M.A.T., Lee, A., Pham, C., Thömmes, J., 2007. Phase behavior of an intact monoclonal antibody. Biophys. J. 93, 610–619.

Akiyoshi, K., Sunamoto, J., 1996. Supramolecular assembly of hydrophobized polysaccharides. Supramol. Sci. 3, 157–163.

Anderson, J.L., Quinn, J.A., 1974. Restricted transport in small pores. A model for steric exclusion and hindered particle motion. Biophys. J. 14, 130–150.

Anderson, J.L., Rauh, F., Morales, A., 1978. Particle diffusion as a function of concentration and ionic strength. J. Phys. Chem. 82, 608–616.

Angelo, J.M., Cvetkovic, A., Gantier, R., Lenhoff, A.M., 2013. Characterization of cross-linked cellulosic ion-exchange adsorbents: 1. Structural properties. J. Chromatogr. A 1319, 46–56.

Angelo, J.M., Cvetkovic, A., Gantier, R., Lenhoff, A.M., 2016. Characterization of cross-linked cellulosic ion-exchange adsorbents: 2. Protein sorption and trasnport. J. Chromatogr. A 1438, 100-112.

Arakawa, T., Ejima, D., Tsumoto, K., Obeyama, N., Tanaka, Y., Kita, Y., Timasheff, S.N., 2007a. Suppression of protein interactions by arginine: A proposed mechanism of the arginine effects. Biophys. Chem. 127, 1–8.

Arakawa, T., Philo, J.S., Tsumoto, K., Yumioka, R., Ejima, D., 2004. Elution of antibodies from a Protein-A column by aqueous arginine solutions. Protein Expr. Purif. 36, 244–248.

Arakawa, T., Timasheff, S.N., 1982. Stabilization of protein structure by sugars. Biochemistry 21, 6536–6544.

Arakawa, T., Tsumoto, K., Nagase, K., Ejima, D., 2007b. The effects of arginine on protein binding and elution in hydrophobic interaction and ion-exchange chromatography. Protein Expr. Purif. 54, 110–116.

Armenante, P.M., Kirwan, D.J., 1989. Mass transfer to microparticles in agitated systems. Chem Eng Sci 44, 2781–2796.

Arnold, F.H., Blanch, H.W., Wilke, C.R., 1985. Analysis of affinity separations: I: Predicting the performance of affinity adsorbers. Chem. Eng. J. 30, B9–B23.

Arnold, F.H., Schofield, S.A., Blanch, H.W., 1986. Analytical affinity chromatography. I. Local equilibrium theory and the measurement of association and inhibition constants. J. Chromatogr. 355, 1–12.

Axen, A., Glad, G., Ihre, H., Larsson, A., Norrman, N., 2008. Manufacture of Chromatography Matrices. U.S, Patent 2008/0237124 A1, filed August 30, 2006, and issued October 2, 2008.

Bai, Y.-X., Li, Y.-F., 2006. Preparation and characterization of crosslinked porous cellulose beads. Carbohydr. Polym. 64, 402–407.

Banerjee, S.K., Pogolotti, Jr., A., Rupley, J.A., 1975. Self-association of lysozyme. J. Biol. Chem. 250, 6977-6982.

Baynes, B.M., Wang, D.I.C., Trout, B.L., 2005. Role of arginine in the stabilization of proteins against aggregation. Biochemistry 44, 4919–4925.

Berg, H., 2003. Process for the Production of a Porous Cross-Linked Polysaccharide Gel and its Use as a Gel Filtration Media and in Chromatography. U.S. Patent 6,602,990 B1, filed April 7, 1997, and issued August 5, 2003.

Berg, H., Hansson, H., Kagedal, L., 2002. Adsorption/Separation Method and a Medium for Adsorption/Separation. U.S. Patent 6,428,707 B1, filed February 3, 1998, and issued August 6, 2002.

Boeden, H.F., Pommerening, K., Becker, M., Rupprich, C., Holtzhauer, M., Loth, F., Müller, R., Bertram, D., 1991. Bead cellulose derivatives as supports for immobilization and chromatographic purification of proteins. J. Chromatogr. A 552, 389–414.

Boschetti, E., 1994. Advanced sorbents for preparative protein separation purposes. J. Chromatogr. A 658, 207–236.

Boschetti, E., Coffman, J.L., 2008. Enhanced diffusion chromatography and related sorbents for biopurification. In: Bioseparation and Bioprocessing. Wiley Online Library, pp. 157–198.

Bowes, B.D., 2011. Protein transport and adsorption in polymer-modified ion-exchange media. Ph.D. thesis, University of Delaware.

Bowes, B.D., Koku, H., Czymmek, K.J., Lenhoff, A.M., 2009. Protein adsorption and transport in dextran-modified ion-exchange media. I: Adsorption. J. Chromatogr. A 1216, 7774–7784.

Bowes, B.D., Lenhoff, A.M., 2011a. Protein adsorption and transport in dextran-modified ion-exchange media. II: Intraparticle uptake and column breakthrough. J. Chromatogr. A 1218, 4698–4708.

Bowes, B.D., Lenhoff, A.M., 2011b. Protein adsorption and transport in dextran-modified ion-exchange media. III: Effects of resin charge density and dextran content on adsorption and intraparticle uptake. J. Chromatogr. A 1218, 7180–7188.

Bowes, B.D., Traylor, S.J., Timmick, S.M., Czymmek, K.J., Lenhoff, A.M., 2012. Insights into protein sorption and desorption on dextran-modified ion-exchange media. Chem. Eng. Technol. 35, 91–101.

Brenner, H., Gaydos, L.J., 1977. The constrained brownian movement of spherical particles in cylindrical pores of comparable radius. J. Colloid Interface Sci. 58, 312–356.

Breslow, R., Guo, T., 1990. Surface tension measurements show that chaotropic salting-in denaturants are not just water-structure breakers. Proc. Natl. Acad. Sci. U. S. A. 87, 167–169.

Brewer, S.H., Glomm, W.R., Johnson, M.C., Knag, M.K., Franzen, S., 2005. Probing BSA binding to citrate-coated gold nanoparticles and surfaces. Langmuir 21, 9303–9307.

Canfield, R.E., 1963. The amino acid sequence of egg white lysozyme. J. Biol. Chem. 238, 2698–2707.

Carberry, J.J., 1960. A boundary-layer model of fluid-particle mass transfer in fixed beds. AIChE J. 6, 460–463.

Carignano, M.A., Szleifer, I., 2002. Adsorption of model charged proteins on charged surfaces with grafted polymers. Mol. Phys. 100, 2993–3003.

Carta, G., Jungbauer, A., 2010. Protein Chromatography, Process Development and Scale-Up. Wiley-VCH Verlag GmbH & Co. KGaA, Weinheim.

Chae, B.S., Furst, E.M., 2005. Probe surface chemistry dependence and local polymer network structure in F-actin microrheology. Langmuir 21, 3084–3089.

Champagne, J., Cvetkovic, A., Balluet, G., Bengio, S., Toueille, M., Gantier, R., 2013. A salt-tolerant anion-exchange chromatography sorbent for flexible process development. Bioprocess Int. 11, 50–57.

Chang, C., Lenhoff, A.M., 1998. Comparison of protein adsorption isotherms and uptake rates in preparative cation-exchange materials. J. Chromatogr. A 827, 281–293.

Chaufer, B., Rabiller-Baudry, M., Lucas, D., Michel, F., Timmer, M., 2000. Selective extraction of lysozyme from a mixture with lactoferrin by ultrafiltration. Role of the physico-chemical environment. Lait 80, 197–203.

Chen, W.-D., Dong, X.-Y., Sun, Y., 2002. Analysis of diffusion models for protein adsorption to porous anion-exchange adsorbent. J. Chromatogr. A 962, 29–40.

Coen, C.J., Blanch, H.W., Prausnitz, J.M., 1995. Salting out of aqueous proteins: Phase equilibria and intermolecular potentials. AIChE J. 41, 996–1004.

Cooper, J.T., Harris, J.M., 2014. Imaging fluorescence-correlation spectroscopy for measuring fast surface diffusion at liquid/solid interfaces. Anal. Chem. 86, 7618–7626.

Cooper, J.T., Peterson, E.M., Harris, J.M., 2013. Fluorescence imaging of single-molecule retention trajectories in reversed-phase chromatographic particles. Anal. Chem. 85, 9363–9370.

Crank, J., 1975. The Mathematics of Diffusion, 2nd ed. Clarendon Press, Oxford.

Curtis, R.A., Prausnitz, J.M., Blanch, H.W., 1998. Protein-protein and protein-salt interactions in aqueous protein solutions containing concentrated electrolytes. Biotechnol. Bioeng. 57, 11–21.

Curtis, S., Lee, K., Blank, G.S., Brorson, K., Xu, Y., 2003. Generic/matrix evaluation of SV40 clearance by anion exchange chromatography in flow-through mode. Biotechnol. Bioeng. 84, 179–186.

Danckwerts, P.V., 1953. Continuous flow systems. Chem. Eng. Sci. 2, 1–13.

Daniels, C.R., Kisley, L., Kim, H., Chen, W.-H., Poongavanam, M.-V., Reznik, C., Kourentzi, K., Willson, R.C., Landes, C.F., 2012. Fluorescence correlation spectroscopy study of protein transport and dynamic interactions with clustered-charge peptide adsorbents. J. Mol. Recognit. 25, 435–442.

de Oliveira, W., Glasser, W.G., 1996. Hydrogels from polysaccharides. I. Cellulose beads for chromatographic support. J. Appl. Polym. Sci. 60, 63–73.

Deen, W.M., 1987. Hindered transport of large molecules in liquid-filled pores. AIChE J. 33, 1409–1425.

DePhillips, P., Lenhoff, A.M., 2000. Pore size distributions of cation-exchange adsorbents determined by inverse size-exclusion chromatography. J. Chromatogr. A 883, 39–54.

DePhillips, P., Lenhoff, A.M., 2001. Determinants of protein retention characteristics on cation-exchange adsorbents. J. Chromatogr. A 933, 57–72.

Donnan, F.G., Barker, J.T., 1911. An experimental investigation of Gibbs' thermodynamical theory of interfacial concentration in the case of an air-water interface. Proc. R. Soc. Lond. A 85, 557–573.

Du, K.-F., Yan, M., Wang, Q.-Y., Song, H., 2010. Preparation and characterization of novel macroporous cellulose beads regenerated from ionic liquid for fast chromatography. J. Chromatogr. A 1217, 1298–1304.

Dumetz, A.C., Chockla, A.M., Kaler, E.W., Lenhoff, A.M., 2008. Protein phase behavior in aqueous solutions: crystallization, liquid-liquid phase separation, gels, and aggregates. Biophys. J. 94, 570–583.

Dziennik, S.R., 2002. Effect of ionic strength and stationary phase on protein adsorption and transport in ion-exchange particles. Ph.D. thesis, University of Delaware.

Dziennik, S.R., Belcher, E.B., Barker, G.A., DeBergalis, M.J., Fernandez, S.E., Lenhoff, A.M., 2003. Nondiffusive mechanisms enhance protein uptake rates in ion exchange particles. Proc. Natl. Acad. Sci. 100, 420–425.

Dziennik, S.R., Belcher, E.B., Barker, G.A., Lenhoff, A.M., 2005. Effects of ionic strength on lysozyme uptake rates in cation exchangers. I: Uptake in SP Sepharose FF. Biotechnol. Bioeng. 91, 139–153.

Ejima, D., Yumioka, R., Tsumoto, K., Arakawa, T., 2005. Effective elution of antibodies by arginine and arginine derivatives in affinity column chromatography. Anal. Biochem. 345, 250–257.

Elender, G., Kfihner, M., Sackmann, E., 1996. Functionalisation of Si/SiO_2 and glass surfaces with ultrathin dextran films and deposition of lipid bilayers. Biosens. Bioelectron. 11, 565–577.

Fang, F., Satulovsky, J., Szleifer, I., 2005. Kinetics of protein adsorption and desorption on surfaces with grafted polymers. Biophys. J. 89, 1516–1533.

Fang, F., Szleifer, I., 2001. Kinetics and thermodynamics of protein adsorption: a generalized molecular theoretical approach. Biophys. J. 80, 2568–2589.

Fang, F., Szleifer, I., 2003. Competitive adsorption in model charged protein mixtures: Equilibrium isotherms and kinetics behavior. J. Chem. Phys. 119, 1053-1065.

Fernandez, M., Carta, G., 1996. Characterization of protein adsorption by composite silica-polyacrylamide gel anion exchangers. I. Equilibrium and mass transfer in agitated contactors. J. Chromatogr. A 746, 169–183.

Follman, D.K., Fahrner, R.L., 2004. Factorial screening of antibody purification processes using three chromatography steps without protein A. J. Chromatogr. A 1024, 79–85.

Fuh, C.B., Levin, S., Giddings, J.C., 1993. Rapid diffusion coefficient measurements using analytical SPLITT fractionation: application to proteins. Anal. Biochem. 208, 80–87.

Gong, P., Szleifer, I., 2004. Competitive adsorption of model charged proteins: the effect of total charge and charge distribution. J. Colloid Interface Sci. 278, 81–90.

Gottschalk, U., Brorson, K., Shukla, A.A., 2012. The need for innovation in biomanufacturing. Nat. Biotechnol. 30, 489–492.

Graham, E.E., Fook, C.F., 1982. Rate of protein absorption and desorption on cellulosic ion exchangers. AIChE J. 28, 245–250.

Gräslund, T., Ehn, M., Lundin, G., Hedhammar, M., Uhlén, M., Nygren, P.Å., Hober, S., 2002. Strategy for highly selective ion-exchange capture using a charge-polarizing fusion partner. J. Chromatogr. A 942, 157–166.

Groves, M.L., 1960. The isolation of a red protein from milk. J. Am. Chem. Soc. 82, 3345–3350.

Hagel, L., Östberg, M., Andersson, T., 1996. Apparent pore size distributions of chromatography media. J. Chromatogr. A 743, 33–42.

Halasz, I., Vogtel, P., 1980. Determination of morphological properties of swellable solids by size exclusion chromatography. Angew. Chem. Int. Ed. Eng. 19, 24–28.

Han, N.-W., Bhakta, J., Carbonell, R.G., 1985. Longitudinal and lateral dispersion in packed beds: Effect of column length and particle size distribution. AIChE J. 31, 277–288.

Harinarayan, C., Mueller, J., Ljunglöf, A., Fahrner, R., Van Alstine, J., van Reis, R., 2006. An exclusion mechanism in ion exchange chromatography. Biotechnol. Bioeng. 95, 775–787.

Hayat, M.A., 2000. Principles and Techniques of Electron Microscopy, 3rd ed. Cambridge University Press, Cambridge.

Helfferich, F., 1962. Ion Exchange. McGraw Hill, New York.

Honciuc, A., Harant, A.W., Schwartz, D.K., 2008. Single-molecule observations of surfactant diffusion at the solution-solid interface. Langmuir 24, 6562–6566.

Hubbuch, J., Kula, M.-R., 2008. Confocal laser scanning microscopy as an analytical tool in chromatographic research. Bioprocess Biosyst. Eng. 31, 241–259.

Hubbuch, J., Linden, T., Knieps, E., Ljunglof, A., Thommes, J., Kula, M.-R., Ljunglöf, A., Thömmes, J., Kula, M.-R., 2003. Mechanism and kinetics of protein transport in chromatographic media studied by confocal laser scanning microscopy Part I. The interplay of sorbent structure and fluid phase conditions. J. Chromatogr. A 1021, 93–104.

Huh, J.Y., Furst, E.M., 2006. Colloid dynamics in semiflexible polymer solutions. Phys. Rev. E 74, 31802.

Huh, J.Y., Lynch, M.L., Furst, E.M., 2007. Microscopic structure and collapse of depletion-induced gels in vesicle-polymer mixtures. Phys. Rev. E 76, 051409.

Isailovic, S., Li, H.-W., Yeung, E.S., 2007. Adsorption of single DNA molecules at the water/fused-silica interface. J. Chromatogr. A 1150, 259–266.

Jerabek, K., Revillon, A., Puccilli, E., 1993. Pore structure characterization of organic-inorganic materials by inverse size exclusion chromatography. Chromatographia 36, 259–262.

Juza, M., Mazzotti, M., Morbidelli, M., 2000. Simulated moving-bed chromatography and its application to chirotechnology. Trends Biotechnol. 18, 108–118.

Kang, S.H., Shortreed, M.R., Yeung, E.S., 2001. Real-time dynamics of single-DNA molecules undergoing adsorption and desorption at liquid-solid interfaces. Anal. Chem. 73, 1091–1099.

Kang, S.H., Yeung, E.S., 2002. Dynamics of single-protein molecules at a liquid/solid interface: implications in capillary electrophoresis and chromatography. Anal. Chem. 74, 6334–6339.

Kawai, T., Saito, K., Lee, W., 2003. Protein binding to polymer brush, based on ion-exchange, hydrophobic, and affinity interactions. J. Chromatogr. B 790, 131–142.

Kihm, K.D., Banerjee, A., Choi, C.K., Takagi, T., 2004. Near-wall hindered Brownian diffusion of nanoparticles examined by three-dimensional ratiometric total internal reflection fluorescence microscopy (3-D R-TIRFM). Exp. Fluids 37, 811–824.

Kim, J.T., Anderson, J.L., 1989. Hindered transport through micropores with adsorbed polyelectrolytes. J. Memb. Sci. 47, 163–182.

Kim, J.T., Anderson, J.L., 1991. Diffusion and flow through polymer-lined micropores. Ind. Eng. Chem. Res. 30, 1008–1016.

Kisley, L., Chen, J., Mansur, A.P., Dominguez-Medina, S., Kulla, E., Kang, M.K., Shuang, B., Kourentzi, K., Poongavanam, M.-V., Dhamane, S., Willson, R.C., Landes, C.F., 2014. High ionic strength narrows the population of sites participating in protein ion-exchange adsorption: a single-molecule study. J. Chromatogr. A 1343, 135–142.

Knox, J.H., Ritchie, H.J., 1987. Determination of pore size distribution curves by size-exclusion chromatography. J. Chromatogr. A 387, 65–84.

Koku, H., 2011. Microstructure-based analysis and simulation of flow and mass transfer in chromatographic stationary phases. Ph.D. thesis, University of Delaware.

Koshari, S.H.S., Wagner, N.J., Lenhoff, A.M., 2015. Characterization of lysozyme adsorption in cellulosic chromatographic materials using small-angle neutron scattering. J. Chromatogr. A 1399, 45–52.

Kremer, M., Pothmann, E., Roessler, T., Baker, J., Yee, A., Blanch, H., Prausnitz, J.M., 1994. Pore-size distributions of cationic polyacrylamide hydrogels varying in initial monomer concentration and cross-linker/monomer ratio. Macromolecules 27, 2965–2973.

Kuhner, M., Sackmann, E., 1996. Ultrathin hydrated dextran films grafted on glass : preparation and characterization of structural, viscous, and elastic properties by quantitative microinterferometry. Langmuir 12, 4866–4876.

Kwok, K.C., Yeung, K.M., Cheung, N.H., 2007. Adsorption kinetics of bovine serum albumin on fused silica: population heterogeneities revealed by single-molecule fluorescence microscopy. Langmuir 23, 1948–1952.

Langford, J.F., Schure, M.R., Yao, Y., Maloney, S.F., Lenhoff, A.M., 2006. Effects of pore structure and molecular size on diffusion in chromatographic adsorbents. J. Chromatogr. A 1126, 95–106.

Larsen, T.H., Furst, E.M., 2008. Microrheology of the liquid-solid transition during gelation. Phys. Rev. Lett. 100, 146001.

Laurent, T.C., Killander, J., 1964. A theory of gel filtration and its experimental verification. J. Chromatogr. A 14, 317–330.

Lenhoff, A.M., 2008. Multiscale modeling of protein uptake patterns in chromatographic particles. Langmuir 24, 5991–5995.

Lenhoff, A.M., 2011. Protein adsorption and transport in polymer-functionalized ion-exchangers. J. Chromatogr. A 1218, 8748–8759.

Levins, D.M., Glastonbury, J.R., 1972. Application of Kolmogoroff's theory to particle—liquid mass transfer in agitated vessels. Chem. Eng. Sci. 27, 537–543.

Lewus, R.A., Darcy, P.A., Lenhoff, A.M., Sandler, S.I., 2011. Interactions and phase behavior of a monoclonal antibody. Biotechnol. Prog. 27, 280–289.

Lewus, R.A., Levy, N.E., Lenhoff, A.M., Sandler, S.I., 2015. A comparative study of monoclonal antibodies. 1. Phase behavior and protein – protein interactions. Biotechnol. Prog. 31, 268-276.

Lewus, R.K., Altan, F.H., Carta, G., 1998. Protein adsorption and desorption on gel-filled rigid particles for ion exchange. Ind. Eng. Chem. Res. 37, 1079–1087.

Lewus, R.K., Carta, G., 1999. Protein diffusion in charged polyacrylamide gels. Visualization and analysis. J. Chromatogr. A 865, 155–168.

Lins, R.D., Pereira, C.S., Hünenberger, P.H., 2004. Trehalose-protein interaction in aqueous solution. Proteins Struct. Funct. Genet. 55, 177–186.

Lipson, A., Lipson, S.G., Lipson, H., 2010. Optical Physics, 4th ed. Cambridge University Press, Cambridge.

Ljunglöf, A., Hjorth, R., 1996. Confocal microscopy as a tool for studying protein adsorption to chromatographic matrices. J. Chromatogr. A 743, 75–83.

Ljunglöf, A., Thömmes, J., 1998. Visualising intraparticle protein transport in porous adsorbents by confocal microscopy. J. Chromatogr. A 813, 387–395.

Mabry, J.N., Skaug, M.J., Schwartz, D.K., 2014. Single-molecule insights into retention at a reversed-phase chromatographic interface. Anal. Chem. 86, 9451-9458.

Migliorini, C., Mazzotti, M., Morbidelli, M., 1998. Continuous chromatographic separation through simulated moving bed under linear and nonlinear conditions. J. Chromatogr. A 827, 161–173.

Miksa, D., Irish, E.R., Chen, D., Composto, R.J., Eckmann, D.M., 2006. Dextran functionalized surfaces via reductive amination: morphology, wetting, and adhesion. Biomacromolecules 7, 557–564.

Miksa, D., Irish, E.R., Chen, D., Composto, R.J., Eckmann, D.M., 2011. Biomimetic surfaces via dextran immobilization: grafting density and surface properties. MRS Proc. 826, V2.2.

Moore, S.A., Anderson, B.F., Groom, C.R., Haridas, M., Baker, E.N., 1997. Three-dimensional structure of diferric bovine lactoferrin at 2.8 A resolution. J. Mol. Biol. 274, 222–236.

Morrison, C., Lähteenmäki, R., 2015. Public biotech in 2014—the numbers. Nat. Biotechnol. 33, 703–709.

Müller, E., 2005. Properties and characterization of high capacity resins for biochromatography. Chem. Eng. Technol. 28, 1295–1305.

Müller-Späth, T., Krättli, M., Aumann, L., Ströhlein, G., Morbidelli, M., 2010. Increasing the activity of monoclonal antibody therapeutics by continuous chromatography (MCSGP). Biotechnol. Bioeng. 107, 652–662.

Muschol, M., Rosenberger, F., 1997. Liquid-liquid phase separation in supersaturated lysozyme solutions and associated precipitate formation/crystallization. J. Chem Phys. 107, 1953-1962.

Narambuena, C.F., Angelo, J., Longo, G.S., Lenhoff, A., Szleifer, I., in preparation. Competitive adsorption of small globular proteins on ion-exchange media: tuning preferential adsorption using pH and salt concentration.

Narambuena, C.F., Longo, G.S., Szleifer, I., 2015. Lysozyme adsorption in pH-responsize thin-films: the non-trivial role of acid-base equilibrium. Soft Matter 11, 6669–6679.

Necina, R., Amatschek, K., Jungbauer, A., 1998. Capture of human monoclonal antibodies from cell culture supernatant by ion exchange media exhibiting high charge density. Biotechnol. Bioeng. 60, 689–98.

Ni Dhubhghaill, O.M., Sadler, P.J., Tucker, A., 1992. Drug-induced reactions of bovine serum albumin: proton NMR studies of gold binding and cysteine release. J. Am. Chem. Soc. 114, 1118–1120.

Niimura, N., Minezaki, Y., Ataka, M., Katsura, T., 1995. Aggregation in supersaturated lysozyme solution studied by time-resolved small angle neutron scattering. J. Cryst. Growth 154, 136-144.

Norton, R.S., Allerhand, A., 1977. Participation of tryptophan 62 in the self-association of hen egg white lysozyme. J. Biol. Chem. 252, 1795-1798.

Nozaki, Y., Bunville, L.G., Tanford, C., 1959. Hydrogen ion titration curves of β-lactoglobulin. Phys. Inorg. Chem. 81, 5523-5529.

Ogston, A.G., 1958. The spaces in a uniform random suspension of fibres. Trans. Faraday Soc. 54, 1754-1757.

Perez-Almodóvar, E.X., Tao, Y., Carta, G., 2011. Protein adsorption and transport in cation exchangers with a rigid backbone matrix with and without polymeric surface extenders. Biotechnol. Prog. 27, 1264–1272.

Perez-Almodóvar, E.X., Wu, Y., Carta, G., 2012. Multicomponent adsorption of monoclonal antibodies on macroporous and polymer grafted cation exchangers. J. Chromatogr. A 1264, 48–56.

Peters, T.J., 1985. Serum albumin. Adv. Protein Chem. 37, 161–245.

Peterson, E.A., 1970. Cellulosic ion exchangers. In: Work, T.S., Work, E. (Eds.), Laboratory Techniques in Biochemistry and Molecular Biology. North-Holland Publishing Company, Amsterdam.

Peterson, E.A., Sober, H.A., 1956. Chromatography of proteins. I. Cellulose ion-exchange adsorbents. J. Am. Chem. Soc. 78, 751–755.

Peula-Garcia, J.M., Hidaldo-Alvarez, R., De Las Nieves, F.J., 1997. Protein co-adsorption on different polystyrene latexes: electrokinetic characterization and colloidal stability. Colloid Polym. Sci. 275, 198–202.

Plate, K., Beutel, S., Buchholz, H., Demmer, W., Fischer-Frühholz, S., Reif, O., Ulber, R., Scheper, T., 2006. Isolation of bovine lactoferrin, lactoperoxidase and enzymatically prepared lactoferricin from proteolytic digestion of bovine lactoferrin using adsorptive membrane chromatography. J. Chromatogr. A 1117, 81–86.

Ries, J., Petrov, E.P., Schwille, P., 2008. Total internal reflection fluorescence correlation spectroscopy: effects of lateral diffusion and surface-generated fluorescence. Biophys. J. 95, 390–399.

Satterfield, C.N., 1970. Mass transfer in heterogeneous catalysis. M.I.T. Press, Cambridge, MA.

Sawyer, L., Kontopidis, G., 2000. The core lipocalin, bovine beta-lactoglobulin. Biochem. Biophys. Acta 1482, 136–148.

Seidel-Morgenstern, A., Keßler, L.C., Kaspereit, M., 2008. New developments in simulated moving bed chromatography. Chem. Eng. Technol. 31, 826–837.

Sherwood, T.K., Pigford, R.L., Wilke, C.R., 1975. Mass Transfer. McGraw Hill, New York.

Shi, Q.-H., Jia, G.-D., Sun, Y., 2010. Dextran-grafted cation exchanger based on superporous agarose gel: adsorption isotherms, uptake kinetics and dynamic protein adsorption performance. J. Chromatogr. A 1217, 5084–5091.

Skaug, M., Mabry, J., Schwartz, D., 2013. Single-molecule tracking of polymer surface diffusion. J. Am. Chem. Soc. 136, 1327–1332.

Slater, G.W., Rousseau, J., Noolandi, J., Turmel, C., Lalande, M., 1988. Quantitative analysis of the three regimes of DNA electrophoresis in agarose gels. Biopolymers 27, 509–524.

Sophianopoulos, A.J., Rhodes, C.K., Holcomb, D.N., Van Holde, K.E., 1962. Physical studies of lysozyme. I. Characterization. J. Biol. Chem. 237, 1107–1112.

Staby, A., Jensen, I.H., Mollerup, I., 2000. Comparison of chromatographic ion-exchange resins. I. Strong anion-exchange resins. J. Chromatogr. A 897, 99–111.

Staby, A., Jensen, R.H., 2001. Comparison of chromatographic ion-exchange resins II. More strong anion-exchange resins. J. Chromatogr. A 908, 149–161.

Stone, M.C., Carta, G., 2007. Protein adsorption and transport in agarose and dextran-grafted agarose media for ion exchange chromatography. J. Chromatogr. A 1146, 202–215.

Stone, M.C., Tao, Y., Carta, G., 2009. Protein adsorption and transport in agarose and dextran-grafted agarose media for ion exchange chromatography: Effect of ionic strength and protein characteristics. J. Chromatogr. A 1216, 4465–4474.

Strauss, D.M., Gorrell, J., Plancarte, M., Blank, G.S., Chen, Q., Yang, B., 2009. Anion exchange chromatography provides a robust, predictable process to ensure viral safety of biotechnology products. Biotechnol. Bioeng. 102, 168–175.

Sukhishvili, S.A., Granick, S., 1999. Adsorption of human serum albumin: Dependence on molecular architecture of the oppositely charged surface. J. Chem. Phys. 110, 10153–10161.

Swinnen, K., Krul, A., Van Goidsenhoven, I., Van Tichelt, N., Roosen, A., Van Houdt, K., 2007. Performance comparison of protein A affinity resins for the purification of monoclonal antibodies. J. Chromatogr. B Anal. Technol. Biomed. Life Sci. 848, 97–107.

Szleifer, I., 1997. Protein adsorption on surfaces with grafted polymers: a theoretical approach. Biophys. J. 72, 595–612.

Tao, Y., Carta, G., Ferreira, G., Robbins, D., 2011a. Adsorption of deamidated antibody variants on macroporous and dextran-grafted cation exchangers: II. Adsorption kinetics. J. Chromatogr. A 1218, 1530–1537.

Tao, Y., Carta, G., Ferreira, G., Robbins, D., 2011b. Adsorption of deamidated antibody variants on macroporous and dextran-grafted cation exchangers: I. Adsorption equilibrium. J. Chromatogr. A 1218, 1519–29.

Tao, Y., Chen, N., Carta, G., Ferreira, G., Robbins, D., 2012. Modeling multicomponent adsorption of monoclonal antibody charge variants in cation exchange columns. AIChE J. 58, 2503–2511.

Tao, Y., Perez, E.X., Carta, G., Ferreira, G., Robbins, D., 2011c. Adsorption kinetics of deamidated antibody variants on macroporous and dextran-grafted cation exchangers. III . Microscopic studies. J. Chromatogr. A 1218, 8027–8035.

Teo, W.K., Ruthven, D.M., 1986. Adsorption of water from aqueous ethanol using 3 Å molecular sieves. Ind. Eng. Chem. Process Des. Dev. 25, 17–21.

Teske, C.A., Simon, R., Niebisch, A., Hubbuch, J. 2007. Changes in retention behavior of fluorescently labeled proteins during ion-exchange chromatography caused by different protein surface labeling positions. Biotechnology Bioeng. 98, 193–200.

Thompson, N., 1981. Measuring surface dynamics of biomolecules by total internal reflection fluorescence with photobleaching recovery or correlation spectroscopy. Biophys. J. 33, 435–454.

Thompson, N.L., Axelrod, D., 1983. Immunoglobulin surface-binding kinetics studied by total internal reflection with fluorescence correlation spectroscopy. Biophys. J. 43, 103–114.

Traylor, S.J., 2013. Novel approaches to understand and predict multicomponent protein sorption and kinetics in chromatographic materials. Ph.D. thesis, University of Delaware.

Traylor, S.J., Bowes, B.D., Ammirati, A.P., Timmick, S.M., Lenhoff, A.M., 2014. Fluorescence recovery after photobleaching investigation of protein transport and exchange in chromatographic media. J. Chromatogr. A 1340, 33–49.

Tsumoto, K., Umetsu, M., Kumagai, I., Ejima, D., Philo, J.S., Arakawa, T., 2004. Role of arginine in protein refolding, solubilization, and purification. Biotechnol. Prog. 20, 1301–1308.

Ubiera, A.R., Carta, G., 2006. Radiotracer measurements of protein mass transfer: kinetics in ion exchange media. Biotechnol. J. 1, 665–674.

Vandenberg, E.T., Bertilsson, L., Liedberg, B., Uvdal, K., Erlandsson, R., Elwing, H., Lundström, I., 1991. Structure of 3-aminopropyl triethoxy silane on silicon oxide. J. Colloid Interface Sci. 147, 103–118.

Walsh, G., 2010. Biopharmaceutical benchmarks 2010. Nat. Biotechnol. 28, 917-924.

Wang, D., Sun, Y., 2007. Fabrication of superporous cellulose beads with grafted anion-exchange polymer chains for protein chromatography. Biochem. Eng. J. 37, 332–337.

Wang, D.-M., Hao, G., Shi, Q.-H., Sun, Y., 2007. Fabrication and characterization of superporous cellulose bead for high-speed protein chromatography. J. Chromatogr. A 1146, 32–40.

Weaver, L.E., Carta, G., 1996. Protein adsorption on cation exchangers: comparison of macroporous and gel-composite media. Biotechnol. Prog. 12, 342–355.

Wesselingh, J.A., Bosma, J.C., 2001. Protein ion-exchange adsorption kinetics. AIChE J. 47, 1571–1580.

Wetter, L.R., Deutsch, H.F., 1951. Immunological studies on egg white proteins. IV. Immunochemical and physical studies of lysozyme. J. Biol. Chem. 192, 237–242.

Xie, G., Timasheff, S.N., 1997. The thermodynamic mechanism of protein stabilization by trehalose. Biophys. Chem. 64, 25–43.

Xu, X., Lenhoff, A.M., 2009. Binary adsorption of globular proteins on ion-exchange media. J. Chromatogr. A 1216, 6177–6195.

Yang, K., Bai, S., Sun, Y., 2008. Protein adsorption dynamics in cation-exchange chromatography quantitatively studied by confocal laser scanning microscopy. Chem. Eng. Sci. 63, 4045–4054.

Yang, K., Shi, Q.-H., Sun, Y., 2006. Modeling and simulation of protein uptake in cation exchanger visualized by confocal laser scanning microscopy. J. Chromatogr. A 1136, 19–28.

Yao, Y., Czymmek, K.J., Pazhianur, R., Lenhoff, A.M., 2006. Three-dimensional pore structure of chromatographic adsorbents from electron tomography. Langmuir 22, 11148–11157.

Yao, Y., Lenhoff, A.M., 2004. Determination of pore size distributions of porous chromatographic adsorbents by inverse size-exclusion chromatography. J. Chromatogr. A 1037, 273–282.

Yao, Y., Lenhoff, A.M., 2006. Pore size distributions of ion exchangers and relation to protein binding capacity. J. Chromatogr. A 1126, 107–119.

Yu, L.-L., Shi, Q.-H., Sun, Y., 2011. Effect of dextran layer on protein uptake to dextran-grafted adsorbents for ion-exchange and mixed-mode chromatography. J. Sep. Sci. 34, 2950–2959.

Yu, L.-L., Sun, Y., 2013. Protein adsorption to poly(ethylenimine)-modified Sepharose FF: II. Effect of ionic strength. J. Chromatogr. A 1305, 85–93.

Yu, L.-L., Tao, S.-P., Dong, X.-Y., Sun, Y., 2013. Protein adsorption to poly(ethylenimine)-modified Sepharose FF: I. A critical ionic capacity for drastically enhanced capacity and uptake kinetics. J. Chromatogr. A 1305, 76–84.

Zhou, X.-P., Li, W., Shi, Q.-H., Sun, Y., 2006. Analysis of mass transport models for protein adsorption to cation exchanger by visualization with confocal laser scanning microscopy. J. Chromatogr. A 1103, 110–117.

Zydney, A.L., Harinarayan, C., van Reis, R., 2009. Modeling electrostatic exclusion effects during ion exchange chromatography of monoclonal antibodies. Biotechnol. Bioeng. 102, 1131–1140.

Appendix A

ADSORPTION ISOTHERMS FOR SEPHAROSE AND CAPTO MATERIALS

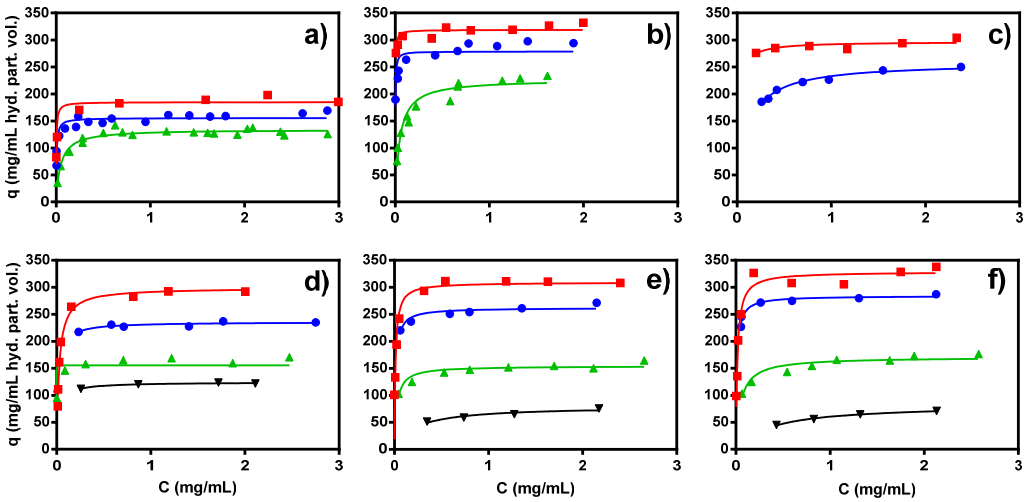

Figure A.1 Adsorption isotherms for lysozyme (a, b, c) and lactoferrin (d, e, f) on SP Sepharose Fast Flow (a, d), SP Sepharose XL (b, e) and Capto S (c, f). Performed in 10 mM sodium phosphate, pH 7 at 20 (■), 50 (●), 100 (▲), and 200 (▼) mM TIS. Data borrowed from Bowes et al. (2009) and shown with fits to the Langmuir isotherm for each condition.

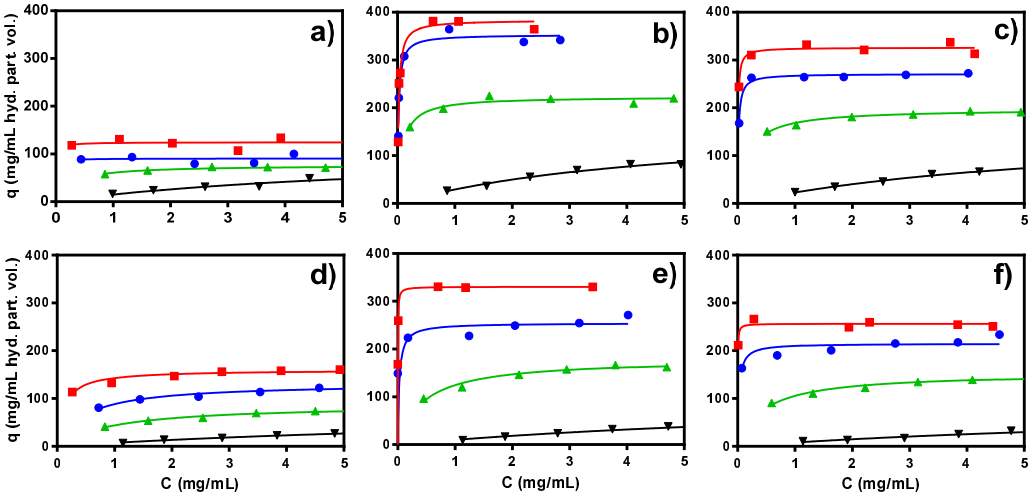

Figure A.2 Adsorption isotherms for β-lactoglobulin (a, b, c) and BSA (d, e, f) on Q Sepharose Fast Flow (a, d), Q Sepharose XL (b, e) and Capto Q (c, f). Performed in 50 mM bis-tris, pH 7 at 20 (■), 50 (●), 100 (▲), and 200 (▼) mM TIS. Data shown with fits to the Langmuir isotherm for each condition.

Appendix B

RATE MODELS FOR COLUMN ELUTION

B.1 Differential-Column Model

The simplest model is one in which all the particles behave identically, and the elution rate is low enough, or the intraparticle concentration is high enough, that the mobile-phase concentration remains negligible relative to that in the particles. In this case Equations 4.3 and 4.5 apply simultaneously to all particles and again the long-time trend of the mobile-phase concentration should be a monoexponential decay, from which D_e can be estimated.

The assumption of synchronous behavior of all particles is most simply satisfied for a differentially short column, but more generally for one in which the mobile-phase residence time is much shorter than the characteristic time for diffusion out of a particle, $R_p^2 = D_e$. There is a second assumption implicit in this model as well, namely that the eluent reaches all the particles simultaneously; this assumption is also satisfied for practical purposes in the short-residence-time limit, where the high diffusivities of salts used as eluents in ion exchange help to ensure the minimization of intraparticle gradients.

B.2 Long–Column Model

Allowing for axial variation along the column accounts for multiple effects. One is the different arrival times with axial position of the eluent and hence the

different desorption times of the protein, resulting in different t = 0 points for the efflux described by Equation 4.5. A second is the fact that the eluent arriving at the column exit at any time receives protein from particles at different axial positions at different points in the efflux process in Equation 4.5. Although these two effects should follow essentially the same time course because the axial delay in each case is due to axial flow, there may be additional subtle differences, so allowance for axial variation is appropriate.

We approach this using a Lagrangian viewpoint in which a body of mobile phase receives efflux at different axial positions at different effective times τ' in the efflux process, where $\tau = tD_e/R_p^2$. The value of τ' is affected by the axial position both in that it determines the time of contact and the time of desorption. Therefore the protein concentration in the eluate is

$$c_{eluate} \propto \int_{\tau-\tau_r}^{\tau} \sum_i a_i e^{-\beta_i \tau'} d\tau' = -\sum_i \frac{a_i}{\beta_i}\left(1 - e^{\beta_i \tau_r}\right)e^{-\beta_i \tau} \qquad \text{(B.1)}$$

and again $e^{-\beta_i \tau}$ dependence is recovered at long times.

B.3 General Rate Model

For a more complete description of column behavior we use what is usually referred to as the general linear rate model, although the specification of linearity is redundant in the present case because of the absence of adsorption. Now the intraparticle Equation 4.2.1 is augmented by the conservation equation for the concentration in the mobile phase, c_m,

$$\frac{\partial c_m}{\partial t} + u\frac{\partial c_m}{\partial z} = D_m \frac{\partial^2 c_m}{\partial z^2} - \frac{3(1-\varepsilon)}{\varepsilon}\frac{k}{R_p}\left(c_m - Kc_s|_{r=R_p}\right) \qquad \text{(B.2.1)}$$

with the boundary conditions (Danckwerts, 1953)

$$uc_m - D_m \frac{\partial c_m}{\partial z} = 0, \; z = 0 \tag{B.2.2}$$

$$\frac{\partial c_m}{\partial z} = 0, \; z = L \tag{B.2.3}$$

In addition, the boundary condition at the particle surface, Equation 4.2.3, must be modified to account for the finite mobile-phase concentration

$$-D_e \frac{\partial c_s}{\partial r} = k(Kc_s - c_m), \; r = R_p \tag{B.3}$$

In this formulation, u is the mobile-phase velocity, D_m is the axial dispersion coefficient, ε is the column interstitial porosity and K is a partition coefficient between the mobile-phase and the particle interior. An initial condition must of course be specified for a complete solution, but it is unnecessary for the approach taken here.

A formal solution for this model can be developed by separation of variables; this is facilitated by introducing dimensionless variables and parameters, of which the independent variables are $\tau = tD_e/R_p^2$ and $\eta = r/R_p$, as well as $\zeta = z/L$. The solution takes the form

$$\begin{pmatrix} c_m \\ c_s \end{pmatrix} = \sum_m Z_m(\zeta) \sum_n A_{nm} T_{nm}(\tau) \begin{pmatrix} B_{nm} \\ R_{nm}(\eta) \end{pmatrix} \tag{B.4}$$

which converges unreasonably slowly to use for computing full elution profiles. However, the form is convenient to exploit in the long-time limit that is readily accessible experimentally, so further elaboration of the solution is appropriate.

The eigenfunctions Z, T and R can be determined straightforwardly; of these the two of greater immediate interest for our purposes are the radial eigenfunctions R_{nm} and the temporal eigenfunctions T_{nm}, both of which take the same functional form as those in Equation 4.3,

$$R_{nm}(\eta) = \frac{\sin \beta_{nm} \eta}{\eta} \tag{B.5}$$

$$T_{nm}(\tau) = e^{-\beta_{nm}^2 \tau} \tag{B.6}$$

It follows from the form of Equation B.6 that even for this more complex model, the long-time behavior reduces to a monoexponential decay similar in form to that obtained previously. Again it is this decay and its decomposition based on the magnitudes of the leading eigenvalues that are critical in estimating the effective pore diffusivity D_e. However, additional complexity is concealed in the fact that the eigenvalues β_{nm} now have two indices because of the coupling to phenomena in the mobile phase. These are accounted for partly via the axial eigenfunctions

$$Z_m(\zeta) = e^{Pe\zeta/2}\left(\lambda_m \cos\lambda_m\zeta + \frac{Pe}{2}\sin\lambda_m\zeta\right) \tag{B.7}$$

where $Pe = uL/D_m$ and $E_m = D_m/D_e$, and the eigenvalues λ_m are the roots of the characteristic equation

$$Pe\lambda_m + \left(\frac{Pe^2}{4} - \lambda_m^2\right)\tan\lambda_m = 0 \tag{B.8}$$

If the axial boundary condition (Equation B.2.2) is changed to a purely convective one, the form of the axial eigenfunctions (Equation B.7) is altered somewhat by the elimination of the cosine term, but at the high Péclet numbers, *Pe*, prevailing in systems of interest, the difference in algebraic complexity is much more significant than the numerical effect on the eigenvalues. Specifically, at high values of *Pe* the leading eigenvalue is π in the purely convective limit, while Equation B.8 becomes approximately $\tan\lambda_m = -4\lambda_m/Pe$ in the high *Pe* limit, which again has its first root $\lambda_m = \pi$.

The coupling of mobile-phase and intraparticle phenomena occurs via the differential equation for the mobile phase (Equation B.2.1) and the surface boundary condition for the stationary phase (Equation B.3), which result in a characteristic equation for the eigenvalues β_{nm}:

$$\beta_{nm}\cot\beta_{nm} + \mathrm{BiK}\left(1 - \frac{\xi \mathrm{Bi}}{\delta^2 \mathrm{E_m}\left(\lambda_m^2 + \frac{Pe^2}{4}\right) - \beta_{nm}^2 + \xi \mathrm{Bi}}\right) - 1 = 0 \qquad \text{(B.9)}$$

where $\delta = R/L$ and $\xi = 3(1-\varepsilon)/\varepsilon$. Equation B.9 differs from the characteristic equation (Equation 4.4) for the isolated particle only in that the Bi term is modified by the presence of the partition coefficient K and the second term in parentheses, with the deviation of the latter term from zero being the key determinant of the deviation of the leading eigenvalues from that of β_1 for the isolated particle. For the experiments performed here, flow velocities are of order hundreds of cm/hr, particle radii of order 50 μm, column lengths of order cm and free-solution diffusivities of order 10^{-6} to 10^{-7} cm^2/s, and ξ and K are of order unity. Therefore particle Péclet numbers based on the free-solution diffusivity would be of order 10^2 or higher, and for such values E_m would be of order 10^2 or higher (Han et al., 1985), with D_m significantly greater than and D_e less than the free-solution diffusivity. It follows that, for the leading axial eigenvalues λ_m, $Pe^2 >> \lambda_m^2$, as a result of which the magnitude of the second term in parentheses is determined by $\delta^2 E_m Pe^2/4\xi\mathrm{Bi} = (u/k)(\delta Pe/4\xi)$, which is independent of D_e and of order 10 or greater in our work, making the perturbation small relative to the isolated particle. Furthermore, the leading eigenvalue of Equation 4.4 varies little for Bi values significantly > 1, as is the case here; β_1 increases monotonically from 2.8363 to π as Bi increases from 10 to ∞ (Crank, 1975). Therefore basing estimation of D_e on the leading eigenvalue for the isolated particle introduces relatively little error.

Appendix C

ADDITIONAL COLUMN ELUTION RESULTS FOR STAR AX HYPERCEL

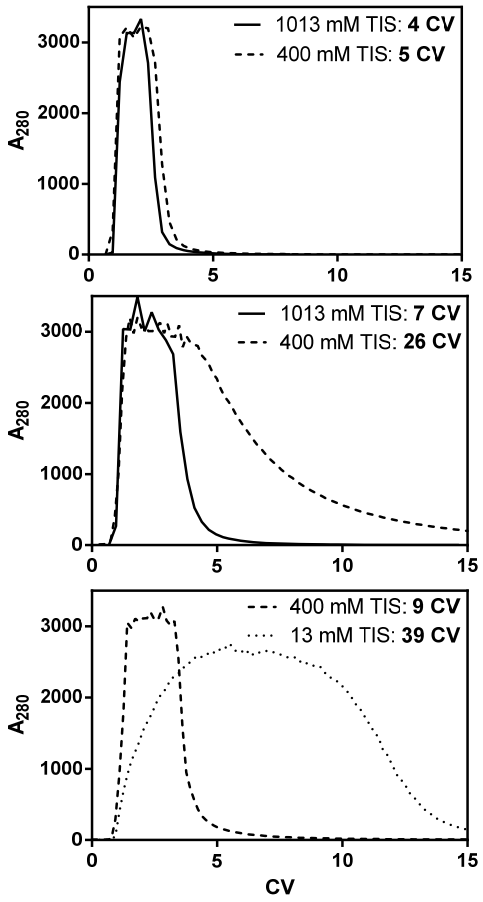

Figure C.1 β-lactoglobulin elution profiles on Q HyperCel at pH 7 (top), STAR AX HyperCel at pH 7 (middle) and STAR AX HyperCel at pH 4 (bottom) at varied TIS conditions. Column volumes required for full elution of protein (to 100 mAU) are shown on each plot following a loading period to 60% of the total DBC in each case. The reduction in pH from pH 7 to pH 4 assists in the more complete recovery of the protein at 400 mM TIS in the salt tolerant material.

Appendix D

PUBLICATION REPRINT PERMISSIONS

Content in Chapter 2 of this dissertation is reprinted from the Journal of Chromatography A, 1319, James M. Angelo, Aleksandar Cvetkovic, Rene Gantier, and Abraham M. Lenhoff, Characterization of cross-linked cellulosic ion-exchange adsorbents: 1. Structural properties, Pages 46-56, Copyright 2013, with permission from Elsevier (doi:10.1016/j.chroma.2013.10.003).

Content in Chapter 3 of this dissertation is reprinted from the Journal of Chromatography A, 1438, James M. Angelo, Aleksandar Cvetkovic, Rene Gantier, and Abraham M. Lenhoff, Characterization of cross-linked cellulosic ion-exchange adsorbents: 2. Protein sorption and transport, Pages 100-112, Copyright 2016, with permission from Elsevier (doi:10.1016/j.chroma.2016.02.019).

Content in Chapter 4 of this dissertation is reprinted from the Journal of Chromatography A, 1440, James M. Angelo and Abraham M. Lenhoff, Determinants of protein elution rates from preparative ion-exchange adsorbents, Pages 94-104, Copyright 2016, with permission from Elsevier (doi:10.1016/j.chroma.2016.02.048).